Bodies of cunicularity in supersonic flow

Sabrina Gabrielle Myburgh

A thesis submitted to the Faculty of Engineering and the Built Environment, University of the Witwatersrand, Johannesburg, in fulfilment of the requirements for the degree of Doctor of Philosophy.

Johannesburg, August 2024

Declaration

I declare that this thesis is my own, unaided work, except where otherwise acknowledged. It is being submitted for the degree of Doctor of Philosophy in the University of the Witwatersrand, Johannesburg. It has not been submitted before for any degree or examination at any other university.

Signed this 16th day of August 2024

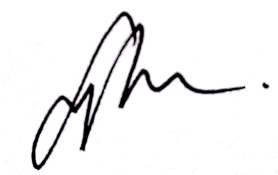

Sabrina Gabrielle Myburgh

To my brother, Renier.

Acknowledgements

I would like to thank my supervisor Professor Craig Law for his guiding wisdom, motivation and profoundly knowledgable guidance during his supervision of my dissertation. Your passion for gas dynamics, level of expertise and your ability to reduce the most complicated problems to simple explanations is a skill I greatly admire, and strive to emulate. Thank you for taking me on as a student, and for allowing me the freedom to master my research in the direction of my own choosing. The outcome has been rather extraordinary. I am sincerely grateful to you, for everything that you have done for me.

To Professor Beric W. Skews. It was after attending a lecture given by you in 2018 that I decided to peruse a path in compressible gas dynamics. You have been a source of motivation, inspiration and knowledge that I am so grateful for. Your teachings have been the foundation for all of this research, and I thank you for this.

To Dr. Randall T. Paton, thank you for your contribution and advisement for this research, and for your assistance in passing down your numerical and experimental fluids knowledge.

To Mr. Michael Boer, thank you for all of the support, encouragement and advice you have given me during my years at Wits. You have provided much guidance, and I am very grateful for your teachings.

To the staff members of the North West Engineering workshop, in particular to Mr. Shaun Riekert, Mr. Andrew Heydenrych and Mr. Vernondran (Rowan) Parumal. Thank you for your extensive technical assistance, patience and excellent manufacturing of the force balance, test rig and conic models used to obtain the experimental results. Your committent to the

students and to maintaining the quality of the MIA laboratory is always appreciated. Thank you for imparting so much of your knowledge and experience to me over the years.

I would like to thank several individuals for their contributions to the research; To Mr. Dean van Aswegen, for assisting in the 3D resin printer laboratory set-up and calibration which made the porous model manufacture (and by extension this research) possible; to Mr. Tristan Strydom, for assisting in the set-up and calibration of the force balance; to Professor Bruce Watson at the Wits School of Mathematics, for your guidance and assistance in understanding the mathematics behind the porous structure; to Mr. Francesco Pietra and Professor Wei Hua Ho, for your advice and guidance on many topics. To Mr. Charles Crosby and his team at the Centre for High Computing (CHPC) South Africa for providing the computational resources and technical support required to successfully run the models. Your quick-responses, patience and time spent on this project are very much appreciated.

A most appreciated thank you to my family, in particular my parents, Connie and Gudrun, for supporting and pushing me to achieve only the best throughout my studies. Your guidance, encouragement and support during the development of this dissertation has been invaluable. Finally, to my partner, Pano. Thank you for making this experience bearable, and for never letting me give up.

Abstract

Prior studies outlined the success of using randomised High Porosity Cellular Material cylinders both numerically and experimentally, however showed limited applicability to real-life aerodynamics applications. The primary effect of supersonic flow over porous media is to attenuate the bow wave by reducing the angle of incidence and redistributing the flow field, significantly reducing wave drag.

The aim of this work was to investigate the drag-reduction effect of organised porosity within conic bodies of revolution on the supersonic flow field. Various organised porous cone-cylinders were developed to investigate the effect of the porous structure on the flow field, including shock waves, momentum changes and flow structures in and around the porous body. Several conic profiles were investigated.

A numerical and experimental investigation was carried out in steady, supersonic flow at Mach 3.5 ($\mathrm{Re} = 3.9 \times 10^{-5}$). The conic models had a porosity of $\approx 60\%$. The blow down supersonic wind tunnel facility at the University of the Witwatersrand was used for the experimentation, where schlieren photographs were captured along with drag force measurements of the solid and porous baseline cones. Numerical CFD simulations were carried out for a wider range of porous configurations using ANSYS Fluent R22.2. The numerical, experimental and literature C_d and flow visualisation were used to validate the numerical method, showing good agreement across data sets.

Certain cunicular arrangements effectively reduced the drag in some shapes, while others worsened the drag. The greatest drag reduction of 40% was achieved in the cunicular BS4 Ellipsoid. The change in drag was associated with three sources, namely wave drag, jet

interaction, and momentum addition by the jet. These changes resulted from the flow interactions occurring within the inlet, internal and venting structures. Changes in drag depended on several factors, including vent geometry, expansion ratio, exit angle, inlet geometry and the crossflow condition, to name a few. Wave drag reduction was dependent on shock attenuation and reducing the wave angle, which was generally ensured by the conic surface pores absorbing energy from the bow wave. The jet interaction and momentum recovery were dependent on vent expansion ratio, exit angle and crossflow condition.

The jet interaction had the greatest increase on the drag of the system, however, the effects of this were mitigated by using low vent angles with correct expansion ratios to maximise momentum recovery from the jet. The effect of the combined system was specific to the particular case, where the solid cone shape greatly influenced the overall performance. The effect on drag reduction was cumulative, sensitive and highly dependent on the individual case. The cunicular system is a viable drag reduction mechanism in conic bodies, however careful balancing of the porous inflow, outflow, bow wave and venting conditions is required in order to achieve significant drag reduction.

Published Work

- SG Myburgh, C Law, Angled Expanding Jet Impingement in Supersonic Crossflow, Proceedings of the Thirteenth South African Conference on Computational and Applied Mechanics, SACAM24, Stellenbosch, 22-23 January 2024
- SG Myburgh, RT Paton, BW Skews, Aerodynamic Structures Exhibiting Reduced Drag at Supersonic Speeds, Provisional patent application, Application No. 2023/11115, Filing Date - 1 December 2023, University of the Witwatersrand, Johannesburg

COPY OF PROVISIONAL SPECIFICATION

Application No.	2023/11115
Filing Date	1 December 2023
Your Ref	Aerodynamic Tunnel Technology
Our Ref	P96923ZP00
Name of Applicant(s)	University of the Witwatersrand, Johannesburg
Name of Inventor(s)	MYBURGH, Sabrina Gabrielle PATON, Randall Tyrone SKEWS, Beric William
Title of Invention	AERODYNAMIC STRUCTURES EXHIBITING REDUCED DRAG AT SUPERSONIC SPEEDS
Completion Date	1 December 2024

The specification has been drafted and the patent application has been filed on the assumption that the invention is "new". The fact that we have undertaken to file this application should NOT be interpreted as an indication or guarantee that a valid patent will be obtained for the invention.

If a patent based on this application is granted then its term will be 20 years commencing with the date of filing of the complete specification, subject to payment of renewal fees.

Please keep us promptly advised of any change of contact details.

Pretoria Office
012 432 6000
Lynnwood Bridge
4 Daventry Street
Lynnwood Manor
Pretoria

Johannesburg Office
011 895 1000
2nd Floor
34 Fredman Drive
(Corner 5th Street)
Sandton

Cape Town Office
021 418 8560
28th Floor
1 Thibault Square
Corner Long Street &
Hans Strijdom Avenue
Cape Town

Durban Office
031 536 8240
Suite 2, Level 3
21 Richefond Circle
Ridgeside Office Park
Umhlanga Ridge
Durban

FORM P1

REPUBLIC OF SOUTH AFRICA

PATENTS ACT, 1978

APPLICATION FOR A PATENT AND ACKNOWLEDGEMENT OF RECEIPT

[Section 30 (1)-Regulation 22]

The granting of a patent is hereby requested by the undermentioned applicant on the basis of the present application.

Official Application No.			Applicant's or Agent's Reference
21	01	**2023/11115**	P96923ZP00

71	Full Name(s) of Applicant(s)
	University of the Witwatersrand, Johannesburg 1 Jan Smuts Avenue, Braamfontein, 2001, SOUTH AFRICA

54	Title of invention
	AERODYNAMIC STRUCTURES EXHIBITING REDUCED DRAG AT SUPERSONIC SPEEDS

The applicant has claimed priority (if any) as set out in the abovementioned international application

~~This application is for a patent of addition to patent application No.~~

21	01	

~~This application is a fresh application in terms of section 37 and based on Application No.~~

21	01	

This application is accompanied by:

X	1.	A single copy of a provisional specification of 17 pages.
X	2.	Drawings of 11 sheet(s).
	3.	Publication particulars and Abstract(Form P8)
	4.	A copy of Figure of the drawings (if any) for the abstract
X	5.	Assignment of invention
	6.	Certified priority document(s)
	7.	Translation(s) of the priority document(s)
	8.	Assignment of priority rights
	9.	A copy of the Form P.2 and the specification of S.A Patent Application (if applicable).
X	10.	A declaration and power of attorney on Form P3
	11.	Statement on the use of indigenous Biological Resource, Genetic Resource, Traditional Knowledge or Use on Form P26
	12.	Request(s) for ante-dating/delay of acceptance on Form P4
	13.	Request for classification on Form P4

74	Address of Service:
	Adams & Adams Lynnwood Bridge, 4 Daventry Street, Lynnwood Manor, PRETORIA SOUTH AFRICA

Dated this 1st day of December 2023

Digitally signed by : Philip Pla-Pillans

.....

Signature of Applicant(s)

This is returned to the applicant's
address for service as proof of lodging.

RECEIVED
Official Date Stamp
..... Registrar of Patents

CONFIRMATION

This document has been generated by CIPC on this 4th day of December 2023

Contents

Declaration i

Acknowledgements iii

Abstract v

Published Work vii

Contents x

List of Figures xx

List of Tables xxxii

List of Acronyms xxxiv

1 Introduction 1

1.1 Cunicularity 1

1.2 Porous projectiles in supersonic flow 1

1.3 Aerodynamic drag 2

1.4 Shock waves . . . 3
1.4.1 Oblique shock waves . . . 4
1.4.2 θ-β-M relationship . . . 5
1.4.3 Conical shock formation . . . 8
1.4.4 Detached shock waves . . . 9
1.5 Porosity in aerodynamics . . . 11
1.5.1 Introduction . . . 11
1.5.2 Subsonic flow through and around a porous medium . . . 12
1.5.3 Supersonic flow through and around a porous medium . . . 15
1.6 Bibliometric study . . . 17
1.6.1 Existing literature . . . 17
1.6.2 Literature gap . . . 21
1.7 Critical Research Question . . . 22
1.8 Objectives . . . 22

2 Literature Review **23**

2.1 Introduction . . . 23
2.2 Porous supersonic flow for wave drag reduction . . . 24
2.2.1 Pseudo-steady state modelling . . . 29
2.3 Reflection of shock waves from porous materials . . . 31

2.3.1 Porous flat plates in supersonic flow 32

2.3.2 Organised supersonic flow 38

2.4 Additional relevant studies 42

2.4.1 The effect of porosity on the supersonic boundary layer 42

2.4.2 Jetting into supersonic cross flow 43

2.5 Conclusions 45

3 Research Method **46**

3.1 Research overview 47

3.2 Research methodology 48

3.3 Experimental method overview 49

3.4 Numerical method overview 51

3.5 Validation and verification overview 52

3.5.1 Numerical validation 53

3.5.2 Experimental validation 55

3.6 Design of conical test specimens overview 56

3.6.1 Conic model fundamentals 56

3.6.2 Conic model internal dispersion 57

3.6.3 Cone manufacture 60

3.6.4 Conic model testing and expansion 60

3.7 Conclusions 61

4 Experimentation **63**

4.1 Introduction 63

4.2 Supersonic wind tunnel testing facilities 64

4.2.1 Testing facility overview 64

4.2.2 Supersonic wind tunnel operation 64

4.2.3 Additional processes 65

4.2.4 Static pressure and electronic data measurements 66

4.3 Sting design 67

4.3.1 Sting components 68

4.4 Force Balance 73

4.4.1 Force balance design 73

4.4.2 Strain gauge arrangement 76

4.5 Flow Visualisation and Optical Instrumentation 78

4.6 Conic model design and development 79

4.6.1 Baseline (zeroth iteration) porous model design 82

4.6.2 First iteration porous models 92

4.6.3 Second iteration models 93

4.7 Experimental model manufacturing 96

4.7.1 3D printing processes for conic sections 96

4.7.2 Conic model strength testing 97

4.7.3 Conic model manufacturing 99

5 Numerical Modelling **100**

5.1 Introduction 100

5.2 Domain Geometry 100

5.2.1 Domain sizing 103

5.3 Meshing 104

5.3.1 Boundary conditions 104

5.3.2 Mesh generation 105

5.3.3 Domain discretisation 105

5.3.4 Steady-state solver specifications 107

5.4 Adaptive mesh refinement 110

5.4.1 Adaptive mesh refinement settings 112

5.4.2 Conclusions 113

6 Verification and Validation **114**

6.1 Numerical results 116

6.1.1 Time Convergence of the BS0 Cone 116

6.1.2 Numerical uncertainty 122

6.1.3 Solver uncertainty . . . 124
6.1.4 Critical analysis of boundary condition . . . 126
6.2 Experimentation . . . 128
6.2.1 Sting calibration . . . 128
6.2.2 Data collection . . . 130
6.3 Experimental Results . . . 132
6.3.1 Uncertainty . . . 133
6.3.2 Discussion . . . 137
6.4 Experimental Drag - Literature Comparison . . . 139
6.4.1 External flow - literature comparison . . . 139
6.4.2 Drag coefficient coherence- SSWT vs CFD . . . 143
6.4.3 Experimental C_d - literature comparison . . . 143
6.4.4 External flow - Numerical and Experimental Comparisons . . . 146
6.4.4.1 External flow - Right Triangular Cone . . . 147
6.4.4.2 External flow - Secant Ogive . . . 152
6.4.4.3 External flow - Ellipsoid . . . 154
6.4.4.4 External flow - Hemisphere . . . 156
6.4.5 Internal flow - literature comparison . . . 160
6.4.6 Venting flow - visual comparison . . . 161
6.5 Conclusions . . . 162

7 Results and Discussion 164

7.1 Non-porous baseline . . . 165

7.2 Flow field characteristics and porous flow topology . . . 168

7.3 Conic cunicular drag results . . . 169

7.4 Hypothesis of drag attribution . . . 171

7.4.1 Wave drag . . . 171

7.4.2 Jet interaction . . . 172

7.4.3 Momentum addition by the jet . . . 172

7.4.4 Flow field aspects of interest . . . 173

7.5 Inlet Flow Field . . . 173

7.5.1 BS0 - BS4 Overview . . . 175

7.5.2 The effect of mass flow rate on bow wave reduction . . . 179

7.5.3 Effect of vent angle on bow wave attenuation - BS0, BS1, BS4 . . . 180

7.5.4 Effect of inclined pores on bow wave attenuation - BS2, BS3 . . . 185

7.5.5 Effect of mass flow on wave angle . . . 190

7.5.6 Conclusions . . . 192

7.6 Venting Flow Field . . . 192

7.6.1 Overexpanded configuration . . . 195

7.6.2 Underexpanded configuration . . . 203

7.6.3 Horizontal Vent . . . 208

7.7 BS4 in Ellipsoid, Hemisphere and Secant Ogive . . . 210
7.7.1 BS4 Ellipsoid . . . 210
7.7.2 BS4 Hemisphere and BS4 Secant Ogive . . . 213
7.8 Internal Flow Field . . . 216
7.8.1 Internal network fluid behaviour . . . 216
7.8.2 Pressure gradient in the internal structure . . . 220
7.8.3 Jet Momentum . . . 221
7.9 Limitations . . . 224

8 Conclusions **225**

8.1 Validity and confidence . . . 226
8.2 Conic model drag reduction . . . 227
8.3 Bow wave attenuation . . . 227
8.4 Jet interaction . . . 228
8.5 Inflow - Outflow . . . 229
8.6 Momentum addition by jet . . . 230
8.7 BS4 in Cone, Ellipsoid, Hemisphere and Secant Ogive . . . 230
8.8 Drag reduction mechanisms - summary . . . 232
8.9 Recommendations . . . 232

References **236**

A Apparatus/Equipment Specifications **245**

B Safety during experimentation **248**

C Manufacturing apparatus **252**

C.1 Engineering drawing of the left side plate of the sting apparatus 253

C.2 Engineering drawing of the right side plate of the sting apparatus 254

C.3 Engineering drawing of the centre plate 255

C.4 Engineering drawing of the inner sting 256

C.5 Engineering drawing of the right side block 257

C.6 Engineering drawing of the left side block 258

C.7 Engineering drawing of the solid right cone 259

C.8 Engineering drawing of the bottom plate 260

C.9 Engineering drawing of the top block 261

C.10 Engineering drawing of the outer sting 262

C.11 Engineering drawing of the section views of the outer sting 263

D Nose Cone Profile **264**

D.1 Conical Profile 265

D.2 Secant ogive 266

D.3 Ellipsoid profile 267

E Creality LD-002R 3D Printer

- Technical Specifications **268**

E.1 Printer function 268

E.2 3D printing safety precautions 270

E.3 3D Conic model manufacturing 271

F 3D Printed Cone Iterations **274**

G Experimental schlieren Mach 3.5; Mach 3 results **277**

G.1 CFD Pointed Cone Mach 3 - BS0/Solid 280

G.2 Results of Unvented Combined Pointed Cone Mach 3.5 281

H Conic model schematics **282**

H.1 Pointed cones - Combined/Radial/Longitudinal models 283

H.2 Pointed cones - BS0 - BS4 284

H.3 Pointed cones vent-specific - OE, UE and CE 286

H.4 Pointed cones miscellaneous- HV and 72 Holes 287

H.5 Hemisphere and secant ogives - Solid and BS4H/S 288

List of Figures

1 Schlieren image of the flow field around a) a supersonic bullet b) a pointed cone 4

2 Schematic of a) supersonic flow approaching a corner with an oblique shock wave (and velocity components) b) detached shock wave 5

3 Chart showing the oblique shock angle (β), as a function of the corner angle, (θ), for lines of constant upstream Mach number (M_1) lines 7

4 Schematic of a) oblique shock formation over a cone b) shock polar in the pressure ratio-flow deflection angle plane for a Mach number of 1.8 and a specific heat ratio 1.4. 8

5 Schematics of porous materials: (left) closed-cell foam (right) open-cell foam . 12

6 Diagrams of porous structure: a) uniform material removal within structure b) uniform structure with external material removed c) spheres arranged uniformly in a spherical shape d) spheres arranged uniformly in a cube 13

7 Plots showing a) the number of publications issues per year that match the Maslov keyword search b) Plot of the number of citations per year for Maslov group keyword-specific search 19

8 Plots showing a) the number of publications issues per year that match the Skews keyword search b) Plot of the number of citations per year for Skews group keyword-specific search 20

9 Schlieren images of a) solid rod b) rod with frontal porous material (65 % porous) 25

10 Photographs of the a) cylinder models frontal HPCM inserts b) purely high-porous cylinder with pore diameter = 1 mm c) the 3D skeleton toroidal model of the high-porosity material 26

11 Schematic of the fluid movement resulting in drag reduction for a cylinder with a frontal gas-permeable insert 27

12 CFD images of streamlines for a) solid cylinder b) cylinder with the frontal gas-permeable porous insert 28

13 Computed isolines of density gradient for a) solid cylinder b) and cylinder with the gas-permeable insert c) Mach number isolines for a cylinder with gas-permeable porous insert 28

14 Interferograms of shock propagation over slitted wedge; model A for M =2.96; a) $\alpha = 44$ ° b) $\alpha = 40$° 33

15 Numerical shadowgraph images for different wall angles, percentage blockage ratio, and Mach number. a) 45 °, 25 %, M=1.367, b) 60 °, 33 %, M=1.352, c) 75 °, 50 %, M=1.359, d) 90 °, 33 %, M=1.508 33

16 Schematics of the a) the main features of the flow field, including key points b) normalised stagnation pressure difference as a function of wall angle and blockage ratio percentage 34

17 Numerical shadowgram of the effect of gap aspect ratio on a Mach 1.51 moving shock impinging on a 50% porous grid at 60° incidence; a) AR Gap = 1 b) AR Gap = 2 c) AR Gap = 4 37

18 Wedge models a) Alumina and SiC blocks. b) SiC models of various wedge angles. c) Organised rod structure models 38

19 Shadowgraph images of the flow field of the a) longitudinal rod model. b) transverse rod model 39

20 Schlieren images of the porous material wedges a) M=1.53, δc= 10°. b) M=1.56, δ=20 °. 40

21 Schematic of the a) blunt-body model of transverse injection into the supersonic flow b) circular gas injection into supersonic cross flow 44

22 Flow chart showing the research method process 48

23 Schematic comparing the porous hemisphere, ellipsoid, secant ogive and pointed cone BS4 vented model conical shapes characteristics 57

24 Blow-down supersonic wind tunnel diagram 64

25 Schematic of the supersonic wind tunnel (SSWT) and associated apparatus . 65

26 Static pressure traces of the SSWT settling chamber equivalent to test section stagnation pressure (Pa) during a 6 second Mach 3.5 test versus time (s). 66

27 Combined inner and outer sting with the flyer plate 68

28 Combined sting, flyer plate and support blocks. 70

29 Sting assembly a) side view c) front view 71

30 Wind tunnel sting assembly with force balance (left) flyer plate with strain gauges attached (right) 73

31 Annotated sting assembly with the strain gauges and wiring 74

32 a) back view of the sting c) front view the sting 75

33 Schematic of schlieren flow visualisation set-up 78

34 SSWT photographs of porous pointed cone BS0 models at Mach 3.5 using a) schlieren b) shadowgraph. 79

35 Baseline conic test model with dimensions 80

36 Isolated toroidal structures inside the cone cylinder a), isometric c), side section-view with removed toroids c), full-view with filled toroids d) 84

37 Isolated longitudinal channels inside the cone cylinder a), isometric c), side section-view with removed longitudinal channels c), full-view with filled channels d) 85

38 Isolated radial and toroidal channels inside the cone cylinder a), isometric c), side section-view with removed radial and toroidal channels c), full-view with filled channels d) 85

39 Combined vented porous cone-cylinder with BS4 venting configuration a) isometric view, c) complete side view, c) front view, d) half-section view showing internal structure. 86

40 Section view of the unvented pointed cone showing a) radial-toroidal dispersion c) longitudinal/radial dispersion c) combined dispersion (longitudinal, toroidal and radial) 88

41 Section view of the cone showing a) vented-only longitudinal dispersion c) vented combined dispersion (BS0) 89

42 Section view of the hemispherical a) toroidal-radial dispersion c) longitudinal-radial dispersion c) combined dispersion d) vented longitudinal-radial dispersion in the hemispherical case 89

43 Various views of the BS0 90° (a-d), hemisphere (e-h) pointed cone 90

44 First iteration porous pointed cones (a,c) BS1, (c,d) BS2, (e,f) BS3, (g,h) BS4 93

45 Second iteration BS cones venting configurations: (a,c) overexpanded (OE), (c,d) underexpanded (UE) 94

46 Various views of BS4 the ellipsoid (BS4 E) (a -d) and cone (BS4) (e-h) 95

47 Various views of BS4 inside(a-d), the hemisphere (BS4 H) (e-h) the secant ogive (BS4 SO) 95

48 Finite element analysis results of the BS4 cone under SSWT test conditions (left) total deformation (mm) (right) equivalent (von Mises) stress (MPa) . . 98

49 Domain geometry of quarter-model with a coordinate system, boundary conditions and dimensions 101

50 Image of the global quarter-domain mesh 106

51 Image of a) the body of influence mesh refinement region b) the inflation layer and face meshing region 106

52 Schematic of pointed cone validation cases a) solid b) BS0 (90° elbow vent). Isometric view (left) and sliced ZY-symmetry plane view, where internal structure is visible. 115

53 Density flood plot of the long-time scale BS0 CFD solution at Mach 3.5 a) 10 000 iterations, b) 20 000 iterations, c) 36 000 iterations. 117

54 Density flood plot of the short-time scale BS0 CFD solution at Mach 3.5 a) 19 000 iterations, b) 20 000 iterations, c) 21 000 iterations. 117

55 Velocity magnitude stream traces for the flow inside the BS0 cone at Mach 3.5. 118

56 Mach 3.5 CFD drag coefficient (Cd) versus number of simulation iterations, for the cone BS0, with converged CFD value with ± 5% error. 119

57 Calibration curve of the force balance 129

58 Bending and ±axial strain (μ/m), and calibrated drag coefficient (C_d) curve fit, during the 6 s Mach 3.5 SSWT test on the BS0 cone 132

59 Poplavskaya et al. (2017), Mach 4.85, $L/D = 1.9$. a) Solid cylinder schlieren, 180° - $\beta_{2,s}$, b) Porous-insert cylinder schlieren, c) Porous-insert cylinder computed Mach isolines, 180° - $\beta_{2,s}$ > 180° - $\beta_{2,p}$. All images numerical. . . . 140

60 Mach 3.5, $L/D = 1.5$, cone angle $\theta = 18.43°$ a) Solid cone schlieren, 180° - $\beta_{1,s}$, BS0: b) schlieren with porous geometry overlay, c) Flooded Mach contour plot, 180° - $\beta_{1,s}$ > 180° - $\beta_{1,p}$. 140

61 Experimental (points) and numerical (curve) dependences of the drag force of the porous model versus porous insert length ($\Delta x/D$). 144

62 Experimental (1, 2) and numerical (3, 4) normalised drag coefficient of the Maslov porous cylinder versus Reynolds number. 145

63 Annotated schlieren photograph (left), and CFD Mach contour plot (right) of solid pointed cone at Mach 3.5 (L/D = 1.5). 148

64 Annotated schlieren photograph (left), and CFD Mach contour plot (right) of BS0 pointed cone at Mach 3.5 (L/D = 1.5). 148

65 Plot of the shock angles for the solid and BS0 WT, CFD and theoretical pointed cone at Mach 3.5 (L/D = 1.5). 150

66 Annotated schlieren photograph (left), and CFD Mach contour plot (right) of solid SO at Mach 3.5. 153

67 Annotated schlieren photograph (left), and CFD Mach contour plot (right) of BS0 SO at Mach 3.5. 153

68 Plot of the shock angles for solid and BS0 the WT, CFD and theoretical SO at Mach 3.5. 154

69 Annotated schlieren photograph (left), and CFD Mach contour plot (right) of solid ellipsoid at Mach 3.5. 155

70 Annotated schlieren photograph (left), and CFD Mach contour plot (right) of BS0 ellipsoid at Mach 3.5. 155

71 Plot of the shock angles for solid and BS0 the WT, CFD and theoretical ellipsoid at Mach 3.5. 156

72 Annotated schlieren photograph (left), and CFD Mach contour plot (right) of solid hemisphere at Mach 3.5. 157

73 Annotated schlieren photograph (left), and CFD Mach contour plot (right) of the BS0 hemisphere at Mach 3.5. 157

74 Plot of the shock angles for the solid and BS0 WT, CFD and theoretical hemispheres at Mach 3.5. 158

75 a) Velocity vectors coloured by static pressure for the BS0 cone, b) Drag reduction mechanism for the HPCM frontal-insert cylinder (Mironov, Maslov et al. (2015)) 160

76 BS0 exit vent plots at Mach 3.5 a) Greyscale density plot b) Schlieren image with geometry overlay. 161

77 Mach number flood plots of solid models at freestream Mach 3.5 a) pointed cone b) secant ogive c) ellipsoid d) hemisphere. 166

78 Velocity surface plots at freestream Mach 3.5 of the a) pointed cone b) secant ogive c) ellipsoid d) hemisphere, with side-view. 167

79 Mach contour flood plot of ZY-plane pointed cone a) BS0 b) BS1 c) BS4 at Mach 3.5. 175

80 Mach contour flood plot of ZY-plane pointed cone a) BS2 b) BS3 at Mach 3.5. 175

81 Mach 3.5 shock surface plot (a-solid cone, b-BS0, c-BS3, d-BS4) 178

82 Mass flow rate (g/s) vs shock angle β (°) for internal porous structure of BS0 - BS1 pointed cones at Mach 3.5 179

83 Mach 3.5 velocity shock surface plot of the pointed cone a) solid b) BS0 c) BS1 d) BS4 181

84 Mach 3.5 ZY-plane Mach contour flood plot of the a) solid pointed cone, b) BS4 cone. 183

85 Mach 3.5 velocity shock surface plot a) BS2 b) BS3 185

86 Mach 3.5 contour flood plot of ZY-symmetry plane a) solid cone, b) BS3 cone. 186

87 Enlarged view of the Mach number contours a) and velocity streamlines b) of the BS3 inlet structures. 187

88 Mach 3.5 freestream Mach flood plots of the a) BS3 cone b) BS4 cone, at the ZY symmetry plane. 188

89 Schematic of the vented BS4 configurations (above-isometric cone view, below symmetry slice exposing internal structure) a) overexpanded b) linearly expanded c) underexpanded. 193

90 Contour flood plots of a) Mach number and b) velocity for the cylinder nozzle at Mach 3.5, nozzle expansion ration (A/A^*)= 14.31 195

91 Velocity streamlines of the overexpanded jet a) global view b) near-wall view. 197

92 Static pressure contour flood plot of the overexpanded nozzle jet impingement region for the cylinder nozzle at Mach 3.5, nozzle expansion ration $(A/A^*) = 14.31$. 198

93 Mach flood plot of the BSUE model a) velocity b) static pressure in the ZY symmetry plane at Mach 3.5. 204

94 Mach flood plot of the a) HV model in the ZY symmetry plane at Mach 3.5 (Mach 6 shown to include base jetting). 208

95 Mach flood plot of the a) BS4 Ellipsoid b) BS4 Cone models in the ZY symmetry plane. 211

96 Mach 3.5 BS4 Ellipsoid critically expanded a) Mach contour flood plot b) static pressure contour flood plot in the ZY-symmetry plane. 212

97 Mach flood plot of the a) BS4 Hemi b) BS4 Secant Ogive models in the ZY symmetry plane. 214

98 Velocity streamlines the BS4 cone coloured by greyscale Mach number, key internal flow features labelled. 217

99 Schematic of the equivalent converging-diverging nozzle created by the porous cone. 218

100 Velocity streamlines the BS4 cone coloured by greyscale Mach number. The inlet 'converging', outlet 'diverging', and choking sections are illustrated. . . . 219

101 The network diagram of the equipment controlling the air compression and direction into the tunnel. 247

102 Schematic of the general case nose cone dimensions 264

103 Curves of the different types of nose cone profiles 265

104 Schematic of the pointed nose cone profile 266

105 Schematic of the secant ogive profile 266

106 Schematic of the ellipsoid profile 267

107 Image showing (a) the Creality 3D resin printer (b) a diagram showing the different parts of the printer 270

108 Image showing the sliced DLP 3D printer image (a) full view (b) section view showing internal supports 270

109 Combined unvented cone a) half model after sanding c) aligned but not joined c) bonded/joined halves d) base view of the joined model 272

110 Annotated 3D printed BS0 cone a) seam-view c) view of smooth side 273

111 Unvented combined half-cone on the Chitubox build plate, with supports. . . 273

112 Image showing the first print iteration (a) supports used (b) side view (c) front view 275

113 Image showing the second print iteration (a) supports (b) first derivative (c) second derivative 275

114 Image showing the comparison between the solid printed cone (a) front view before machining (b) side view before machining (c) front view after machining (d) side view after machining 275

115 Image showing the solid printed cone before machining 276

116 Image showing (a) and (b) the solid cone after machining (c) the damage caused by machining 276

117 Schlieren images of pointed cones (a) solid M3.5 (b) solid M3 (c) BS0 cone M3.5 (d) BS0 cone M3. 277

118 Schlieren images of secant ogive (a) solid M3.5 (b) solid M3 (c) BS0 M3.5 (d) BS0 M3. 278

119 Schlieren images of ellipsoid (a) solid M3.5 (b) solid M3 (c) BS0 M3.5 (d) BS0 M3. 278

120 Schlieren images of hemispheres (a) solid M3.5 (b) solid M3 (c) BS0 M3.5 (d) BS0 M3. 279

121 Flooded contour plots of pointed cones at Mach 3 (a) solid Mach plot (b) BS0 Mach plot (c) solid static pressure (d) BS0 static pressure. 280

122 Images of the unvented combined cone at Mach 3.5 a) flooded CFD contour plots b) CFD velocity isosurface of the bow wave c) schlieren photograph. . . 281

123 Schematics of pointed cones BS (a) Toroidal UV (b) Combined UV (c) Longitudinal UV (d) Longitudinal Vented. 283

124 Schematics of pointed cones (a) solid (b) BS0 (c) BS1. (outside and internal view) 284

125 Schematics of pointed cones (a) BS2 (b) BS3 (c) BS4 (outside and internal view). 285

126 Schematics of pointed cones BS (a) OE (overexpanded) (b) UE (underexpanded) (c) CE (critically expanded) (outside and internal view). 286

127 Schematics of cone (a) HV (b) 72 Holes (outside and internal view). 287

128 Schematics of cone (a) solid ellipsoid (b) BS4 ellipsoid (c) solid hemisphere (outside and internal view) 288

129 Schematics of cone (a) BS4 hemisphere (b) solid secant ogive (c) BS4 secant ogive 289

List of Tables

1 SSWT Specifications 64

2 Table showing the meshing settings 106

3 Table showing the detailed solver specifications 109

4 Table showing the adaptive mesh refinement settings 112

5 Final (total) CFD BS0 drag coefficients at various solution iterations. Percentage difference from the converged solution shown, with pressure and viscous components tabulated. 121

6 Experimental and numerical drag coefficient statistical uncertainty (BS0 and solid cone, Mach 3.5), for CI = 95% 136

7 Experimental (WT) and numerical (CFD) drag coefficient results for the zeroth vented conic models, tested as sets. The percentage difference between the numerical and experimental data sets is shown. 137

8 C_d of the solid and porous cones (select venting configurations), and the percentage difference (%Δ) between them for the relevant shape family 169

9 Air drier specifications 245

10 Supply pressure vessel specifications] 245

11 Test section pressure transducer specifications 245

12 Settling chamber pressure transducer specifications 246

13 Programmable time delay unit specifications 246

14 Induction motor specifications 246

15 Compressor specifications 246

16 Creality LD-002R 3D Printer Specifications 269

17 Table showing the 3D printed model iterations and the key factors affecting outcome 274

List of Acronyms

3D three-dimensional.

AMR Adaptive Mesh Refinement.

BOI body of influence.

CD Converging-Diverging.

CE Critically expanded.

CFD computational fluid dynamics.

CHPC Centre for High Performance Computing.

DAQ Data Acquisition System.

DLP Digital Light Processing.

FEA Finite Element Analysis.

HPCM Highly Porous Cellular Material.

HV Horizontal Vent.

ISO International Organisation of Standardisation.

LE Linearly Expanded.

LV Longitudinal Vented.

OE Overexpanded.

PPE Personal protective equipment.

SO secant ogive.

SSWT supersonic wind tunnel.

UE Underexpanded.

Chapter 1

Introduction

1.1 Cunicularity

In this work, the term 'cunicular' has been devised to describe the subsequently investigated system of organized, interlinked channels within a solid structure through which fluid may enter and/or exit. This is distinct from 'porous' or 'porosity', which refers to random or organised minute holes dispersed through a solid (Merriam-Webster (2021)). Whilst cunicularity is undoubtedly a form of porosity, this term is useful to emphasise the difference between the hole arrangement presented in this research, versus the typical porous structures described in prior investigations.

1.2 Porous projectiles in supersonic flow

Supersonic projectiles with conical forebodies generate strong shock waves, which are responsible for significant wave drag. Examples of such projectiles include missiles, ballistics, rockets and supersonic aircraft. The nose cone of a projectile is designed to regulate the behaviour of the approaching airflow and minimise aerodynamic wave drag by reducing the effect of shock waves acting on the body. In supersonic flow applications, porous materials

have the ability to reduce the strength of the incident waves and redistribute the flow field within the pores (Poplavskaya et al. (2017)).

In this context, porosity is quantitatively defined with respect to the volume fraction[i], i.e. the volume of the pores in a curved geometry. Specifically, porosity here (used in conjunction with the term 'cunicularity'), refers to bodies where a portion of the solid mass has been removed. However, instead of minute holes or spaces (as traditionally understood in porosity), the mass removal is in the form of a series of hollow, organised and interconnected channels through which fluid may pass. In this research, all of the models have the same quantity of porosity, ($\approx 60\%$ porous), regardless of geometry or cunicular arrangement.

By designing a porous structure specifically for conic body applications, it is possible to harness the effects of porosity to reduce the aerodynamic wave drag effects acting on these high-speed projectiles. The porous conic bodies of revolution achieve this by reducing the incident shock wave strength and redistributing the momentum in the flow field to create a global flow field of greater efficiency.

1.3 Aerodynamic drag

The generation of shock waves, specifically bow waves, on a conic body of revolution significantly hinders the aerodynamic performance of the projectile. Shock wave drag occurs when a body travels above the speed of sound (Mach 1), after which shock waves are generated around the surface of the body (Anderson (2001)). Waves are formed when a disturbance moves through a medium, an example being a supersonic body traveling through air. The stagnant air ahead of the body is suddenly compressed, resulting in a discontinuous change in properties, including increased pressure and decreased temperature. A considerable pressure difference is created between the front and back of the body, resulting in wave drag. Additionally, the formation of these shock waves causes a considerable energy loss which also contributes to drag. The shock shape and wave formation change according to the particular geometry of the body (Anderson (1990)). Oblique shock waves tend to form on pointed

[i]The ratio of the volume of the voids or pore space divided by the total volume, expressed as a percentage (Wisconsin Geological and Natural History Survey (2023)).

bodies, and detached bow shocks on rounded bodies. At supersonic speeds, oblique shock waves on conic profiles tend to produce less drag than blunt bodies with bow shocks due to the particular properties associated with the wave.

Expansion waves (fans) are regions where pressure drops due to an expansion in the surrounding flow field. These regions also contribute to wave drag. The expansion of the air disrupts the smooth, continuous airflow around the body, leading to large energy losses and momentum changes (Liepmann and Roshko (2001)). Wave drag has a significant effect on the overall performance of a high-speed vehicle, as it greatly affects aerodynamic performance, stability, and, fuel efficiency. Aerodynamic design of the nose cone is critical for reducing and managing these shock waves and the effect that they have on drag performance.

1.4 Shock waves

Flow that is compressible and encounters little obstruction (area change ahead of it which forces the flow direction to change), is known as reversible and isentropic (Liepmann and Roshko (2001)). When a body travelling faster than the speed of sound encounters an obstruction, the air is further compressed even and shock waves are generated. Across the shock wave, static pressure, temperature, and density suddenly increase. These changes in properties are irreversible, and entropy increases (Anderson (2001)). In this, the flow is non-isentropic, with the stagnation enthalpy and temperature remaining constant. A pressure difference exists across the shock wave, whereby the downstream pressure (post-shock) of the shock wave is always greater than the upstream pressure (pre-shock). Mach number and velocity decrease across the shock wave. The properties that change across the shock wave (velocity, pressure, and density) are the same properties present in the drag force equation. Consequently, the manner in which the shock wave behaves directly influences the drag response.

1.4.1 Oblique shock waves

A discontinuous change in fluid properties is experienced across a shock wave. To describe the normal shock wave behaviour, compressible gas equations were derived from the conservation of mass, energy, and momentum equations. Normal shock waves are the reference condition, existing perpendicular to the flow direction, such as travelling blast waves. However, gas usually interacts with solid geometric bodies.

The shock wave may be inclined to the incoming flow direction (known as an oblique shock wave), depending on the geometry of the body and the incoming flow conditions (Ben-Dor (2001)). Conservation of mass, momentum, and energy for a compressible gas is used to derive the equations that describe two-dimensional flow without head-addition and viscous effects, where an oblique shock occurs for a unique free-stream Mach number and flow deflection angle. A bow shock (a normal shock wave detached from the body) is generated if the deflection angle is too high for the incoming Mach number, or if the incoming Mach number is too low for the deflection angle. Fig. 1 shows the bow shock a) and oblique waves b) acting on a blunted and pointed body, respectively.

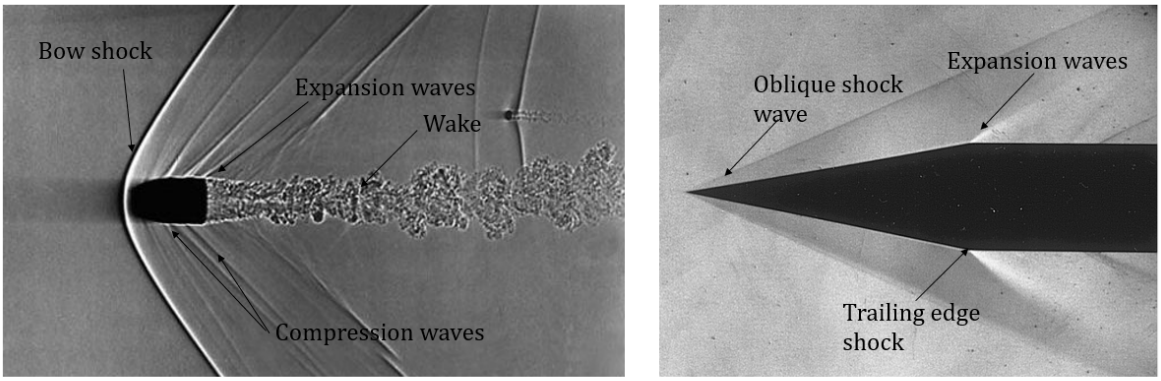

Figure 1: Schlieren image of the flow field around a) a supersonic bullet b) a pointed cone (adapted from Schmidt (2015))

Fig. 1 represents the supersonic projectiles, such are aircraft, rockets, and missiles, where oblique shock waves are generated at the nose, wing leading edge, and tail structures (or fins for the latter). Flow features characteristic to conic bodies are shown in a) and b), including bow shock, compression, and expansion waves. As the air flows over the body, shocks also

form at the trailing edges of certain lifting surfaces. This occurs as the shock-affected flow from upstream returns to the free-stream condition.

Oblique shock waves also form inside supersonic and hypersonic engine intakes and nozzles. If the expanded pressure downstream of the nozzle is different from that of the free stream condition, an oblique shock wave will form to ensure continuity of mass by adjusting to the free stream. Supersonic inlets are purposefully designed to generate oblique shock waves that compress the air entering the engine. In doing this, the pressure is increased such that the air may be utilised more efficiently by the engine, whilst reducing the more dramatic efficiency losses characterised by normal shock waves.

1.4.2 θ-β-M relationship

The formation of oblique shock waves on pointed cones is described by the θ-β-M relationship. Consider a sharp corner inclined at an angle of θ with the incoming supersonic flow, as in Fig. 2 a). According to the conservation of mass, the flow must remain parallel to the wall after the corner, as the existence of any other flow angle implies the spontaneous creation or destruction of mass (Anderson (1990)). Because the presence of the corner cannot be communicated upstream, a shock wave forms at an angle β such that the flow may be turned through the required angle, as in Fig. 2 a). Necessarily, there will be a change in non-isentropic flow properties across the shock wave.

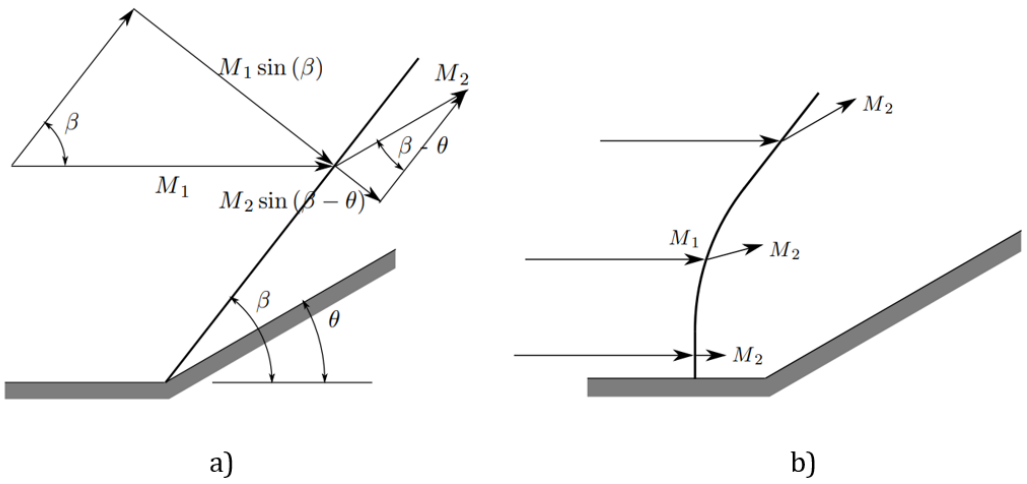

Figure 2: Schematic of a) supersonic flow approaching a corner with an oblique shock wave (and velocity components) b) detached shock wave (Anderson (1990))

The flow turn angle is calculated by resolving the incoming flow velocity into its parallel and perpendicular velocity components with respect to the shock wave (Ben-Dor (2001)). The velocity component parallel to the shock remains constant, however, the perpendicular component decreases in accordance with the normal shock equations. The component breakdown may be seen in Fig. 2. The deflection angle is determined by combining the components downstream of the shock.

By manipulating the components according to Anderson (1990), an equation is formulated to isolate the shock angle β for a particular θ, M_1 (upstream Mach number) and γ (specific heat capacity). From this, the key relationship emerges relating to the downstream Mach number, M_2 in terms of the upstream conditions:

$$2\gamma {M_1}^2 \sin^2(\beta - 1) \tan\theta = 2 \cot\beta \frac{{M_1}^2 \sin^2\beta - 1}{{M_1}^2(\gamma + \cos 2\beta) + 2} \tag{1}$$

The above equation is known as the θ-β-M relationship and characteristically describes two-dimensional shock waves. Fig. 3 depicts a plot of the oblique shock angle as a function of the corner angle, for lines of constant M_1. Several upstream Mach numbers are plotted (Mach 1.1 - infinity, represented as staggered, solid black lines). The red line separates the strong and weak shock solutions, and the blue line represents the region where the downstream Mach number becomes sonic (Anderson (1990)). The chart uses $\gamma = 1.4$ for an ideal gas. The chart represents the solution to Equation 1, where for a given M_1, θ, and β, the downstream Mach number M_2 of the corner may be determined.

In the θ-β-M relationship, a maximum corner angle θ_{max} exists for any upstream Mach number. When $\theta > \theta_{max}$, the oblique shock wave is unable to remain attached to the corner, and instead becomes a detached shock wave (Ben-Dor (2001)). In Fig. 3, θ_{max} is represented by the dashed red line. As Anderson (1990) outlines, the θ-β-M relationship produces two possible shock angles (β) for a particular corner angle (θ) and M_1, where the larger β is known as the strong shock solution and the smaller as the weak shock solution. In this research, only the weak shock solution is of interest as only this solution was possible in the experimentation.

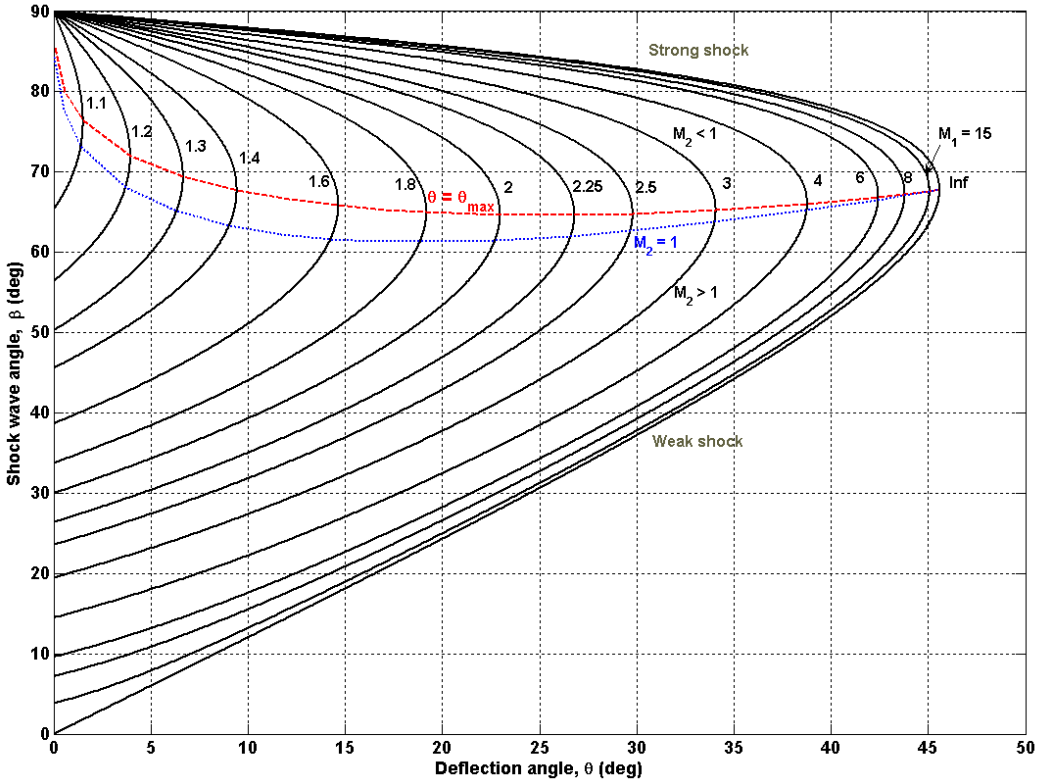

Figure 3: Chart showing the oblique shock angle (β), as a function of the corner angle, (θ), for lines of constant upstream Mach number (M_1) lines (Anderson (1990))

The strong shock solution represents the transition from a supersonic Mach number to a subsonic Mach number (as in detached shocks), as opposed to the higher supersonic to lower supersonic transition experienced in the weak shock solution (as in oblique shocks). Comparatively, the strong shock solution encounters a far greater energy and momentum loss in the flow field than the weak shock solution. The same holds true for blunt and pointed bodies in supersonic flow.

For a given corner angle θ and M_1, a reduced wave angle β would imply that the incident shock strength had reduced. By reducing the wave angle, the normal component of the wave $V_n, 2$ was decreased while $V_t, 2$ was increased. Because $V_n, 1$ ahead of the shock is constant, a smaller $V_n, 2$ caused a reduced $\Delta V_n, a/V_n, 2$ across the wave, weakening the bow wave. This reduced wave strength resulted in a lower ΔP and $\Delta\rho$ across the shock.

1.4.3 Conical shock formation

Taylor-Maccoll flow refers to the steady flow behind a conical shock wave that is attached to an axisymmetric solid cone (Taylor and Maccoll (1933)). The simplified definition is shown below. Figure 4 a) depicts the formation of an oblique shock wave over a cone. The cones in this research utilise the Taylor-Maccoll conical shock model.

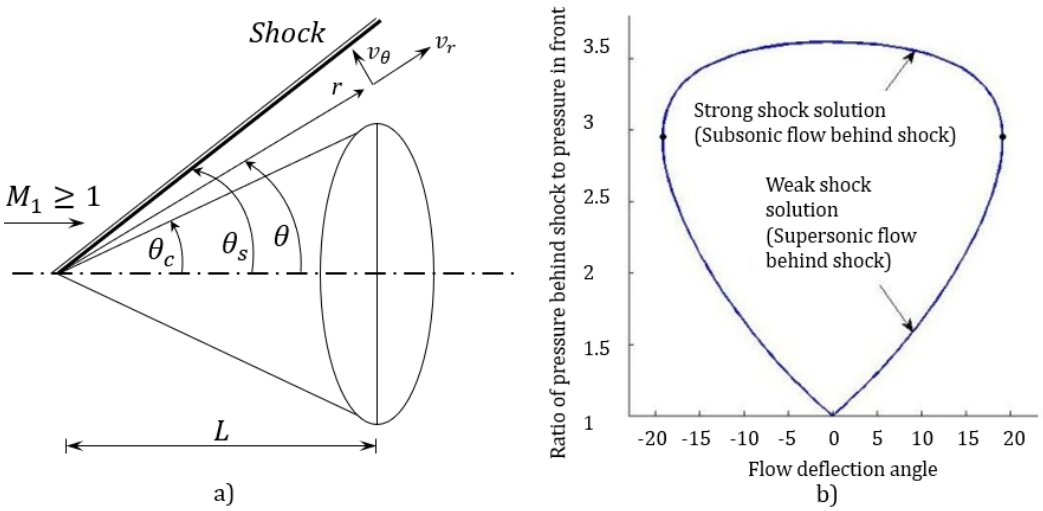

Figure 4: Schematic of a) oblique shock formation over a cone b) shock polar in the pressure ratio-flow deflection angle plane for a Mach number of 1.8 and a specific heat ratio 1.4 (Taylor and Maccoll (1933)).

For a steady supersonic flow over a solid cone with a half angle θ_c, a conical shock wave forms with the vertex of the shock wave coinciding with the vertex of the solid cone. In a two-dimensional problem, as described above, the incoming stream would be deflected through an angle θ_c upon crossing the shock such that streamlines behind the shock wave would be parallel to the wedge wall.

However, this approach is not possible for the conic case. After passing through the shock, the streamlines become curved due to the three-dimensional shape, only approaching the walls of the cone asymptotically. The curving of the streamlines is accompanied by the gradual increase in density and decrease in velocity as the cone height increases, in addition to the changes in property affected at the shock itself.

The magnitude and direction of the velocity immediately behind the oblique shock wave is described by a weak branch of the shock polar (the locus of all possible states after an

oblique shock, (Anderson (2001), Busemann (1929), shown in Figure 4 b)). This suggests that for each given freestream Mach number M_1, there exists a maximum M_{max}, beyond which the shock polar provides no solution (as in the θ-β-M relationship). In this case the conical shock wave necessarily detaches from the solid surface (as with Mach reflection). The detached cases are not considered here. The flow immediately downstream of the oblique conical shock wave is typically supersonic. However, when θ_c approaches $\theta_{c,max}$ (as in the M_{max} case, e.g. blunt cones) the flow along the face may become subsonic. Downstream of the shock wave, the supersonic flow will become subsonic as it develops. Figure 4 b) shows a schematic of a shock polar at Mach 1.8 (Busemann (1929)), demonstrating the maximum flow deflection condition coupled with the strong and weak shock solution, similar to the *2D* wedge relationship described previously. The shock angle for a three-dimensional cone will always be less that for the two-dimensional case.

Because all incident streamlines intersect the conical shock (bow wave) at an identical angle, the intensity of the shock wave is constant throughout. In this, the change in entropy across the shock wave is also constant. The formation of conical flows is pertinent to this research due to the shape of the bodies under investigation. The addition of the porous network will inherently alter the conical shock shape in terms of size, angle and formation, and as such it is critical to understand these parameters in the context of the solid shapes such that the porous flows may be interpreted correctly. To perform the Taylor-Maccoll analysis, existing software (Hinman (2024)) was utilised due to the complexity of the approach.

1.4.4 Detached shock waves

In Fig. 3 b), as outlined by Anderson (1990), if $\theta > \theta_{max}$, a detached 'bow' shock forms a small distance upstream of the wedge leading edge. Downstream of the stem of the normal shock wave, the flow is subsonic, however as the flow adjusts to the wedge geometry, curving the shock wave towards the wedge as the flow properties change. This adjustment causes both supersonic and subsonic flow regions to form within the shock.

As the conic body becomes less pointed, the corner angle increases. Once θ_{max} is exceeded, a blunt body is effectively created. When a blunt body travels supersonically, a bow shock is

generated and the flow downstream of the incident shock wave is subsonic. A pointed body travelling at the same Mach number may produce an attached shock wave with the supersonic downstream flow. The difference lies in the apparent corner angle of each body. Bodies with slightly different geometry in an identical free stream may experience significantly different momentum within the flow field depending on how pointed the body is. The condition of the flow field around the body is thus dictated by the kind of shock wave produced, and most notably its strength. More pointed bodies produce oblique shock waves which are weaker than the geometrically equivalent blunted bodies, having a lesser impact on aerodynamic behaviour.

Due to the greater pressure loss experienced, larger energy losses are associated with detached shock waves when compared to oblique shock waves. The intensity of these incident waves can be lessened by reducing the effective deflection angle in order to weaken the shock wave. Reducing the strength of the wave improves performance irrespective of shock type. In order to lessen the energy losses incurred by conic bodies on account of these shock waves, a mechanism must be employed to mitigate the causes and effects as far as possible.

H. Li and Ben-Dor (1997) found that the onset of an irregular interaction depends on both the strength and the orientation of the incident shock wave, as well as the geometry of the body to which the Mach reflection wave configuration is attached. This suggests that whilst the incoming flow cannot be altered, it is possible to alter its behaviour by changing the material which interacts with the flow. Porous materials in supersonic flow exhibit strong potential shock reflection properties due to their ability to absorb fluid and redistribute fluid (Ali et al. (2018)). It is appropriate to consider this with reference to conical shock waves. In the same manner described, by utilising a different material for the conical body (for example making it porous), the bow shock generated by the body would similarly be altered. This suggests that by carefully considering the body shape in conjunction with the material and porous structure, the strength of the bow wave may be attenuated.

Porous structures have the ability to affect momentum (energy) movement within the flow field and reduce incident shock strength (Poplavskaya et al. (2017)). In reducing the shock wave, drag reduction would occur as a result of the improved energy transfer between the

shock wave and flow field. Additionally, porous materials are capable of transforming a detached shock wave into an attached wave, further reducing the effect of the shock wave (Mironov, Kirilovskiy et al. (2019)). The incident wave is also affected by the physical structure upon interacting (Maslov et al. (2019)), indicating that the overall wave and flow field performance will be positively affected.

Shock waves occur on all nose cones in supersonic flow, irrespective of geometry. It is key to reduce the pressure loss experienced by the body, directly caused by these shock waves as far as possible to improve the efficiency of the flow field. In accordance with the θ-β-M relationship, the flow must be redistributed, weakened, or altered in some such that the shock wave and its effects are also weakened. Porosity may be harnessed to alter the flow field in the manner required.

1.5 Porosity in aerodynamics

1.5.1 Introduction

Porosity has the ability to alter the flow field and reduce the drag force acting on the material by altering the way in which the fluid interacts with the body. Porosity is defined as the ratio of the volume of pores of a substance, to the total volume of mass (Merriam-Webster (2021)). It refers to the amount of negative space within a material or object. This negative space is typically random in distribution, where the 'pores' may be interconnected, or isolated.

Porous materials have a profound effect on the thermal, physical, and transport properties of a material (Ali et al. (2018)). This is significant for supersonic fluid mechanics, where the sudden change in gas properties caused by shock waves hinders the aerodynamic performance of the body. Since porosity has the ability to affect many of the characteristic changes present in supersonic flow, its implementation may be used to balance and reduce some of these negative consequences. In particular, the effect of porosity on fluid transport is noteworthy (Mironov, Kirilovskiy et al. (2019)). Mass transfer is described by mass flux, or the rate of

mass flow. In the context of porosity, it is the mass fraction of the air that travels through the porous material. A solid body has a mass fraction of 0%.

1.5.2 Subsonic flow through and around a porous medium

Fluid is transported through a porous medium according to the physical principles outlined by Darcy's Law and the coupled concept of permeability (Whitaker (1986)). Fluid transport is greatly affected by the porous structure, in particular the arrangement of the pores and their distribution. Flow direction and momentum are critical to transportation, as fluid moves through the interconnected regions of the porous body, always following the path of least resistance. The path that the flow takes depends on both the porous structure, as well as the permeability distribution. Fluid transport phenomena should also be taken into consideration, such as bulk flow, diffusion, and dispersion within the porous medium, as they influence the movement of the fluid (Whitaker (1986)). The pressure gradient is the driving force for fluid transport through a porous medium, where the flow moves from a region of higher pressure to that of lower pressure.

Pore structure may be classified as either open-cell or closed-cell structure. Fig. 5 demonstrates the foam-type open-cell (left) and the closed-cell (right) structures.

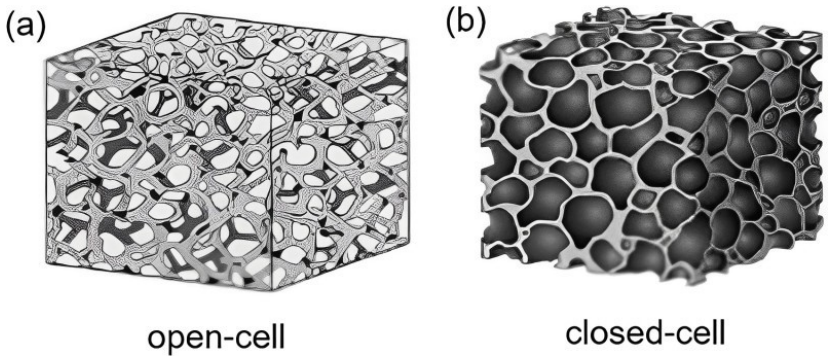

Figure 5: Schematics of porous materials: (left) open-cell foam (right) closed-cell foam (Y. Chen et al. (2021))

Open-cell indicates that fluid is able to enter, move through, and escape the material at some location. This type of structure is semi-permeable due to the arrangement of the cells within the material being broken, rather than closed. This allows fluid to permeate and pass through more easily, creating a highly porous and absorbent material commonly

used for acoustic absorption and airflow control. Open-cell porous materials allow the fluid to communicate within the structure, implying that energy and momentum within the fluid may be transferred through the pores in the solid. Subsonic fluid movement through the porous material is governed by the parameters of effective pore radius, friction (viscous forces), and permeability under Darcy's law (Whitaker (1986)).

In closed-cell arrangements, the fluid becomes trapped between the pores and is unable to escape. The cells are closely packed with no gaps, and the material is vapour semi-impermeable. This creates a denser, more rigid material than open-cell, which is able to withstand greater pressure. Closed-cells is are unsuitable for fluid control as the fluid is unable to exit the material, making energy transfer out of the material largely impossible. Closed-cell structures have limited applicability for aerodynamics in that they cannot be easily formed and manufactured into aerodynamic shapes (e.g. pointed cones). Additionally, foams of this kind are greatly affected by impact loading and are highly susceptible to damage. This is unsuitable for aerodynamic structures, which must be robust and durable to withstand harsh operating conditions. Only open-cell porosity will be examined in this work since this type alone allows for the required fluid transport behaviour.

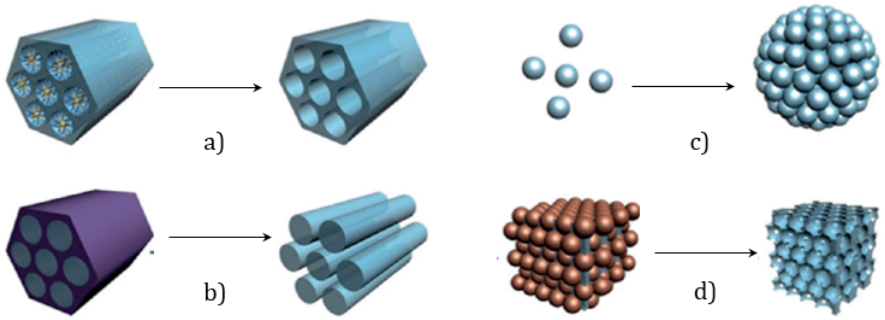

Figure 6: Diagrams of porous structure: a) uniform material removal within structure b) uniform structure with external material removed c) spheres arranged uniformly in a spherical shape d) spheres arranges uniformly in a cube (Lal, Uthaman and S. Thomas (2022))

Both cell types in Fig. 5 depict randomised porosity, however, organised porosity was of interest for this work. Fig. 6 a)-d) depicts various organised porous configurations. Fig. 6 b), c), and d) show spherical and cylindrical cells arranged in patterns to create closed-cell material structures. These structures are commonly used for waterproofing, insulation and force absorption. Conversely, Fig. 6 a) shows an open-cell arrangement where cylindrical cells

have been removed from the bulk material to create structured, patterned channels. This structure provides transport channels for fluid movement and property transfer within the bulk material. Whilst a complete shape made only of open-cell foam is not viable (due to the lack of structural integrity and manufacturing impossibility), the concept of removing material from the bulk matter in an organised open-cell structure is significant.

The ability for the fluid to escape the open-cell porous structure is known as 'venting'. Transport phenomena including mass, energy, and momentum transfer are observed. The highest density of transport occurs during venting as the built-up fluid energy is allowed to escape the structure. In order for these phenomena to effectively work, the porous structure must be designed correctly such that fluid communication or dispersion may occur. Here, flow communication/dispersion is defined as the exchanging of information between fluid particles. The terms 'communication' and 'dispersion' are used interchangeably in this regard.

The level of complexity and twisting present in a particular path is known as tortuosity and also affects fluid flow. Its effect on porosity is that turns and large geometric changes in the fluid path lead to momentum losses in the fluid (Fu, H. Thomas and C. Li (2021)). This indicates that highly tortuous flow paths are not conducive to a design focused on performance improvements. Additionally, tortuosity is a concept largely impossible to streamline into a repeatable, examinable manner from the design stage (Fu, H. Thomas and C. Li (2021)). As such, to aid in simplifying the research methodology, the tortuosity parameter was ignored.

It is useful to designate how dispersion may occur inside the porous material with regard to structure. Clearly, a randomised porous structure will create randomised flow behaviours. However, if an organised structure was employed, then dispersion types based on orientation and direction may be defined. For example, if the fluid travels in a ring-like structure, then the fluid dispersion type is defined as toroidal. It is necessary for the communication to be defined in this way so that the separate effects that each type has on mass transfer may be clearly observed. Within the context of the porous models designed here, the dispersion structures are defined in Section 3.6.2.

Communication is necessitated by permeability. Permeability quantifies the ability of a material to allow fluid to pass through it. Additionally, it describes the ease at which a fluid may

pass through a porous medium and the capacity for the material to transport fluids under the influence of a pressure gradient. The effects of porosity and permeability are dependent on each other. This property is dependent on many factors, including pore size, shape, hole arrangement, and fluid properties. The degree of blockage and connection of the pores also influences the flow. Higher numbers of pore connections allow for the merging of the flow and increased communication and transfer. High permeability specifies that fluid travels easily through the structure, while low permeability restricts the movement of the flow.

1.5.3 Supersonic flow through and around a porous medium

In supersonic flow, transporting fluid through a porous medium is slightly different. Although much of the governing physics and influencing factors are the same, the presence of shock waves in supersonic flow and their associated phenomena and interaction with the porous medium create a complex flow field.

If supersonic airflow interacted with a porous bed, as studied by Doyle and Skews (1999), both a transient and steady component of the flow field would exist. A portion of the fluid passing over the porous bed surface would be absorbed by the pores and dispersed throughout the porous channels by mass transfer. The flow inside the porous bed was highly complex and transient in nature. Additionally, the moving shock wave passes through the porous bed and reflects off of the impermeable structure. This shock wave stabilised, eventually maintaining a constant speed along the floor of the bed. The behaviour of the shock wave reflecting off of the porous surface indicates a steady-state behaviour.

The distinction between the behaviour of the wave acting on the porous surface and the wave within the porous structure is significant, as the internal and external flow fields vary differently over time. Transient behaviour is investigated by passing moving blast waves over porous bodies, whereas steady-state models focus on stationary models with the incoming supersonic flow. Steady-state flow is defined as the flow condition where the pressure in the reservoir vessel remains constant over time. In the transient regime, the flow velocity and pressure change with time. The pseudo-steady state regime is where the pressure decreases consistently over time, at any point in the reservoir vessel.

The pseudo-steady results are significant when considering regular reflection. In a reference frame attached to the reflection point of the shock, the incident and reflected shock waves are stationary, and the regular reflection becomes pseudo-steady (Ben-Dor (2001)). Thus, the energy of the flow field remains constant. When modelling the flow around a body, the drag is determined by comparing the energy at the inlet with the energy at the outlet. A pseudo-steady time regime is thus an unsuitable formulation to use for drag-monitoring solutions. It is relevant to note that while the work of Ben-Dor (2001) aids in furthering the understanding of the supersonic porous flow phenomenon, the work involves moving shock waves rather than stationary waves in steady flow. As discussed in Chapter 2, the physics of the reflection of moving shocks and the establishment of oblique shock waves in supersonic flows around obstacles are distinctly different processes and should not be confused.

As supersonic flow is transported through a porous medium, shock waves are generated upon as the flow transitions from the supersonic free stream to the subsonic condition upon interacting with the pores. Since the pores act as an area disturbance, shock waves occur and the flow field is altered. Pressure and velocity changes within the pores will occur due to the shock interaction with the pores, creating reflected shocks inside the structure. Shock waves represent energy changes, and since porous materials absorb energy, the strength of the shock wave may be reduced. The extent of the reduction in energy as a result of the energy absorption is dependent on the free stream Mach number and porous structure.

The effects of permeability and porosity still stand in supersonic flow fields. High permeability is advantageous since this enables supersonic fluid transport, whilst low permeability causes flow resistance, increasing the risk of shock wave formation. The presence of pores leads to significant changes in pressure, density, temperature, and velocity due to the compression the fluid experiences upon interacting with them. This compression generates high temperatures, and the associated heat transfer affects the flow inside the pores. Thermal expansion, phase changes, and thermal degradation are possible depending on the material. Due to the complexity of the flow interactions, it is recommended that both comprehensive numerical simulations and experimental tests be performed.

1.6 Bibliometric study

1.6.1 Existing literature

It is necessary to perform a bibliometric analysis in order to provide a structured and objective assessment and understanding of the academic landscape. The analysis gives a comprehensive overview of the research field being investigated and aids in identifying gaps in the scientific literature by examining citations, patterns of publication, and research trends. The information provides valuable direction, insight, and context for the new research being undertaken. Citation and keyword analysis are commonly used in bibliometric analysis and are most relevant to this research.

Citation analysis measures the impact of a particular publication or researcher. Publications cited by other researchers are generally recognised as contributing meaningful information to the field, serving as a form of validation for research findings. The number of citations a paper receives is used here as an indicator of its influence within a particular discipline. Low citation rates may indicate areas receiving low interest, however may also indicate potentially beneficial areas not yet drawn upon by researchers.

Only publications were considered for this bibliometric study, making keyword analysis appropriate. Keywords refer to terms or phrases within a publication that describe the main themes or subjects of the research. Keyword analysis involves the examination and evaluation of the keywords associated with academic publications to identify lesser-seen or absent terms. Keywords are then searched on a citation database to determine the frequency of the particular term in the existing literature. A lack of publications containing specific keywords in the database may indicate areas of sparse research. This too is critical for identifying areas of novelty and opportunity in the field for future investigation.

Publications found using the keywords of the grouped Masvlov research will be referred to say the 'Maslov et.al group'. Similarly, all publications found using the keywords from the Skews (and similar to Skews) research will be referred to as the 'Skews group'.

The primary keywords for this research include steady, supersonic, porous material, and shock interaction. The secondary keywords include cone, drag, organised. As discussed in the Literature Review, this research is based on the combined works of two groups. Group 1 consisted of Mironov, Maslov et al. (2015) et. al. and Maslov et al. (2019) (referred to as the Maslov group). Group 2 consisted of the works of Skews (2005) and Onodera and Takayama (1990) (referred to as the Skews group). The keywords for the Maslov group include: supersonic flow, gas-permeable porous materials, numerical simulation, and experiment. The keywords for the Skews group include: porous material and shock interaction. Notably, the literature keywords overlap with the presented keywords. Scopus (Elsevier) was used as the abstract and citation database for this analysis.

Few publications were found (fourteen between 2019 - 2023) for the Maslov et.al group. All of the papers found were authored by the same research team, and their works are also cited together (as co-citation). A high degree of conceptual similarity exists between these papers (bibliometric coupling). From the range of publications, the team extensively investigated many variations of the subject. 'Drag' was a main theme in these papers.

The Maslov et.al group focused on the steady flow around Highly Porous Cellular Material (HPCM) porous cylinders. Whilst the models had limited real-world applicability, the implications on performance were transferable to other applications. The physical phenomena surrounding porous drag reduction were rigorously and successfully investigated, providing a strong basis for future research.

According to Scopus, the coverage of the keywords relevant to the Maslov et. al group is sparse, as in Fig. 7 a). Fig. 7 a) demonstrates the number of publications per year that match the Maslov keyword search, and b) demonstrates the number of citations for the same group. The trend indicates that few papers are published per year on this topic. It is acknowledged that the Maslov topic has a very strong overlap with the presented topic, indicating that very little work in the presented area has been published.

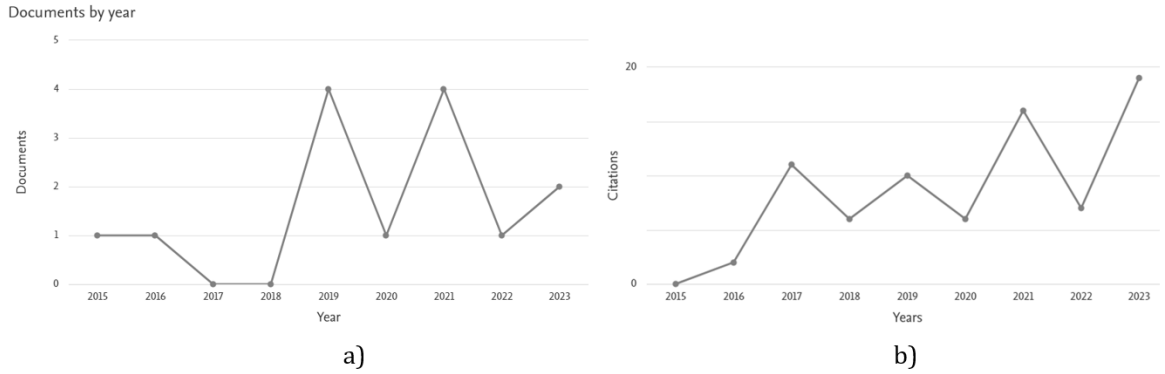

Figure 7: Plots showing a) the number of publications issues per year that match the Maslov keyword search b) Plot of the number of citations per year for Maslov group keyword-specific search

Scopus demonstrated that Mironov and Poplavskaya were the most prominent authors in this group of publications. As of 2023, the grouped literature has 77 citations, with the most citations occurring for Mironov, Maslov et al. (2015) (22 citations total for the paper). Mironov and Poplavskaya, each have a high number of total of 754 and 536 citations, respectively. The journals in which these papers are published also have fairly high impact factors, including the Journal of Physics (IF = 2.1), the American Institute of Physics (AIP) Conference Proceedings (IF = 1.68), Journal of Fluid Mechanics (IF = 4.25).

The high number of citations and presence in high-impact journals indicates that the quality of research outputted by these researchers is high and that they have contributed meaningful information to the field. This work is based on foundational research, and as such it is important that the founding researchers be of high quality. This suggests that their work is reliable, repeatable, and sound.

An h-index was provided by Scopus. The h-index (an author-level metric measuring the citation impact of the publication) for this group of publications is 4. The total number of citations and h-index for this literature is fairly low, however this is understandable based on the field of research. Due to fluid mechanics (and many related topics in engineering) being highly specialised, lower topic growth occurs and thus fewer citations arise.

Performing the same analysis on the Skews group, a higher keyword overlap occurred (244 documents). This is understandable, as the Skews group keywords were broader and thus were likely to include more publications. From this, it is clear that Maslov's research was

a highly focused branch of porous fluid mechanics. Most of the papers related to unsteady flows are for thermal (cooling and ventilation (Liu et al. (2024))), vibrational (Reshetova et al. (2018)), acoustic or blast wave applications using metal foams (Skews (2005), Kobayashi, Adachi and Suzuki (1995), Onodera and Takayama (1990)).

Research regarding porous interactions with shock waves was mostly aimed at shock trapping for buildings using shock tubs. In this, porosity was used to mitigate the negative effects of these different disturbances. The majority of this research had a materials-science focus, in particular for random porous compositions such as HPCM and foams. This kind of experimental design has little relevance in aerodynamics.

Scopus showed a total of 4731 citations for the Skews group (244 documents) from 1997-2023. Many different authors contributed to this group of literature, and many different subject areas were investigated. The journals in which these papers are published have high impact factors, including the Journal of Applied Physics (IF = 3.3), Shock Waves (IF = 1.9), Journal of Fluid Mechanics (IF = 4.25), Defence Technology (IF = 4), Journal of Nanobiotechnology (IF = 10.2) and Progress in Aerospace Sciences (IF = 8.6). It must be appreciated that Maslov's work is highly specialised and niche, and is thus less likely to be frequently cited. Other considerations include Masvlov's work having very limited scope and applicability, making it less likely to be published in very high-impact journals.

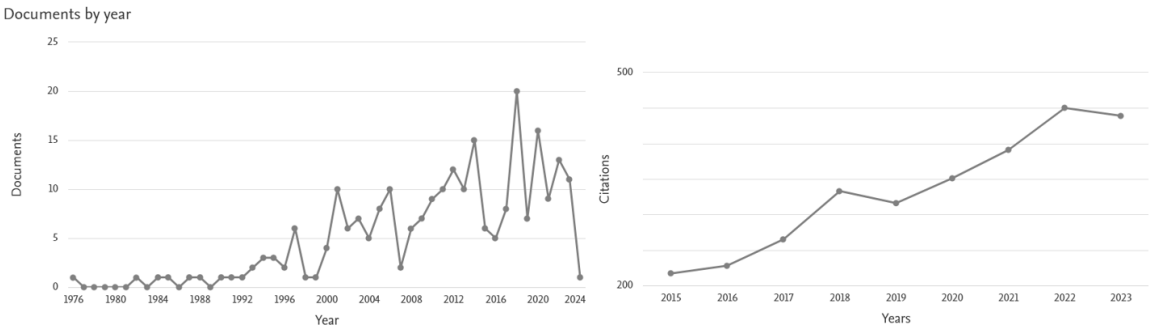

Figure 8: Plots showing a) the number of publications issues per year that match the Skews keyword search b) Plot of the number of citations per year for Skews group keyword-specific search

The h-index for this group of publications is 36 (nine times greater than the Maslov group). This is understandable as this research had a far greater reach than the aerodynamics-based

group. The combined data, as shown in Figure8 indicates that this sector of porous research is highly researched and recognised. Fig. 8 a) demonstrates the number of publications per year that match the Skews group keyword search, and b) demonstrates the number of citations for the same group.

The keyword and citation analysis indicated that the general field has been widely researched, and is well-cited by the academic community. The majority of work has focused on unsteady transient flow and shock disturbance control using porous materials. Aerodynamics was not of key interest due to manufacturing and material limitations.

The analysis indicated that strong foundational research exists with regard to the effect that porous materials have on supersonic flows, and how these materials may reduce drag. Randomised porous structures and non-aerodynamic bodies such as beds and spheres have been thoroughly investigated.

1.6.2 Literature gap

The analysis revealed a significant gap in the literature. The phrases 'cone', 'drag', and 'organised' returned no paper in Scopus when combined with the other keywords. Along with the lack of citations and publications surrounding the founding literature, this suggests that the topic presented here is largely unknown.

As opposed to the widely-researched random structure, the effects of organised (systematically arranged) porosity in supersonic flow remains unknown. The combination of using organised porous cones, specifically designed for drag reduction, is still open for exploration. The shock wave interactions and general supersonic flow field in organised porous arrangements and porous cones remains unknown.

The literature gap represents an untapped research area with strong potential in the field of aerodynamics. The success of the founding literature offers the possibility of an applicable supersonic drag reduction mechanism using porous conic bodies of revolution.

1.7 Critical Research Question

How does the introduction of organised porosity into solid, conic bodies of revolution in steady supersonic flow affect aerodynamic performance, specifically wave drag reduction?

1.8 Objectives

The aim of this work is to investigate the use of organised porosity within conic bodies of revolution to understand the effect this has on the flow field. In particular, the effect on aerodynamic drag is of interest. Conical bodies of revolution containing different variations of organised porous structures were developed to investigate the objectives. A number of conic profile shapes were considered.

Based on the literature gap outlined in Section 1.6.2, the following research objectives were formulated and explored using experimental and numerical simulation methods and techniques:

1. Determine the overall effect of the conical porous arrangement on the flow field with regards to channel design and structure.
    - The shock wave reflections and interactions, expansion waves, momentum change, and flow structures in and around the porous body (inlet, internal, and outlet structures) are of interest, and the flow physics causing and affecting the behaviour.
2. Determine the effect of the conical porous arrangement on aerodynamic drag, and the drag reduction mechanisms occurring.
    - The flow field topology and quantitative drag data are considered.
3. Compare the experimental results with those obtained in both the literature and computational fluid dynamics simulations in order to validate the numerical method.

Chapter 2

Literature Review

2.1 Introduction

Drag in supersonic flows is reduced by introducing porosity in several ways. As the supersonic flow passes over the porous structure, the shock waves are partially diffused, reducing their strength and the associated drag. The porous structure then decelerates the shock waves, reducing the pressure fluctuations at the body surface. This is significant as the pressure loss incurred by shock waves is a significant contributing factor to drag. Additionally, the kinetic energy from the incoming flow is absorbed and converted into thermal energy, dissipating it to reduce drag.

Until now, research has been focused on understanding the interactions of shock waves with porosity, with introductory studies into porosity use as a drag reduction mechanism. The founding literature and the extended literature review are presented below.

The literature is separated into three sections: the Russian studies, Skews group and additional relevant studies. The research activities most relevant to this research are the grouped works of Maslov, Mironov and Poplavskaya (referred to as the primary section: 'Russian studies'), as the governing objectives and methods were most similar to the presented investigation. The second section is the grouped works of Skews et. al. While overall the Skews investigation served as the basis and inspiration for much of the presented work (due to his

involvement in the model development and in general WITS flow research), it is important to note the key differences between this set of literature and the presented work in terms of the physical flow behaviour.

In the Russian studies, an unorganised porous material was used which could change shape when subjected to supersonic flow. In contrast, the Skews group comprises studies of the interaction of a moving shock wave with objects having both unorganised and uniform porosities. These two shock behaviours (stationary versus moving) represent very different flow field processes. The moving shock wave is inherently unsteady and remains transient throughout, only involving shock reflection and diffraction processes, as well as the subsonic post-shock flows that are negotiating the pores. The Skews works show several parallels to the current research in terms of the post-shock flow field and the significant of porous arrangement, and serve only as a secondary reference for this research. The Russian studies are of primary interest due to their focus on the influence that porosity had on the shock reflection pattern.

2.2 Porous supersonic flow for wave drag reduction

After the work of Skews (discussed below), little work was done in the field of supersonic porosity due to both computational and materials science limitations. However, as the sophistication of both of these fields improved fairly recently, porosity as a possible drag reduction mechanism arose. The recent research relevant to this study was largely driven by the team at Khristianovich Institute of Theoretical and Applied Mechanics.

V. M. Fomin, Mironov and Serdyuk (2009) proposed the first experimental investigation into the effects of gas-permeable materials placed ahead of a cylinder as an aerodynamic drag reduction mechanism for supersonic airflow. They found this condition significantly decreased the wave drag in the system, with corresponding changes in the flow field due to the porous insert. They also noted that the traditional drag reduction mechanisms, such as aerospikes, have disadvantages such as pressure oscillations, higher energy usage and the need for consumable materials, whilst also not being very effective.

They offered an alternative of using highly permeable materials ahead of the solid body to redistribute the incoming flow and create a flow field closer to that around a more streamlined, pointed body. They found that earlier, associated investigations (V. Fomin et al. (2001)) involving grids positioned ahead of cylinders in supersonic flow supported this, however no direct experimental investigation or force measurements of this phenomenon were taken. A supersonic wind tunnel with a strain-gauge balance was used to conduct the experiments. Two designs were tested as support for the gas-permeable material, the first with three longitudinal slots for air passage, and the second a continuous cylindrical tube. The drag was monitored according to the protrusion of these tubes. The experimental results demonstrated that gas-permeable materials ahead of a blunt body in supersonic flow significantly reduce wave aerodynamic drag, and additionally, this reduction is unrelated to viscous forces within the materials. The schlieren images of the porous and solid cylinder can be seen in Fig. 9.

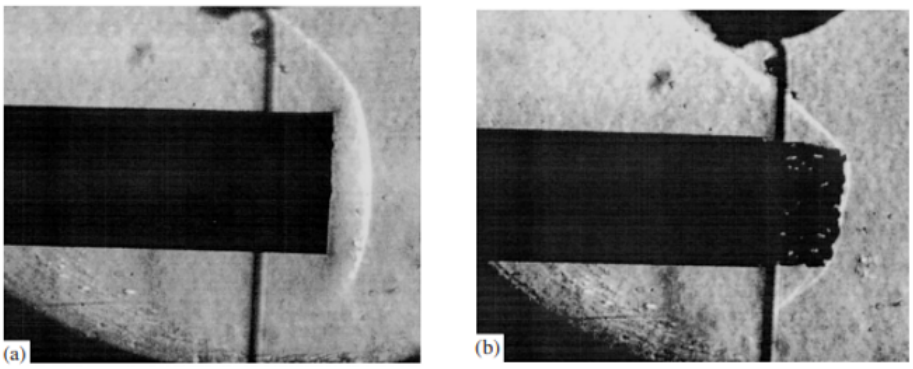

Figure 9: Schlieren images of a) solid rod b) rod with frontal porous material (65 % porous) (V. M. Fomin, Mironov and Serdyuk (2009))

The work of Fomin was extended by Mironov, Maslov et al. (2015), Maslov et al. (2019), and Mironov, Kirilovskiy et al. (2019). Here, they are grouped since all studies used the same nickel foam HPCM gas-permeable porous insert test pieces. Mironov, Maslov et al. (2015) fitted a solid cylinder with the frontal gas-permeable insert, in steady hypersonic flow (Mach 4.8), creating a body of 95 % porosity, with mean pore diameters of 1 - 4 mm. They presented a generalised approach to ANSYS Fluent numerical modelling of supersonic flows around a streamwise-aligned cylinder with a cylindrical gas-permeable insert attached to the front face. The objective of the study was to detect the physical mechanisms of wave drag reduction and to ascertain the key factors of the porous material that affect the drag. The wave drag of

the model was calculated as a function of the permeable insert length and Reynolds number. Fig. 10 shows the experimental models.

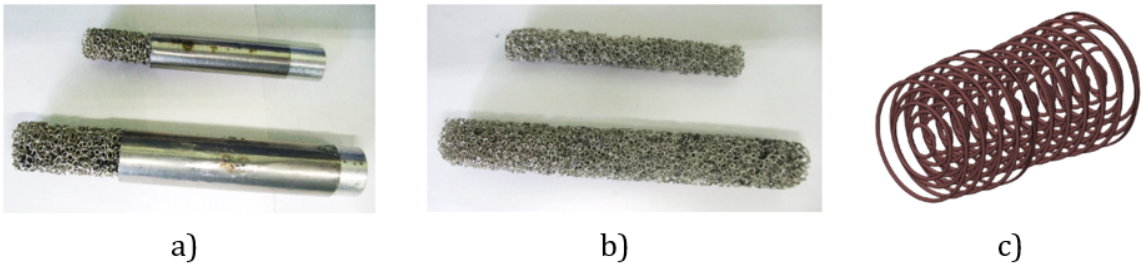

Figure 10: Photographs of the a) cylinder models frontal HPCM inserts b) purely high-porous cylinder with pore diameter = 1 mm c) the 3D skeleton toroidal model of the high-porosity material (Valiullin et al. (2023))

They also used a system of two-dimensional differential Navier–Stokes equations, solved using the SST k – ω turbulence model, second-order implicit time scheme, and second-order implicit scheme. The flux-splitting Roe-FDS method was also used. The inlet boundary was located some distance upstream of the frontal face of the model. The width of the computational domain was decided based on the requirement that the shock wave did not interact with the upper boundary of the computational domain. The outlet boundary existed some distance away from the model base such that the flow in the outlet plane was fully supersonic. The computational domain was separated into three subdomains (before the body, the porous insert, and aft of the insert); the computational grid was refined near the bow shock and on the cylinder surface. Regions near the porous insert and the bow shock required high refinement. The porous material structure was modelled as: “a system of staggered rings of different diameters aligned in both the radial and longitudinal directions." (Valiullin et al. (2023)).

Maslov et al. (2019) showed that the flow field inside porous material and the subsequent drag force of the combined cylinder-porous-insert are primarily governed by the inertial (quadratic) term in the Darcy–Forcheimer equation. At high Mach numbers, the friction force present in the pores directly behind the shock wave is small, and the wave drag is decided by the flow around the structure of the porous medium. At low free stream Mach numbers, the coefficient of inertial losses is far lower, however is still noticeably larger than the friction drag coefficient. This implies that within the porous structure, after supersonic flow interaction has occurred,

the flow is largely inviscid. This is significant as whilst the relationship between the walls of the pores and the boundary layer in the porous system, and the interaction of the outer versus inner structure, must be considered.

They also found that an increase in the porous insert length contributed to the weakening of the bow shock wave, reduced the penetrative effect of the bow shock into the porous medium, and reduced the angle of incidence between the shock and incoming flow (note that in Figure 11, the turn angle of the flow is β_1 and β_1 respectively for the solid and porous cases). It was noted that further downstream, a high-pressure region formed in the porous structure. This occurred as the air from this region in the radial direction, leading to the formation of another oblique shock in the external flow due to the meeting of subsonic inside flow escaping to meeting the supersonic free stream

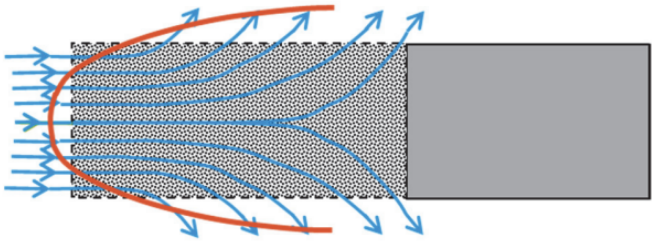

Figure 11: Schematic of the fluid movement resulting in drag reduction for a cylinder with a frontal gas-permeable insert (Maslov et al. (2019))

They found that the drag was reduced by 40 %. This occurred as two distinct processes; by reducing the force of the bow shock by transforming it into a system of weaker shock waves, and by creating an effectively pointed body (Mironov, Maslov et al. (2015)) (i.e. an aerodynamic nose cone-like structure), as illustrated in Fig. 11. The drag reduction observed in both experiments and numerical analyses is caused by the replacement of the rounded bow shock present at the solid cylinder to a system of two attached, oblique shock waves on the porous insert cylinder, whereby the loss in momentum experienced by the flow is greatly reduced. Additionally, the porous insert weakened the incident shock wave to a large enough extent that a significant drag reduction was experienced over the entire body. It was also observed that the secondary shocks in the system had been weakened, indicating that boundary layer separation was also affected. The investigations of the Russian group also typically involved a compliant material, which was able to deform under the impact of

the supersonic flow. This too contributed to the reduction in flow angle and therefore drag. The transformative effect of the internal and inlet flows on the bow wave requires a more controlled investigation and analysis.

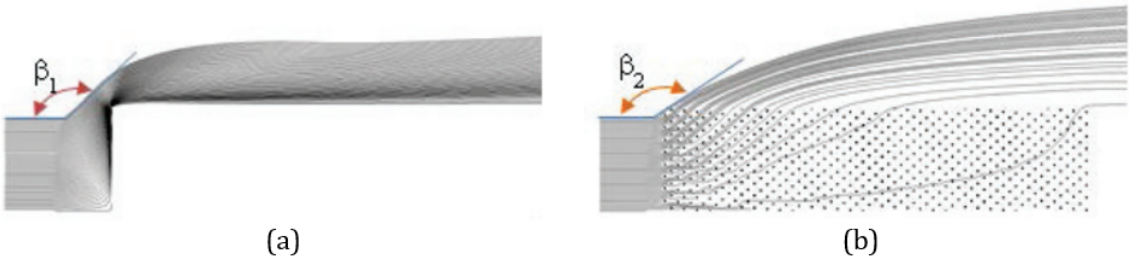

Figure 12: CFD images of streamlines for a) solid cylinder b) cylinder with the frontal gas-permeable porous insert (Poplavskaya et al. (2017))

The work of Mironov, Maslov et al. (2015) was further analysed numerically by Poplavskaya et al. (2017), using the same frontal-insert porous insert on both plate and cylinder models.

Utilizing a skeleton model of a porous material, numerical simulations of the absorption of acoustic disturbances at hypersonic flow over a porous plate with a step were carried out. Due to the structure of the skeleton model, the flow field inside the porous structure could clearly be visualised. The structure of the skeleton model was a three-dimensional toroidal skeleton model of the high-cellular porous material.

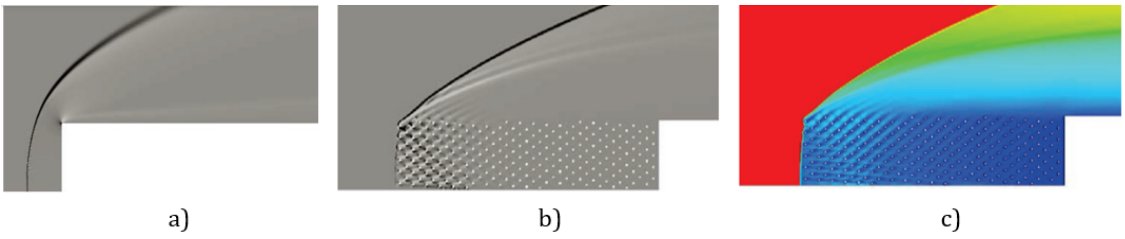

Figure 13: Computed isolines of density gradient for a) solid cylinder b) and cylinder with the gas-permeable insert c) Mach number isolines for a cylinder with gas-permeable porous insert (Maslov et al. (2019), (Poplavskaya et al. (2017)))

Skeleton models allow for gas flow through the porous material to be modelled directly, as in Fig. 12, whereby the flow inside the porous skeleton can clearly be seen. In this toroidal skeleton model, the material (HPCM) existed as a set of staggered coaxial circular rings, as in Fig. 10 c). The advantage of using the skeleton was that only the data on this structure was gathered, removing any unnecessary empirical data related to the filtration of the material. This approach is thus more suitable for visualising and isolating the physics resulting from

a supersonic flow interaction with porous bodies, in particular for ascertaining how the drag reduction occurs. Since the parameters of the airflow within the pores change dramatically along the insert, measures must be taken to isolate this, something which is very difficult experimentally.

Fig. 13 shows the numerical simulation result comparison between the solid and porous cylinders. The turn angle β of the porous insert flow is smaller than that of the solid cylinder (complementary angle 180° - β_1 > 180° - β_2). This showed that the introduction of porosity redistributed the fluid flow. This confirmed the pointed body induced by porosity phenomena that Mironov, Maslov et al. (2015) found.

2.2.1 Pseudo-steady state modelling

The numerical work of Poplavskaya and Maslov et. al was computed using a pseudo-steady state approach (Mironov, Maslov et al. (2015), Poplavskaya et al. (2017) and Maslov et al. (2019)). This was done for several reasons. Steady-state flow is understood as the physical flow being unchanging with time, with transient flows changing with time.

In steady flow modelling, the Reynolds-Averaged Navier-Stokes (RANS) equations are commonly used. The RANS equations give a time-averaged description of the flow field while neglecting unsteadiness. This method is most suitable for models where the flow field exists in a quasi-steady state, where changes over time are relatively small. Steady-state modelling allows for a decrease in computational time and expenses. Quicker solution convergence is facilitated through more efficient and simpler calculations, as only a single time point is considered. Additionally, the time-averaged nature of the steady-state solution means that results are often easier to validate against experimental data. This is particularly advantageous for supersonic wind tunnel testing, where the resulting schlieren photographs *are* indeed the time-averaged results comparable to the steady state CFD solution.

There are, however, limitations to this approach. Steady-state modelling may also be applied to problems involving time-dependent phenomena, including unsteady flow regimes or vortex

shedding. Neglecting these transient effects may result in inaccurate results and predictions, in particular with regards to non-steady forces.

If the only way to obtain accurate results is to explicitly model the flow unsteadiness, then transient CFD is necessary. In a time-transient model the intermediate solutions are individually converged *and* final solution are converged (i.e. between each time step there is convergence), in contrast to only the final solution converging in the steady state calculation.

This allows for the dynamic flow phenomena and resulting impact on the behavior of the system to be captured. While these models give a more comprehensive representation of the fluid behaviour, their use comes with several disadvantages. Due to the added time dimension, transient simulations are more computationally expensive than steady-state, requiring longer computation times and resources. Additionally, the interpretation and post-processing of transient results is often highly complex due to the presence of time-dependent features.

In problems with high geometric complexity, using steady-state modelling poses a higher risk of divergence within the solution due to the asymmetric grids likely to be present in the mesh (Ferziger and Peric (2002)). A solution to this is to utilise pseudo-transient (or pseudo-steady) modelling (Yanbo and Tong (2019), Badcock et al. (2000)). In this approach, the intermediate solutions are not converged, only the final solution is converged. Here, the model aggressively steps through time to achieve the steady solution as efficiently and stably as possible without diverging. The solution is also found in as few iterations as possible, making it very computationally efficient. Since only the final solution is required, and not the evolution of the flow field, the pseudo-steady approach is highly useful for complicated flow geometries (such as the presented porous bodies) that contain a mixture of steady and unsteady flow features, such as porous geometries.

For the presented research, the unsteady elements that were present would likely cause divergence in a purely-steady solution, and only the final solution was required. As such, the pseudo-steady approach was chosen as it was capable of handling the unsteadiness while efficiently providing the final solution. The computational expense of a fully time resolved solution was not warranted given the exploratory nature of the work.

It is important to note the kind of data pseudo-steady models may provide, such as oscillations present in the drag monitor. In a steady-state problem, high symmetry and a structured, symmetric grid are favoured as the final solution is calculated and approaches a single converged value. In a pseudo-steady approach, it is impossible to mesh the complex geometry with a structured grid. The solver tries to find the steady-state symmetric solution but cannot, as it is impossible to to the unsymmetric grid present in the complex geometry (ANSYS Inc. (2023e)). The numerical solution then oscillates around the SS solution just as if it was unsteady, and as such a 'time-averaged' result is deemed acceptable (Ferziger and Peric (2002)). Further, these oscillations suggest the transient behaviour present in the system (from different Mach regimes, boundary layers or turbulence), however the pseudo-steady approach sufficiently captures the results.

The above discussion provides an explanation of the physics causing the numerical drag response, such that conclusions regarding subsequent reductions in drag can effectively be made in this research. Additionally, the studies outline validated computational methods for modelling supersonic porous flows. The successful drag reduction results using limited shapes warrant the further exploration of porosity in aerodynamic shapes, such as cone cylinders. Additionally, the use of HPCM materials, whilst yielding positive effects, has limited applicability as these materials cannot be used in real-life aerodynamic vehicles due to their material properties and structure, manufacturing limitations and the functional requirements of bodies such as nose cones. Thus, the benefits of porosity must be harnessed in an applicable manner.

Little work on organised porosity in three-dimensional bodies has been done following Skews (1994), and no work on organised porosity applied to aerodynamic cones for drag reduction. The aforementioned founding work serves as the basis for this continued study.

2.3 Reflection of shock waves from porous materials

The following section describes the secondary references for the presented work, where porosity interactions with moving shock waves have been studied. While not the primary focus

of this work, several parallels exist which aid in the understanding and interpretation of the research and results. Specifically, in terms of understanding the flow into the porous material and the fluid interactions with/within the pores, such as blockage, interaction patterns and the effect of pore arrangement.

The introduction of porosity and permeability in supersonic flows, and its effects, have long been studied. The body of work mostly includes porosity of the following types:

- Randomised porosity, either existing as HPCM, foam, or wool-like structures (applied to beds, cylinders, prisms, plates - the most common material).
- Organised pattern of holes (drilled into plates or beds).
- Organised pattern of slits/holes (presented in plates, wedges).

2.3.1 Porous flat plates in supersonic flow

The earliest relevant study in this field, conducted by (Friend (1958)), investigated the effects of detonation on a perforated plate, and the resultant shock wave interaction. In this experiment, holes in a uniformly distributed pattern were drilled into the surface of a plate to give a blockage ratio of 50 %. The blockage ratio parameter is defined as the ratio of the area of solid material to that of perforated material. As such, 50 % of the plate frontal area was missing due to the presence of holes. Holes of 6 mm diameter were drilled onto a thin plate. Using a shock tube, strong shocks were passed through the perforated plate to induce flow choking, whereby a meaningful boundary condition was created for theoretical study.

This work was expanded by Onodera and Takayama (1990), who studied the interaction of a plane shock wave with slitted wedges in supersonic flow to establish the conditions required for shock transition from Mach to regular reflection of the shock wave. Fig. 14 shows the schlieren images of the shock propagation over the slitted wedge. This work described the effects of blockage on the flow, as well as the organised structure and angle of inclination to the incoming flow.

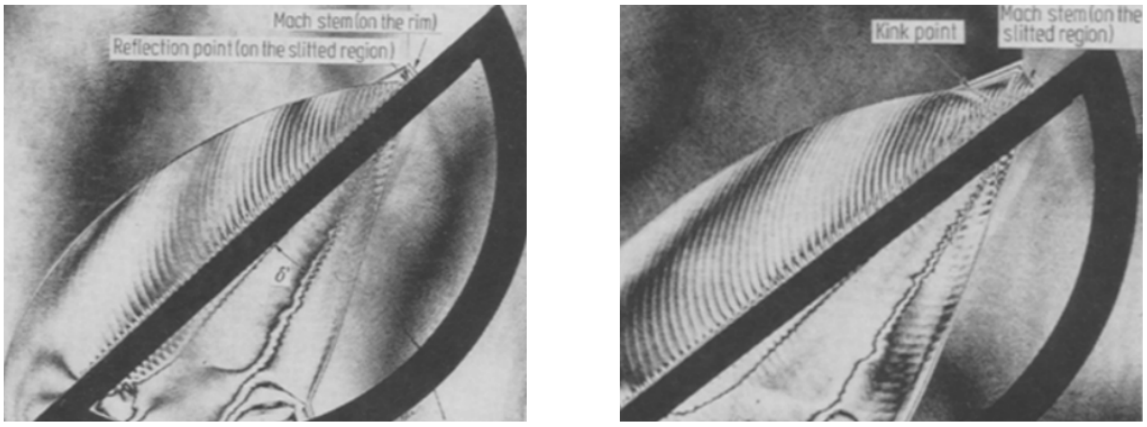

a) b)

Figure 14: Interferograms of shock propagation over slitted wedge; model A for M =2.96; a) $\alpha = 44$ ° b) $\alpha = 40°$ (Onodera and Takayama (1990))

Shock wave interaction with porous plates was rounded out by Skews (2005), as in Fig. 15, whereby the impact on perforated plated with regularly-spaced slits was further investigated in terms of blockage rations and angles of incidence resulting in both regular and Mach reflection. This study directly references and refers back to much of the previous work done on this topic. The flow induced by the grids and the effects of blockage on the flow subject to shock impact were studied using new plate geometries with regard to gap distance comparison (gas guidance) with the same frontal blockage ratio. Significantly, it was found that secondary reflected and transmitted waves occur in the flow field due to the complex interactions within the grid spaces. A complex vortex pattern was also generated underneath the plate due to these interactions.

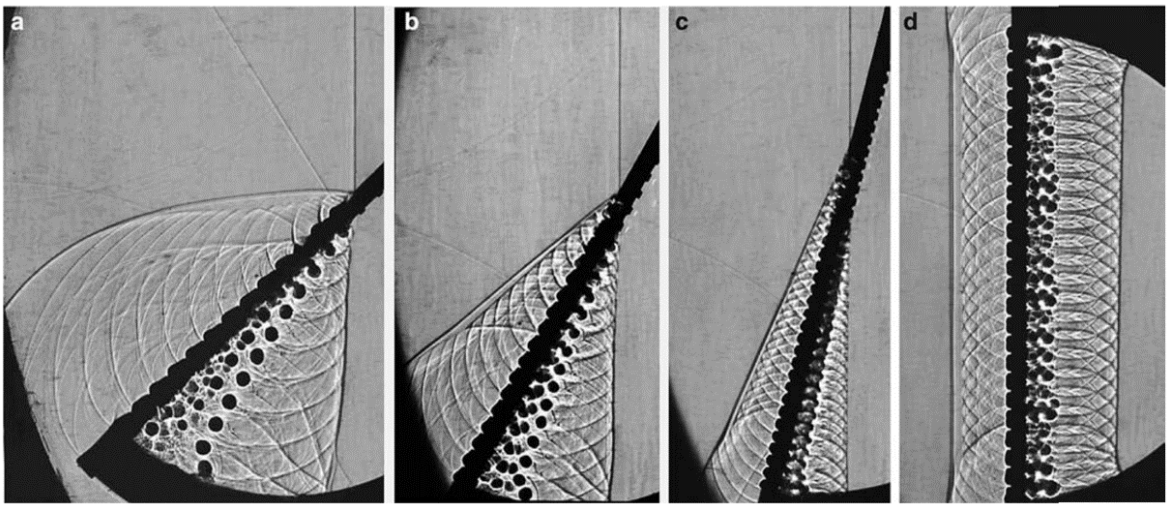

Figure 15: Numerical shadowgraph images for different wall angles, percentage blockage ratio, and Mach number. a) 45°, 25%, M=1.367, b) 60 °, 33%, M=1.352, c) 75 °, 50%, M=1.359, d) 90 °, 33%, M=1.508 (Skews (2005))

For a perforated plate angled with positive incidence, it was found that the angle of the reflected shock, measured relative to horizontal, decreases with the plate blockage ratio. With an increasing blockage ratio, the inflow angle to the plate decreases. It was also found that the pseudo-steady flow assumption used was a reasonable approximation, as confirmed by the underside of the plate. Earlier work showed that wall roughness and permeability reduced the angle of reflection, weakening the shock for bodies with an inclined surface.

A strong correlation existed between increasing the blockage ratio and increased reflection angles. A noteworthy finding was that regular reflection occurred for all tests on a 45° wall. However, this should be impossible for a solid, impermeable wall at this angle condition, whereby Mach reflection should always occur. This may be seen in Fig. 15 a). This implies that the presence of porosity has the ability to transform the shock wave such that very different flow behaviour can be induced. The effect of the inclination angle of the plate was significant. It was initially thought that the flow into the system was perpendicular to the inlet surface, however this was disproven in this study. It was found that the inflow here was largely inclined to the surface, whereby the angle was less than the wall angle. This indicated that the reflected wave was not a sound wave, and that blockage of the flow had occurred. Additionally, from the non-dimensionalised inflow velocities, it was found that the resultant (exiting) absolute and normal velocity components increased with increasing wall angle and permeability level and that this was largely dependent on the blockage ratio.

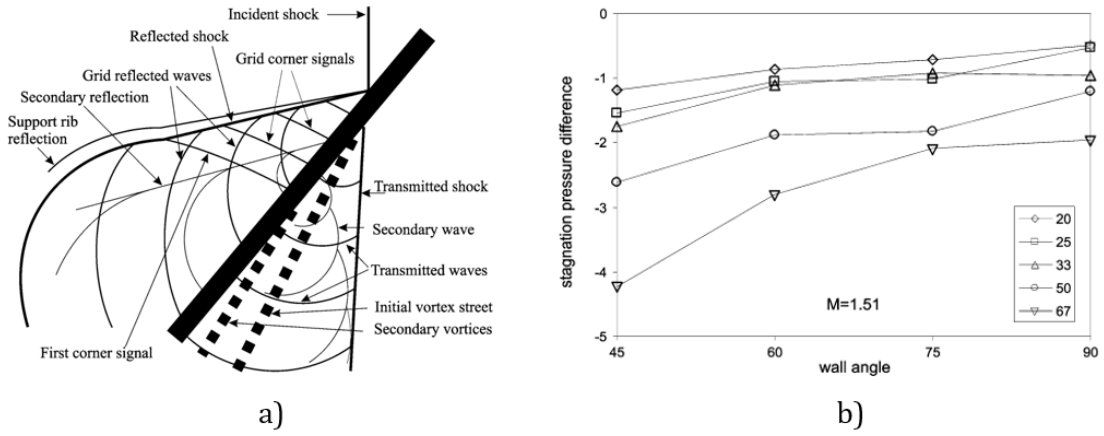

Figure 16: Schematics of the a) the main features of the flow field, including key points b) normalised stagnation pressure difference as a function of wall angle and blockage ratio percentage (Skews (2005))

The behaviour within the gaps of the model was also noted. The inclined inflow caused the formation of a separation bubble at the upstream corner of each gap in the grid, and this consistently occurred regardless of wall angle and blockage ratio. Both the pressure difference across the plate, as well as the stagnation pressure loss, were examined. It was found that the pressure difference increased with increasing free stream Mach and blockage ratio, whereby the pressure of the flow after interacting with porosity was lower than that of the inlet. The stagnation pressure across the plate was found to increase with decreasing wall angle. Higher blockage ratios also led to larger pressure losses. The main features of the flow field, as well as the stagnation pressure changes across the permeable wall, can be seen in Fig. 16.

The above research describes some of the fundamental gas dynamics and flow interactions commonly associated with supersonic flow over permeable bodies, mainly the interaction of a (by definition supersonic) shock wave with porous surface. In this, the flow that follows the shock wave passing through the pores is fully subsonic. It is critical to note that while the moving shock processes are useful for providing context and understanding to the general problem landscape, **only** stationary shock waves (i.e. not moving shock waves which try to pass through an area of porosity) were investigated in the current research. The porosity features that have the greatest influence on the flow field are also described. These factors (as outlined above) will be focused and expanded upon for this research, and include:

- Blockage ratio - due to this ratio being characterised by the ratio of porous to solid frontal areas, this can be adapted for use in terms of area ratios.
- Pressure loss across the permeable surface - the pressure ratio existing between the atmosphere and the post-permeable flow field.
- Mach number control - in particular using the above factors of area, pressure and Mach number combined to control the flow.
- Permeable surface angle, or the incident surface angle.
- The presence of separation regions in the porous flow field.
- The level/percentage of pores present in the solid.

- The arrangement of the pores/channels - slots, slits, holes or channels in an organised or randomised arrangement.

The work described above was critical in developing the body of work for permeable bodies in supersonic flow, as well as in gleaning an understanding of the highly complex physical flow phenomena which govern this type of flow. Whilst invaluable to the understanding of this topic, the work was fairly limited geometrically, experimentally and numerically.

Most of the research related to this was performed using primarily one-dimensional techniques and analyses to establish the primary literature involved with shock wave interactions with porous materials. Skews (2005), Skews (1994) and Skews et al. (1997) reviewed and refers to this extensively. Blast tubes were mainly used, whereby moving, normal shock waves passed over the permeable body. Whilst useful for understanding specific flow behaviours relevant to certain applications (such as explosions and how they react to certain materials), it does not explore steady-state shock waves which occur on aerodynamic bodies such as aircraft. Geometrically, plates with randomised grids, or holes drilled in an organised pattern, were looked at. These plates were usually flat and rather thin, even at various angles of attack. The work done by Skews (2005) was key since the orientation of the permeable plate could possibly represent the leading edge of a wedge-like body. However, clarification was required making regarding aerodynamic geometry.

Law and Skews (2009) drew from the above porous flat plate research. They investigated perturbed wave patterns in the flow field behind a shock wave reflecting off of a porous wall. Figure 17 demonstrates numerical shadowgram images of a Mach 1.5 moving shock wave impinging on a porous grid inclined 60° to the freestream at various gas aspect ratios (AR).

In this study, the effect of gap aspect ratio (AR) on the flow features below the porous grid was also of interest. Three gap aspect ratios were investigated: at AR = 1, AR = 2 and AR = 4. They found that before the porous grid, AR had no effect. Downstream of the grid, the effect of AR on the pore-affected shock front was to: “increase the number of gaps the incident shock transits before the transmitted component of the wave emerges below the grid” (Law and Skews (2009)). I.e., the higher the aspect ratio (i.e. the longer and narrower

the gap), the lesser the effect of the transmitted wave on the downstream side of the porous grid.

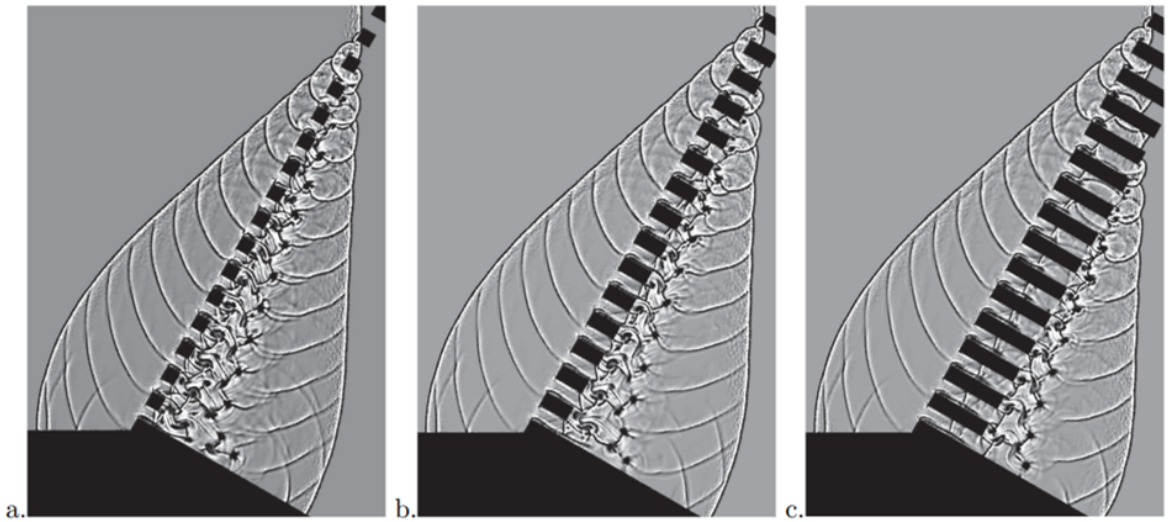

Figure 17: Numerical shadowgram of the effect of gap aspect ratio on a Mach 1.51 moving shock impinging on a 50% porous grid at 60° incidence; a) AR Gap = 1 b) AR Gap = 2 c) AR Gap = 4 ((Law and Skews (2009))).

Figure 17 indicates that the gap AR significantly affects the fluid behaviour above, within (the gaps), and under the grid. Some critical observations were made with regard to the grid-affected flow field, including the formation of shock waves under the grid, the creation of vortex streets in the wake downstream of the gaps, and the discrete change of the gap flow with changes in geometry (AR). The key effect of the AR was on the flow field within and under the gaps between the grids. Most notably, for AR ≥ 1, the gap flow converges to a supersonic nozzle flow bounded by the shear layer generated from the leading corner of the grid element. The shear layer forms a throat, whereafter a non-planar shock pattern develops post-throat. The non-planar quality of this shock wave is associated with its interaction with the shear layer. This shear layer interaction, among others (Mach number, gap geometry), required further investigation due to the complexity of the flow field. The behaviour of gap flow is significantly influenced by the gap AR, with AR ratios creating a converging supersonic flow resembling the flow within a nozzle flow. Lower ARs formed a truncated contact surface off of the leading corner, with a supersonic nozzle flow and a shock wave generated at the grid exit plane of the grid. In this, too low an AR meant that the gap was not long enough for the nozzle-and-shock pattern to form.

The shock wave transmitted through the grid underwent numerous interactions and diffractions, finally forming a planar-transmitted shock under the grid. The number of gaps the incident wave passed over determined this behaviour, whereby the higher aspect ratios required the wave to pass over more gaps. As each transmitted shock exited the gaps and diffracted around the exit corners, vortex sheets were formed. the vortices then interacted with shock waves, causing vortex shedding to occur. Every grid was found to shed a pair of vortices, which subsequently interacted with the adjacent vortices to form a line of vortex streets propagating away from the grid.

The flow through the grid was choked for aspect ratios greater than 1, placing a limit on the amount of mass flow rate through the grid. It was speculated that the effect of incident shock Mach number on the choking behaviour through the grid would be significant, however investigation is required. The relevance of the work done by Law and Skews (2009) pertains to this research with respect to the flow behaviour within the internal network, particularly hole arrangement (hole separation, depth and aspect ratio) and geometry (body shape and angle of inclination).

2.3.2 Organised supersonic flow

The introduction of permeability into aerodynamic bodies was introduced by Skews (1994), where the effect of moving shock waves on a porous wedge was investigated. For a Mach number range of 1.1 - 1.7, various wedges of different incidence angles were tested in a shock tube with schlieren flow visualisation.

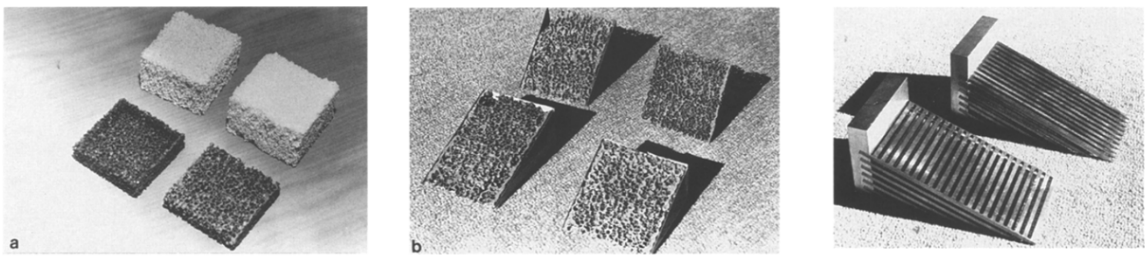

Figure 18: Wedge models a) Alumina and SiC blocks. b) SiC models of various wedge angles. c) Organised rod structure models (Skews (1994))

The primary material of interest was a silicon carbide (SiC) matrix with a mean pore diameter of 2.5 mm, and 73% porosity. Alumina specimens were also tested at 82% porosity. Fig. 18 shows the test pieces. The strength of the porous material was previously tested using pressure drop tests under steady flow conditions to ensure resistance ability to the flow, showing that the SiC had the highest permeability. These models were rectangular blocks.

Two additional unique 20° wedge models were designed which exhibited organised porosity, to allow for better flow visualisation and clarification of the results. The first model featured an organised arrangement of 3.45 mm square-section brass rods, positioned longitudinally parallel to the wedge leading edge surface. The second model had the same rods aligned transversely. The transverse arrangement also featured thin (1 mm) rims on the outer edges of each rod layer, to ensure structural integrity during testing. The design of the test pieces enabled the capturing of the shock wave passage through the wedge while introducing a slight element of three-dimensionality.

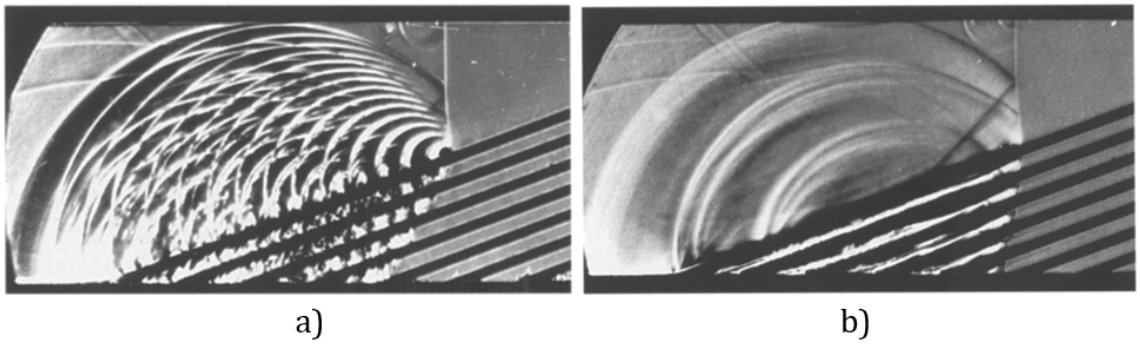

Figure 19: Shadowgraph images of the flow field of the a) longitudinal rod model. b) transverse rod model (Skews (1994))

Since the pressure changes across the porous body were still a key factor under investigation, upstream pressure, as well as the pressure underneath the model, was measured using pressure transducers. Critically, the study confirmed that the choice of porous material (and its associated permeability), as well as the porous arrangement, significantly influenced the shock wave behaviour and interactions with the wedge. In this, it was found that the arrangement of holes on the surface and the resultant inflow pattern of the fluid greatly affect the shock wave reflection pattern. Fig. 19 shows the shock interaction with the rod-models clearly visualised. For cases of Mach reflection, it reduces the trajectory angle of the triple point and

greatly reduces the reflection angle in cases of regular reflection. Fig. 20 shows the highly porous, less permeable models of random structure and their shock interaction.

The permeability of the flow, and thus the amount of resistance the flow encounters upon interacting with the porous material, greatly reduces the strength of the reflected shock wave. In some cases, the strength of the reflected was so attenuated that it almost disappeared, suggesting that permeability has the ability to adjust the behaviour of the shock waves, in addition to porosity.

The pressure measurements revealed the presence of oscillations in the porous structure. These oscillations have a characteristic shape of each particular wedge geometry, irrespective of Mach number, suggesting that the arrangement of porous structure influences the nature of the pressure fluctuations across the body. The study showed that the shock wave was transmitted into the wedge, and depending on the properties of the porous material, was attenuated by varying degrees, showing that the presence of porosity has a damping, weakening effect on the transmitted wave. Interestingly, weaker supersonic free stream Mach numbers showed that the mean propagation velocity of the transmitted wave was far less inside the pores when compared to the existing free-stream post-shock Mach number. This is significant as it indicates that the flow is slowed down greatly (thereby energy is being removed) inside the material.

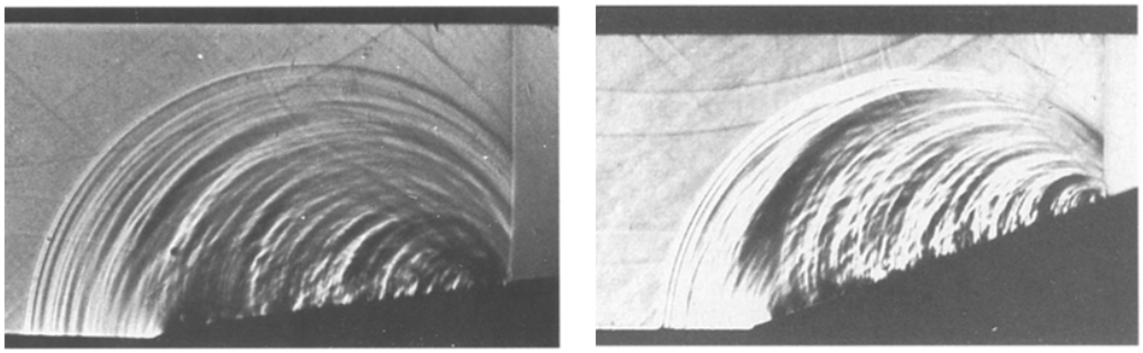

Figure 20: Schlieren images of the porous material wedges a) M=1.53, wedge angle = 10°. b) M=1.56, wedge angle =20 ° (Skews (1994)).

The ability for the flow to be slowed in this manner implies that the porosity may be used as a mechanism to control the flow field. The above research shows that the governing

principles of porous flow phenomena include the elastic properties of the interstitial gas, the composition/design of the solid material in between the pores, and their relative magnitudes. The flow resistance to percolation (the moving of the fluid through a fine-holed structure) is additionally a factor. The Darcy-Forcheimer[i] equation suitably describes resistance in both compressible and rigid skeleton models. The strong resemblance of these wedges to the results of other studies in the area of shock reflection from rough surfaces and from inclined slitted/slotted plates was noted, as well as the complexity of the wave systems that arise from the shock wave propagation and transmission over the wedges of grid-like structure.

This study highlights the important features of the shock wave interactions with porous wedges, such as porous structure, flow resistance and model design. The work draws parallels between these findings and the previous research in this field. The findings of these studies introduce the idea that the flow can be positively manipulated by the introduction of porosity. The significance of this study also lies in it being one of the first studies to introduce organised porosity (the rod models) into a three-dimensional aerodynamic shape, i.e. the wedge. The wedge has high transferability to other shapes, more applicable shapes, such as cones. Additionally, this study introduces the idea of longitudinal and transverse directions as a potential means for flow communication. The arrangement of the rods and their ability to attenuate the shock wave indicates that these types of arrangements of channels reduce the strength of the shock wave, and hence have the ability to reduce drag when a porous configuration based on this is implemented.

It again should be emphasised that the work described in this section is largely unrelated to the work described in this Section 2.2, whereby the only commonality is the porosity of the object and the flow supersonic regime.

The cunicular[ii] models developed in Section 4.6 drew insight from the original organised porous models investigated by Skews (1994). Several successful elements of the Skews models were carried through to the cunicular models, including pore diameter and channel arrangement.

[i] An empirical equation relating the pressure loss due to friction across a porous medium, with respect to the velocity of the flow inside of the medium (Oezcan (2020)).

[ii] A system of organized, interlinked channels within a solid structure through which fluid may enter and/or exit. Distinct from 'porous', which refers to random or organised minute holes dispersed through a solid.

2.4 Additional relevant studies

2.4.1 The effect of porosity on the supersonic boundary layer

Meng et al. (2020) numerically investigated the effect of drag force and heat flux reduction mechanisms caused by the presence of an aerospike on a blunt supersonic nose cone. The aerospike created a pointed nose cone-type structure. Three-dimensional Navier-Stokes equations and an SST k-ω turbulent model were used, where the freestream Mach number of 4.94 was tested. They established that the drag force at this Mach number was reduced by 24.6% when using the aerospike. This showed that the performance of blunt bodies is significantly improved by the attachment of a streamlined drag-reduction mechanism, such as an aerospike. While the work of Meng et al. (2020) is recent and somewhat limited-in-scope, it is strongly corroborated by the broader review paper of Ahmed and Qin (2011).

The effect of porosity on the boundary layer has also been looked at. Ali et al. (2018) examined the fluid interaction between the boundary layer and a porous, permeable wall. Three varieties of porous materials with different porosities and permeabilities for a long flat plate were used, and the interaction of a zero-pressure gradient turbulent boundary layer flow with a rough permeable surface was assessed experimentally. Several parameters were measured, including the boundary layer growth, the energy content of the turbulent fluid structures within the boundary layer, and the surface pressure fluctuations (before, along and after the porous section) Ali et al. (2018).

The introduction of porosity was shown to significantly modify the energy flow within the boundary layer. The pressure fluctuations also increased over the porous region. This suggests that porosity may attenuate the bow shock while disturbing the boundary layer and reducing drag.

2.4.2 Jetting into supersonic cross flow

Due to the benefits associated with venting, the effect of angled jet impingement on a supersonic cross flow is relevant. An option for removing the gas from the porous medium after interacting is by inducing jetting from the medium. For a supersonic free stream Mach number, the jet interaction will be complex.

Papamoschou and Hubbard (1993) performed experiments using argon and helium gas on the impingement of round sonic and supersonic jets normal to a supersonic cross flow. The generated bow shock ahead of the jet dominates and heavily influences the flow field, the presence of which is emphasised in Fig. 21 b) (taken from Zmijanovic et al. (2013), referring to the same jetting effect). In the helium jets, pressure waves emanating from the jet exit caused the bow shock to become wrinkled, likely caused by turbulent eddies of the jet moving supersonically in contrast with the surrounding air. The resultant impingement was found to be primarily dependent on the flow momentum ratio, dependent to a lesser extent on the cross-flow Mach number, and independent of the jet flow properties, such as Mach number, pressure and density ratios. The side effect of penetration for supersonic flows was found to be similar to subsonic flows. The work focused on pressure-matched jets, where shock waves and expansion waves are not present around the jet orifice. In this, the jet pressure matched the pressure of the free stream, a key factor in achieving better jet impingement penetration and improved ability of the jet and free stream to mix. This is because under-expanded jets create under-expansion due to the jet static pressure being higher than the cross-flow pressure, generating shock waves that disrupt the jet flow. Strong injection was also found to generate a bow shock. Schlieren visualisation in a supersonic wind tunnel was used to visualise the flow field, showing the shock structure and turbulence in the jet for various Mach numbers and flow parameters. The shock structure present in the cross-flow was found to be highly unsteady, emanating pressure waves from the jet orifice. Increasing the free stream Mach number mildly improved penetration. The resultant flow field was found to be very unsteady, a disadvantage for practical applications. The jetting examined in this study is demonstrated in Fig. 21.

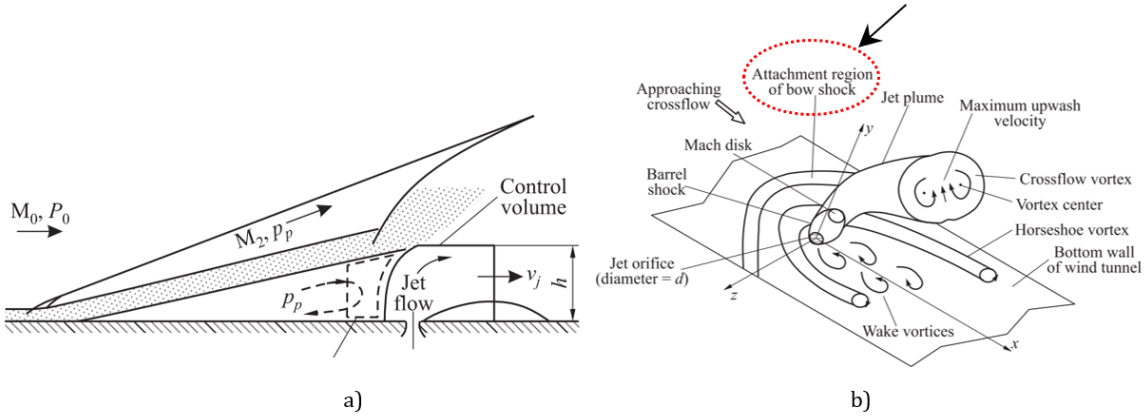

Figure 21: Schematic of the a) blunt-body model of transverse injection into the supersonic flow b) circular gas injection into the supersonic cross flow (Zmijanovic et al. (2013))

Sebastian, Lurkens and Schreyer (2020) expanded on this by examining the flow field around a spanwise-inclined jet in supersonic cross-flow numerically. Implicit, large eddy simulations were carried out at a supersonic cross-flow speed of Mach 2.5. It was noted that the flow features were similar to that of the perpendicular injection mentioned by Papamoschou and Hubbard (1993), however, the overall flow field was more complex and asymmetrical. It was noticed that in the near-wall jet wake, an oblique quasi-herringbone separation formed. The angled jet resulted in flow asymmetry which caused the formation of an oblique shock wave and separation bubble upstream of the jet injection position. The major counter-rotating vortex pair was noticed (as with normal injection), however several secondary counter-clockwise rotational surface-trailing vortices were also induced by the recirculating flow of the separation region behind the jet. These vortices eventually merged into a single vortex rotating counter-clockwise. It was observed that the outer flow was only minimally disturbed in the direct vicinity of the injection site.

Jet injection into the supersonic boundary layer inclined to the spanwise direction includes both an oblique bow shock and barrel shock. This initiates separation regions both upstream and downstream of the injection site. The crossflow interaction downstream of the jet is strong with with jet wake, creating a highly asymmetric series of vortices. Momentum within the boundary layer is uniformly redistributed downstream of the jet injection, where the high-momentum fluid is transported from the outer region of the boundary layer to the near-wall region, creating a boundary layer resistant to flow separation. A dynamic mode decomposition analysis of the flow field showed several interesting findings, namely the momentum

redistribution in the crossflow downstream of the jet, and the interaction between the turbulence present in the boundary layer and the shock waves. Additionally, they found that the near-wall turbulence recovered twenty times the characteristic dimension downstream of jet injection and that the flow redistributes and equilibrates quickly after injection further downstream. This finding is highly advantageous for control applications since quicker recovery of the boundary layer and minimal disturbances to the external flow imply drag reduction abilities. The spanwise-inclined jetting behaviour may be found in Section 7.6

2.5 Conclusions

Porosity in supersonic flow provides highly complex flow fields with shock interactions. Organised porosity may be used for mass removal behind a bow shock to reduce wave angle and provide a form of boundary layer suction. By utilising supersonic jetting and jet impingement, the removed mass is injected back into the flow field, modifying the drag behaviour of the body. A better understanding of the interaction of these phenomena could help develop design rules that may prove useful for future ballistic vehicles.

Chapter 3

Research Method

An investigation into organised porosity inside conic bodies of revolution in supersonic flow as a mechanism for wave drag reduction was undertaken. The flow field and resultant shock wave interactions both around the cones and within the porous structures were examined. The research methodology included both an experimental and numerical approach.

The majority of the research focused on the numerical results, where the experimentation served mainly for validation purposes. This was done because the flow field inside the porous structure was the key phenomenon being observed, and this region was concealed in the experimental results. The numerical data allowed for significantly more data and understanding to be extracted, and as such was used exclusively for the later conic models. The combined results allowed for a sufficient description of the flow field. Shock wave interactions and their effects around the cones and within the porous structures were examined from the qualitative data. The quantitative drag data was evaluated with uncertainty analysis.

The experimental and numerical data were compared to validate the numerical method. This instilled confidence and reliability in the numerical model such that it could be used for the more focused conic model versions later on. Using the proven numerical model, the research question was comprehensively investigated

3.1 Research overview

The flow chart of the overarching research process is depicted in Fig. 22. It broadly outlines the research methodology undertaken for this research. The flowchart aided in decision-making for the presented thesis, integrating both the computational and experimental methods. This was achieved after careful framing of the research under the guidance of the literature review and gap analysis. Management planning was enforced using this method, where verification and validation of the research methodology were ensured before discussion of the results was carried out.

The flow chart and its elements are summarised in the following sections. A detailed discussion of the experimental and numerical research method is provided in Chapter 4 and Chapter 5. The validation of the numerical method and experimental and numerical results is presented in Chapter 6. The results are presented and discussed in Chapter 7. Sections 8.1 - Section 8.8 provides the conclusions of the presented research, concerning the research objectives and critical research question. Section 8.9 communicates areas of further work to be done.

Figure 22: Flow chart showing the research method process

3.2 Research methodology

To answer the research question, a mixed methodological approach was used. A qualitative and quantitative approach was employed using both experimental and numerical research methods. This was required due to the complexity of the experiment - both visual and numerical data were required to adequately represent and understand the flow field. The mixed method also ensured the validation and verification of the numerical method.

Quantitative research was required for the collection and analysis of numerical data from the flow field (e.g. drag, pressure and velocity data). Qualitative research was necessary to analyse non-numerical data (e.g. flow visualisation images, plots, isosurfaces). The combination of data types comprehensively evaluated the flow field and physical phenomena present. It enabled detailed, contextualised insights to be gained from the qualitative data, and broad, externally valid insights from the quantitative data.

Conducting experimental research allowed for almost complete control of the study, allowing for variability and repeatability while maintaining validity. The limitations of experimental design include the availability and accuracy of equipment, as well as design limitations. Physical experimentation is subject to uncertainty and error in the form of measurement errors, random variation, apparatus accuracy and damage by wear and tear.

Numerical studies are advantageous as they provide information with greater detail and accuracy than physical experiments. This is especially true in complex flow systems. Simulation results provide a deeper visual understanding of flow behaviours and physical phenomena within a system that is often not possible with experiments. Numerical models are limited as they are only approximations and may not accurately represent the entire system. Simulations are subject to uncertainty and error, caused by factors such as mesh size, boundary conditions, and turbulence modelling.

Neither research method should be used in isolation. Experimental and numerical models should complement and confirm each other in the investigation of a particular phenomenon (Georgiadi-Stefanidi et al. (2011)). The combined research approach utilised here ensured validation in this way.

3.3 Experimental method overview

Experimental testing was conducted using the supersonic wind tunnel and associated equipment. Additional apparatus included a drag monitoring sting balance to measure the drag force on the conic models and an optical flow visualisation set-up. From this, drag data and schlieren photographs were collected. Mach 3 and Mach 3.5 were tested.

Porous conic models were designed which allowed the research objectives to be met. Autodesk Inventor Professional Academic 2022 was utilised for this purpose. The experimental models were manufactured using Digital Light Processing (DLP) resin 3D printing and mounted symmetrically at 0° angle of incidence using a sting apparatus placed in the SSWT.

The quantitative experimental data was gathered using a drag monitoring system. A sting balance using a Wheatstone bridge strain gauge system was positioned on the sting. This system was linked to an external Data Acquisition System (DAQ) which measured the drag force acting on the conic models during SSWT tests. The compressive axial strain during testing was accurately measured and collected by the DAQ before it was converted to coefficient form for comparison to the numerical data.

The drag monitoring system was not very robust and failed after the first set of cones were tested due to weak construction. The data gathered before failure was accurate and comparable to the simulation data. Thus, limited experimental drag data was available. The drag data was analysed using statistical analyses. The means with the data were taken, and standard deviations were used to estimate the uncertainty to 4 σ or 6 σ.

The qualitative experimental data was collected using an optical flow visualisation setup. Schlieren photographs showed the external flow field using density gradients. The schlieren photographs were limited in that only the external flow was visible in the images. The internal porous structure (the region of interest) could not be seen on account of the optics. The schlieren photographs were visually analysed to identify key flow features and explore behaviours visible in the images.

The sting apparatus was calibrated to address the working condition of the strain measuring system. This system was verified and the error present in the instrument reading was confirmed. The compressive force calibration of the sting was achieved using a Universal Tensile Testing Machine. The load cell on the sting was connected to a digital tester which provided a sample result within an acceptable range. The calibration ensured that the sting balance provided accurate drag measurements. The details of the experimentation and calibration are discussed in Chapter 5.

3.4 Numerical method overview

A computational fluid dynamics (CFD) package, ANSYS Fluent R22.2 (academic license), was used to model the flow field with high-performance computing resources Centre for High Performance Computing (CHPC) (South Africa), with some data processing in Tecplot 360 EX 2022 R1. The computational domain modelled the experimental conditions as closely as feasibly possible. Drag data and various visual plots were gathered from the analysis.

The same conical models used in the experimentation were used for the CFD. The conic models were two-plane symmetric, and so a quarter-cylinder domain (with two symmetry planes) was used. The use of symmetry greatly reduced the computational load requirements and allowed for a higher level of refinement at the complex porous region.

The expected flow field was highly turbulent and transitional with several speed regimes. A pseudo-steady transitional k-ω SST turbulence model was used due to the presence of both supersonic and subsonic flows in the system, as well as the presence of both viscous and inviscid flows in the walled system. This turbulence model was successfully used in many porous studies (Poplavskaya et al. (2017), Mironov, Maslov et al. (2015), Maslov et al. (2019) and Mironov, Kirilovskiy et al. (2019)).

The quantitative numerical data (drag force and coefficient C_d) was gathered using a drag convergence monitor on the cone wall. The drag coefficient based on frontal area was calculated so that it could be directly compared with the experimental data. Due to the pseudo-steady nature of the flow field (due to the presence of unsteady flow features), the drag data exhibited a damped oscillatory pattern. To determine the steady-state converged value around which the plot was oscillating, the time averaged drag coefficient between 10 000 - 20 000 and 20 000 - 36 000 iterations was determined. These results were equivalent within a 0.95 confidence interval, indicating the true steady state final value had been correctly obtained by 36 000 iterations.

The cone region required careful refinement to resolve the internal porous flow correctly. A body of influence (BOI) surrounded the cone and refined the incident shock wave internal

porous flow. Wall sizing was used around the entire cone body to adequately resolve the pore geometry. Inflation was used around all wall boundaries due to the inherent boundary layer effects present in the porous flow.

The boundary conditions represented reflected a projectile in ideal, steady supersonic flight constrained to one direction only. The gauge pressure and temperature in the domain were set at 9000 Pa and 100 K for an operating pressure of 0 Pa respectively. This matched the experimental conditions inside the SSWT test section, with free-stream speeds of Mach 3.5 and Mach 3.

The qualitative data included contour plots of Mach number, velocity and density to describe the features of the overall flow field. Vectors of velocity magnitude were plotted such that the flow within the pores could be described, with particular reference to the recirculation and direction of the flow. The incident shock wave was isolated with isosurfaces such that the attenuation and effect on this wave were clear. Isosurfaces of velocity showed the flow within the venting structures.

Due to local unsteady flow features, it was typically necessary to run for up to 60,000 iterations to achieve an acceptable level of convergence on drag data.

The detailed description of the numerical modelling, as well as the uncertainty and sensitivity, may be found in Chapter 4.

3.5 Validation and verification overview

The concept of validation has different definitions depending on the particular discipline and application of interest. Here, validation is used to determine the degree to which the numerical model represents the real world (experimentation), and as a way of obtaining credibility and trustworthiness for the computational model (Borg, Paulsen and Nja (2014)). The computational domain was designed to mirror the experimental conditions as closely as feasibly possible. The results of the experimental and numerical models were compared. The research methodology was then validated and verified.

The quantitative data was compared by directly comparing the drag coefficients between the two data sets. The qualitative data was compared in stages. The visible external flow from the schlieren images was compared with numerical density shadowgraph plots and by using overlaying images. This was done because the internal schlieren flow was invisible. The schlieren flow was found to match the numerical plots exactly in terms of the visible external flow features.

3.5.1 Numerical validation

In numerical models, validation is regarded as a measure of computational model accuracy between the predicted values of said model and the real world. Here, the real world is represented in experiments, where experimental measurements of a particular quantity are compared to numerical model predictions of that same quantity. In this study, both quantitative (drag coefficient) and qualitative (flow visualisation) data are compared for validation purposes.

When a model is validated for use in a particular set-up, every variable within that set-up must be adequately described or accounted for. Additionally, a validated model implies that users are confident that the model is sufficient for the intended purpose in terms of accuracy, uncertainty and applicability (Borg, Paulsen and Nja (2014)). The degree to which the experimental and numerical model prediction agree is considered to be the model accuracy and forms the basis for validation of the model.

Triangulation was applied to facilitate rigorous validation of the numerical method and data through cross-verification from more than two sources. This included using multiple datasets, methods, and extensive use of the literature and multiple authors to examine the research question (Thurmond (2001)). Applying triangulation enhanced the validity and credibility of the findings while mitigating the presence of any research biases. In summary, triangulation was used to ensure that the same conclusion was achieved using several different approaches (numerical, experiment, and literature).

The numerical method was validated using extensive comparison to published literature. The computational domain was set up to align with the well-established work of Valiullin et al. (2023), Mironov, Maslov et al. (2015), Poplavskaya et al. (2017) and Mironov, Kirilovskiy et al. (2019) (the founding literature).

The presented work used the same numerical method and processed data in the same way as Valiullin et al. (2023) and Mironov, Kirilovskiy et al. (2019) such that they could be compared directly for validation. This included the designation of boundary conditions, mesh and solver settings, and the chosen turbulence model. The drag data from this group matches the experimental data very closely (±1% different in some cases), indicating very high-quality validation and reliable, accurate results. It is useful to utilise these previously successful studies to improve the quality and output of this research.

The founding literature method was referenced as it is regarded as reliable and accurate. The method of testing and validation also used mixed methods and multiple repetitions of experimentation, and their numerical validation was very rigorous. The founding literature research team specialises in the field of supersonic porosity for drag reduction. The literature also has a fairly high citation count, indicating that the studies are of high quality.

Validation was also achieved using convergence. This type of validation compared the convergence value (here the converged drag coefficient) of the simulation model with the reference result (the drag coefficient of the founding literature). These results are compared comparison knowing that the modelled solution is not the best, but assuming that the simulated results have converged. Here, the simulated (normalised to match the founding scale) drag coefficient was within ±2% of the founding value. This very close result was acceptable, especially when accounting for the sophistication and refinement of the founding literature model (both of which exceeded the simulation).

3.5.2 Experimental validation

The experimental method was validated by designing the experiment according to previously successful WITS flow research projects. Additionally, it was ensured that the design aligned with similar experiments presented in the published literature.

The sting apparatus (and elements of the conic models) used were designed according to previously successful stings used at WITS over many years, including Surujhlal (2018), Filippi (2017) and many projects by B.W Skews. The sting was to securely mount the conic models horizontally and avoid pitching. Several design improvements were made to ensure this, including reinforcing several components. By replicating elements of stings that gathered successful results, the validity of the experimental apparatus was increased.

The conic models also contained elements inspired by previously successful results (e.g. Skews (1994)), including the cone and pore size, and certain pore shapes. These elements were already successfully visualised in a shock wave environment (and within an aerodynamic shape), indicating that a similar visualisation effect should be noted in this research. Again, this adds to the validity of the experimentation.

The force balance design was based on the design outlined by Bernstein and Pankhurt (1975). The balance was very successful for the first data set, however failed thereafter. Failure occurred due to of wear-and-tear on the sting and strain gauge system due to the supersonic flow exposure. The data from the first testing set closely matched the applicable numerical data set (within $\pm 2\%$, acceptably close), however some sources of error and discrepancies existed due to the slightly primitive drag monitoring approach, as indicated by the statistical analysis of the drag data. Due to these factors, the installation method used for the force balance as described in Chapter 4 is not recommended. Improvements to the force balance are outlined in Section 8.9.

The schlieren images produced were of excellent quality, as indicated by the clarity and focus of the images. Additionally, the solid pointed cone schlieren images were compared to CFD density plots (for the same simulation settings), and identical shock angles were produced. This implies that the porous models are also likely to have a strong resemblance to the CFD.

The experimental test pieces were manufactured using strong materials and new methods not before used in the laboratory. The models withstood the forces of the wind tunnel successfully and produced results directly comparable to the numerical, 'true-to-design' cones.

The experimental method had an acceptable level of reliability and validity, however, the experimental use is limited due to the force balance failure and the invisible region in the schlieren image. Improvements to the experimental design are detailed in Section 8. However, the results that were produced by the experimentation were of very high quality and agreed with several different sources, including literature, validation-case (solid cone) numerical data, and the actual numerical data. The drag data was also very close to both the simulation and the published data. The success of the results confirms that the experimental method is valid and that the results are reliable when used in conjunction with the numerical study.

3.6 Design of conical test specimens overview

Several different types of organised porous structures were designed within various conical bodies of revolution. The porous structure was designed according to the particular flow direction element being investigated. This assisted in describing the effect each element had on drag.

3.6.1 Conic model fundamentals

The cone dimensions were chosen according to the constraints of the WITS SSWT blockage ratio. If this was not upheld shock generation could not occur. The pore dimensions were based on those successfully used by Skews (1994).

Four conic profiles were chosen, namely the pointed right cone, hemisphere, ellipsoid and secant ogive. The shock behaviour according to any body of revolution can be focused on three parameters; shock attachment type, radius of curvature and profile radius; such that the universal effect on other bodies of revolution irrespective of shape, can be inferred. All

models were two-plane symmetric to reduce computational time. Fig. 23 shows the shape comparison between the conic models.

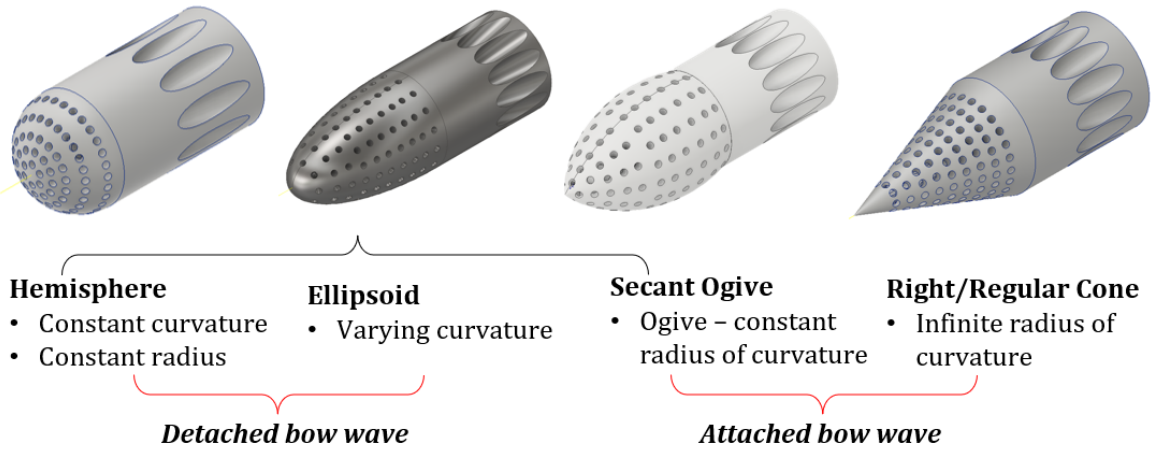

Figure 23: Schematic comparing the BS4 hemisphere, ellipsoid, secant ogive and pointed cone porous vented model conical shapes characteristics

All of the conic models were created by hand using Autodesk Inventor Professional Student 2022. Cone-cylinders were created by attaching the cones to a solid cylinder base. The detailed model dimensions may be found in Section 4.6. The pores were circular holes of 2 mm - 2.5 mm diameter for manufacturing and flow visualisation purposes (based on Skews (1994)). No channel overlap was allowed, as this caused divergence in the computational models.

Porosity levels of 0% (solid) and $\approx$ 60% ($\pm$2% error) were tested. After applying ANSYS R22.2 Finite Element Analysis (FEA) Static Structural compression modelling, this was the maximum achievable possible porosity without structural failure of the models, as presented in Section 4.7.2. The error exists as it is impossible to repeat the identical porous structure across all different shapes.

3.6.2 Conic model internal dispersion

Several porous networks were designed, consisting of variations of three interconnected systems: the inlet, internal, and outlet networks. The inlet network allowed for fluid to flow into the porous cone. The internal network allowed for fluid mixing and pressure redistribution, as well as movement. The outlet network was the system by which the flow was simultaneously

accelerated and directed out of the system. The network was constant across all of the shape families tested. The results of each designed cone iteration were compared and then altered accordingly to improve performance. The composition and purpose of the inlet, internal and venting networks are briefly described below, however, the full description (with dimensions and schematics) may be found in Section 4.6.

Inlet network

The inlet network is comprised of the many surface holes positioned on the cone-cylinder. The distance between hole centres, irrespective of direction, was no less than 1 mm apart, otherwise warping and collapse risk existed. The maximum number of surface holes was always preferred while taking the manufacturing constraints into account. The cell size of the internal network was chosen in accordance with the literature (see Chapter 5) due to the small separation distance between holes. This was such that the internal flow field could be adequately represented and resolved.

Internal network

The internal network held three flow dispersion channel types located in the solid cones: toroidal, longitudinal, and radial, as described below. The exact effect on the flow (due to the dispersion type) was then able to be identified and isolated.

Toroidal

- Hollow equidistant ring channels (known as toroids) staggered within the conic body.
- The overall toroid diameter increased as the cone base was approached.
- Allows for the flow to circulate continually within each plane, whilst also creating a space in which the longitudinal and toroidal flow could mix simultaneously as the hollow channels merged. The first toroid accounted for the delicate porous tip of the cone, which was vulnerable to breakage during printing if there was too little material present.

Longitudinal

- Multiple linear channels patterned around the cone axis, inclined slightly to the z-axis.
- Longitudinal channels are always spaced equally around the z-axis to ensure symmetry across at least the mid-plane, no channel overlap, and maximum channel count (essential for maximum inflow). Longitudinal pore ran between the first and last toroid, i.e., linking all the toroids together.
- Acted as the main source of outflow initialization due to its slight positive incline, as well as it being the global pore connecting all the structures, including the vent inlet.
- Linked vents with internal porous structure smoothly, such that fluid momentum was easily transferred to the vents.

Radial

- At each toroid, and at multiple equidistant positions around it, linear channels extended through the solid, to always exit the body perpendicular to the cone surface, known as the inlet pores.
- Inlet pores were equally spaced, with as many holes extruded such that the required common porosity level was always met, whilst also maintaining a safe printing separation distance and zero overlap.
- The larger toroidal diameter was to allow for adequate mixing and account for channel overlap discrepancies occurring during merging. The toroid separation was decided based on both the maximum number of rings which could fit within the shape within the manufacturing and strength constraints, as well as the refinement capabilities of the DLP printer.
- The radial channels allowed for the inflow of the fluid into the structure from the outer field.

Outlet network

The outlet network was a series of channels connected to the inlet network, extruding through the cylindrical base. The vent design was critical to the drag performance, and multiple vent

geometries were examined. The vent allowed for the subsonic flow within the pores to be accelerated and escape from the porous structure. Vents are equally spaced around the cylinder, without overlap at either the vent inlet or outlet. The basic factors affecting vent geometry are as follows:

- Duct geometry - asymmetric variable area (converging/diverging) or constant area.
- Inlet face extends from long-channel, exit face located downstream of the cylinder body, above the shoulder.
- Exit diameter varies. The two faces are lofted together linearly, i.e. linear expansion of flow through vents.
- Vent expansion ratio (A/A*) corresponding to a particular free-stream Mach number exit condition.

Throughout the research project, many different vent configurations were investigated. Isolated porous designs were also explored to investigate the effects of particular channels, including models without vents network, longitudinal pores or toroidal channels respectively. The detailed porous cone design and manufacturing are discussed in Chapter 5.

3.6.3 Cone manufacture

All experimental models were 3D printed using the Creality LD-002R 3D Resin Printer located in the WITS MIA Laboratory. This manufacturing method greatly constrained the hole separation and hole sizes. Resin 3D printing was the only suitable manufacturing process due to the complex geometry and the requirement of no internal supports.

3.6.4 Conic model testing and expansion

The design outlined above was applied to create unvented, vented, and solid baseline models implemented into all four shapes. These models were tested both experimentally and computationally to gain the baseline results. The two data sets were then rigorously compared

and were found to be in good agreement. The experimental tests validated the numerical method and the results were deemed reliable.

The baseline (zeroth iteration) results indicated that only the combined (longitudinal-toroidal-radial) vented pointed cone (BS0) had a meaningful drag reduction effect (3%) due to its porous structure. As such, the BS0 drag-reduced model alone was focused on and expanded upon, being further investigated to include more venting network configurations.

The extended conic models were only analysed numerically since the experimentation had validated the numerical method. The first iteration of ducts examined the effects of changing the inlet pore angle, vent area changes and the effects of toroids. From these results, a final, second iteration of models was created. This second iteration kept the most successful inlet/internal network configuration, however expanded purely on vent geometry. The vent geometry consisted of the nozzles with area ratios described as: linearly expanded, underexpanded, overexpanded, and purely horizontal constant area.

The respective conic model iterations are described below:

- Zeroth iteration - solid models and unvented/vented porous (BS0, LV for all shapes).
- First iteration - Vented porous models. Inlet angle, vent geometry, toroid diameter - (BS1, BS2, BS3, BS4, cone focused).
- Second iteration - Vented porous models. Extended vent geometries (OE (overexpaned), UE (underexpanded), HV (horizontally expanded), etc. in cones and particular vent geometries in other shapes).

3.7 Conclusions

The cumulative data confirmed that the combined vented porous arrangement implemented into the pointed cone reduced the drag by 3%. From the second iteration of models, the ideal configuration corresponded to the vent designed to pressure-match the free-stream condition

behind the incident shock wave, with a similar result to the BS4[i] model. In this model, the inflow and outflow of the entire system were balanced such that maximum subsonic flow was drawn into the structure, choked at the minimum area location, and expanded through the asymmetric, diverging vent such that constant mass flow was maintained. The pressure ratio between the exit plane of the vent and the free stream was close enough that minimal shock interference and turbulence were generated. The boundary layer was minimally disrupted, whilst the incident shock wave was meaningfully attenuated. This porous structure was repeated in the other shapes with similar effects.

[i]BS4 indicates the naming convention that was adopted (using the initials of previous members of the WITS Flow Laboratory, combined with the model iteration number) to name and group models based on the features/parameters being tested

Chapter 4

Experimentation

4.1 Introduction

The SSWT in the University of the Witwatersrand (WITS), supplied by the Aerolab Supply Company was used to conduct the experimental testing component of this research. The SSWT is fitted with an optical system that was configured for both schlieren and shadowgraph flow visualisation. The system is mounted on an adjustable light bench that can ensure consistent configuration of the light paths across experiments. The SSWT was controlled remotely using a computer system housed in the SSWT control room of the laboratory. The tunnel features static pressure measurement instrumentation and a variable contour sliding block nozzle which allows for variation of the test section Mach number. A sting was designed to mount the conic models in the test section, and a force balance was developed to take drag measurements on the models during testing. The detailed specifications of the associated equipment and instrumentation used in the experimentation work can be found in Appendix A.

4.2 Supersonic wind tunnel testing facilities

4.2.1 Testing facility overview

The SSWT specifications provided by the Aerolab Supply company are presented in Table 1.

Table 1: SSWT Specifications

Wind tunnel type	Blow-down
Calibrated Mach range	1.1 - 3.8
Test section dimensions	101.6 mm x 101.6 mm
Operational stagnation pressure	250 kPa

4.2.2 Supersonic wind tunnel operation

A supersonic wind tunnel is an apparatus used to reproduce steady supersonic flow phenomena, including pressure, Mach number and temperature. The schematic of the blow down supersonic wind tunnel used in this experimentation is shown in Fig. 24. The SSWT consists of four main sections: the pressure reservoir, nozzle, test section and diffuser. The pressure reservoir provides air to the nozzle, which is used to expand the working fluid (air), to produce steady supersonic flow conditions in the test section.

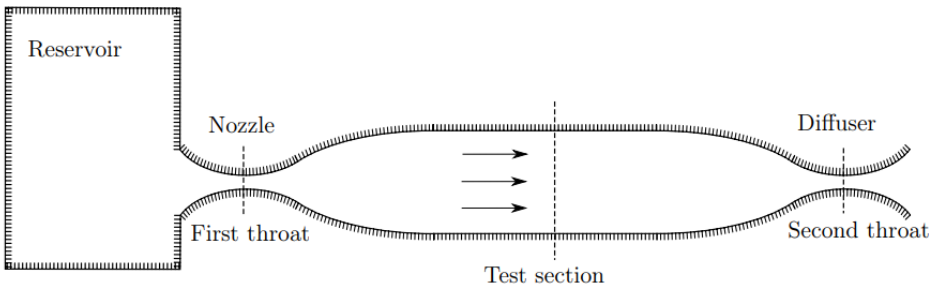

Figure 24: Blow-down supersonic wind tunnel diagram

For the wind tunnel to be started so that supersonic flow is achieved in the test section, specific flow requirements must be met. The diffuser throat must be larger than the nozzle throat. This is so that the diffuser can absorb the mass flow passing through the tunnel, and to ensure that the nozzle throat chokes before the diffuser throat. When air is released into the nozzle via a valve, it is accelerated to the sonic condition (Mach 1) at the nozzle throat. As the supply pressure continually increases from the reservoir on account of the valve

opening, a shock wave is generated in the diverging section of the nozzle. As the pressure is further increased, the shock moves downstream until it reaches the nozzle exit. This occurs so that continuity is maintained while the pressure increases, and is necessary since both throat areas are fixed. In this, by increasing the supply pressure from the valve, this startup shock jumps to the diverging section of the diffuser. This mechanism initiates steady supersonic flow in the test section. The generation of steady supersonic flow occurs once the valve is completely opened, providing constant stagnation conditions during the wind tunnel test.

4.2.3 Additional processes

The SSWT requires several additional external processes to operate, as depicted in Fig. 25.

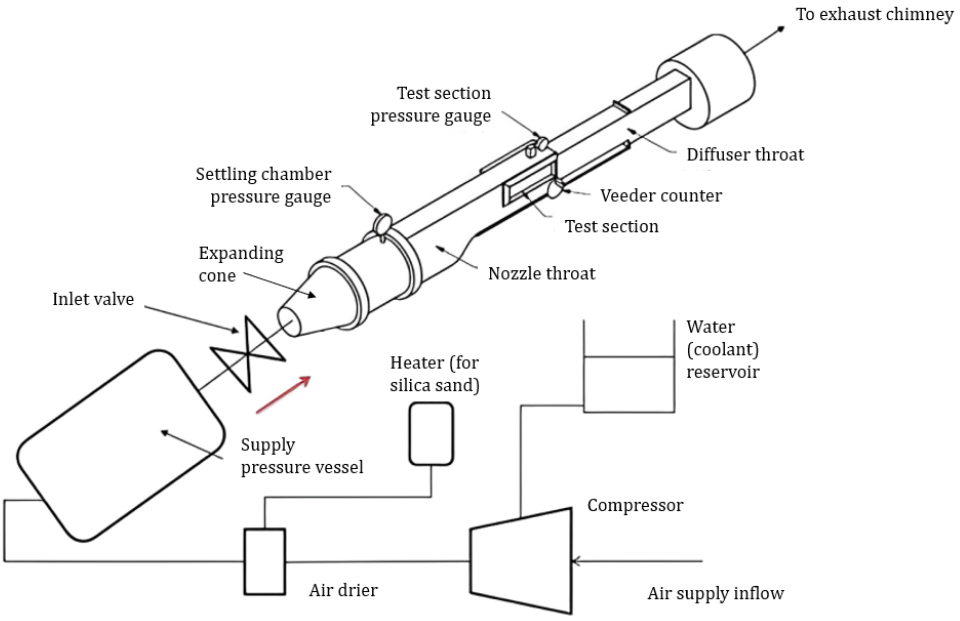

Figure 25: Schematic of the SSWT and associated apparatus

The large pressurised vessel supplies the air which flows through the tunnel. An 18.7 kW compressor was used to supply the pressure vessel with air from the atmosphere. The silica sand drier tank was used to remove any moisture from the air before it entered the pressure vessel. The maximum rated pressure of the pressure vessel was 17 bar, and the compressor automatically shut off once the vessel reached 15 bar to prevent reaching or exceeding the maximum value. At the end of each day of testing, the air drier and heater were turned on to restore the silica sand in preparation for the next day.

4.2.4 Static pressure and electronic data measurements

During supersonic testing (from the time of tunnel startup to termination), static pressure data was automatically recorded using the computer system which controlled the tunnel. This data monitored the operation of the tunnel, such that if the tunnel became blocked during a test, it would shown on the computer monitor.

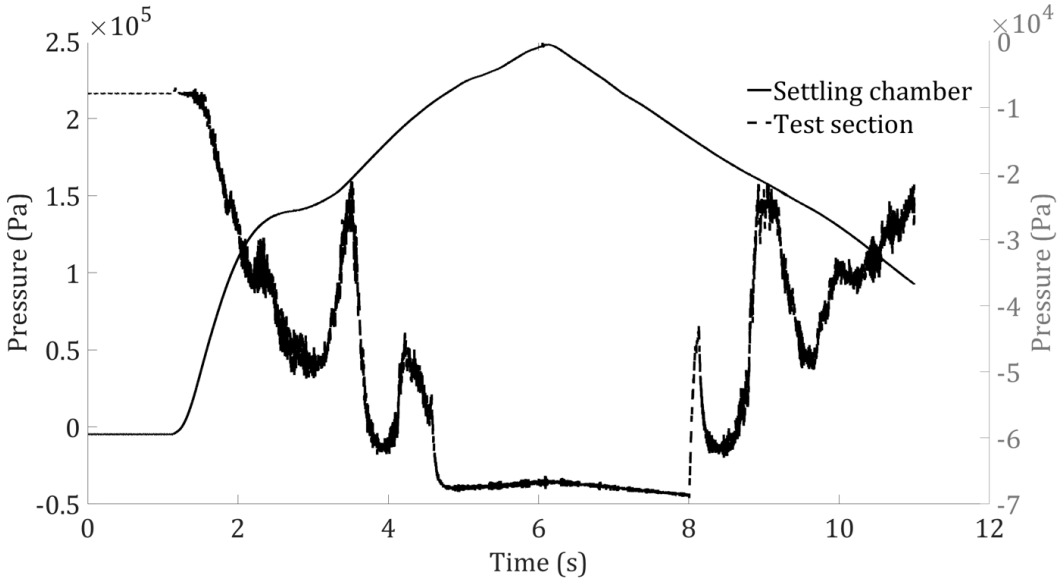

Figure 26: Static pressure traces of the SSWT settling chamber equivalent to test section stagnation pressure (Pa) during a 6 second Mach 3.5 test versus time (s).

Fig. 26 demonstrates the supply pressure trace ('settling chamber', primary y-axis), and the pressure within the test section ('test section', secondary y-axis) for a 6 second (time, x-axis) SSWT test. The pressure traces were collected using the pressure transducers manufactured by Kyowa Electronic Instruments Company (Ltd), which were wired to an electronic 1008C Automotive Oscilloscope/DAQ (8 Channels) system. The DAQ received and plotted the pressure signal amplitude in real-time, which represented the wind tunnel conditions changing during testing. A sample rate of 20 samples/second (20 Hz) was used for the experimentation. This sufficiently captured the data set. The DAQ had a rise time of 3.5 ns.

During testing, the input parameters of available supply pressure, Veeder counter number and test run time were entered into the SSWT computer system. As Fig. 26 demonstrates, during a test the tunnel starts at around 1 s. The settling chamber experienced a steep increase in pressure due to the inlet valve being opened by the control system, resulting in a

surge of air from the supply tank. The settling chamber became pressurised as the subsonic air expanded into it. As the valve was opened further, the speed of the air in the settling chamber accelerated, thus accelerating the airflow into the test section. This resulted in the large drop in settling chamber pressure visible in the trace in Fig. 26, following the initial startup peak.

The flow inside the test section is then supersonic, as represented by the constant region of the test section pressure trace from 1.8 s to 7.2 s. This indicates that the flow is steady, that minimum static pressure has been achieved, and that the desired supersonic Mach number has been successfully reached in the test section. The schlieren flow visualisation is carried out during the ±4 s window of steady flow. This longer test length (6 s) was required to adequately capture the flow visualisation.

By 8 s, the full run-time was reached, and shut down of the SSWT was initiated, as indicated by the instabilities in the test section trace just after 8 s. Once the run time has been reached, the control system automatically closes the inlet valve. As the valve is closed, the once-constant pressure in the test section begins to increase, resulting in fluctuations in the trace as the pressure increases and eventually regulates. The tremor in test section pressure at 9 s indicates that the test is over, as the expansion wave returns to the diffuser and the system. Both pressure traces approach zero as the inlet valve closes completely and the SSWT operation is terminated. The standard post-test procedures were then carried out.

4.3 Sting design

The drag force behaviour produced by the conic bodies is a major focus of this research. This behaviour was monitored in both the numerical and experimental schemes. Validation of the numerical investigation method required both flow visualisations obtained through schlieren imaging and measurement of the drag on cunicular bodies to quantify momentum loss.

In order for the required data to be gathered, a robust sting apparatus was designed which accurately measured the forces acting during the test period using a force balance and electronic data acquisition system. The sting provided consistent, secure and repeatable mounting of

the conic model at zero pitch and yaw so that these effects could be eliminated from the flow field. This allowed for the numerical scheme to be mirrored as closely as possible through a robust, accurate and repeatable experimental model.

4.3.1 Sting components

The experimental testing apparatus was newly designed and manufactured for this research to accommodate the conic models and improve the quality of the data. The apparatus design was restricted to what was feasible for the WITS wind tunnel, and as such component sizing and design agreed with this. Many of the decisions made regarding the presented apparatus design aimed to improve upon problems experienced with the WITS wind tunnel research.

The rig was designed with vibration and pitching prevention in mind, as these were problems frequently experienced in prior WITS tunnel projects. The resulting schlieren photographs from pitched models were of poor quality, and the drag readings would be affected. This was especially important since model symmetry and 0° incidence angle were of primary importance to the outcome and quality of this research data. The design measures taken ensured that no vibration or pitching of the apparatus occurred during testing.

The conic test models were mounted in the wind tunnel test section using a sting assembly (referred to as the 'sting'). The sting comprised several components, many of which were modified from standardised parts.

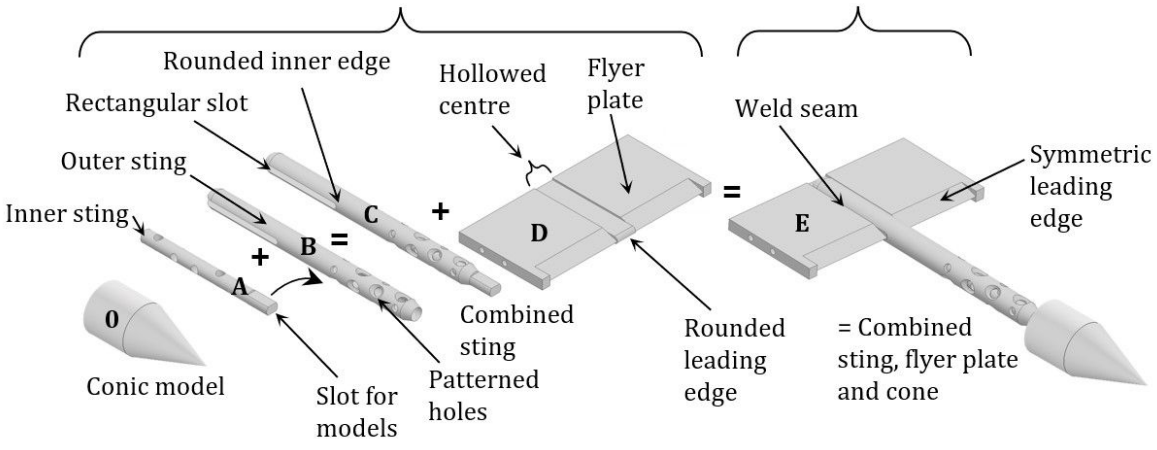

Figure 27: Combined inner and outer sting with the flyer plate

Fig. 27 shows the mounting apparatus holding the conic models. The design of the central sting part ensured models could be securely and repeatedly mounted in the tunnel with a fixed orientation throughout a test. The following list describes the centre sting mount in detail, as well as the fittings into the other parts:

- Part 0 = conic model. A cone attached to a solid cylinder, with a circular-rectangle-shaped slot in the base.
- Part A = inner sting. A solid circular shaft with four through-threaded holes drilled at alternative 90° angles and a small length of circular-rectangle-shaped shaft exposed. Many individual inner stings were manufactured since each conic model was bonded to its own inner sting, and thus the inner stings could not be reused. Part 0 fitted onto Part A at the circular-rectangle slot. The joint was permanently bonded with Pratley Epoxy Resin.
- Part B = outer sting - a circular shaft of three sections. The aft section had a central rectangular slot with a rounded inner edge. The middle third was solid. The front third was a tube with various hole placements. Part A fitted into Part B as a sliding joint. Each set of holes allowed for countersunk screws to secure the inner sting and mount the conic model. The hole pattern was introduced to investigate the effects of model azimuthal angle on the flow field for an unrelated project. As such the detailed hole specifications are neglected here. The inner sting was fastened to the outer sting in alternate pairs, i.e. a hole in set 1 would be fastened with a matching hole in set 3. This allowed for an evenly distributed load on the combined sting.
- Part C = combined sting. Created by sliding Part A into Part B (aligning the holes) and fastening with two flat head screws. Fig. 27 shows the inner sting inside the outer sting (Part C).
- Part D = flyer plate. A solid plate with a hollowed central strip (hollowed region had a rounded leading edge). The remainder of the plate had symmetric wedge leading edge (knife-edge) and square overhangs at the corners. Flyer plate fitted into the central slots of the side plates.

- Part E = combined sting(s), flyer plate and cone. The combined sting's rectangular slot fitted over the matching hollowed strip on the flyer plate with a sliding fit. The rounded inner edge or the outer sting matched the rounded leading edge of the hollowed strip. The combined part was welded together along the seam of the meeting joint (as shown in Fig. 27 e)). This created a very secure, permanent, single part.

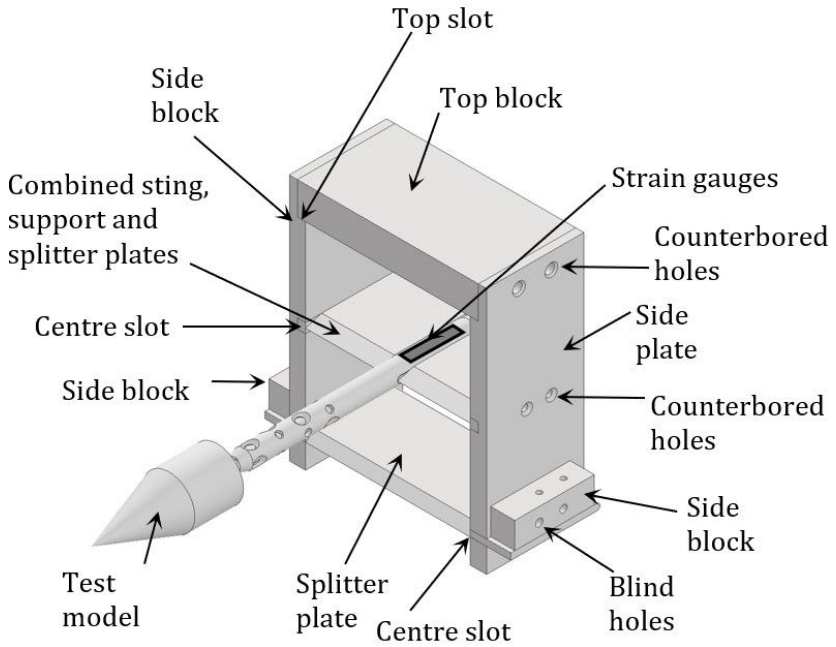

Figure 28: Combined sting, flyer plate and support blocks.

The isometric view of the final sting assembly (without the drag balance) is shown in Fig. 28. Part E was mounted in the test section using a secondary apparatus consisting of two side plates, a top block, a bottom (splitter) plate, and two side blocks. The two shorter side plates were fastened to a rectangular top block with a fixed fit using countersunk screws. The combined part was flush with the test section opening. The top block rested on the ledge cut into the side plates.

The side plates had two partial slots on the inside faces. The slots were located at the centre and bottom of the plate, respectively. Two counterbored holes were drilled above the centre slot, and two blind holes above the bottom slot. Neither slot ran the full width of the side plate, and 5 mm of excess material remained at the back of each plate. This securely fixed the position of both the flyer and splitter plate into the assembly once bolted.

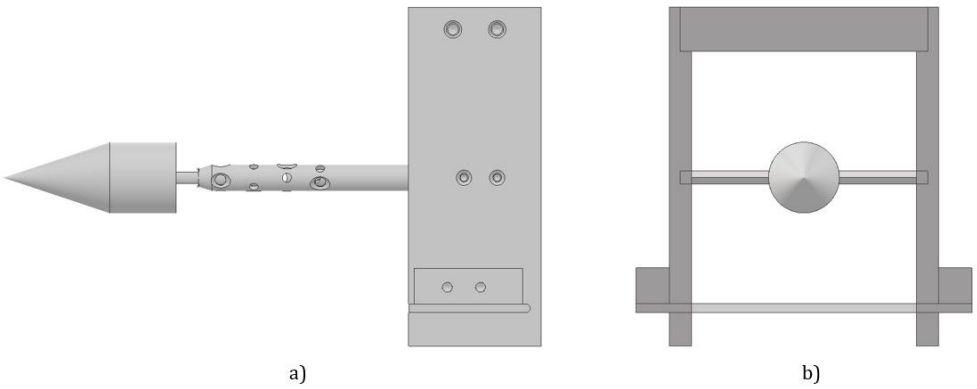

Figure 29: Sting assembly a) side view c) front view

The splitter plate had a slight overhang material to support additional side blocks. The side blocks had two vertical through-holes and two lateral threaded holes. The vertical holes fastened directly onto the top of and through the bottom plate, and thereafter the bolts were threaded through the lateral holes such that they pushed onto the side plates through the fastened side blocks. This ensured that the bottom plate was very securely positioned. The splitter plate lay flush with the bottom of the tunnel, with a sharp inclined leading edge which cut and straightened the flow during testing. The finite slots ensured that the horizontal plates could move neither laterally (in the x-y direction), nor longitudinally (z-direction). This prevented any potential pitching and asymmetry which arose with conventional, unslotted designs. Asymmetry in these plates could cause irregular flow and blocking of the tunnel. The presence of the slots was further strengthened by the fasteners chosen, which were dense and drilled deeply into the thickened flyer plate. The outer surfaces of the apparatus aligned with the wind tunnel test section, producing minimal disturbance to the flow field. The side and front view of the test model assembly, including the mounting apparatus, is shown in Fig. 29.

The conic models were sized according to the WITS SSWT maximum percentage area blockage ratio for the tunnel - generally accepted as 9% of the test section area. If the total frontal area encountered by the incoming flow inside the test section was greater than 9%, the tunnel would choke (confirmed by partial blockage of a 9.25% conic model). The blockage still occurred on the cusp of the 9% rule since the bow shock generated by these models considerably increased the frontal area encountered by the incoming flow. Blockage was only

eliminated by reducing the model frontal area to 7.8% (32 mm cylinder diameter), and as such this diameter (32 mm) was used for all of the conic models. The sizing was necessary to ensure that proper shock waves could be repeatedly generated by the conic models in the tunnel in order to capture the correct data.

The remaining conic design was based on the dimensions required by the tunnel. However, the maximum frontal area rule was also applied to the flyer and splitter plates, and as such these plates were sized accordingly while meeting the strength requirements. The flyer plate was thick, as it was required to hold long, heavy screws and the entire weight of the Part E. The splitter plate was thus very thin to compensate. This was made possible by using the side block design, as no screws were required to go through the thinnest part of the plate, but rather through the main body of the plate. The design was also useful in that once assembled, only the inner sting fasteners needed to be removed to change the conic model. This increased testing efficiency. All of the parts were made of bright steel for maximum strength, except for the conic models, which were printed out of resin.

The apparatus was symmetric about the horizontal centre line. This was so that the flow interaction around the porous cone could be seen as clearly as possible and to avoid viscous effects from occurring during shock boundary layer interactions at the walls. These flow interactions could possibly change the shapes and interaction patterns of the shock waves, leading to an inaccurate flow field representation. Cellophane tape was used to cover the unused holes in the sting to eliminate the effects they may have on the developing flow field near the cone. This was necessary since, in regions of subsonic flow, disturbances from these holes could affect the flow conditions upstream. The design measures undertaken here were due to the sensitivity of the porous cones to asymmetry, and the necessity to reduce this as much as possible.

Once the conic model was mounted in the secondary apparatus, the tunnel doors were securely fastened using clamps to prevent the tunnel door from opening during testing. The engineering drawings of the separate and assembled apparatus parts may be found in Appendix C.

4.4 Force Balance

In order for a data set to be gathered that correctly represented the forces present during the test period, a force balance (or balance, the system designed to measure forces (Newtons)) was installed on the sting. The force balance was wired to a DAQ which gathered live strain readings during tests. The strain data was then converted into drag force. The design of the balance and its installation onto the tunnel apparatus is described in this section. This includes the combination of strain gauges and wiring installed on the sting.

4.4.1 Force balance design

Apparatus was designed which could capture the drag force acting on the models during experimental tests. The apparatus was restricted to what was feasible for the WITS wind tunnel, and as such a modified force balance was designed which fitted the existing tunnel apparatus. The numerical conic model was stationary, existing symmetrically at 0° incidence angle. In order to validate the numerical scheme, the experimental apparatus was required to replicate this. The balance was required to be very robust in design and capable of withstanding the tunnel environment.

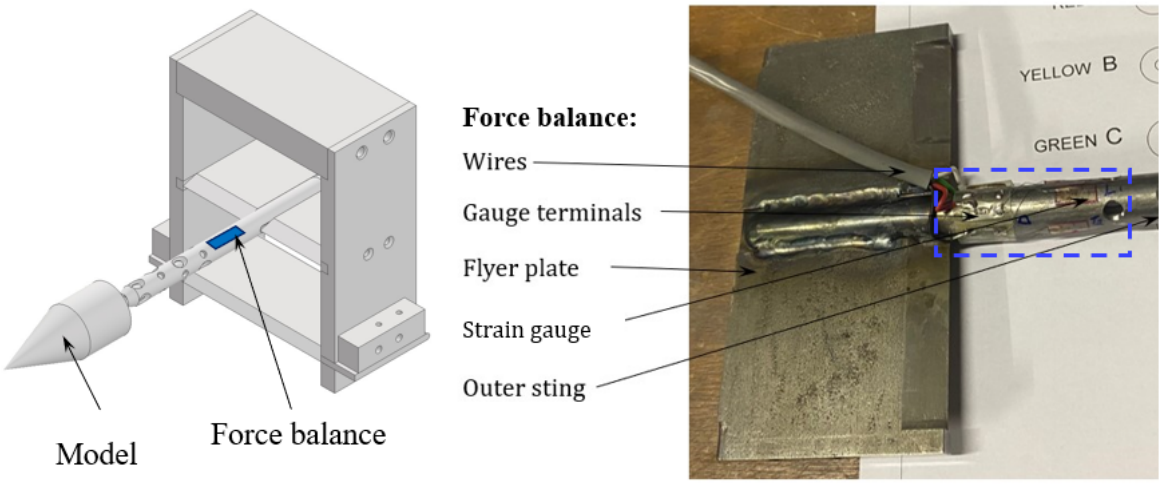

Figure 30: Wind tunnel sting assembly with force balance (left) flyer plate with strain gauges attached (right)

To directly measure the aerodynamic forces acting on the model, a three-component force balance was used to measure the components of lift, drag and pitch. The combined sting acted as a fixed part in the tunnel to prevent any moments or side forces from acting on the model during testing. The balance utilised full strain gauge bridges to measure the loads and moments acting on the beam holding the model in the tunnel. Full strain gauge bridges were used as they have higher sensitivity compared to half bridges and better temperature compensation. A single strain gauge is a transducer used to convert the mechanical deformation into usable electrical output, whereby an array of strain gauges converts the mechanical load into usable units.

Fig. 30 shows the SSWT sting apparatus with the force balance containing the strain gauges. The balance was positioned at the solid region of the outer sting. Half of the outer sting had precise holes drilled into it, while the other half was solid. Bright steel was used to manufacture the outer sting as it has closer dimensional tolerance and better machinability than other commonly used materials such as tool steel. The cold drawing of bright steel also increases the yield and tensile strength of the part. Due to the sting having many low-tolerance holes drilled at various angles, bright steel was an appropriate choice as it provided strength and precise machinability.

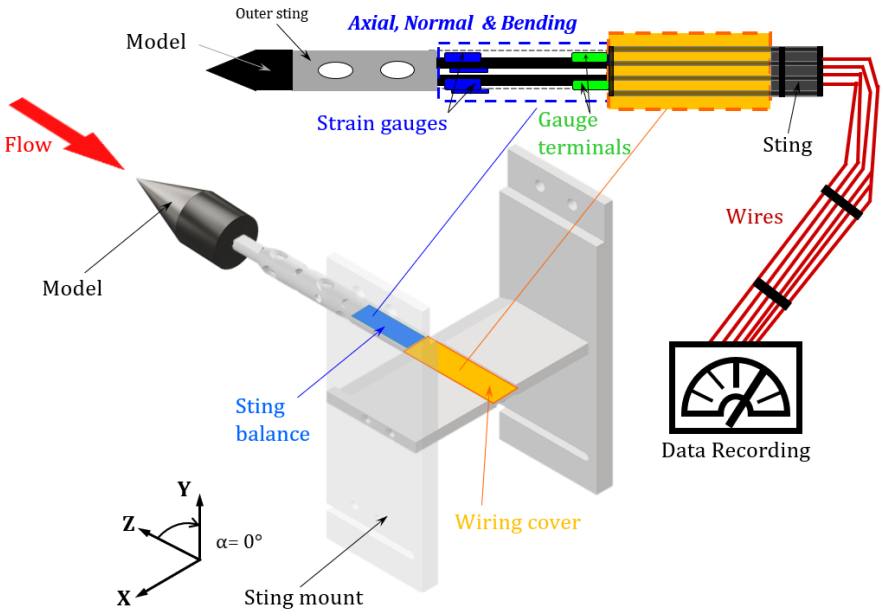

Figure 31: Annotated sting assembly with the strain gauges and wiring

Fig. 31 shows the detailed force balance and apparatus. Gauge terminals were installed on the outer sting base between the connecting cables and the strain gauges to ensure proper solder joints and provide strain relief for the gauge connections.

It was necessary to protect the balance from the high wind speed, forces, temperature and shock waves present in the tunnel during testing. Whilst strongly bonded, if unprotected, the gauges would be destroyed during testing. Precautions were taken to ensure limited damage to the balance, however the gauges were mostly protected by the short duration of the tests. The entire balance region was covered with several layers of masking tape, followed by insulation tape. The balance was then protected, and its function was unaffected.

The effect of shock waves was also considered. The presence of a shock on the sting represented a pressure change, and thus an additional strain on the sting that was not due to the test article. If shock waves passed over the uncovered strain gauges, damage was likely. This would result in incorrect or inaccurate readings from the DAQ. Repairs to the gauges after damage were undesirable. The taped force balance covering created a small step on the sting which would generate a shock. To mitigate this, the taped covering was entirely covered with a layer of silicon sealant. This filled in the leading edge gap smoothly so that no shock could be generated.

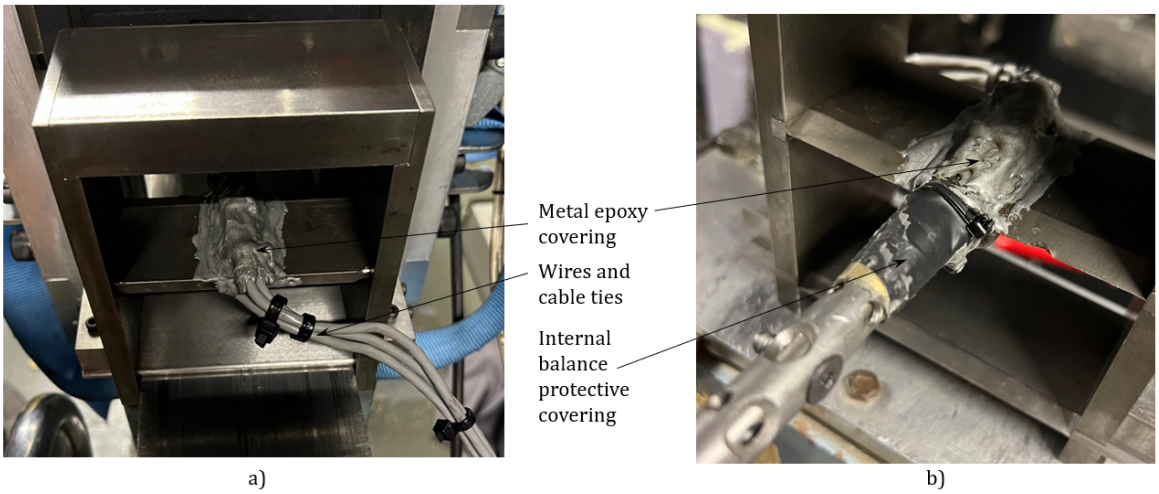

Figure 32: a) back view of the sting c) front view the sting

The exposed wires extending from the force balance were epoxied to the flyer plate using Pratley Epoxy Metal Filler/Bonder to ensure no movement during testing. The result was a

smooth covering of the force balance, soldered terminals and wires that were fixed in position whilst protecting the delicate internal components.

The remaining wires extending from the gauge terminals were zip-tied together and fed out of the wind tunnel test section between the test section doors, where they were connected to the drag DAQ. During a test, the bunch of wires was made taught before the tunnel doors were closed and clamped. This process was necessary as modifications to the WITS tunnel were impossible, and none of the existing holes in the tunnel could accommodate the wires. Wires with a very thick coating were used, and it was observed that no deformation or damage to the wires occurred during testing. By making the wires reasonably taught before door closure, movement from the wire bunch was limited.

The drag monitoring system was successful for a short period before yielding of the materials occurred. The above wiring method likely affected the data, presumably from the wires pulling on the protective covering and harming the gauges during testing. The system mismatched the tunnel and likely contributed to the breakage of the force balance and divergence of the latter data sets discussed in Chapter 6. Improvements to this design may be found in Section 8.9. Fig. 32 shows photographs of the covered internal balance installed on the sting.

Some vibration was present in the drag data due to the presence of cumulative signal noise from around the laboratory and surrounding environment. To filter the error and uncertainty caused by the signal noise, a sting calibration is presented in Section 6.2

The time was measured during the test, allowing these disturbances to be removed from the data set. Mach 3.5 and Mach 3 steady-state conditions were tested. The conic models were each bolted to the sting set-up in the wind tunnel, ensuring safety during testing. The bolting applied here ensured compliance with the wind tunnel safety requirements.

4.4.2 Strain gauge arrangement

The gauges converted strain in the solid outer sting material into a voltage difference across a Wheatstone bridge. A Wheatstone bridge with four strain gauges was used, which had high accuracy and temperature compensation abilities (Pieterse (2002)). This was advantageous

as it accounted for temperature changes on the model during testing, which was important in the SSWT where the temperature fluctuated heavily due to the rapid property changes. The balance could detect both the axial (±) and bending loads along the axis perpendicular to the axial (and normal) axes (Bernstein and Pankhurt (1975)). From this the lift, drag and pitch of the model were measured. Only drag was considered for this study. Side force, roll, yaw, lift and pitch were ignored as they were irrelevant to this study.

The gauges were applied to the sting at the solid base, where the maximum deflection occurred. The voltage at each gauge component was measured and then related to the particular force being measured. The rise time of the gauges was limited by the time it took for stress waves to propagate through the sting. This time was negligible compared to the 2 s steady test period.

Strain gauges are sensitive to several factors. Correct alignment of the gauges (accurate positioning relative to each other and the sting) onto the beam ensured that the correct strain was transferred from the model to the gauge element. It can be difficult to apply strain gauges perfectly to complex apparatus, and misalignments have the potential to disrupt the quality of readings. To prevent this, the strain gauges used in this research were applied with precision and caution. To further prevent discrepancies resulting from misalignment of the gauges, a universal connection was used between the mounting base and force balance.

Strain gauges are sensitive to thermal effects, and large temperature fluctuations may affect the accuracy of readings. The SSWT test section reached a temperature of 100 K during testing, which would affect the gauges. The Wheatstone bridge arrangement reduced the thermal effect significantly (Pieterse (2002)). Vibrational noise in the area surrounding the gauges was also of concern. Noise acts as an unwanted signal which interferes with the strain gauge output. During testing, the force balance picked up moderate amounts of signal noise emanating from various external sources around the laboratory. This signal noise was identified and removed during data processing.

The data collection, uncertainty and calibration of the force balance is detailed in Chapter 6.

4.5 Flow Visualisation and Optical Instrumentation

The experiments were conducted in the SSWT control room at the University of the Witwatersrand. The walls are to further block out light, with a single collimated light source passed through the optical system by the programmable time delay unit connected to the light source, with a camera exposure time of 3300 μ. A remotely controlled Canon 350D digital camera was used for all experimentation.

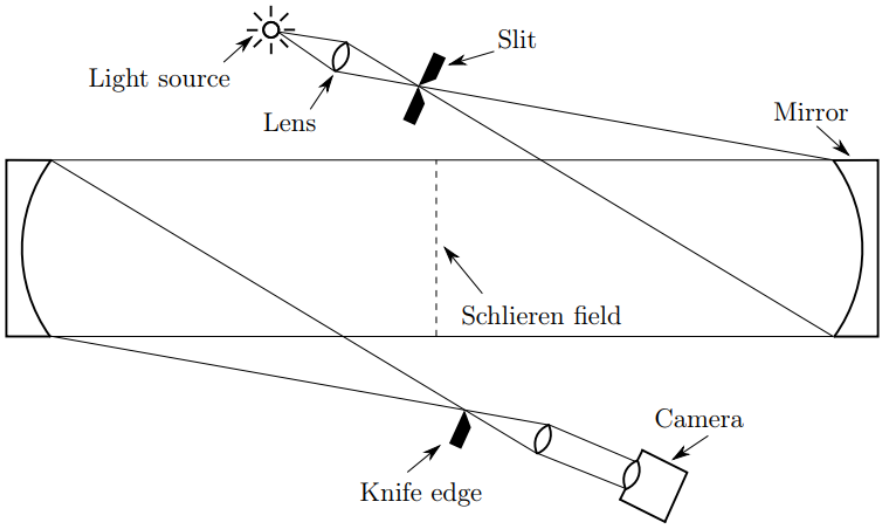

Figure 33: Schematic of schlieren flow visualisation set-up (Filippi (2017))

Flow field phenomena, including shock waves, alter the density of the compressible gas in which they are formed. The change in fluid density causes a change in refractive index, thus affecting the way in which the light passes through the fluid. By utilising the density changes in these density-sensitive flow fields, the phenomena of interest may be visualised. Visualisation occurs by rather the disturbances within it that are manipulating the light and not the flow itself (Kleine (2001)). Two optical flow visualisation methods were considered: shadowgraph and schlieren. The shadowgraph method is used for visualisation variations of density gradients, or the s derivative of density (Merzkich (1987)). In this, only the discontinuous density zones such as shock waves and shear layers are detected (Kleine (2001)). The schlieren method is used to visualise moderate density changes, comparable to the first derivative of density (Kleine (2001)), which includes regions such as expansion fans.

Fig. 33 depicts a typical schlieren optical system, where light passes perpendicularly through the test section, developing the schlieren field. In order to change a shadowgraph optical system to a schlieren system, the knife edge immediately ahead of the camera is removed. Monochromatic schlieren alone was used in this research.

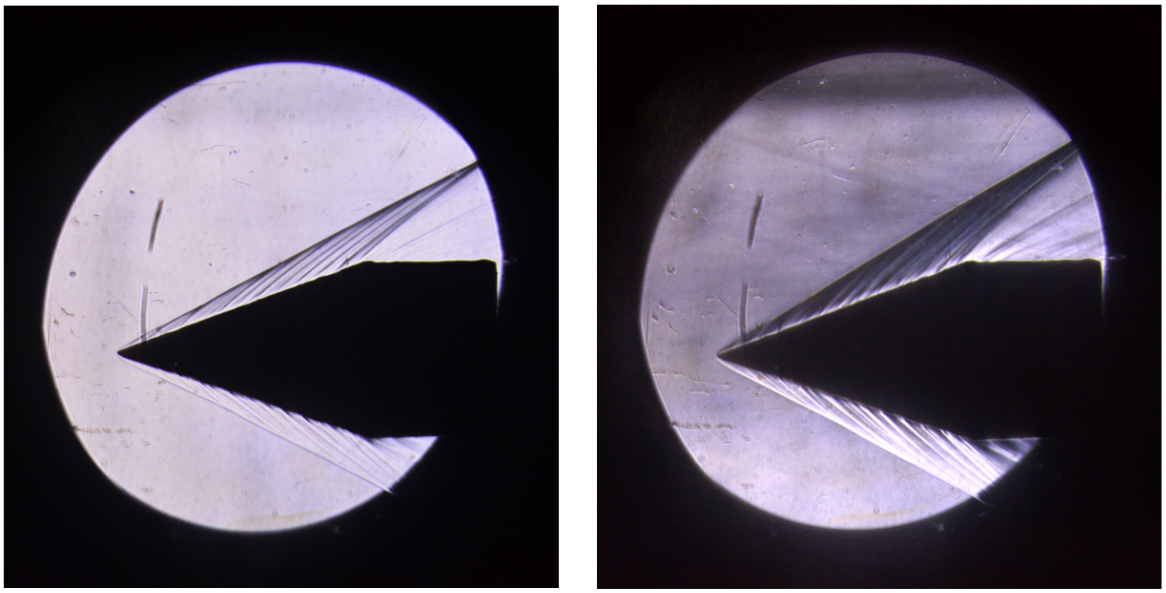

a) b)

Figure 34: SSWT photographs of porous pointed cone BS0 models at Mach 3.5 using a) schlieren b) shadowgraph.

Both the schlieren and shadowgraph techniques provided a projected line-of-sight view. Shadowgrams can clearly depict discontinuities (since they record the second derivative of density) while schlieren images can also show non discontinuous changes due to them capturing the first derivative. The difference in images is visible in Figure Fig. 34. Finely focused schlieren images were mainly used for this research (as depicted in a)) as they provided fine, detailed shock images. The shadowgraph images (depicted in c)) provided much darker photographs with significant shadowing, which made identifying the more delicate flow features difficult.

4.6 Conic model design and development

In this research, the nose cone shape alone was considered. Additional vehicle elements, such as wings/fins (including positioning and sizing), weight and part distribution were ignored

The major dimensions of the models were determined according to the tunnel blockage area ratio and to fit adequately inside the test section window for the schlieren photographs. All of the test models consisted of a conic section (porous or solid) attached to a solid cylinder of fixed dimension. Specific porous cone variations were then applied to the cylinder. The dimensions of the cone cylinder are demonstrated in Fig. 35.

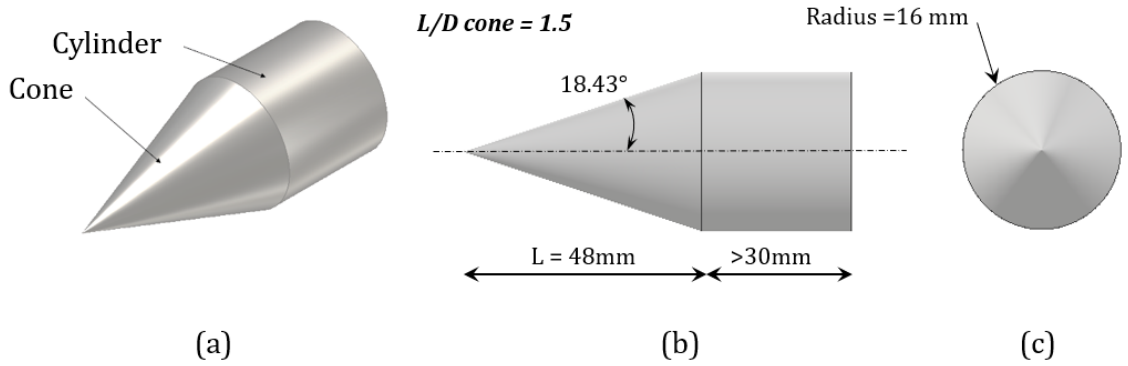

Figure 35: Baseline conic test model with dimensions

The cone L/D and pore diameter were based on the wedge model geometry presented by Skews (1994), whose dimensions successfully allowed for flow visualised in the porous network. These models experienced no blockage or failure during testing, indicating that the studied porosity percentage and structure were capable of withstanding the testing conditions well.

The major dimensions included:

- L/D - 1.5 (excluding hemisphere, $L/D = 1$).
- Base-to-vertex length - 48 mm.
- Base radius - 16 mm.
- Cylinder height - 30 mm or greater, depending on vent size.
- Cone half-angle - 18.43 °.
- Number of inlet holes - 144 (except for 72 Hole BS4, 72 inlet holes).

To ensure that a common L/D ratio of 1.5 was maintained, the base-to-vertex height and radius were constant across all of the shapes tested (excluding the hemisphere, whose height and radius = 16 mm).

The minor dimensions of hole and channel size were required to be large enough that the air could easily flow through, as well as have a visible effect on the flow under schlieren conditions. 2 mm circular channels were chosen, 12.5% of the characteristic radius. 2 mm channels were also successfully visualised in the models made by Skews (1994). Every model was designed according to several geometric commonalities such that only profile shape and pore dispersion type were the changing variables.

In previous research, only vertical or randomised structures within flat plates or cylinders were examined. To define the internal porous structure within a body of revolution, it was necessary to define both the porosity percentage and how the pores were dispersed geometrically within the body. A method of arranging the pores around the vertex-axis within the body of revolution was created, such that the exact effect on the fluid according to geometry could be visualised and explained. The final models were expected to have highly complex internal flow behaviours. In order to simplify the experiment, all of the models were designed to have as many elements of commonality as possible irrespective of shape or size, such that the effects of organised porosity could be examined in as clear a manner as possible.

The internal geometry was created according to the dispersion type. Dispersion type refers to the manner in which the fluid can mix, communicate and distribute within the porous structure, according to the available geometry. Three dispersion types were defined, namely:

1. Longitudinal
    - Consists of channels which run longitudinally (aligned in the z-direction) through the solid cone, and
    - Inlet pore arrangement (the holes in the cone surface which allow inflow)
2. Toroidal

- Consists of hollow ring channels dispersed at planar intervals along the length of the cone and,
- Inlet pore arrangement (the holes in the cone surface which allow inflow)

3. Combined longitudinal-toroidal

- Consists of both prior structures super-imposed and,
- Inlet pore arrangement (the holes in the cone surface which allow inflow)

The fluid entered the internal porous network (regardless of combination type) through the inlet pore arrangement. The inlet pore arrangement was defined as the holes on the cone surface which allowed the fluid to enter into the body. As such the inlet pore arrangement is always included in the porous description. This structure consisted of several pores which extended outwards towards the body surface from the internal structure, irrespective of dispersion type. In this, the air could communicate both externally via the inlet pores, or internally via the channels. 'Arrangement' refers to the number of holes, their separation, diameter and position around the solid shape.

4.6.1 Baseline (zeroth iteration) porous model design

The final baseline models had a combination of toroidal, radial, longitudinal and venting (if relevant) pores. The subsequent organised pore systems always consisted of combinations of the subsequently described basic components:

1. Toroidal: Hollow equidistant rings (known as toroids) stacked within the conic body, with the first ring, always positioned 25 % behind the leading edge. The rings repeat incrementally depending on the shape length, with the backmost ring always located 90 % behind the leading edge. The overall ring diameter increased as the cone base was approached. The internal ring diameter was always 2-3 mm depending on the space available, and ± 1 mm apart edge-to-edge. The larger toroidal diameter was to allow for adequate mixing and account for channel overlap discrepancies occurring during merging. The toroid separation was decided based on both the maximum number of

rings which could fit within the shape, as well as the refinement capabilities of the SLA printer. Additionally, it was recommended that the distance between hole centres, irrespective of direction, be no less than 1 mm apart. If this distance was decreased, a high risk of warping and collapse existed. Fig. 36 a), c) shows the solid cone-cylinder with the stacked toroidal channels (TC) removed from the cone. For clarity, c), and d) show the filled-in view of the toroids.

2. Longitudinal: Multiple 2 mm ⌀ linear channels inclined at 9° to the z-axis (50% of the cone half angle of 18.43°). Longitudinal channels are always spaced equally around the z-axis to ensure both symmetry, no channel overlap, and maximum channel count. Channels always begin at the first toroid and ended at the last toroid, i.e. linking all the toroids together. Fig. 37 a), c) shows the solid cone-cylinder with the longitudinal channels (LC) removed from the cone. For clarity, c), d), and e) show the filled-in view of the longitudinal channels.

3. Radial: From each multiple positions around each toroid, 2 mm straight channels extended through the solid, to always exit the body perpendicular to the cone surface. These holes were known as the inlet pores. Inlet pores were always 1-1.5 mm apart edge-to-edge, with as many holes extruded such that the required common porosity level was always met, whilst also maintaining a safe printing separation distance and zero overlap. Fig. 38 a), c) shows the solid cone-cylinder with both the radial channels (RC) and toroids removed from the cone. For clarity, c), d), and e) show the exaggeratedly-long filled-in view of the radial channels. Note that the filled-in (inverted) view of all of the above dispersion types is for understanding purposes only.

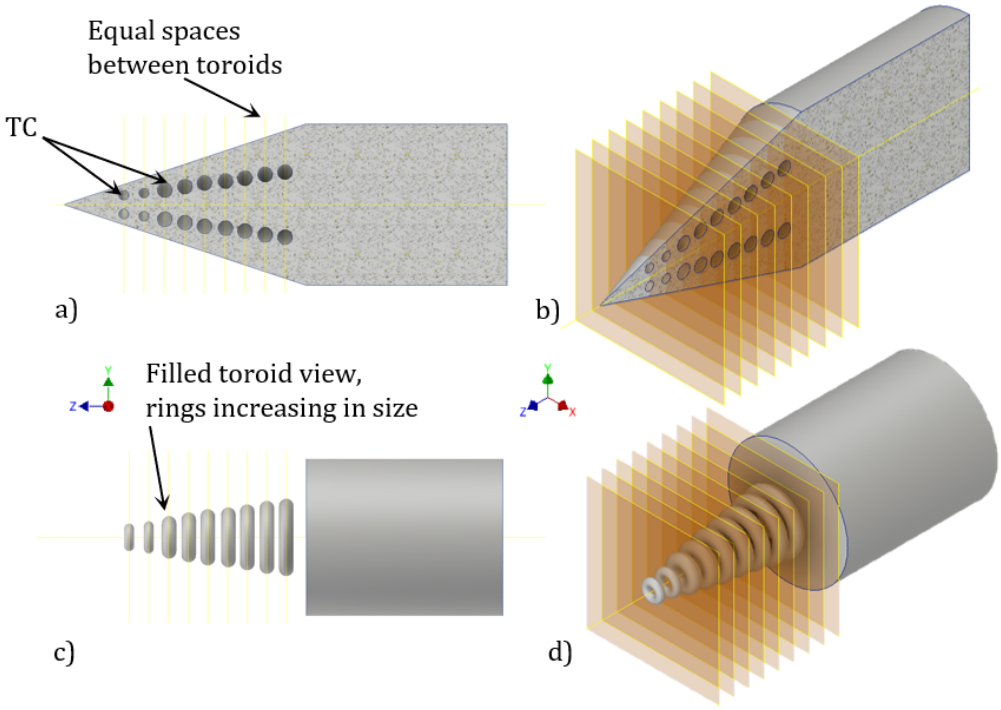

Figure 36: Isolated toroidal structures inside the cone cylinder a), isometric c), side section-view with removed toroids c), full-view with filled toroids d)

The final model was symmetric about both the ZX and ZY plane such that a quarter model could be used for the numerical models for reduced computational time. The location of the first toroid accounted for the delicate porous tip structure of the cone, which was vulnerable to breakage during printing. The method described above was applied across all shapes, such that no matter the unique geometric shape, the internal porous structure retained the same characteristic properties in that every shape result could be compared. Fig. 39 shows the cone cylinder a) isometric view, c) side complete-view, c) front view, d) half-section with exposed radial, toroidal, longitudinal and venting channels.

With each dispersion type, the flow could recirculate and redistribute in different ways. The radial type allowed for the inflow of the fluid into the structure from the outer field. The toroidal channels allowed for the flow to circulate continually within each plane, whilst also creating a space in which the longitudinal and toroidal flow could mix simultaneously as the hollow channels merged. The longitudinal type acted as the main source of outflow initialisation due to its slight positive incline, as well as it being the global pore connecting all of the structures.

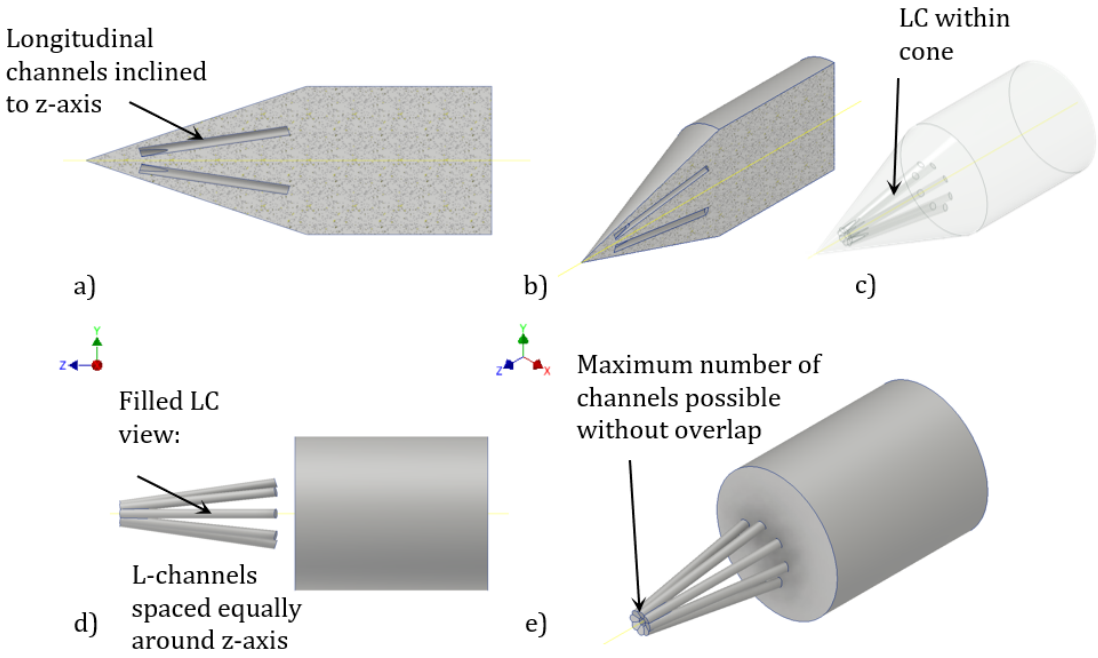

Figure 37: Isolated longitudinal channels inside the cone cylinder a), isometric c), side section-view with removed longitudinal channels c), full-view with filled channels d)

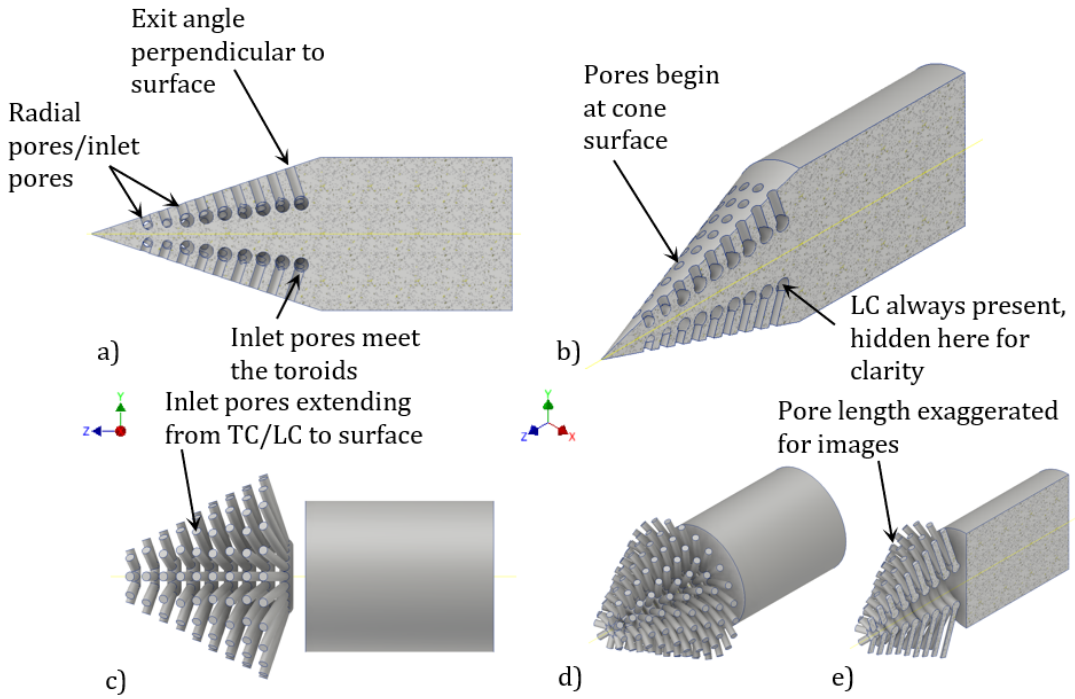

Figure 38: Isolated radial and toroidal channels inside the cone cylinder a), isometric c), side section-view with removed radial and toroidal channels c), full-view with filled channels d)

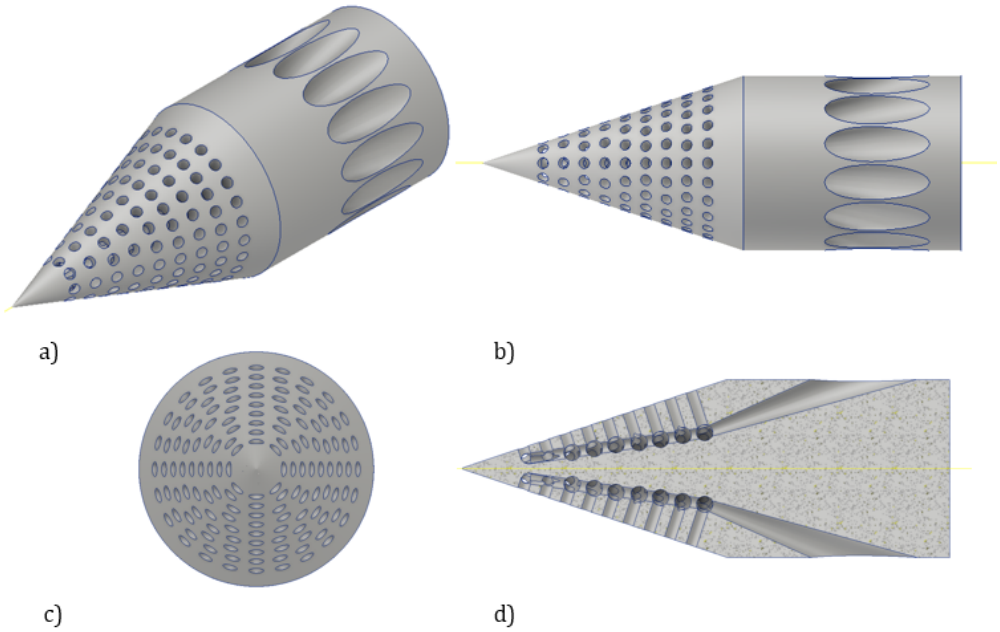

Figure 39: Combined vented porous cone-cylinder with BS4 venting configuration a) isometric view, c) complete side view, c) front view, d) half-section view showing internal structure.

It is pertinent to again refer to the term *cunicular*: A system of organized, interlinked channels within a solid structure through which fluid may enter and/or exit. Distinct from 'porous', which refers to random or organised minute holes dispersed through a solid.

Whilst the phrase 'porous' is loosely used here to describe the hole structure, porosity generally refers to random or organised minute hole formations dispersed through a solid. The presence of organised, hollow channels in a solid is not fully described by 'porosity', and as such it is necessary to define the type of structure specifically used in the presented conic models. The term *cunicularity* has thus been defined to describe the presented models, from the Latin '*cuniculus*'[i]. Whilst the cone may still be classified (and referred to broadly) as a porous body, when referring to its specific design and arrangement of channels, the term 'cunicular' (and the like) will be used.

The first set of cunicular models were known as the 'unvented' models since the airflow that entered the structure had no designed exit structure. The unvented models were used to understand the effect of the pore structures on the flow field so that their effect on drag

[i]The presence of low underground passages or tunnels

may be discounted later when considering the effect of mass removal on bow shock shape. While the design of the unvented models is rigorously described for clarity, the performance of these models is only ever analysed when **combined** with the venting network. The CFD and experimental results of the unvented combined cone may be found in Appendix G.2.

These models investigated whether additional outflow jetting was required for drag reduction, as opposed to pure suction inflow from the cone structure. As such, a second set of models were designed to investigate controlled outflow, known as 'venting'. The various vent geometries explored will be discussed in due course. The vents existed in a pattern around the body such that the maximum number existed, whilst ensuring that no intersection between vents occurred. An example of the venting structure may be seen in Fig. 39, where a), c) show the exit holes patterned around the cylindrical base, and d) shows the half-section view and the internal vent structure.

Only the combined and longitudinal dispersion types could support the venting channels as the vent required the presence of the longitudinal pore to effectively transfer mass out of the body. The vented models investigated the effects of boundary layer, suction, and mass transferability. Thus, five final pore dispersion types were theorised, allowing various dispersions to be described comprehensively, as summarised below. These were the baseline models for the research upon which all subsequent models and design decisions were made.

The unvented and vented baseline (zero iteration) models tested are summarised below:

- **Unvented Models** - cone, hemisphere, ellipsoid, secant ogive
  - Combined - known as Unvented Combined (UC)
  - Longitudinal - known as Unvented Longitudinal (UL)
  - Toroidal - known as Unvented Toroidal (UT)
- **Vented Models** - cone, hemisphere, ellipsoid, secant ogive
  - Combined - known as Combined Vented (CV), or BS0.
  - Longitudinal - known as Longitudinal Vented (LV)

All of the baseline models were manufactured and tested in both experimental and numerical methods. The internal structures of the unvented pointed cones may be seen in the half-section view in Fig. 40, a) toroidal and radial (UT), c) longitudinal (UL), c) combined (UC) (toroidal, longitudinal and radial channels). The unvented models aimed to investigate the effects of cunicularity on the cone in isolation regarding the drag, as well as the behaviour of the flow in a semi-closed-cell arrangement (no outlet possible).

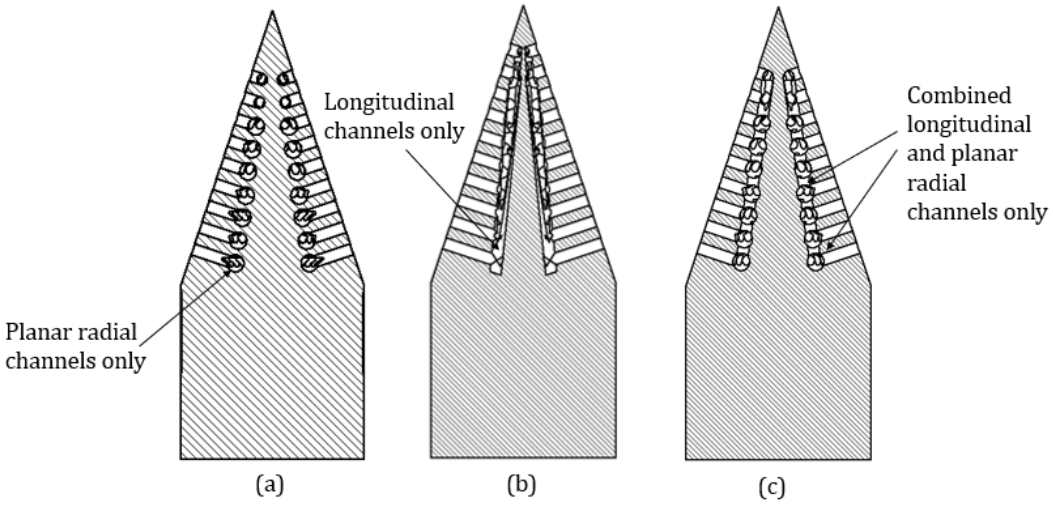

Figure 40: Section view of the **unvented** pointed cone showing a) longitudinal dispersion c) combined dispersion c) planar-radial dispersion

The baseline vented pointed cones are shown in the half-section view in Fig. 41, a) the longitudinal vented (LV), c) combined vented (CV, or BS0) shows the half-sections of the unvented models. The venting channel extending from the longitudinal pore is shown. After the zero iteration of porous cones was tested, the CV cone was referred to as the 'BS0'[ii] cone, since the 90° elbow vent was the 'zeroth' vent configuration tested and also represented the worst momentum-addition venting case, and thus represented the reference condition. BS0 is referred to extensively hereafter as the first vented model to be investigated and is also the porous validation case referred to in Chapter 6.

[ii]BS0 refers to the naming convention of the vented porous condition, where 'BS' stands for 'Beric Skews' (a founding author of the porous supersonic literature), and '0' refers to the particular venting condition, here the '0^{th}' vent geometry.

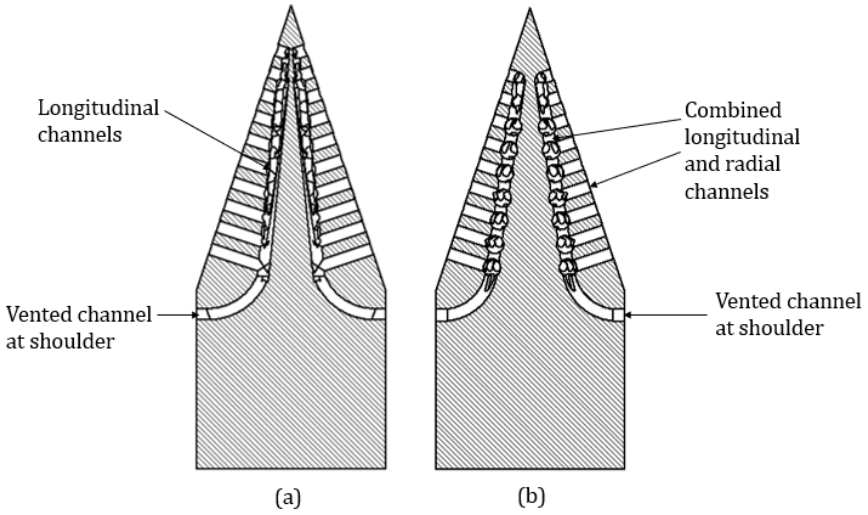

Figure 41: Section view of the cone showing a) vented longitudinal dispersion c) vented combined dispersion (BS0)

Fig. 42 shows the hemispherical half-section views for a) UT, c) UL, c) UC, and d) LV dispersion types. The models were designed to retain consistency in the pore arrangement across shape families, accepting slight differences. The 90° vents were also applied to the other shapes, however no meaningful drag reduction was noted.

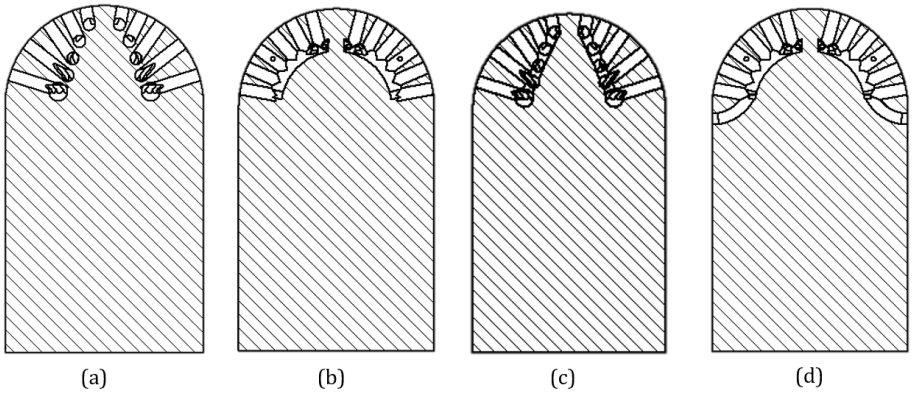

Figure 42: Section view of the hemispherical a) toroidal-radial dispersion c) longitudinal-radial dispersion c) combined dispersion d) vented longitudinal-radial dispersion in the hemispherical case

The maximum porosity percentage within the cones was determined based on the results of FEA on the BS4 pointed cone (Section 4.7.2). This confirmed that the porous structure was capable of withstanding the forces in the SSWT.

The FEA cone-cylinder material properties were set to SLA resin to match the material of the manufactured cones. It was found that cones designed with a porosity greater than

65% deformed in the simulated pressure conditions of the wind tunnel. The yielding of the material at higher porosities was due to the structural integrity of the part being reduced, combined with the low compressive strength of the SLA resin.

Poplavskaya et al. (2017) showed that porosity level was directly proportional to drag reduction. Thus, the highest porosity possible was chosen whilst accounting for the material strength limitations of the SLA resin. Very high porosity inside the cones was impossible to achieve in the confined volume without channel overlap. The models were additionally required to be two-plane symmetric such that a quarter model could be utilised in the numerical analysis.

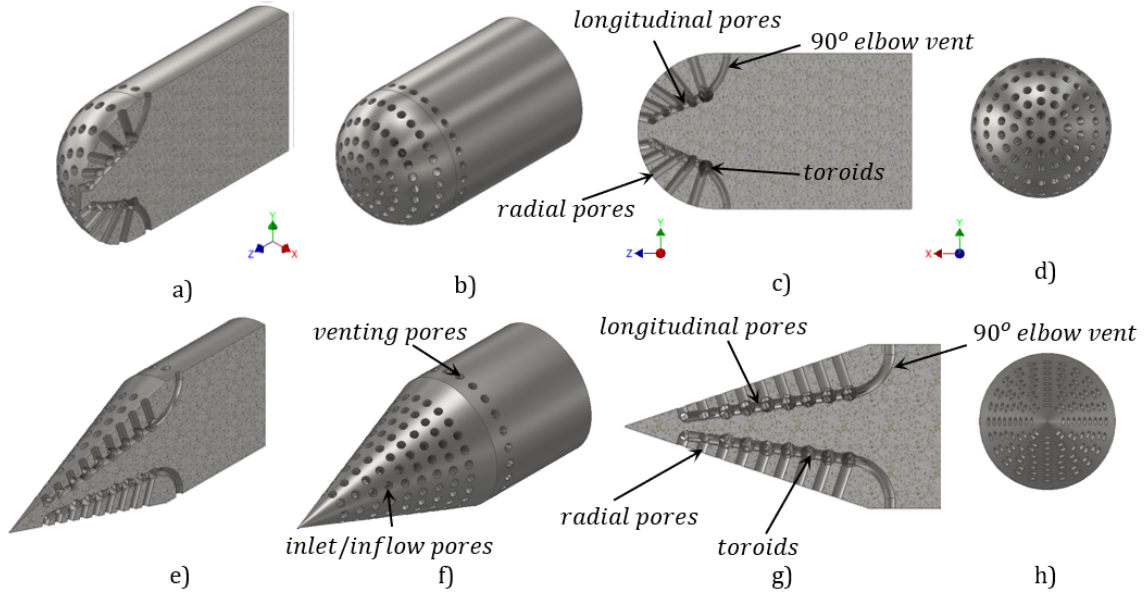

Figure 43: Various views of the BS0 90° (a-d), hemisphere (e-h) pointed cone

A porosity of ≈ 60%±2% was implemented across all of the models, where the error margin accounted for small geometric differences across models (including cone type, hole and channel size, and pore dispersion method). The porosity percentage of the cones included the combined volume of the porous conical forebody and the vents, for each venting configuration. For example, BS0 had 24 small vents over a very short cylinder length, however, BS4 had 14 larger vents over a much longer base - however, both have a total porosity of ≈ 60% (or 40% solidity). This was the greatest amount of porosity (volume fraction) that could be achieved in the volume without channel overlap.

An example of the overlap limitation was the hemispherical model, which had a smaller frontal section than the regular cone. As such, its internal structure, whilst still being 60% porous and longitudinal in dispersion type, was more compressed and with fewer holes than the longer models, as shown in Fig. 43 (b, c) versus (f, g) where the hemisphere has noticeably less available space around the surface, and thus larger gaps between surface hole layers. Even so, all geometric requirements and constraints were met.

Solid (non-porous) models were also made to be compared with the porous models. All of the models were comparable within their specific family shape in terms of dimension (base radius and length (except hemisphere)), porous volume fraction and porous inlet and internal arrangement. This allowed for the effect of differences in nose shape (pointed, bluntness, curvature) to be compared in conjunction with the porosity. Due to the geometric differences, the precise locations of the pores, lengths of channels and distances between holes at the surface vary slightly across the shape families and models. Again, this was due to the size constraints and it being impossible to replicate the exact same internal structure across all models.

The five pore dispersion types were applied to the aforementioned four shapes: the cone, ellipsoid, secant ogive and hemisphere. Various views of the zero iteration combined vented hemisphere and cone are depicted in Fig. 43 to compare the hole arrangement depending on the body shape.

In addition to the porous network held within the cone, the vent design was critical. The baseline venting (BS0) structure was known as the *elbow vent*. Coinciding with the last toroid, a smooth 90° elbow duct was extruded through the base to exit the cylinder perpendicular to the free stream (behind the shoulder). Several of these vents were equally spaced around the cone axis. Fig. 43 c), (g) show the multiple elbow exit vents patterned around the cylindrical base.

By beginning the vent at the last toroid position, the internal porous structure was smoothly joined to the venting network such that fluid momentum was easily transferred to the vents. The number of vents created was chosen such that no overlap would occur at either the vents' starting toroid position or at the vent exit (since the later vents had expanding geometries).

The vent inlet was set as 2 mm ⌀ to maintain uniformity across the models. The elbow vent was introduced into all of the combined dispersion shapes and served as the control case, whose results were applied to the later vented configurations.

From the baseline porous cone discussed later, it was found that the combined-vented right cone configuration (BS0) yielded the highest drag reduction (3% reduced). The other configurations, regardless of shape, all yielded either a far smaller reduction or worsened the drag. As such, it was decided to focus on the BS0 configuration and expand on it. The modifications to BS0 were explored in three separate iterations, briefly outlined below. As with the elbow type, all subsequent vent designs merged with the last toroid.

4.6.2 First iteration porous models

After reviewing the results of the zero iteration group, specifically BS0, the first iteration of vents was designed, comprising of BS1, BS2, BS3 and BS4. BS1 - BS4 consisted of the same combined conical forebody as BS0 (with some internal geometry changes), with different venting geometries (1-4). Each vented cone variant is described below, as well as the effect being investigated for the particular geometry. BS2 and BS3 also investigated the effects of inlet pore inclination and toroid area. The number of inlet pores was fixed, as well as the inlet pore dimensions for continuity.

- BS1: 2 mm ⌀ constant-area duct. Linearly extending at 35° to the z-axis from the last toroid out of the cylinder (vent angle = 35°). 24 vents.
  - Larger venting exit angle.
- BS2: 3 mm ⌀ constant-area duct. Inlet pores angled 45° to inlet flow. 24 vents. Vent angle = 18°.
  - Larger venting exit angle and increased vent ⌀.
  - Inclined inlet pores.

- BS3: 3 mm inlet ⌀ variable-area duct. Diverging vent geometry, with expansion ratio (A/A^*) corresponding to Mach 2.8 exit flow. Inlet pores angled 45° to inlet flow. 14 vents. Vent angle = 18° to horizontal.
  - Diverging exit vent.
  - Inclined inlet pores.
- BS4: 2 mm inlet ⌀ variable-area duct. Diverging vent geometry, with expansion ratio (A/A^*) corresponding to Mach 3.43 exit flow. Inlet pores angled 90° to inlet flow. 14 vents. Vent angle = 18° to the horizontal.
  - Larger diverging exit vent.
  - Perpendicular-to-flow inlet pores.

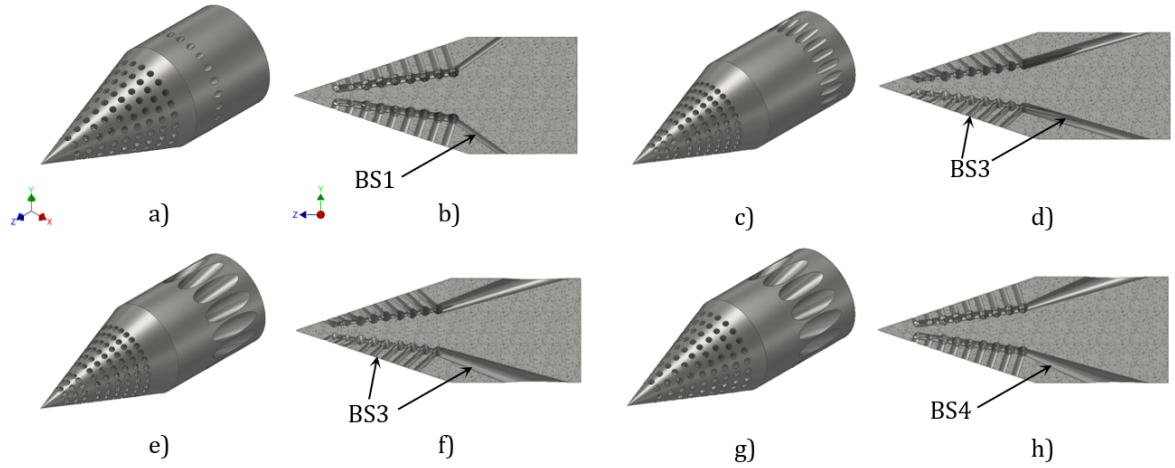

Figure 44: First iteration porous pointed cones (a,c) BS1 (c,d) BS2 (e,f) BS3 (g,h) BS4

BS1 - 4 is demonstrated in Fig. 44. From the first iteration results, BS4 had the greatest drag reduction of 39%. It was decided to focus and expand upon this internal structure.

4.6.3 Second iteration models

For the second iteration of porous pointed cone models, the BS4 internal conic structure was retained, while isolating the vent geometry. Again, the number of vents was the maximum that could exist around the cylinder with no overlap at either the inlet or the outlet, particularly for the vents with large ratios. The overexpanded vent was the limiting case, with the

largest possible exit diameter without overlap. The number of vents was kept constant (even for the smaller (A/A^*) vents) so that the effect of the expansion ratio could be examined independent of vent count and overlap effects. The network had fourteen vents, always inclined 18° to the z-axis, irrespective of expansion ratio. The following vent geometries were investigated:

- Underexpanded (UE): (A/A^*) corresponding to Mach 3.15.
- Overexpanded (OE): (A/A^*) corresponding to Mach 4.33.
- Linearly Expanded (LE): (A/A^*) corresponding to solid cone freestream condition Mach 3.5.
- Horizontal Vent (HV): $(A/A^*) = 1$ exiting the cylinder purely horizontally (aligned with the z-axis).

An additional modified BS4 model was created to include the investigation of fewer inlet holes on the flow field (72 inlet holes instead of 144), known as '72 Hole BS4' as it retained the same structure as BS4, only halved the amount of inflow.

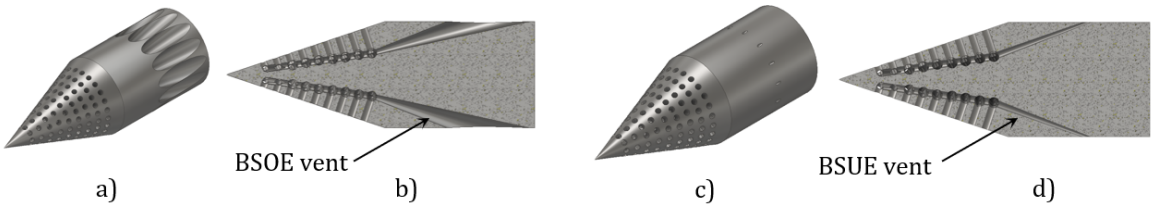

Figure 45: Second iteration BS cones venting configurations: (a,c) overexpanded (OE), (c,d) underexpanded (UE)

Fig. 45 demonstrates the overexpanded BS cone venting configuration, and (c,d) the underexpanded configuration. The vents were always created in Autodesk Inventor Professional 2022 Student, in the same manner, to maintain consistency across models. The following aspects were kept constant across the venting configurations:

- The exit plane of the vent was always located 32 mm downstream of the cone shoulder, with the exit circle centred at 21 mm above the cone centre line.

- The vent inlet location and area (2 mm ⌀) was fixed.
- The exit area was then changed according to the particular geometry requirement, except the HV, where the duct alignment was purely horizontal.

After numerical analysis of the first iteration models, the best configuration overall was still the BS4 vented pointed cone type. The BS4 internal porous geometry (porous forebody and venting structures) was then applied to the hemisphere (BS4 H), secant ogive (BS4 SO) and ellipsoid (BS4 E) in addition to the pointed cone, to investigate its effect on other shapes. Fig. 46 and Fig. 47 show the various views of the BS4 porous configuration in other shapes.

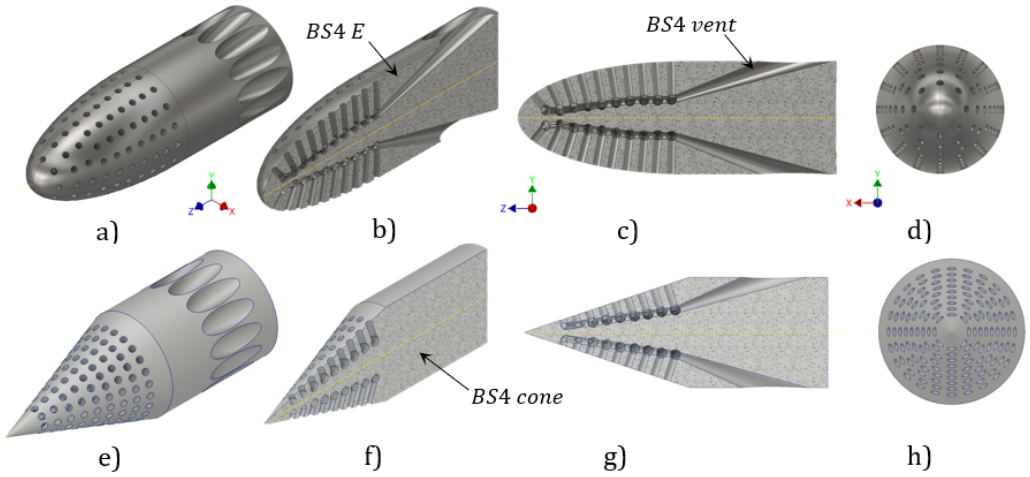

Figure 46: Various views of BS4 the ellipsoid (BS4 E) (a -d) and cone (BS4) (e-h)

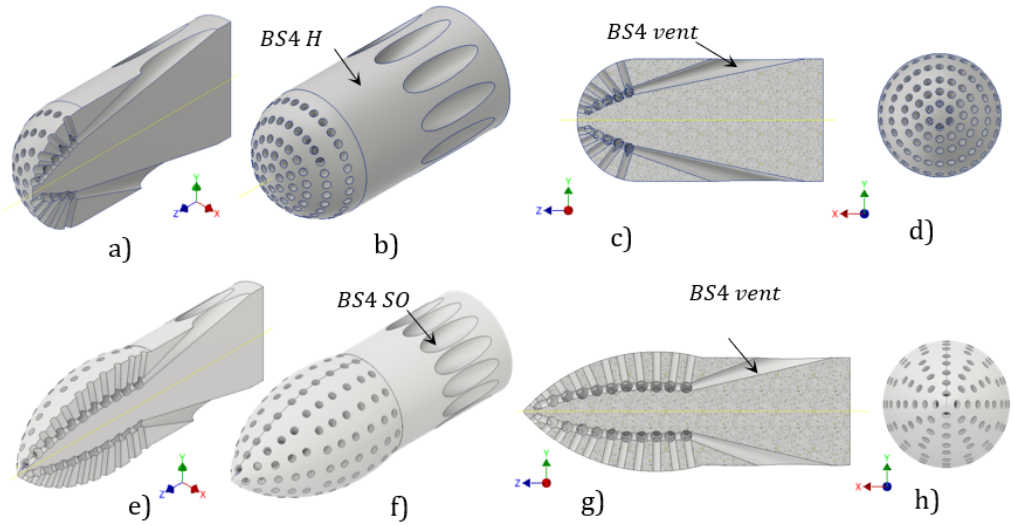

Figure 47: Various views of BS4 inside(a-d), the hemisphere (BS4 H) (e-h) the secant ogive (BS4 SO)

The area of interest in the models was the flow within the porous structure. During experimental testing, the internal structure was hidden on account of the apparatus and model design. Thus, the photographic data gathered from experimental testing was of very limited use for this work when compared to the visual CFD data (where the internal structure could be seen). As such, only the baseline unvented and elbow-vented models (all shapes) were experimentally tested. The tunnel data from these initial models provided the necessary validation of the numerical method such that the purely computational exploration of the new vented models could be completed with confidence.

Whilst the wind tunnel data was a necessary validation tool, the most meaningful results could only be gathered using computational methods both visually and for the drag data. Schematics of all of the conic models may be found in Appendix H.

4.7 Experimental model manufacturing

Traditional manufacturing methods such as casting and tooling were not possible in this research due to the geometric complexity of the models. Resin three-dimensional (3D) printing was used to manufacture the models as this method produced symmetric, true-to-size conic models with clear pores and channels suitable for the SSWT.

4.7.1 3D printing processes for conic sections

The conic models were printed using the Creality LD-002R 3D Resin Printer housed in the 3D printing laboratory at the University of the Witwatersrand Engineering Laboratory, supplied by Shenzhen Creality 3D Technology Co., LTD. The resin 3D printer used DLP technology.

The 3D models from Autodesk Inventor were imported in STEP format to Chitubox, the slicing software. The software prepared the 3D image for the printer by slicing it into many micron-thin layers. The 3D resin printer then used the sliced data to create the final part by building and curing layers of the body successively. Monocure 3D Rapid Resin in the

colour ‘Gunmetal Grey’ was used for this research. This resin was used as the optical flow visualisation techniques required a dark, non-reflective and opaque material finish.

The conic models were manufactured using DLP 3D resin printing, as this was the only feasible method which was capable of capturing the geometric complexity of the cones. The high degree of feature accuracy (specifically hole size and channel geometry), smoothness and manufacturing efficiency were of primary importance. This, in addition to the presence of the many hidden, curved channels within the solid bodies meant that most traditional manufacturing methods (such as CNC, casting or forming) were unable to produce the models, be it partially or completely.

Resin 3D printers consistently produce higher resolution, more accurate parts than FDM printers (Kafle et al. (2021)) in short periods of time (approximately 4 hours per model). Less force is applied to the part during printing, resulting in a smoother, more precise and detailed finish without significant surface machining, as was required for the conic models. Most importantly, the internal cunicular structure required clear passages, meaning that internal supports were impossible. In this case, this could only be achieved with a resin printer (Kafle et al. (2021)).

The resolution of the 3D printer used was 2560 $\times$ 1600 pixels, with an XY-axis positioning accuracy of 0.075 mm. This indicated that the printer was capable of handling the smallest meaningful feature in the cones (a hole separation of 0.5 mm). Approximately 50 ml of resin was used to manufacture one cone.

4.7.2 Conic model strength testing

It was necessary to perform a FEA on one of the conic models to determine if the resin 3D printing method produced a porous conic model which was capable of withstanding the compression forces present in the wind tunnel during testing. ANSYS Static Structural R22.2 was used for the simulation. The material was photopolymer resin material, and as per the resin manufacturer (Monocure), the compressive modulus was 249 MPa.

The FEA set-up simulated the conditions of a porous resin model mounted in the wind tunnel (at zero-incidence) during a Mach 3.5 supersonic test. A fixed-support boundary condition was applied to the cone base to model the mounting. A uniform, normal pressure of 9000 Pa was applied to the surface of the cone. This was the test section pressure, simulating the compressive force acting on the cone during a Mach 3.5 supersonic wind tunnel test. Fig. 48 depicts the FEA results of the cone.

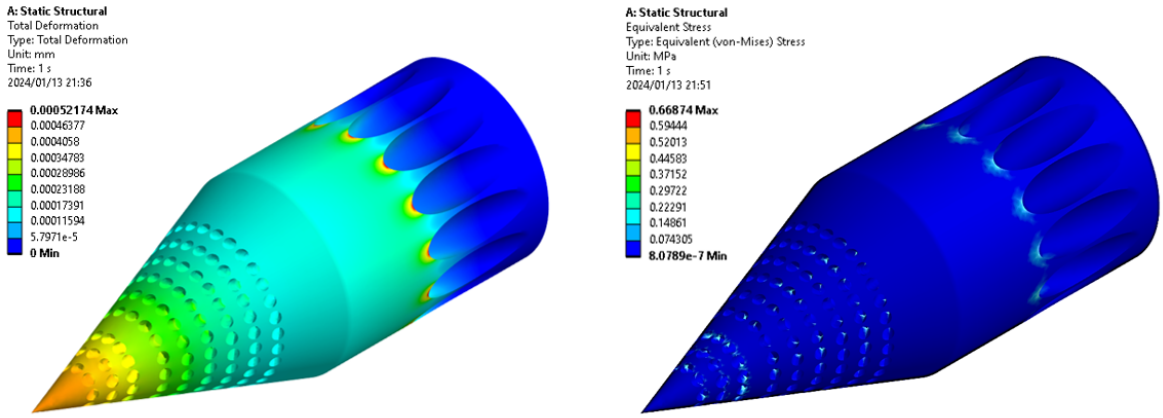

Figure 48: Finite element analysis results of the BS4 cone under SSWT test conditions (left) total deformation (right) c) equivalent (von Mises) stress (MPa)

The maximum deformation experienced by the cone during a standard wind tunnel test was 0.00052 mm, as depicted in Fig. 48 (left). The cone experienced negligibly small deformation, confirming that the material was very resistant to deformation from compression loading. Fig. 48 (right) demonstrates the equivalent von Mises stress experienced by the cone during compression. The maximum equivalent stress experienced was 0.668 MPa, which is less than 0.27% of the compressive yield strength. This indicates that the resin model was more than capable of withstanding the compression.

If the pressure was increased to 40 000 Pa (the downstream shock wave pressure of the equivalent solid cone in Mach 3.5 flow), the equivalent stress increased to 3.86 MPa, or 1.55% of the compressive yield strength. The deformation remained unaffected. The very low stress and deformation of both sets of FEA results indicated that the material choice provided sufficient compressive strength to the printed models when under the required loading. The analysis verified the method of manufacture, proving that the printed porous models were capable of withstanding the forces of the wind tunnel and that no damage would be incurred.

The measures taken to ensure the safety of the experimental testing are described in Appendix B.

4.7.3 Conic model manufacturing

The 3D printed models were required to replicate the true-to-design conic models designed in Autodesk as closely as possible so that they could be directly compared to the numerical results. Whilst some light machining was acceptable (e.g. smoothing rough edges etc.), the model was required to be very high quality before joining and mounting. Several print iterations were required to achieve this, the details of which (as well as the detailed manufacturing method and symmetry criteria) can be found in Appendix F.

The manufactured cones were mounted on an inner sting using Pratley Epoxy Resin, and a lathe was used to ensure that the inner sting, cone and global horizontal wind tunnel axis were coaxial to eliminate pitching. Any pitching visible in the schlieren images was due to slight manufacturing asymmetry. 20 wind tunnel models were made in total across the different shape families.

It was impossible to achieve a perfectly uniform part using the necessary joining method (printed halves joined together). Even so, the overall joined part was smooth, symmetric and largely true-to-design, with some small discrepancies (printer marks, visible edges from the adhesive). All of the symmetry requirements were met, and the experimental models replicated the CAD models to a sufficiently close degree, making them suitable for validation.

Chapter 5

Numerical Modelling

5.1 Introduction

To validate the numerical model techniques and solutions, a thorough comparison was conducted between the numerical findings and the experimental images and data. This validation instils confidence that the numerical model results accurately represent the physical experimental flow conditions such that further investigations, both experimentally and numerically, may be carried out with confidence such that the results are reliable and repeatable.

The following sections describe the computational flow field conditions, including the definition of the domain, its discretisation, and finally, its solution. Computational fluid dynamics software ANSYS Fluent R22.2 was used to model the flow field.

5.2 Domain Geometry

Validation strongly depends on a computational model geometry which is representative of the experimental flow domain. The numerical domain must replicate the experimental conditions as closely as is computationally feasible, and the domain design contributes to this.

The fluid behaviour within the porous structure could only be adequately represented using three-dimensional modelling. The conic test models were two-plane symmetric with a highly detailed frontal conic section, mounted centrally in the streamwise direction of the wind tunnel. Due to the symmetry, a quarter-section of the conic model was used. A quarter-cylinder domain was chosen to surround the quarter-cone, with two symmetry planes present on either flat, rectangular face of the cylinder domain. This left the inner cone geometry exposed on the symmetry planes such that as much of the internal and external flow fields were visible. The quarter model was chosen to reduce the required computational time. This domain mirrored the experimental model closely and allowed for a direct comparison of the flow field using schlieren reconstruction. The sting was not modelled, as is customary for numerical supersonic flow analyses.

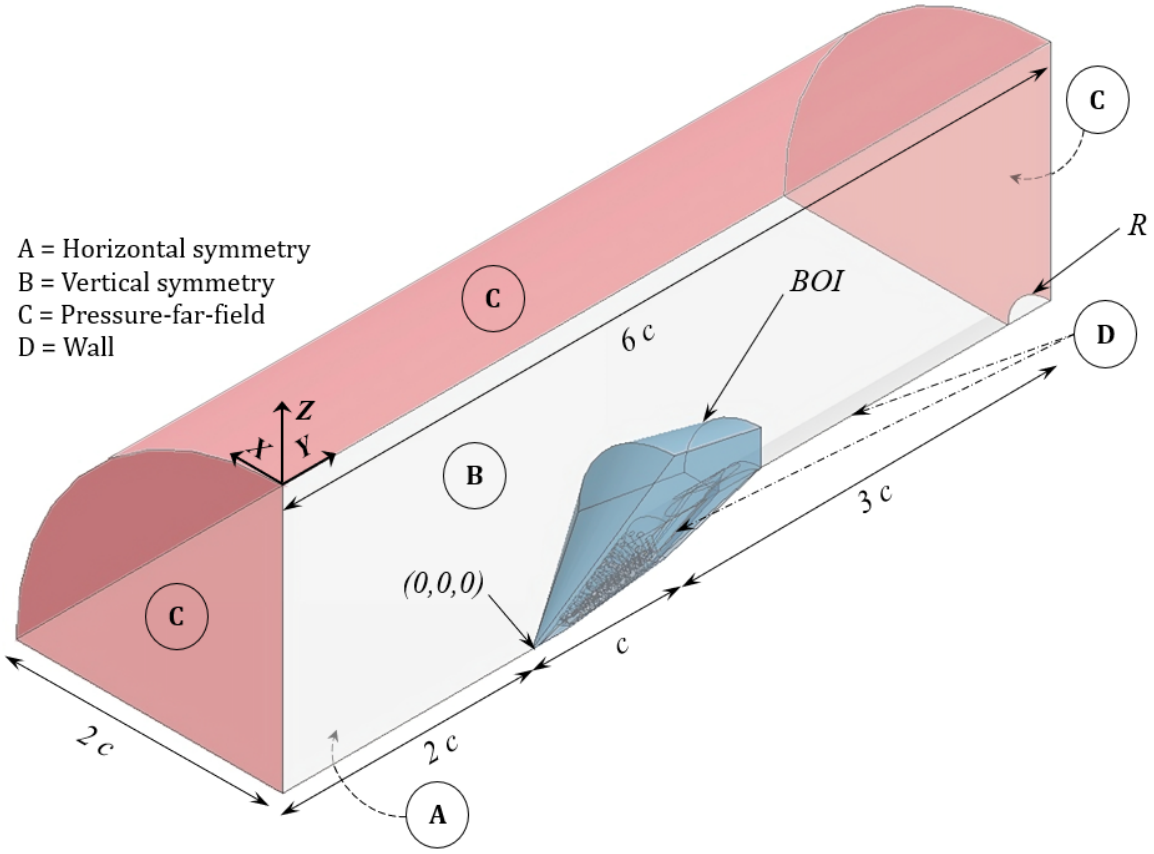

Figure 49: Domain geometry of quarter-model with a coordinate system, boundary conditions and dimensions

The flow within the channels, as well as during and after venting, was expected to have the greatest influence on the flow field. As such, high local refinement was required, and the

domain size was kept as small as possible within reason to accommodate for more nodes in the required areas. The coordinate system used for all post-processing operations is also shown, as well as the boundary conditions.

Figure 49 demonstrates the quarter-cylinder computational domain, with boundary conditions and other features labelled. The origin (0,0,0) is placed at the cone vertex. The characteristic length c of the system is defined as the base-to-vertex height of the cone, where c was 48 mm. The radius of the cone base was 16 mm. For clarity, all subsequent dimensions are written in terms of c. The length upstream of the cone vertex was 2 c, and extended 3 c downstream of the cone base. This provided adequate space for the flow to be generated upstream, and enough area downstream for sufficient visualisation.

The cylindrical base attached to the cone extended through the downstream domain length to conserve nodes and simplify the geometry and flow field. To eliminate any risk of blockage in the computational model arising from the boundary conditions, a larger domain height of 2 c was chosen, approximately double the wind tunnel radius. The total streamwise length of 6 c exceeded the SSWT test section viewing window to allow for downstream-flow visualisation.

To refine the cone region, the BOI tool in ANSYS Mesh R22.2 was used over all regions immediately affected by the channels in the cone. The BOI refined the shock and cone in a manner that mitigated mesh obstruction and ensured high resolution. This method was preferred as it provided a highly refined region while avoiding excessive node usage.

The BOI was a revolved region which covered the bow shock wave, the main cunicular mass within the conic body, and the vents. For the pointed cone half-angle of 18.43°, a wave angle β of 32.83° would occur. The boundary was created just upstream from the leading edge at a slightly exaggerated angle of 34° to fully ensure the capturing and refinement of the shock. The boundary extended a short distance beyond the body and into the domain to adequately resolve the post-vent flow conditions, as this region greatly influenced the rest of the flow field. This BOI method was repeated for the other shape families. The BOI zone can be seen in Figure 49.

The conic model from each configuration was created using Autodesk Inventor Professional 2022 Student. Each model was imported as a STEP file into ANSYS Workbench R22.2 Design Modeler to create the remaining domain.

5.2.1 Domain sizing

The domain dimensions were chosen in accordance with Van Dyke and Widnall (1983). From the origin at the cone vertex, the upstream length of the domain was 2 c. This allowed enough space for the flow to adjust to the presence of the geometry. The primary interest of the research was the immediate flow within the incident shock wave and the pores. This made an overly long downstream domain necessary.

The downstream wake was of little interest, and as such the downstream domain length was 3 c. This was the minimum necessary length for an adequate resolution described by Van Dyke and Widnall (1983). Additionally, the cone-cylinder base extended through the remaining domain, such that little interaction of interest would occur. Downstream, the body would shed a lower-energy wave, also convected by the flow. The shorter length was also supported by assigning the outlet to be a pressure far field. The smaller domain conserved computational resources, whilst adequately resolving the flow field immediately downstream of the vent.

The objective of the study was to focus on the porous cone behaviour. A gap of 2 c width was used on either side of the body to allow for local flow deviation. This was greater than the recommended distance of twice the body width, as the radial effect of the porous flow on the domain was unknown. Blockage in the simulation was also avoided this way.

A quarter-cylindrical domain was used, as this shape is well suited for free stream analysis of an axisymmetric, symmetric or streamlined geometry. It guarantees a constant distance between the sides of the body and the domain boundary and allows for direct definition of a single boundary condition on the cylinder side (Van Dyke and Widnall (1983)).

The choice of boundary conditions, based on literature recommendations, ensured that the numerical model represented a flow field which matched the experimental environment as

closely as feasibly possible. The close corroboration of the numerical and experimental data (discussed below) confirmed that the conditions were suitable.

5.3 Meshing

5.3.1 Boundary conditions

To specify the conditions of the model, named selections for the boundaries were specified as shown in Figure 49. The boundary conditions were chosen so that they mirrored the actual configuration of the SSWT.

Figure 49 demonstrates a labelled schematic of the domain with the assigned boundary types. The wall boundary condition was applied to the entire cone-cylinder structure (for all cone types), to permit airflow to pass through this boundary, where the fluid and solid walled regions were bound. The designation of this wall was unique to each particular cone under investigation, i.e. all of the shape families had the same 'wall' boundary type. The grouped red surfaces were pressure far-fields, where the two XY entry and exit plane surfaces represented the wind tunnel inlet and outlet, respectively. The vertical ZY-plane and horizontal ZX-plane were symmetry planes, greatly reducing computational time.

For the experimentation, full models were required. It would make little difference to the results if a half model was tested in the tunnel. In this case, the exposed internal structure would not be visible anyway due to the schlieren optical arrangement. Additionally, the delicate internal structure would likely fail during testing if exposed to harsh conditions. For the simulations, it was more appropriate to use a quarter domain. This was possible given that the conic models were two-plane symmetric. This approach was preferred as it greatly reduced the computational resources and time required to gather the results. The quarter domain was modelled with two symmetry plane boundaries applied to the two symmetry planes.

The flow field was initialised using the pressure-far-field boundary to ensure that the flow was supersonic at the exit plane. The named selections enabled Fluent to automatically assign

boundary conditions based on the named selections. Flow through the domain was set from left to right to match the flow direction in the SSWT. The validity of the boundary conditions is discussed in Section 6.1.4.

During the numerical simulations, the normalised residuals fell below 10^{-3}, the desired level recommended by Celik (2008). A convergence monitor was enabled at the wall to measure drag force and drag coefficient, acting in the streamwise direction.

5.3.2 Mesh generation

The cell size of the grid was kept to a size of 0.8 mm such that the complicated porous shock reflections and interactions would be adequately resolved with adaptive mesh refinement. An unstructured tetrahedral mesh was chosen to approximate the complex shapes and surfaces present in the 3D cunicular geometry in a more accurate manner (ANSYS Inc. (2023a)). This mesh designation allowed for a smoother transition between areas of varying element size while adequately representing the details of the geometry. Meshing was performed using ANSYS Mesh R22.2. Details regarding mesh refinement are given in the following subsections.

A very small element size was required for face meshing to accurately resolve the flow within the channels, per the pore diameter and internal geometry resolution requirements. The inflation layer accounted for wall-related iterations. The total number of elements for each computational model was approximately 20 - 25 million elements before adaptive mesh refinement was implemented. The same meshing procedure was repeated for all models, irrespective of cone design, such that an independent solution could be obtained.

5.3.3 Domain discretisation

The cone-cylinder body was assigned a wall boundary, and as such an inflation layer was necessary. The layer created thin elements that captured the viscous, rotational and thermal gradients near the wall, increasing the accuracy of the velocity and temperature gradient representation near the no-slip walls. At supersonic speeds, a significant temperature gradient develops across the boundary layer due to large viscous dissipations near the wall.

Table 2: Table showing the meshing settings

	Setting	Designation	Boundary
Domain	Physics preference	CFD	Domain
	Solver preference	Fluent	
	Element order	Linear	
	Element size	8×10^{-4}	
BOI	Element size	$2.5 \times 10^{-}4$	Body of influence
Face meshing	Element size	1.25×10^{-4}	Wall
Inflation layer	Inflation type	First layer thickness	Wall
	First layer height	2.9×10^{-4} m	
	Maximum layers	15	
	Growth rate	1.2	

By the expected flow field behaviour and turbulence model, the first layer thickness inflation method was used with a y+ value of 5 (ANSYS Inc. (2023b), ANSYS Inc. (2023e)). This y+ value sufficiently captured both the viscosity dominated sublayer adjacent to the wall as well as the porous interaction. The first layer thickness was calculated according to the freestream conditions, and 15 layers were set. Tetrahedral mesh elements were used for the inflation layers to better capture the complexity of the porous geometry. The inflation layer and face meshing are demonstrated in Figure 51 b).

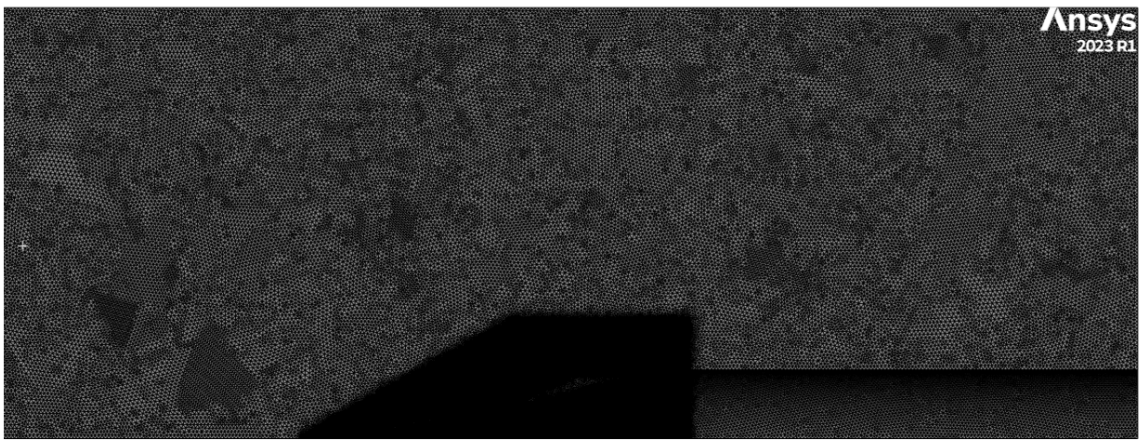

Figure 50: Image of the global quarter-domain mesh

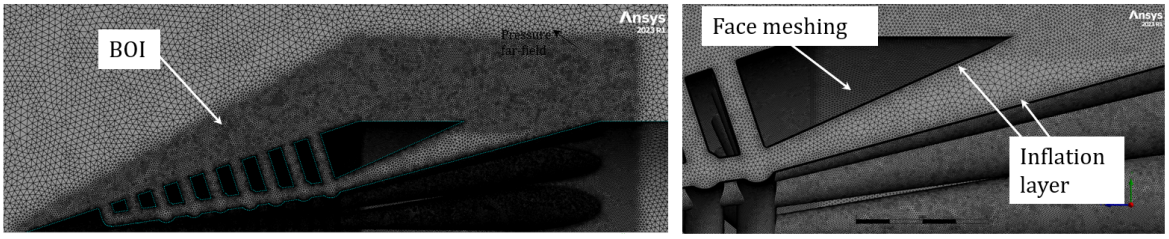

a) b)

Figure 51: Image of a) the body of influence mesh refinement region b) the inflation layer and face meshing region

A target y+ value of 5 was chosen for the walled surfaces of the conic model to model the buffer layer region of the turbulent boundary layer. The buffer layer is the region located just outside of the viscous sublayer in which the time-average velocity gradient is still very high, however the flow is strongly turbulent. In this region, both viscous shear stress and turbulent shear stress are too dominant to ignore. This was a suitable treatment since the flow was highly transitional whilst containing a mixture of low and high-speed flows, as well as bounded and free-flow regions. A y+ value less than 5 would be too conservative, where mainly the viscous linear sublayer would be resolved.

If the buffer layer upper limit of 30 was used, then the risk of under-representing the boundary layer existed. The near-wall modelling greatly affects the fidelity of the numerical solutions, since walls are the main source of average vorticity and turbulence. As such, a y+ value was chosen which would conservatively represent both the large velocity gradients, momentum and other scalar transports adequately at the wall, whilst simultaneously taking the turbulent region into account. This would ensure that successful predictions of the wall-bounded turbulent flow would occur. This best-fit approach was similar to that of Salim and Cheah (2009), who explained strategies for assigning correct y+ values to walled flow.

5.3.4 Steady-state solver specifications

Table 3 indicates the detailed solver specifications and controls used. For all computational models featured in this research, a three-dimensional steady-state solver was chosen. The implicit density-based solver was utilised as it is best suited for compressible flows.

A k - ω SST transitional turbulence model was used since viscous effects were dominant over inertial effects for this high-speed flow configuration (Wilcox (2006)). A transitional model was used because the model experienced high-speed, high-inertia regions over significant areas, including the free-stream, oblique shock wave and surrounding the vent. However, within the channels, the flow existed almost at the stagnation condition. The flow was very low speed, high pressure and nearly purely viscous (as confirmed by running an inviscid test), a distinct flow regime from the outside supersonic flow. Furthermore, the flow was required to move and transition between these two regimes. As such a transitional SST model was

used to better predict the flow separation and adverse pressure gradients present within the transitioning flow (Wilcox (2006), Wilcox (1993)). The k - ω SST transitional turbulence model incorporates mechanisms which account for the effects of vorticity and flow separation (Wilcox (2006)), which is particularly crucial in transitional flows (laminar to turbulent).

The laminar-to-turbulent transition is heavily affected by vorticity (the local rotation of a fluid), which can greatly affect the stability of the boundary layer and therefore the transition process. The k - ω SST models by Menter (1994) expand the model to include capabilities to predict transition prediction, by incorporation of empirical correlations and additional transport equations which respond to the local vorticity and strain rate. These measures aid in predicting the onset and representation of the transition zone more accurately. Transitional models are more sensitive to the adverse pressure gradients which can cause increases in vorticity and potentially flow separation (Wilcox (2006), Wilcox (1993)).

The k - ω SST transitional model alters the turbulence kinetic energy equation to account for the effects of flow separation (Wilcox (2006)). By better predicting the time and location of flow separation from the surface, the model can adjust the turbulence modelling in these areas for an improved representation of the separated flow physics, which is critical for predicting accurate lift and drag (Cummings, Yang and Oh (1995)). Transitional k - ω SST models are also coupled with enhanced wall functions to improve the resolution of the near-wall behaviour, including separation and reattachment (Wilcox (2006), Wilcox (1993)). This provides a closer representation of the turbulence at the near-wall region, including separation factors such as pressure gradient.

Based on the works of Wilcox (2006), Wilcox (1993), Menter (1993), Menter (1994) and Menter et al. (2004), the k - ω SST transitional turbulence model was utilised for this research, as it provided the most accurate representation of the transitional, geometrically complex flow field.

During both the numerical and experimental testing, the only changing parameter across all of the conic models was the Mach number. Double precision accuracy was enabled to improve convergence time. The free stream conditions of supersonic gauge pressure and temperature were set to 9000 Pa and 100 K respectively to match the SSWT test section conditions. The

operating pressure was set to 0 Pa to ensure the correct domain pressure. The ideal gas law was applied since the flow is compressible for temperature and pressure dependency. Angles of incident was set to 0° for all models.

The free stream Mach number was set using the pressure-far-field condition. For this research, Mach 3.5 was the primary Mach number used for all models, with Mach 3 used for certain limiting cases as an investigative tool.

Table 3: Table showing the detailed solver specifications

General	Solver type	Density-based implicit
	Time-state	Steady-state
	Double-precision	Enabled
	Dimension	3D
Models	Energy equation	Enabled
	Viscous model	Transitional k-ω SST (4 eqn)
	Curvature correction	Enabled
Properties	Air	Ideal gas
Boundary Conditions	Viscosity	Sutherland
	Pressure far field	P_b = 101 325 Pa; T = 100 K
Solution Methods	Formulation type	Implicit
	Flux type	Roe-FDS
	Spatial discretisation type	Green-Gauss node based
	Flow	Third-order MUSCL
	Turbulent kinetic energy	Second order upwind
	Specific dissipation rate	Second order upwind
Solution Controls	Courant number	0.5
Convergence Monitors	Drag coefficient C_d	Wall

The CHPC in the Republic of South Africa exclusively provided the computational resources for this research project. Both the 'Aerothermodynamics with vortices, vorticity and shear' group (MECH1532) and (MECH0847) group were used for this research.

The project had a high computational demand due to the highly refined porous cones. Models were solved using the Fluent parallel solver across 19 nodes of 24 cores each, for a total of 456 cores, with approximately 1.8×10^6 cells per core. A typical simulation ran for 36 hours. Convergence was reached at approximately 36,000 iterations. All convergence criteria were set to 10^{-5} and determined by the residual monitors of the model.

A drag monitor was set at the walled boundary type in the streamwise direction. Both drag force and coefficient were calculated, and the force was plotted. The flow within the channels was found to be pseudo-steady due to the flow recirculation present in the toroids. The resulting drag monitor fluctuated slightly, which eventually damped out as the iterations increased. To extract the converged, final drag coefficient, a least-squares curve fit was applied to the numerical drag plot. The detail of this may be found in Section 6.1.2 and Section 6.1. The critical evaluation of the solver is discussed in Chapter 6.

5.4 Adaptive mesh refinement

In CFD, Adaptive Mesh Refinement (AMR) is the method of adapting and increasing the accuracy of a solution within specific sensitive or turbulent regions of the simulation. This adaption occurs dynamically, while the solution is being calculated.

This approach is advantageous for fluid flows where not all of the regions require uniform solution precision and ultra-high refinement. It enforces efficient resource allocation in the grid by refining quantification only in areas that require greater accuracy, while simultaneously maintaining lower levels of precision and resolution for areas of less interest in the flow field. This is particularly useful for compressible flows, where shock waves and boundary layers are present. These regions undergo abrupt changes in flow properties, and a much finer mesh resolution is required to adequately and accurately capture the phenomena (Berger and Colella (1989)).

The AMR method is popular and widely applicable to other complex flow phenomena, efficiently handling turbulent wake flows and vortices as the grid adapts in areas where these behaviours intensify or develop, thereby increasing the resolution and accuracy of the solution (Pang et al. (2021)). The same can be said of unsteady or transient flows, where AMR allows for dynamic grid adaptation based on the solution changing over time (Berger and Colella (1989)). This is particularly useful in flow fields where recirculation is present, or where features disappear and reappear throughout the simulation. AMR is also highly suitable for flow around complex geometries, as it focuses on computational resources on regions with

complicated flow behaviours (Nemec, Aftosmis and Wintzer (2008)). Lastly, the approach reduces the computational time and resources required by the simulation by eliminating redundant elements in regions where the solution is uniform. It advocates efficient resource utilisation by targeting the concentration of mesh refinement to key regions, resulting in a universal reduction in the number of grid points, while maintaining a highly accurate and precise solution (Pang et al. (2021)). The presented research heavily overlaps with the factors described, making it a suitable candidate for AMR.

The adaptive nature of AMR inherently indicates that it is capable of achieving convergence criteria more efficiently. In a numerical simulation that utilises AMR, convergence is achieved by combining the continual refining of the mesh according to the desired refinement threshold and employing the appropriate numerical error methods. This occurs automatically in the ANSYS Fluent package (ANSYS Inc. (2023e)), which is the original source for the mentioned AMR studies.

Several studies have shown that the adaptive mesh refinement technique is equivalent to a grid convergence study in that it achieves the objective of the latter (convergence) in a far more concise simulation process. For the second-order scheme, neither grid adaptation strategy improves numerical solution accuracy compared to a uniform grid with the same number of points.

Struchkov et al. (2020) undertook a numerical simulation of supersonic aerodynamic nose cones using an adaptive mesh refinement algorithm that identified shock waves and refined the mesh accordingly. Shock regions based on pressure and density gradients were analysed, and the results of adapted and automatically generated meshes were compared. The mesh adaptation method was found to provide clearer flow visualisation images and reduced numerical errors in the drag coefficient calculations when compared to corresponding wind tunnel data. Additionally, the adaptive mesh has fewer cells overall, indicating reduced computational time to reach convergence. This concluded that it was preferable to use the mesh adaptation method with local refinement over the automatic mesh.

Wackers et al. (2022) confirmed the findings of Struchkov et al. (2020), demonstrating that adaptive mesh refinement was effective in creating groups of similar meshes for convergence

studies for aerodynamic bodies. The computed forces underwent uncertainty analyses with suitable results. Good convergence in the local flow features was observed. They confirmed that adaptive meshing offered an elegant approach for grid convergence studies, allowing for simulations on different grids by altering the refinement threshold alone. In this, a separate mesh independence study was unnecessary as the adaptive mesh refinement method naturally included it.

The literature discussed confirmed that adaptive mesh refinement was a suitable method for grid convergence in supersonic flow over aerodynamic vehicles, and as such justifies its application here.

5.4.1 Adaptive mesh refinement settings

The adaptive mesh refinement settings used in the numerical simulations are described here. From the starting grid of the domain, cells are identified that possess gradients of particular flow properties which are greater than a certain limiting value, this being known as the refinement threshold. These cells are then divided or refined and the process is continued until such time that convergence is achieved in the solution. The flow property gradients used were density, static pressure, static temperature and velocity. Cells having gradients greater than 0.75% of the global maximum were assigned refinement, and cells greater than 1% of the global maximum assigned to be coarsened. These values are recommended based on the work of ANSYS Inc. (2023f) and ANSYS Inc. (2023e), as these are the standard CFD parameters based on the original adaptive mesh refinement studies.

Table 4: Table showing the adaptive mesh refinement settings

Setting	Parameter
Mesh type	Tri-mesh
Advanced sizing functions	Disabled
Initial grid size	8×10^{-4} m
Gradient variables for adaption	d, T, P, v
Adaption thresholds (refine, coarsen)	1%, 0.75%
Adaption interval	500 iterations
Maximum no. cells	10×10^{-5}

Refinement was automatically performed by ANSYS Fluent R22.2 until the property gradients in each cell no longer met the refinement threshold condition and had reached the required refinement level. In this, convergence was achieved. The drag wall monitor also aided in identifying convergence. To assist in feasible computation times, the minimum cell size was limited to an order of magnitude of 10×10^{-5} to correctly visualise the shock waves and internal turbulent flow in the channels. Table 4 shows the AMR settings. Beyond the channels and shock waves, adaptive refinement also altered the cells in and around the venting structure, shear layers and wakes to ensure acceptable resolution of the entire flow field.

5.4.2 Conclusions

The computational approach and settings chosen for the numerical model mirrored the experimental conditions closely so that the numerical method could validate the experimental method. Literature was used to ratify the decisions made, which are discussed further in Chapter 6.

Chapter 6

Verification and Validation

Verification refers to the techniques used during the research process which contribute to ensuring the reliability, validity, and thus rigour of the study (Morse et al. (2002)). In addition, it is the process of proving that the research tools have been utilised appropriately. Validation refers to the process of establishing evidence which provides a high degree of assurance that the study accomplished its intended objectives and that the end result is proven to be acceptable. Both processes are required for a complete study.

The cunicular structure had never before been investigated, and thus the results of the study were largely unpredictable. To account for this, well-established existing experimental and numerical research inputs and methodology were chosen (such as model dimensions, sting design, numerical domain size, mesh sizing and boundary conditions). These were used to create a categorical research method based on proven data such that the unique and unknown porous result could be interrogated with confidence, and without interference or doubt caused by novelty or other factors.

The experimental and numerical results of the validation case are presented below. To reiterate, the naming convention for the conic models is as follows: Subsequent models which contain venting structures are known as 'BSX' models, where 'BS' refers to the conical forebody containing the combined internal porous structure (longitudinal, radial and toroidal, previously mentioned as 'Combined/C'), and 'X' refers to the particular venting abbreviation.

For example, BS0 refers to a pointed (right triangular) cone where the conical forebody contains the combined internal porous structure, and the '0^{th}' venting geometry is present, i.e. the 90° elbow vent. Note that unless otherwise stated, all models refer to the pointed cone shape unless an additional 'H/SO/E' is directly mentioned.

The validation case for the research method was the baseline BS0 pointed cone. The solid cone was also included as a validation case for comparison purposes where relevant. The geometry of the validation conic cases is presented in Fig. 52. This configuration was the appropriate choice for the validation study as it was successfully tested both numerically and experimentally. In the baseline experiments, it was the only porous model to experience a meaningful drag reduction when compared to the solid model. Because of this, all of the subsequent models were designed based on this configuration.

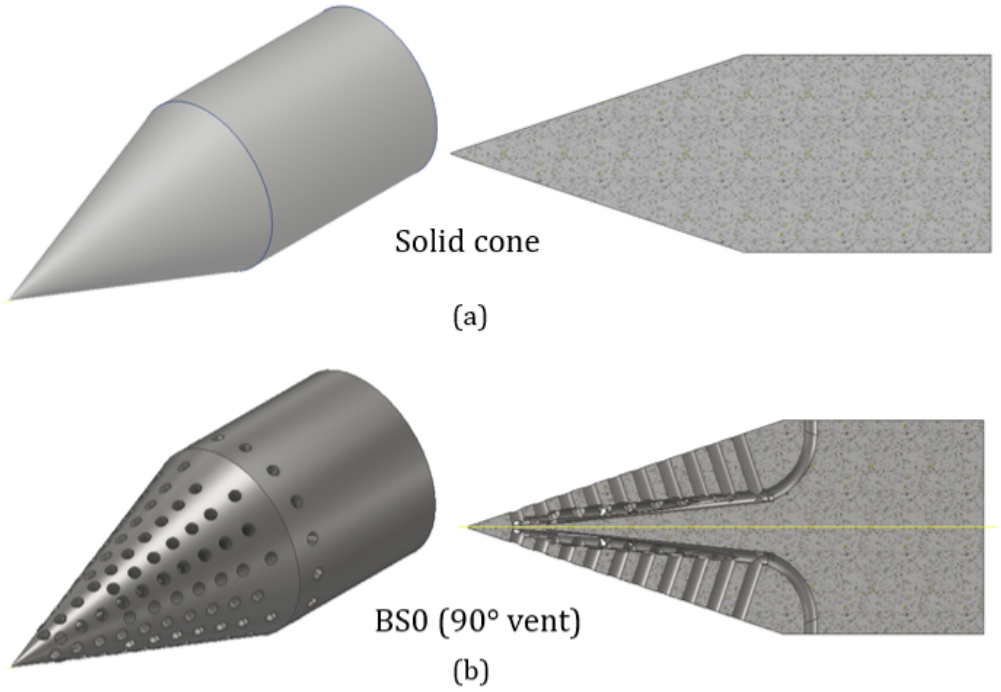

Figure 52: Schematic of pointed cone validation cases a) solid b) BS0 (90° elbow vent). Isometric view (left) and sliced ZY-symmetry plane view, where internal structure is visible.

The validation case flow conditions reflected both the steady-state CFD and experimental flows, at Mach 3.5 and zero angle of incidence. The two sets of results for this geometry were compared, whereby it was determined that the same result was achieved using both methodologies. The results were also compared to the literature for additional validation.

The discussion of the verification and validation of the research method is presented below. Specific aspects from Chapter 2 will be referred to, including the calculated drag values and percentage similarities, as well as particular flow features of interest which are common in both sets of research.

6.1 Numerical results

The numerical results of the validation case are presented, including the numerical drag coefficient data and several sample visual plots. These plots were used to characterise the flow field, enabling the identification of the most important parts of the flow field. The streamwise aerodynamic forces, coefficients, and images were extracted directly from the ANSYS Fluent data, using the existing post-processing features in Fluent. The similarities in boundary conditions and experimental set-up were previously assessed in Chapter 4 and Chapter 5. As stated in Chapter 5, the models were found to converge at 36,000 iterations. This was determined using both the solid cone and zeroth/first iteration cones cases.

6.1.1 Time Convergence of the BS0 Cone

In order to use the numerical results with confidence (thereby ensuring fair comparability with the experimental data), convergence in the numerical solution must be proven using the quantitative and qualitative CFD data of the BS0 cone. This involved establishing convergence in the visual flow field using CFD images, as well as in the numerical drag response.

Numerical time convergence - qualitative

Figures 53 and 54 show the Mach 3.5 density flood plot of the BS0 cone over the long and short time scales. Comparing both sets of images, very little visual variation is present with regards to the key flow features (including the internal flow patterns, the porous shock interaction pattern, conic boundary layer behaviour, shock angle and vent behavior). Figure 53 a) shows high shock curvature at 10 000 iterations, whereas by b) and c) the shock straightens out,

showing that the flow field is converged for the 20 000 and 30 000 iterations. This also indicates that the flow is not fully resolved at 10 000 iterations. At 20 000 and 36 000, no difference in flow features is visually discernible.

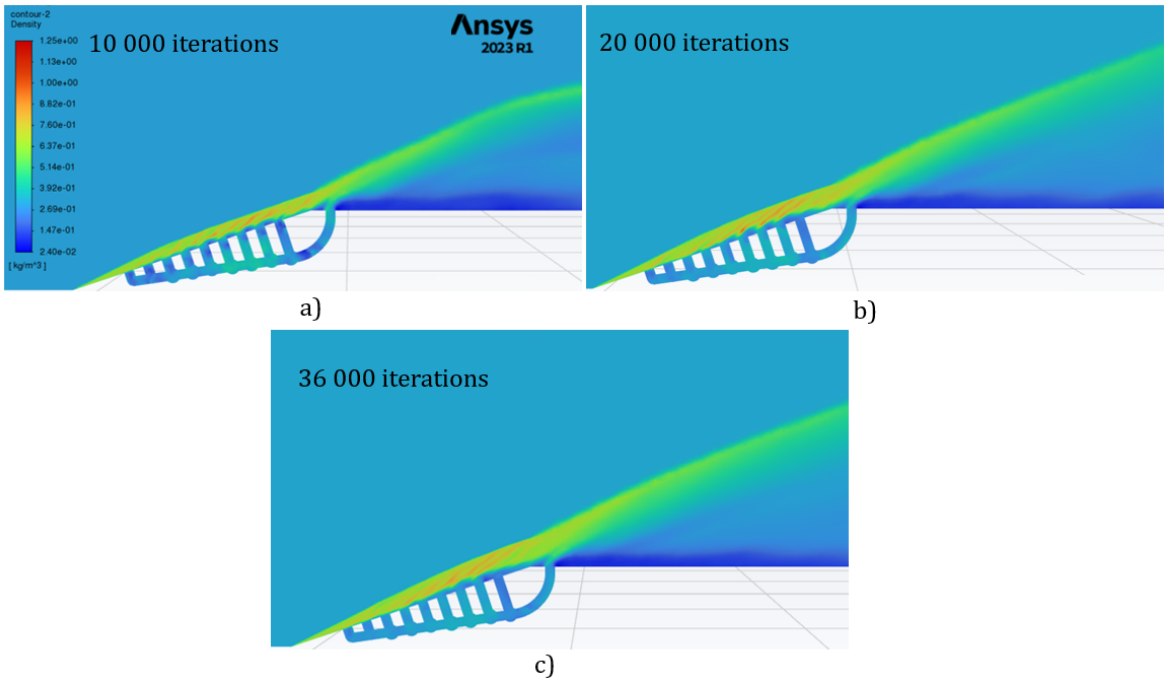

Figure 53: Density flood plot of the long-time scale BS0 CFD solution at Mach 3.5 a) 10 000 iterations, b) 20 000 iterations, c) 36 000 iterations.

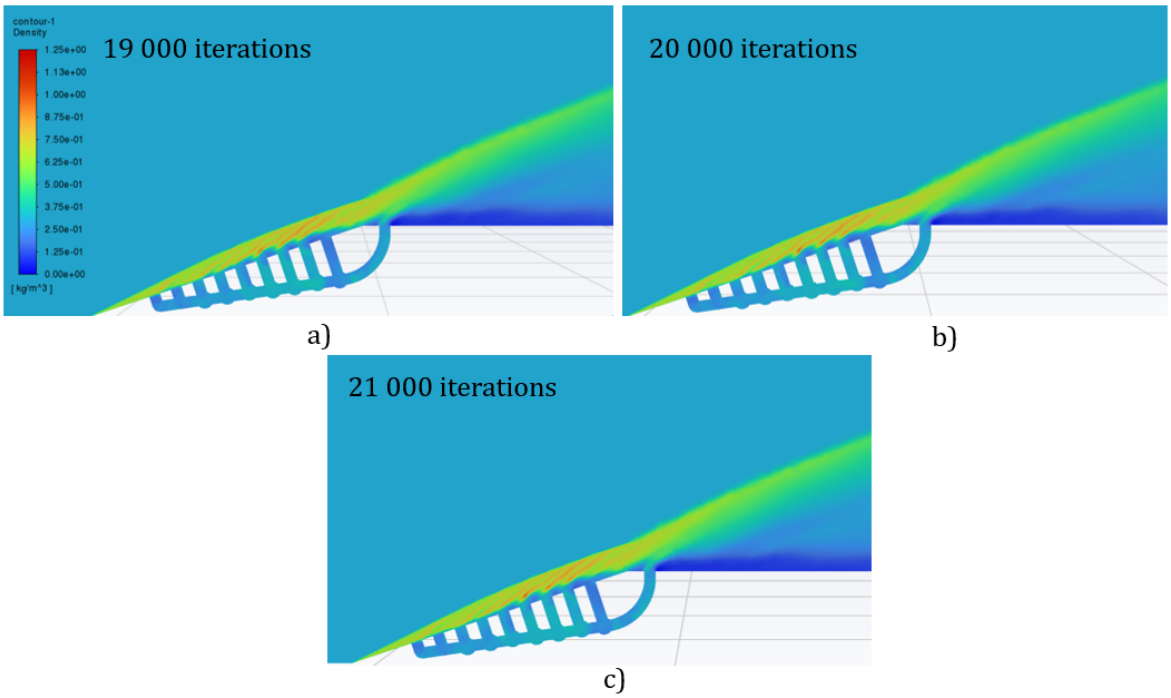

Figure 54: Density flood plot of the short-time scale BS0 CFD solution at Mach 3.5 a) 19 000 iterations, b) 20 000 iterations, c) 21 000 iterations.

Figure 54 shows the variation in flow field across a much shorter time scale. As with the long-scale, the key flow parameters of interest show very strong correlation across the three cases. Since no discernible differences are visible in the flow field from 20 000 iterations onward, the density plot comparisons prove that the steady part of the flow field must be converged.

Thus, it may be said with confidence that by 20 000 iterations the flow field had converged, as shown by the CFD image comparisons. The numerical drag response discussed below shows good agreement with this.

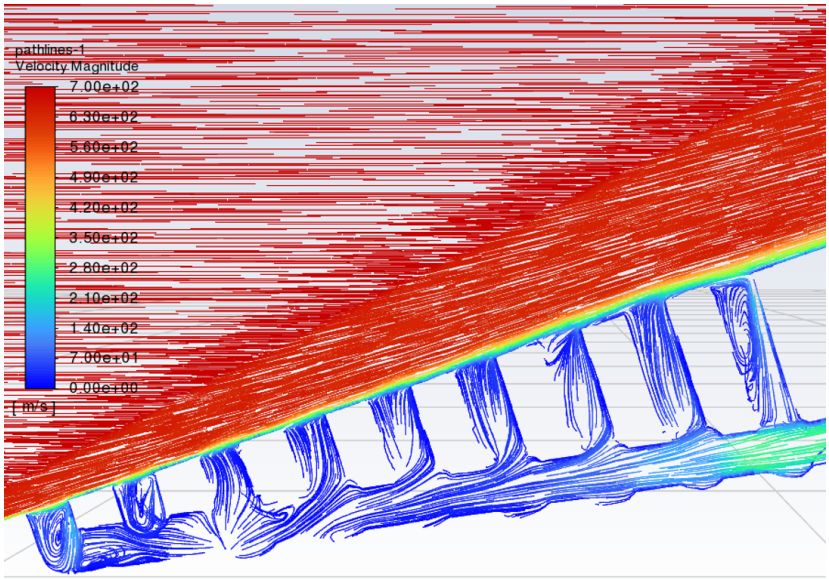

Figure 55: Velocity magnitude stream traces for the flow inside the BS0 cone at Mach 3.5.

The internal behaviour is further corroborated by Fig. 55, which demonstrates the stream traces within the internal porous structure of the BS0 cone validation case (plotted on the ZY-symmetry plane), coloured by velocity magnitude. The recirculation within the toroids (the circular structures), as well as within the radial inlet pores is indicated by the motion and direction of the traces. Within these pores, the traces indicate that little movement is occurring in the free stream direction. The flow pattern around the toroids is mostly circular, showing that inflow (through the inlet pores) was reaching the toroids, and thereafter moving around inside the three-dimensional toroidal structures, eventually moving upstream. This is partly confirmed by the aft-most toroid having a greater velocity than the other toroids. By the aft-most toroid, the mass flow had accumulated, partly due to momentum flowing from the structures upstream. The flow inside this region of the porous network is transient in nature on account of the three-dimensionality and complexity of the porous structure.

The porous system is continuous, whereby the cycle of inflow-recirculation-outflow occurs as long as the conic model interacts with the freestream. During a simulation, flow is constantly recirculating in the toroids, and continually moving through and around the conic porous structure, as shown in Fig. 55. This recurrent intra-porous movement (before venting) is the strongest cause for time-varying flow behaviour visible in the numerical drag plot, in the form of feedback loops and nonlinearities in the simulation. This is caused by the complex geometry and interactions with the external flow field and boundary conditions. As the number of iterations increases, the fluid within the pores has time to stabilise and recirculate within the toroids, gradually reducing the size of the numerical oscillations until such a time that the converged value may be extracted. As Fig. 55 and Fig. 56 show, the flow recirculation is continual, however, the pseudo-steady flow eventually stabilises to convergence.

Numerical time convergence - quantitative

Convergence was also shown in the drag response outputted by the numerical solver. Fig. 56 demonstrates the CFD drag coefficient plot of the BS0 pointed cone during a typical Mach 3.5 ANSYS Fluent simulation. The drag coefficient was calculated in the streamwise (z) direction on the cone-cylinder wall surface, where the reference area was the 360° frontal area of the conic model.

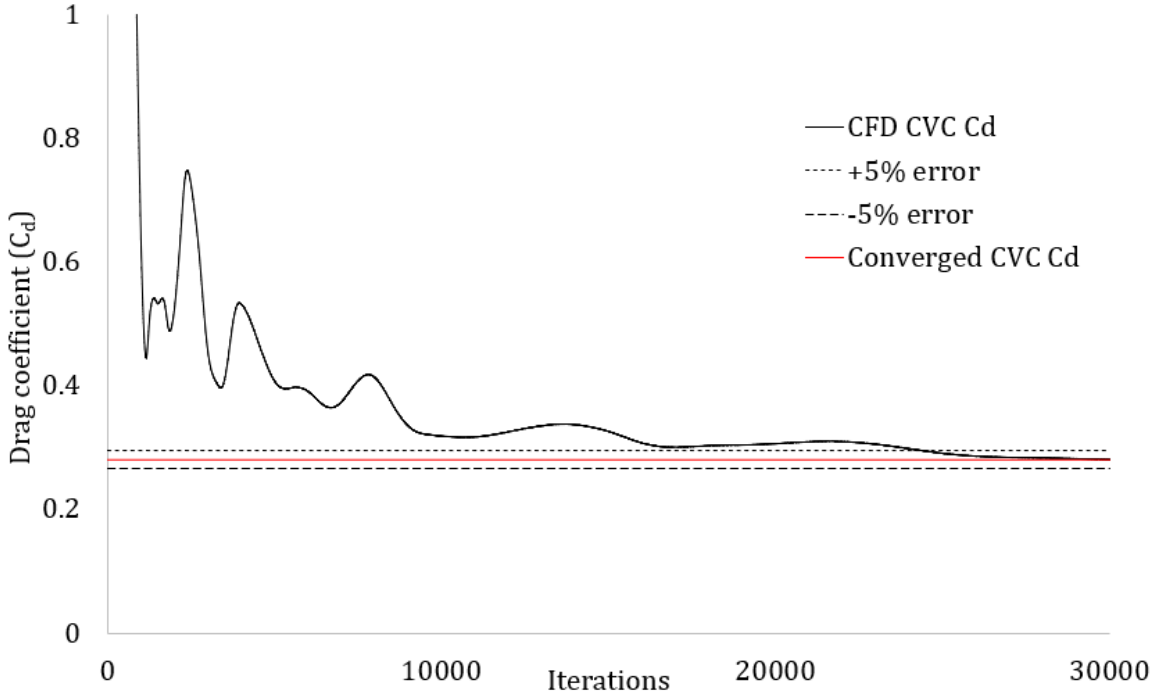

Figure 56: Mach 3.5 CFD drag coefficient (C_d) versus number of simulation iterations, for the cone BS0, with converged CFD value with ± 5% error.

The simulation was pseudo-transient due to the presence of unsteady elements in the flow field, as confirmed by the discussion in Section 2.2.1. The transient effects are visible in Fig. 56, appearing as periodic fluctuations in the converged part of the plot after 21 000 iterations. The unsteadiness was caused by the unsteady flow features that were identified by Yanbo and Tong (2019), Law and Skews (2009) and Skews (2005), and are considered in greater detail in Section 7.8.

The swells in Fig. 56 represent deviations from the steady-state model, where transient flow phenomena cause minor localised changes in the flow field that do not change the flow field away from the zone of influence of the jet interaction. These peaks provide information regarding the transient dynamics of the model and the response to disturbances. During the simulation, the system gradually adjusts to the dynamics and conditions of the problem, eventually reaching the equilibrium position or convergence at 21 000 iterations, shown above in Fig. 56.

To account for these fluctuations, a least squares curve fit was applied to determine the final converged drag coefficient, with a ±5% error bound estimate applied accordingly (shown in Fig. 56 as dotted lines). The decaying nature of the data indicated an under damped response, whereby use of an exponential curve fit was appropriate. This method determined the converged value by iteratively adjusting the parameters until the best-fit value was found. This minimised the sum of the squares of the residuals between the observed data and those predicted by the model. Using this method the converged numerical BS0 drag coefficient was calculated to be $C_d = 0.28$ for 36 000 iterations. This numerical drag closely correlated with the experimentally measured 'time-averaged' drag coefficient.

The pseudo-transient nature of the flow (shown in Fig. 56) is also confirmed by the presence of several of the unsteady elements visible in Figure 53 and 54, including the boundary layer over the porous cone surface and the recirculation regions in the toroidal pores. These features are both associated with the walls of the internal porous structure. The drag monitor was set up to cumulatively calculate the drag along the porous wall, and so the presence of the unsteady near-wall elements likely influenced the drag calculation, resulting in the fluctuations.

To determine if convergence had occurred using the drag response, the drag at each major iteration was recorded, as shown in Table 5. Table 5 shows the total drag coefficient (comprised of the summed pressure and viscous components) for the various solution run times (iterations). The percentage difference (using total the total 36 000 C_d as the reference value) from the converged drag coefficient is also shown.

Table 5: Final (total) CFD BS0 drag coefficients at various solution iterations. Percentage difference from the converged solution shown, with pressure and viscous components tabulated.

Drag Coefficient				
Iterations	Pressure	Viscous	Total	% diff from converged
10 000	0.25	0.06	0.31	10.16
19 000	0.25	0.05	0.30	5.10
20 000	0.25	0.05	0.30	4.51
21 000	0.25	0.04	0.29	2.50
36 000	0.24	0.04	0.28	
42 000	0.24	0.04	0.28	0.06

Table 5 shows that very little variation exists across the different iterations for both the long (10 000, 20 000 and 36 000) and short ($\approx < 5\%$ for 19 000, 20 000, 21 000) time scales. The drag at 10 000 iterations is disregarded the solution will not have converged by that point in the simulation. This is to be expected, as the complexity of the geometry warranted longer run times to be adequately resolved. At 19 000 and 20 000 iterations the drag was just within the acceptable level of error. From 21 000 iterations the calculated drag was very close to the converged vale (within 2.5%). At 42 000 iterations, the drag was virtually the same as that calculated at 36 000 iterations, indicating that no meaningful change had occurred for 6000 iterations. This suggested that by 36 000 iterations the drag solution was converged in the simulation, as the variation between successive drag values is sufficiently small.

Due to the presence of the unsteady elements at the wall, the drag solution requires a longer solution time to fully converge. This also shows that the oscillations in the drag data are not due to convergence issues, but rather the unsteady flow features, further confirming the converged solution behavior.

The analysis of the drag response in conjunction with the various-iteration drag coefficient and visual analysis confirms that the numerical drag calculation and flow field have both converged by 36 000 iterations. Thus, all subsequent numerical results (across all cases) were

extracted at 36 000 iterations and used with confidence for the remainder of this work. The least squares model provided consist numerical drag predictions which closely corresponded to the experimental results, and was applied to all subsequent numerical models.

6.1.2 Numerical uncertainty

Several sources of uncertainty can arise from numerical modelling using CFD. Physical approximation errors are due to uncertainty in the formulation of the model, including deliberate simplifications to the model (Mathelin and Hussaini (2003)). Sources of uncertainty include (Mehta (1991)):

- The phenomenon is not thoroughly understood.
- Parameters utilised in the model are known, but some degree of uncertainty exists.
- Models are simplified, thereby introducing uncertainty.
- Experimental confirmation of the model is either possible or incomplete.
- Discretisation error.

Discretisation errors are the most common source of error, occurring from inaccuracies in the representation of the governing flow equations of the physical model, including time and algebraic expressions in a discrete domain of space (Mathelin and Hussaini (2003)). The level of discretisation error is determined by the quality of the mesh and the manner in which discontinuities (including shocks, shear layers and walls) are represented in the mesh. As discussed in Chapter 5, a high level of refinement in the necessary regions, as well as good mesh quality, were both achieved using adaptive mesh refinement. Strong grid convergence was achieved using this method, and thus a grid convergence study was not required.

Physical approximation errors are examined by undertaking validation studies that focus on particular models, such as turbulence models, turbulent boundary layers, real-gas flows, etc.

The following discussion will outline validation studies undertaken for the numerical model, in which the accuracy of the numerical result is compared with an acceptable standard set of results, which is drawn from the literature for this work.

To validate the accuracy of the numerical results and the modelling approach taken, a comprehensive literature comparison was conducted on the CFD solution from similar studies. Specifically, combined studies of Mironov, Kirilovskiy et al. (2019), Valiullin et al. (2023) and Mironov, Maslov et al. (2015), as in the literature review, were interrogated, hereafter referred to as 'the literature'. The literature and presented research used similar experimental and numerical boundary conditions on the porous models, aiding in the comparison of the data sets.

The models utilised in this study followed similar geometric representation to the literature models. The literature used blunt cylinders and cones, baseline aerodynamic shapes which highlight the porous flow phenomenon. Following a similar thought process, cone variations were used in this study. These shapes had a strong overlap with the literature shapes, meaning that the results of the two studies could be compared and validated. Additionally, this research utilised similar geometric parameters, such as L/D, to further aid in validation. Both the presented study and literature rigorously investigated the same (or similar) simple geometries in many different porous configurations so that the effect of porosity on aerodynamic shapes could be fully investigated. This approach enabled unknown parameters (porosity) to be investigated in well-understood shapes (cones, cylinders) so that meaningful conclusions could be obtained with greater understanding.

The presented study and literature models both utilised a similarly low frontal solidity ratio[i]. A lower solidity ratio reduces the component of drag arising from the shape and surface parameters of an object when passing through a fluid. Reduced solidity ratios indicate a smaller cross-sectional area exposed to the flow, resulting in reduced skin friction and form drag. The literature designed models with a low solidity for this reason, and a similar ratio was applied to the presented models.

[i]The ratio of the total cross-sectional area of an aerodynamic object to the area of the region it fills when viewed from a particular direction

The literature used a HPCM foam, with a randomised cell structure, to create the models. In this, the material itself was porous. Conversely, the presented research used organised channels/pores removed from solid shapes. In this, the flow field in the literature interacted with a randomised porous material, whereas the presented flow field interacted with an organised porous structure. The fundamental flow physics through a porous aerodynamic shape is still transferable from the literature to the presented work, however, the organised structure represents the knowledge gap being investigated. The literature and novel results can then be directly compared to one another so that the presented results may be confirmed and presented with confidence. Additionally, the fundamental similarities to the literature provide greater insight and understanding into the complex presented results, since the literature provides well-established evidence for the porous flow behaviour.

6.1.3 Solver uncertainty

The chosen turbulence model was required to be both compatible with the physical problem and to account for the expected flow characteristics. This included adequately describing regions of subsonic, supersonic and transitional flow inside a single flow field. Both the free-flowing and wall-bounded flows also required suitable treatment. The expected flow field contained both high and low-speed flow regions, and the settings applied to the numerical model must reflect and account for this in order to match the experimental tests.

Supersonic flow occurred in the free stream, post-shock, ahead of the reflected incident shock waves and in the venting pores. Mironov, Maslov et al. (2015) confirmed the presence of subsonic flow occurred inside the porous network, where the flow also experienced choking acceleration and expansion in the outflow pores due to the geometry. The flow thus behaves as inside a quasi-converging-diverging nozzle, whereby transition between the subsonic and supersonic regimes occurs. Multiple transition zones and flow interaction regions also exist as the flow travels from wall-bounded to free-slow states across several different speed ranges.

Transition occurs when the viscous and friction forces required to maintain steady laminar flow are overtaken by inertial forces. Transitional flow refers to the laminar-turbulent flow transition that typically occurs in the context of boundary layers, and interacting flows (such as shear surface interactions). The predicted flow field is highly transitional, where the porous network is a wall-bounded system built into a body positioned in a free stream. The transition between these states (walled and unwalled, and between the different flow regimes), must be accounted for in the numerical model.

The transitional k-ω SST turbulence model was the most suitable choice for this research. This was decided based on the standard Menter Shear Stress Transport (SST) turbulence model successfully used in the founding studies by (Poplavskaya et al. (2017)), (Mironov, Maslov et al. (2015)) and (Mironov, Kirilovskiy et al. (2019)). This model utilised a system of three-dimensional differential Navier-Stokes equations with a k-ω SST turbulence model.

The SST formulation posed several advantages. It is known to have good behaviour in adverse pressure gradients and separating flows (Van Dyke and Widnall (1983)). The supersonic flow interacting with the porous cylinder would induce large pressure and velocity gradients (due to impulsive loading on the flow fields producing sudden shock waves and fluid property changes), and the SST solver is capable of handling this. This dual-equation (switching between k-ω and k-ϵ) model offered improved predictions of adverse pressure gradients while improving upon the strong free stream sensitivity of the k-ω turbulence model (Menter (1993)).

The k-ω form of the SST model was used for the inner boundary layer regions. This made the model directly applicable along the entire wall through the viscous sublayer, which was advantageous for low Reynolds number turbulence models (pertinent here as for the subsonic regions). The SST formulation switched to a k-ϵ form in the free stream, thereby avoiding the common k-ω sensitivity issue regarding the free-stream inlet turbulence properties (Menter (1994)). Another appeal of the k-ω SST model was that it was successfully used and validated in the founding porous studies mentioned, further improving the validity of this study if successfully implemented.

As a further refinement, the transitional option (built into ANSYS R22.2), was enabled. The transitional SST model (Langtry-Menter 4-equation Transitional SST model) makes use of two additional equations for γ and $\mathrm{Re}\theta_t$ (Menter et al. (2004)). This modification of the turbulent transport equation simulates the following states through the boundary layer: viscous, viscous-to-turbulent transition, and turbulence. An intermittency factor was calculated that altered turbulence by gradually introducing turbulent production at the flow transition location (Menter (1994)). This was advantageous as the expected flow field was largely transitional, however the locations and exact parameters of this were impossible to define. The addition of the transitional setting allowed for the transition to be amalgamated and dealt with automatically.

The transition SST turbulence model was the appropriate choice when modelling turbulent flows when a significant proportion of the boundary layer was laminar (Menter (1993)). This was most likely to occur in the porous internal network where the flow regime was largely subsonic and viscous due to the high instance of narrow-walled, bounded flows. Since the overall flow field features regions of laminar, turbulent and transitional flow, it was warranted to use a transitional regime.

The turbulence model chosen appropriately represents the expected regions in the flow field and was the most suitable, comprehensive model for the highly transitional flow field present. By using the same turbulence model as Poplavskaya et al. (2017) and achieving a successful result, the model was further verified.

6.1.4 Critical analysis of boundary condition

The computations of Mironov, Kirilovskiy et al. (2019), Valiullin et al. (2023) and Mironov, Maslov et al. (2015) used a density-based solver, and an implicit scheme of the second-order accuracy. The Roe-FDS method of splitting of convective fluxes was used. The viscosity was determined using the Sutherland formulation, where the heat capacity was constant. It was stated that these conditions for these simulations were consistent with the conditions of experiments referenced above. Identical conditions were applied for this research in the same

way, where the computational boundary conditions matched those of the experimentation precisely.

The density-based solver was the appropriate choice for the high-speed compressible flow study, as confirmed by Wessam and Z. H. Chen (2015) and Ntantis et al. (2023). The domain settings were chosen largely based on bullet simulations studies (Ntantis et al. (2023), Wessam and Z. H. Chen (2015)) (due to the similar geometry, sizing and testing conditions), and the relevant computational porous literature (Poplavskaya et al. (2017), Valiullin et al. (2023)). Additionally, it was ensured that the numerical settings matched the experimentation as closely as feasibly possible for comparability purposes.

Symmetry boundaries were used to reduce the size of the computational model to a symmetric subsection of the overall physical system (ANSYS Inc. (2023c)). This had several advantages. When referring to modelling bullets in supersonic flow, Ntantis et al. (2023) confirmed that a symmetric half-model significantly reduced computation time when compared to a full-bullet domain. By creating a quarter model, the computational time was further reduced. This allowed for a highly refined mesh in the walled and BOI regions and an increased number of inflation layers. These factors aided in achieving a more accurate drag solution and resultant flow field when compared to a whole or half domain.

This smaller, ultra-refined model was more computationally expensive, however the trade-off was a high-resolution solution. Given the detail and complexity of the resultant flow field, this trade-off was acceptable. The symmetry boundary was applicable when the geometry of interest had mirror symmetry where the expected pattern of the flow field solution was located (Wessam and Z. H. Chen (2015)), as in this research. Viscous modelling was used, and the no-slip boundary condition was enforced at all walls by default (ANSYS Inc. (2023b)). The symmetry boundary on the central plane faces also ensured this zero shear wall, however, symmetry conditions were applied for all equations.

The remaining boundaries were grouped and set as far as field density-based. Known as the characteristic boundary condition, it uses characteristic information (Riemann invariants) to determine fluid variables at the boundaries (ANSYS Inc. (2023d)). It enabled the solver to determine the far field boundary conditions and implicitly match the boundary condition to

the specified free stream condition (Ntantis et al. (2023)). The pressure far field condition was used here, as it only requires the Mach number as the input when many variables at the inlet and outlet are unknown.

Triangulation was achieved by arriving at the same result via two different mesh approaches (one including and one excluding the pores) and further confirmed the suitability of the wall treatment used, further discussed below. Triangulation is the preferred method for validation as it ensures reliable and repeatable results. As described in Section 5.4, adaptive mesh refinement was used to obtain a converged drag force prediction without the use of mesh independence.

6.2 Experimentation

6.2.1 Sting calibration

The sting force balance was calibrated according to the International Organisation of Standardisation (ISO) 376:2011 report (BSI British Standards (2011)) and the Shimadzu AG-IC universal testing machine. The calibration of force-proving instruments is performed using the outlined method for the static verification of uniaxial testing machines. It describes the procedure for the classification of these instruments.

The purpose of the calibration was to test the proper functioning of the force balance. In order for the data measured by the force balance to be deemed trustworthy, it was required to match the force applied by the testing machine to a reasonable degree. This verified the measurement system and instilled confidence in the experimental results.

During calibration, the Shimadzu AG-IC universal testing machine applied a steady known compressive load to the exposed inner sting bolted to the sting apparatus. The axial force experienced by the force balance positioned on the sting was measured using the same DAQ and HBM Catman Easy/AP. Version 5.0.1 data acquisition software used in the SSWT experiments to maintain apparatus and measurement system consistency. The calibration testing procedure that was followed is summarised below:

1. Preloading - The cell was preloaded three times to adhere to the ISO standards. Each time, the pre-load was applied with the maximum calibration force of 35 N.

2. Measuring the response two times, with increasing load steps - the force balance was loaded to the maximum calibration force with increasing loads in 8 - 10 steps. After unloading, this procedure was repeated for the same mounting position.

3. Measuring the response at varying mounting positions - the sensor (force balance on the sting) was dismounted, rotated by 120°, and repositioned in the testing machine. Steps 1 and 2 were then repeated. The sensor was rotated another 120° and Steps 1-2 were repeated.

Fig. 57 shows the calibration curve for the force balance. Error bars present on the load are due to the uncertainty caused by very slight fluctuations in the reported force values. The calibration curve confirms that the sting responds linearly to compression loading, or equivalently drag force. Both the measured and actual loading at 0 mm reflected 0 N, indicating zero offset interference from the sting during the compression test.

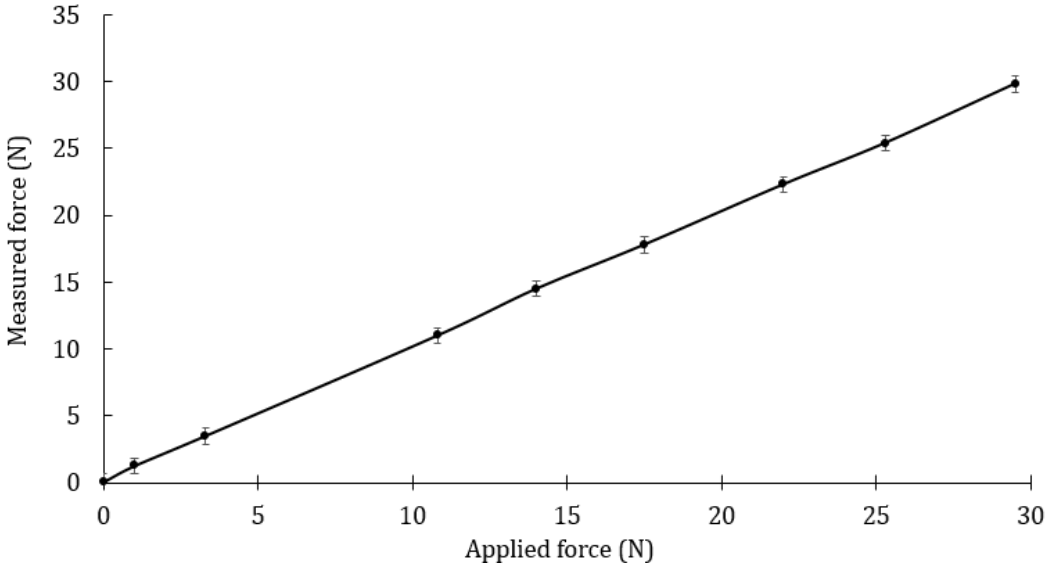

Figure 57: Calibration curve of the force balance

A linear curve fit was applied to the calibration data in Fig. 57. From the slope of the calibration curve, the calibration factor was 1.004 ≈ 1. A calibration factor of 1 indicates a direct linear relationship between the load output of the measurement device and the actual load measurement. This confirms that the force balance is accurately calibrated, providing

readings that directly reflect the true value of the compressive load quantity being measured. It is also implied that the force balance introduces no systematic errors or biases and that the output values may be used with confidence and without further correction. It must be noted that the force balance was calibrated in a zero-interference testing environment, free of external signal noise.

As Fig. 57 illustrates, very little error existed between the measured data and the calibration curve. The correlation coefficient between the data sets was 0.98. The combined analyses confirmed that the force balance measured correct, reliable values and that it could be used in the experimental SSWT tests with confidence.

6.2.2 Data collection

The force balance was wired to a separate DAQ for strain gauge data collection. A Hantek 6022BL 48 MSa/s 16CH PC USB Digital Storage Oscilloscope (DAQ) was used for this purpose. The bending strain, axial strain in direction 1 (normal, upper sting surface) and axial strain in direction 2 (perpendicular, lower surface) were each measured on individual channels to ensure no signal crossover. The combined axial strain was of interest as this measured the force on the cone in the free stream direction during a test. The strain was recorded in μ m/m. All strains were measured and plotted over time (s).

The data from the drag DAQ was collected using the HBM Catman Data Acquisition Software (Catman Easy/AP. Version 5.0.1). The software began recording data just before the tunnel was started and was manually terminated once the test was over. This ensured that the complete data set was captured during a test.

A minimum sampling rate according to the Nyquist Criteria was used Smith (2003). The signal period for the experiments was 0.05 s for a frequency of 20 Hz, the same as the shutter speed of the camera used for the schlieren photography. These settings were successfully used in many other high speed research projects at WITS for adequately capturing the experimental data. The correct sampling rate of the electronic signal was required in order to accurately determine the inertia terms, such that the true aerodynamic signal may be

read. The sampling theorem states that a continuous signal may be correctly sampled if the following expression is met (Smith (2003)):

$$Sampling\ Frequency > 2 \times Frequency\ Signal \tag{2}$$

The relationship above states that, for a frequency signal of 20 Hz, a sample rate greater than 40 Hz is enough for the application. The number of usable data samples obtained during the relevant 2 s of test time (at the given frequency signal) was 40, and thus the Nyquist condition held and the sample rate used was sufficient. Thus, the sample rate of the processed data set was 40 samples/second. The required data was sufficiently captured without signal mixing and aliasing. Some of the random signal origination in the acquisition system (such as vibration from external equipment) could not be ignored by the system and had to be filtered manually, however, the overall gathered data was acceptable.

The sensitivity of the drag DAQ was noted, as it described the smallest absolute amount of change that could be detected by measurement. According to the specification sheet of the drag DAQ, the input sensitivity of the unit was 10 mV/div $\sim$ 5 V/div. The smallest voltage measured during a 3 s Mach 3.5 test was 0.01003 mV. As such, the measured data fitted within the range of the smallest voltage change that could be detected by the DAQ, indicating that the DAQ used was capable of measuring the values in the correct voltage range. The DC accuracy of the drag DAQ was $\pm 3\%$, which is the widely accepted standard for most oscilloscopes (Tucker (2000)). The combined effect of these factors was that the drag DAQ measured the wind tunnel strain data within the correct range, to a high degree of sensitivity and accuracy. As such the data emanating from these measurements was deemed to be largely reliable and comparable to the numerical scheme with uncertainty taken into account.

The raw data was exported to Microsoft Excel and processed to determine the drag force. This was achieved using the Stress and Strain Equations (3) and (4), as well as the conic model frontal area and Young's Modulus of Bright Steel (ASM (1990)).

$$\sigma = \frac{F}{A} \tag{3}$$

$$\sigma = \epsilon \times E \tag{4}$$

6.3 Experimental Results

Fig. 58 demonstrates the typical raw SSWT experimental drag data obtained from a 6 second, Mach 3.5 test. The BS0 pointed cone validation case data is presented here. The primary axis and the filtered strain data (achieved using the above methods) for each direction (bending, axial ±) (μ/m) over time (s). The secondary axis and the linear curve fitted calibrated drag coefficient (C_d), over the 2 s steady-flow period of the SSWT test (6 - 8 s).

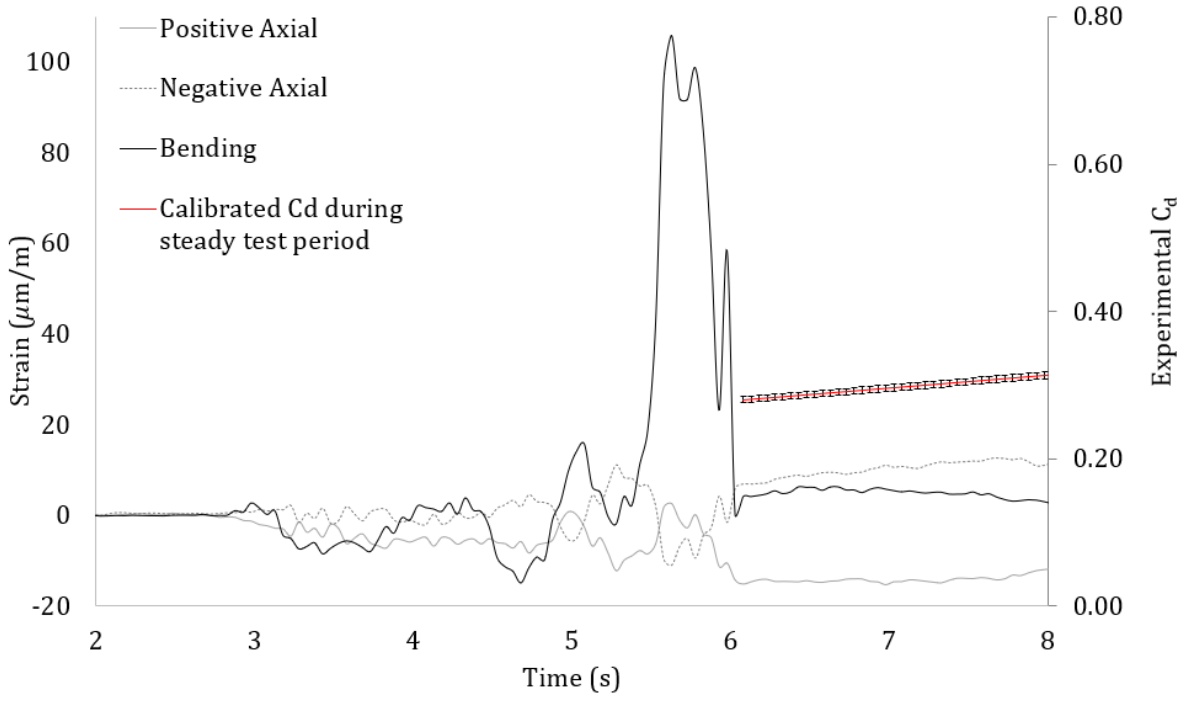

Figure 58: Bending and ±axial strain (μ/m), and calibrated drag coefficient (C_d) curve fit, during the 6 s Mach 3.5 SSWT test on the BS0 cone

The tunnel was non-operational from 0 - 3 s. After starting, the flow in the test section was unstable between 3 - 5.5 s, indicated by the fluctuating signal readings during this period. At 5.5 s, the tunnel startup shock passed over the conic model, visible as the large spike

in bending strain in Fig. 58. Thereafter the flow in the test section was steady-supersonic between 6 - 8 s. During this time an oblique shock wave was generated on the conic model, resulting in the larger, steady ± axial strain readings shown in the plot. The axial strain readings measured the change in aerodynamic forces caused by the conical shock wave. Only during this time was the true steady-state drag force acting, and as such only this period was of interest for the study. After 8 s, the test ended and data capturing was terminated. The non-operational tunnel and bending data were ignored.

The SSWT strain data was processed to obtain the resultant experimental drag coefficient of the conic models, which were later compared to the numerical drag coefficient data. The procedure used to obtain the experimental C_d is as follows:

1. Raw voltage strain was converted to useable strain.
2. ± Axial stress was determined using usable strain and sting CSA (where the gauges were located).
3. ± Axial force calculated using the ± axial stress and the conic model CSA.
4. Resultant drag force (N) on cone determined by summing the ± axial force components.
5. C_d obtained - using resultant drag force in the standard drag force equation, for the described free stream conditions.

6.3.1 Uncertainty

Several factors influenced the error and uncertainty present in this data set, including the calibration of the measurement instruments, laboratory/environmental conditions (appearing as assorted sources of signal noise), and the measurement of readings (e.g. resolution). Here, the signal noise was filtered and removed from the experimental data, as discussed below.

- **Measurement uncertainty**

In the following sections, only the steady drag data between 6 s - 8 s was considered. During this time, the C_d fluctuated slightly but was steady overall. A linear curve fit was applied to

the data, as shown in Fig. 58. A statistical uncertainty analysis was required to evaluate the uncertainty and error present in the SSWT experimentation and force balance measurements, respectively. The experimental drag could then be compared with confidence to the CFD coefficients for validation purposes.

The uncertainty analysis was performed on the raw C_d data (obtained using the above method) for the Mach 3.5 BS0 and solid cone validation cases. This ensured that the sampling rate adequately captured the voltage signal from the force balance. Based on standard statistical evaluation methods (assuming a normal data distribution, Morris (2011)), the uncertainty limits within the 95% confidence interval (4 standard deviations) were determined for each load measurement taken in the steady period.

The standard deviation of the steady drag sample was calculated using the mean drag coefficient, sample size, and each drag coefficient value in the sample. The standard deviation for this data set was low (0.019 for BS0), suggesting the model predictions were accurate and had low variability and uncertainty by tending to be closer to the mean.

The uncertainty in the data was determined by dividing the standard deviation with the square root of the sample size, expressed as a $\pm$ value after the mean experimental C_d. This represented the true experimental C_d for the validation cases at Mach 3.5, which were directly compared to the numerical drag coefficient (taken as the converged simulation value). The error in the data was calculated using $Z = 1.95$, inferring that there was a 95% probability that the true value fell within the defined range. The error was determined by multiplying the Z-value with the uncertainty value. This is expressed as error bars in Fig. 58.

- **Noise and offset uncertainty**

Assorted noise from several possible sources was identified in the raw experimental strain data. It was impossible to isolate and quantify the effects of each vibrational signal. Possible sources included the neighbouring CNC machine, electromagnetic interference, the operation of the tunnel and other stress waves etc. The assorted noise was combined into a single signal, hereafter referred to as 'signal noise'. The signal noise propagated through the drag data as uncertainty. An uncertainty analysis (E) was performed to consider the systematic error in

the wind tunnel experiment, to account for the effect of any confounding signal noise. The initial data was referred to as zero readings in order to estimate the offset error (± shift of the data) and frequency spectrum of the signal noise so that it could be filtered and removed.

The average frequency amplitude was low in comparison to the testing strain (0.28 μm/m for a maximum strain of 105 μm/m), where an error of ±5% was estimated. The signal noise error was acceptably low, and existed within the bounds of the 95% confidence interval used. The low uncertainty indicated that the signal noise had a limited effect on the outcome of the final drag result. The signal noise was thus filtered from the raw drag data.

- **Resolution**

The resolution of the measurement system was assessed to ensure that the measurement system was capable of obtaining reliable data to a high degree of precision. A Hantek 6022BL 48 MSa/s 16CH PC USB Digital Storage Oscilloscope (DAQ) was used for data acquisition. The DAQ measurement range was ± 5.5 V (full scale = 10 V), and the resolution of the card was 8 bits (nominal resolution assuming 5% over range = 160 μV, or in the order of 10^{-5}). The force loads in the sting calibration were fairly low (< 3.56 kg due to the model size).

In this research, the solid model drag coefficients ranged from 0.29 - 0.91. This drag coefficient range was confirmed and validated by comparing to Wendt (1972), who investigated the drag coefficients of many 3D cone geometries in supersonic flow. Applying the standard drag equation to the solid drag coefficients, the anticipated load range for the solid cones was calculated to be 18.2 N - 35.7 N. This corresponded with the drag force order of magnitude presented by Wendt (1972). While the work of Wendt (1972) used a much higher Mach number and lower densities, the drag is dominated by the bow wave, making it comparable with this research.

The above procedure was repeated twice, and the same result was obtained. By achieving a close result under unchanging experimental conditions, the measured data was confirmed as having a high degree of precision. The DAQ was confirmed to measure the loads accurately, where the measured value was close to the accepted value (as discussed below). The standard deviation of the data set was 0.019 for BS0, indicating that the force measurements had a

good degree of precision. Combining the above parameters and uncertainty analysis, the experimental drag force on the solid and BS0 cone validation cases was calculated as 18.21 ± 0.0044 N and 17.43 ± 0.0041 N, respectively, or within the expected range and bounds predicted by the literature. It was concluded that the resolution order of magnitude fits within the guidelines provided by Yen and Brauchle (2000).

- **Final experimental C_d with error and uncertainty**

The above uncertainties were combined to obtain a final experimental drag coefficient value for each validation case in Table 6. Table 6 compares the statistical parameters (standard deviation (σ), error (ε), uncertainty and Z-value) for the validation cases (solid pointed cone and BS0 at Mach 3.5). The numerical and experimental drag coefficients, and percentage differences between them, are also shown. The standard deviation and error are similar for both cases, indicating consistency in the statistical analysis of the results. The error also falls far below the 8% margin of error at the 95% confidence level, which is acceptable (Yen and Brauchle (2000)).

Table 6: Experimental and numerical drag coefficient statistical uncertainty (BS0 and solid cone, Mach 3.5), for CI = 95%

		Cone type	
Statistical data	Confidence interval = 95%; Z = 1.96	Solid	BS0 (BS0, 90°)
	Standard deviation (σ)	0.019	0.023
	Error (ε)	±0.60%	±0.64%
C_d	CFD	0.29	0.28
	SSWT	0.29 ± 0.0042	0.28 ± 0.0050
	Percentage difference (CFD and SSWT)	1.46%	1.76%

The experimental uncertainty of 0.42% (solid) and 0.50% (BS0) is less than 1% of the measured value, indicating that the SSWT drag measurement is precise and has high accuracy. The percentage difference between the CFD and SSWT drag was calculated using the CFD value as the reference (primary), and the upper and lower bound of the SSWT value as the secondary. Precise values (such as those referenced here) signify that repeated measurements of the data give a similar result or high repeatability. The percentage difference between the

SSWT and CFD drag coefficient is also well within 5%, which is an acceptable margin (Celik (2008)).

6.3.2 Discussion

Table 7 shows the experimental drag results for the solid, BS0 and Longitudinal Vented (LV) shapes at Mach 3.5, with the error and uncertainty accounted for. Note that LV had the porous configuration as BS0, only with no toroids present. The percentage differences between the CFD and WT drag were calculated using the CFD value as the primary, and the WT value as the secondary using the standard percentage difference formula. During experimentation, the models were tested in sets, i.e. each shape family was tested on the same day for the specific Mach number, followed by all the variations of the hemisphere family the next day etc. This was done so that the testing conditions and the sting quality were kept as consistent as possible across sets for comparison purposes. The

Table 7: Experimental (WT) and numerical (CFD) drag coefficient results for the zeroth vented conic models, tested as sets. The percentage difference between the numerical and experimental data sets is shown.

		Mach 3.5	CFD C_d	WT C_d	% diff CFD & WT
1^{st} test set	Cone	Solid	0.29	0.295 ± 0.0031	1.70 %
		BS0	0.28	0.286 ± 0.0037	2.12 %
		LV	0.31	0.32	3.17 %
2^{nd} test set	Hemisphere	Solid	0.45	0.38	16.34 %
		BS0	0.68	0.60	12.50 %
		LV	0.68	0.57	17.6 % %
3^{rd} test set	Ellipse	Solid	0.45	0.33	30.76 %
		LV	0.45	0.38	16.86 %
		BS0	0.45	0.31	36.84 %
4^{th} test set	Secant Ogive	Solid	0.50	0.26	63.10 %
		BS0	0.54	0.27	66.66 %
		LV	0.57	0.29	65.11 %

The same force balance was used for all of the experimental models, however the force measurements became increasingly inaccurate across shape families as testing continued. This was due to the strain gauge wiring becoming damaged over time, eventually failing with the secant ogive set. The gradual diverging of the experimental drag data is evident in the percentage differences in Table 7. Only the first set tested (the pointed cone) provided usable

drag data, as after this set the percentage differences between the predicted CFD and measured experimental values were unacceptably large. The remaining experimental drag data was ignored. The effects described were cumulative, meaning that with each test, the data was increasingly affected. The degradation of the force balance is summarised:

- 1^{st} set - Error across the set is low and similar. True measured results.
- 2^{nd} set - Error across the set is larger and fluctuating. $10\% < \text{Error} < 20\%$ - unacceptably high.
- 3^{rd} set - Error across the set is larger and fluctuating. $16\% < \text{Error} < 30\%$ - unacceptably high, divergence begins.
- 4^{th} set - Force balance failure. $\text{Error} > 60\%$ with significant inconsistencies. Failure due to wires under the protective covering becoming damaged due to exposure to strong forces present in the tunnel. Strain gauges no longer report correct measurements.

Due to the damaged equipment, no further tests were conducted with force balance after the secant ogive set. The uncertainty and error analyses were therefore only performed on the conic validation set as these were the only models to provide meaningful information regarding drag performance. The force balance successfully measured the drag of the first set to a high degree of accuracy, as discussed. The ellipse, hemisphere and secant ogive experimental drag data was thus null. Recommendations for an improved drag monitoring system will be given in Section 8.9. The high quality of the pointed cone drag data meant it could sufficiently be used to validate and verify the numerical method when combined with the flow visualisation data captured during testing.

In addition to the experimental drag data, the flow visualisation data captured in the experimental tests (as described in Section 4.5) provided useful information regarding the external flow field and flow interactions. This was achieved using a schlieren optical arrangement. Schlieren photographic data was gathered for all of the test sets and models to aid in visual validation of the CFD model. Whilst only a single set of experimental drag data was usable, high-quality schlieren images were obtained for all of the experimental cones tested. When the external flow field of the experimental schlieren images was compared to the CFD Mach

number plots, a high degree of similarity in the flow features existed, including Mach angle, expansion wave and shock pattern behaviour. The visualisation of these flow features aided in corroborating the measured drag data by describing the physical phenomenon occurring in the system.

The combined numerical and experimental drag data (both visual and measured) enabled for validation and verification of the research method. The experimental and numerical drag coefficient of the pointed cone data set showed a very close correlation ($< 1\%$ difference with $< 1\%$ error and uncertainty), indicating that the numerical and experimental methods sufficiently matched to produce accurate drag results which could be used with confidence.

6.4 Experimental Drag - Literature Comparison

6.4.1 External flow - literature comparison

It is critical to note that across all of the literature mentioned here, the numerical and experimental photographs/images were found to be approximately identical to each other in flow pattern, flow distribution, shock shape and other features. Upon comparing the visual results of the literature and presented research, these same flow phenomena were found to exist in the presented research (both numerically and experimentally). The description of the optical setup may be found in Section 4.5.

Fig. 59 depicts the annotated solid and porous cylinder results from Poplavskaya et al. (2017) at Mach 4.85. As shown, the complementary solid shock angle is greater than the porous model, i.e. 180° - $\beta_{2,s}$ > 180° - $\beta_{2,p}$.

To compare the key visual flow parameters present in the literature with that of the current work at Mach 3.5, Fig. 60 is presented. $L/D = 1.5$ and cone angle $\theta = 18.43°$. The change in complementary shock angle due to the addition of pores is clear, i.e. 180° - $\beta_{1,s}$ > 180° - $\beta_{1,p}$, the same change present in the literature.

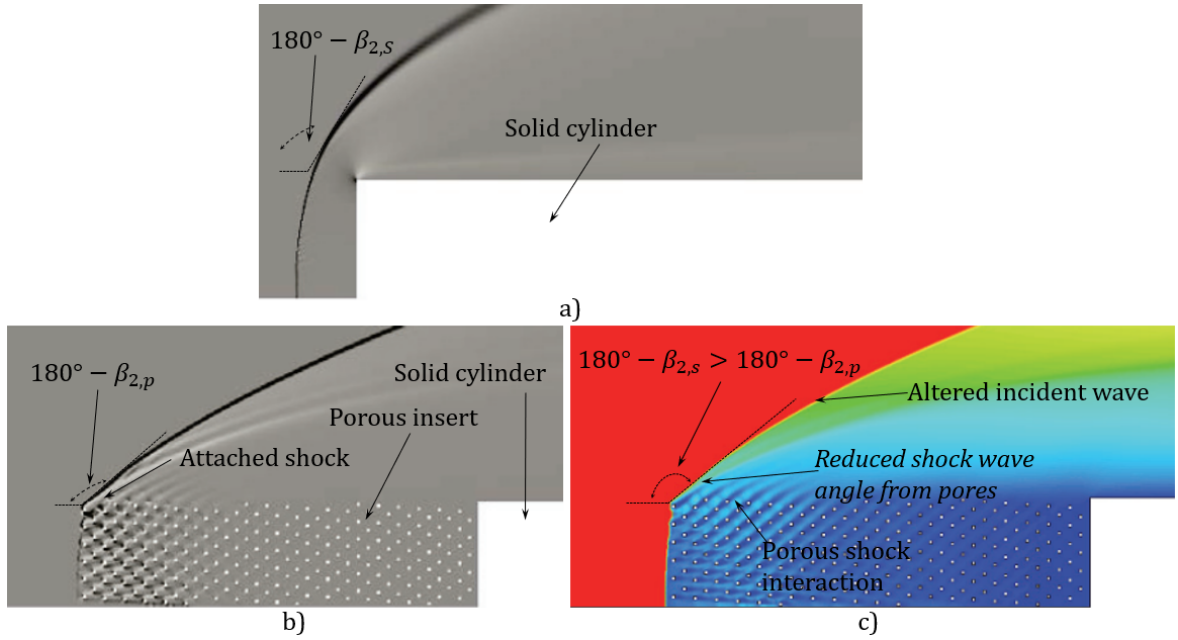

Figure 59: Poplavskaya et al. (2017), Mach 4.85, $L/D = 1.9$. a) Solid cylinder schlieren, 180° - $\beta_{2,s}$. b) Porous-insert cylinder schlieren. c) Porous-insert cylinder computed Mach isolines, 180° - $\beta_{2,s}$ > 180° - $\beta_{2,p}$. All images numerical.

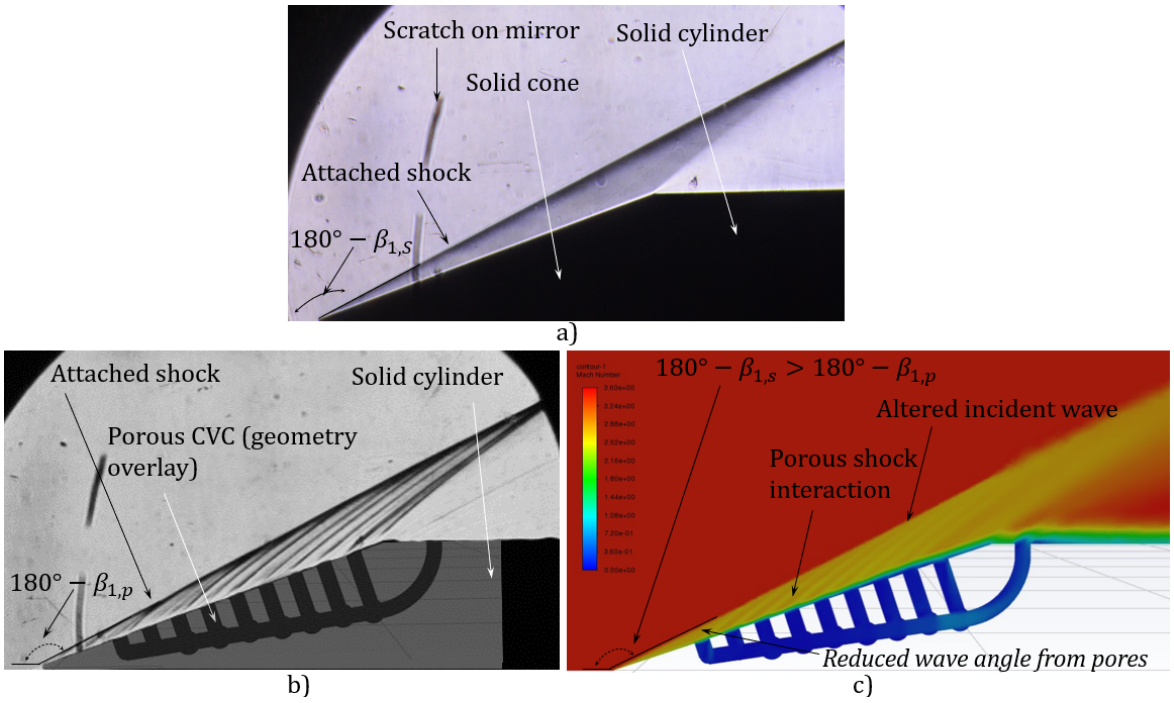

Figure 60: Mach 3.5, $L/D = 1.5$, cone angle $\theta = 18.43°$ a) Solid cone schlieren, 180° - $\beta_{1,s}$, BS0: b) schlieren with porous geometry overlay, c) Flooded Mach contour plot, 180° - $\beta_{1,s}$ > 180° - $\beta_{1,p}$.

Even though the model shape is different (cylindrical in Figure 59 and conic as presented), similarities and differences are observed by comparing Figure 59 and Figure 60. In Figure 59 a) and Figure 60 a), the schlieren bow wave of each solid shape is visible.

In both Figures b), the numerical schlieren image of the porous shape for each case is visible. In Figure 59 b) the detached bow wave has been transformed into an attached wave on the cylinder surface due to the presence of the pores. In Figure 59 b) the attached bow wave has been transformed into weaker wave due to the pores, with the pore interaction pattern visible within the shock. In both cases, the reduction in complementary shock angle when compared to the solid is visible.

Due to the internal geometry not being visible in the schlieren images, in Figure 60 b) an image of the porous BS0 geometry is overlaid over the corresponding schlieren image. This enables the external flow field to be considered more comprehensively by confirming the visual similarities present between the CFD images. The scratch on the SSWT parabolic mirror is visible in Figure 60 a) and b).

Figure 59 c) and Figure 60 c) depict the numerical isolines for each case. Again, the reduction in bow wave strength is clear, where behind both bow waves the post-shock velocity has increased and the overall wave shape reduced. The solid cone and cylinder generate an attached and detached (bow) shock wave, respectively. Whilst the presented work and literature present different incident wave formations, the porous shapes show considerable similarities with regards to: reduction in complementary shock angle, reduction in wave shape/size, porous interaction pattern and reduced bow wave strength.

In Figure 60 b), the porous shock interaction pattern in the BS0 shock wave is visible when compared to the solid cone in a). Comparing a) and c), the complementary shock angle $180° - \beta_{1,s} > 180° - \beta_{1,p}$, where the presence of the BS0 pores weakens the incident shock wave, thereby reducing the wave angle. Comparing the schlieren BS0 image in b) to the computational BS0 Mach plot in c), the shock patterns within the oblique shock wave closely correlated. In both data sets, nine weak oblique waves are generated off of the nine surface pores at the same reflected angle and separation distance. Some weaker shock features in b) are not visible in c) due to the schlieren images capturing limited three-dimensional effects and interactions that the CFD symmetry plane did not.

The wave angle in Figure 60 b) and c) is also the same, indicating that the strength of the wave reduction is identical and thus so is the shock drag reduction. The expansion fan

generated at the cone-cylinder shoulder is visible in both the numerical and experimental BS0 images Figure 60 b) and c), where the expansion wave angle also matches. Only a finite amount of the jetting behaviour from the venting pore is visible in b) and c), as the schlieren optics required greater sensitivity to visualise this completely. While the internal porous flow was hidden in the schlieren photographs, b) and c) demonstrate that the external flow of the numerical and experimental models closely matches in terms of flow features and interactions, which describe the flow phenomenon and physics present in the fluid system.

Similarly, the literature also shows strong correspondence in the flow features between the numerical and experimental image results, shown in Fig. 59 b) and c) (from Poplavskaya et al. (2017)). When comparing the Mach plot of the BS0 and the isolines of the porous-insert cylinder, the same reduction in incident wave angle due to the porosity is observed. The incident shock porous pattern is visible in both Figures c), closely resembling the porous insert structure - correspondence the BS0 a)-c) comparison. The incident shock wave in Fig. 59 a) is also weakened by the presence of the pores (shown in c)), where the shock angle of the porous-insert cylinder is lower than the solid cylinder. This matches the BS0 case, where both incident shock waves are visibly altered by the porosity. The literature shows a very strong similarity between the numerical and experimental images in terms of the flow features visibly matching. The presented research also does this, as demonstrated by comparing (b-c) for both Figures.

In summary, the overall visual comparison of the solid cone and porous BS0 in both experimental versus numerical *and* solid versus porous strongly aligns with the same comparison applied to the literature porous-insert cylinder. The strong similarity of the presented data to the literature assists in validating both the experimental and numerical methods. By achieving a similar result from both the experimental and numerical results, as well as a similar result to the literature, it is confirmed that the design and research method behaves in the same way as the literature and that a similar drag result can be expected. Thus, the presented measurements and data may both be stated as correct and the numerical method may be used for further investigations into the physical phenomenon of interest with confidence and reliability.

6.4.2 Drag coefficient coherence- SSWT vs CFD

At Mach 3.5, the difference between the measured experimental and numerical drag coefficients was approximately 1.7 % - 2.23 %. This difference is attributed to the experiments considering several factors which are absent in the numerical model. These included the effect of strain gauge placement, the wire covering and wire conditions, the effect of model vibration on the flow field and the cumulative effect of the tunnel conditions on the force balance. Additionally, the flexibility of the sting meant that the model was not always exactly aligned with the flow. The effect of these factors was limited, and a close result was achieved between the two approaches. According to the literature (Ntantis et al. (2023), Van Dyke and Widnall (1983), Wessam and Z. H. Chen (2015)), CFD results within 5% of SSWT results are considered acceptable by most standards for supersonic drag.

6.4.3 Experimental C_d - literature comparison

To further validate the accuracy of the drag results, a comprehensive literature comparison was conducted on the CFD solutions and the experimental drag coefficients and schlieren and shadowgraph from similar studies. Specifically, the combined studies of Mironov, Kirilovskiy et al. (2019), Valiullin et al. (2023) and Mironov, Maslov et al. (2015), as in the literature review, were interrogated. These studies employed the same or similar experimental test pieces across their mentioned works, and so the results are broadly discussed.

Poplavskaya et al. (2017) calculated the drag coefficient C_x of a solid cylinder with a porous frontal insert normalised to the drag coefficient of the solid cylinder C_{x0}, resulting in the C_x/C_{x0} term (the ratio of porous to solid drag coefficient of the particular shape). The experimental and numerical C_x/C_{x0} data was plotted against the porous insert length $\Delta x/D$ (with error bars) in Fig. 61. C_x and C_{x0} will be used to denote the literature data while C_d is used for the presented data. They are, however, directly comparable as an estimate of the dimensionless drag of the respective models.

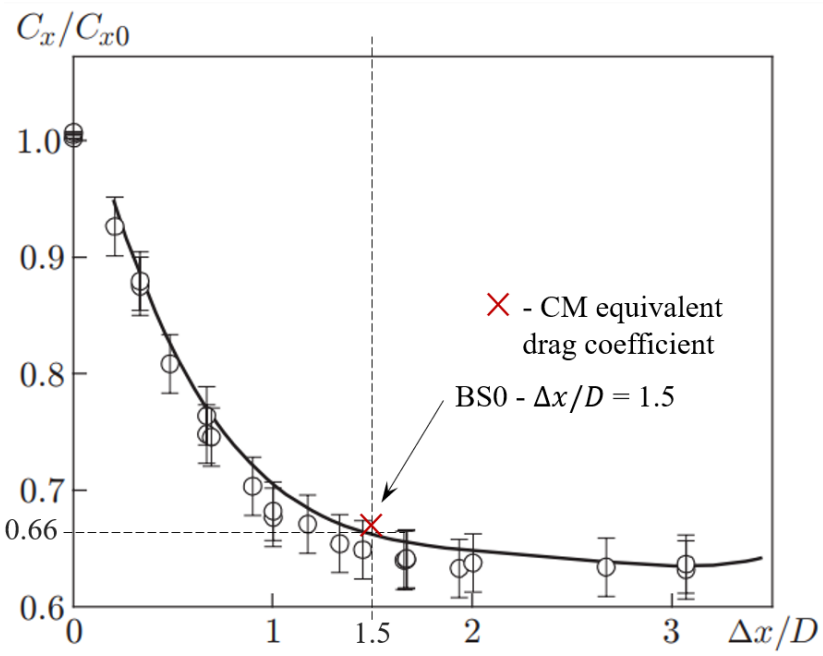

Figure 61: Experimental (points) and numerical (curve) dependences of the drag force of the porous model versus porous insert length ($\Delta x/D$) (Mironov, Maslov et al. (2015)).

The net porosity of the literature and cunicular model was 95% and 60% respectively (for the validation case). Net porosity was used as the factor for comparison since an attached bow was was generated on both the porous literature and cunicular models even though the shapes differed. Because of this, and the similarities of the testing conditions and model geometry, net porosity was the key factor to influence the flow field, and as such was of the greatest interest. In order to compare this research with the literature, the solid cone and BS0 drag coefficients were normalised (using standard statistical min-max scaling methods) to determine $(C_x/C_{x0})_{CM,60\%}$[ii] for the 60% porous BS0. $(C_x/C_{x0})_{CM,60\%} = 0.42$ for the 60% porous BS0 model. Using Fig. 61, the normalised C_d for the 95% porous literature body was found, $(C_x/C_{x0})_{CM,95\%} = 0.66$ at $\Delta x/D = 1.5$ (the BS0 ratio).

To compare the actual C_d for this research '$(C_x/C_{x0})_{CM,60\%}$' with that predicted by the literature '$(C_x/C_{x0})_{CM,95\%}$', ratios were used to convert the 60% porous coefficient '$(C_x/C_{x0})_{CM,60\%}$' to an equivalent 95% porosity coefficient.

[ii]CM - Cunicular Model. Refers to the normalised cunicular drag coefficients calculated from the validation-case BS0 drag coefficient

The equivalent presented $(C_x/C_{x0})_{CM,95\%} = 0.67$, and the literature $(C_x/C_{x0})_{CM,95\%} = 0.66$), for 1.5% difference. The equivalent $(C_x/C_{x0})_{CM,95\%}$ shown as the 'X' in Fig. 61. The value lies on the numerical literature trend line, within the error bars of the experimental literature data. The normalised cunicular method (CM) drag data closely correlates with the drag values presented in the literature for the same porosity and x/D, with low error percentages and uncertainty. Thus, the Poplavskaya et al. (2017) drag results validate the drag data presented in this research.

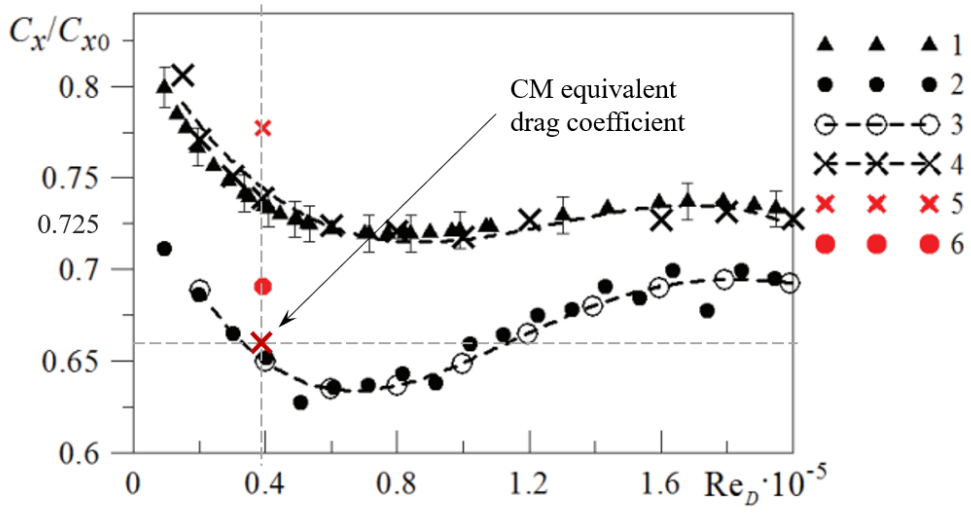

Figure 62: Experimental (1, 2) and numerical (3, 4) normalised drag coefficient (C_x/C_{x0}) of the Maslov porous cylinder versus Reynolds number: (1, 4, 5) - pore d = 1 mm; (2, 3, 6) - pore d = 3 mm; (4, 5, 6) - skeleton model; (1, 2, 3, 4) - Mach = 4.85; (5, 6) - Mach = 7; 3 - continuum model; x/D = 2 (Maslov et al. (2019)).

Fig. 62 illustrates the experimental (points) and numerical (curves) drag coefficient relationship for the same 95% porous cylinder as Poplavskaya et al. (2017), versus Reynolds number ($Re_D \times 10^{-5}$) (Mironov, Maslov et al. (2015)). In Fig. 62 two pore diameter sizes are illustrated, for $\Delta x/D = 2$. Following the same ratio method described above, the equivalent CM drag coefficient is plotted at $Re_D = 0.39 \times 10^{-5}$ (the Reynolds number for this research) on Fig. 62 (Mironov, Maslov et al. (2015) study graph). The CM coefficient closely matches the 3 mm porous diameter Maslov curve in Fig. 62. This is justifiable, as parts of the internal cunicular structure were greater than 2 mm, thereby increasing the average pore size of the body.

For the Mironov, Maslov et al. (2015) results, $(C_x/C_{x0})_{CM} = 0.66$, and $C_x/C_{x0} = 0.65$, or 1.5% difference between the values. Assuming similar error bars for both the 2 mm 3 mm curves, the CM coefficient lies within the error bounds of the literature data. A nearly identical drag result was observed between the Mironov, Maslov et al. (2015) and this research, further validating the research method. In both of the plots presented above, whilst the net porosities of this research and literature were different, the ratios describing the normalised drag relationships were the same across both data sets.

Maslov et al. (2019) emphasised the importance of comparing the flow visualisation of both the numerical and experimental studies. They further confirmed that scatter in the deviation was expected (similar to Fig. 61 and Fig. 62). They showed that the numerical and experimental normalised drag coefficient for a porous-insert cylinder, plotted against a similarity parameter (dependent on cylinder diameter, pore diameter and free stream Mach number), showed generalised straight-line dependence. Again, a deviation in the data of no more than ±5% from the computational line was exhibited in this study, indicating that the drag results of this study lie within an acceptable range (within ±1.5% deviation from the literature for the validation cone cases)

6.4.4 External flow - Numerical and Experimental Comparisons

From the above literature comparison, several visual flow parameters were identified which were found to govern the overall flow behaviour. These parameters all existed in the external flow field, as only this was visible in the experimental schlieren photographs. These governing parameters were present to varying degrees in all of the profile shapes investigated, and included:

- Bow wave shape (curvature, attached/detached).
- Bow wave angle.
- Porous interaction pattern near the cone surface.
- Separation distance (for detached shocks).

- Shoulder expansion wave location and behaviour.
- Venting flow behaviour (location, angle, shape and downstream condition).

In the following sections, the schlieren and CFD images of both the solid and porous combined vented (BS0, 90° exit vent) models for each of the conic profiles are presented. Within each set of data (solid and porous), the relevant governing parameters (as listed above) are identified and annotated on the images. The experimental and numerical images from each data set with relevance to their governing parameters are then compared.

By demonstrating that the key flow features show strong correspondence in the experimental and numerical images across the solid and porous models, the numerical approach is demonstrated to capture the primary flow field and thus the numerical results can be used with confidence to interrogate the flow field in greater detail.

The pointed cone and ellipsoid will be discussed in detail, and thereafter the secant ogive and hemisphere will be referred to broadly given the inherent similarities between the flow fields. In the following sections, the particular schlieren and CFD images for the solid shapes are compared, followed by the porous version of the shape. The images are all annotated to reflect the relevant governing flow parameters.

6.4.4.1 External flow - Right Triangular Cone

Figure 63 depicts the schlieren photograph of the solid pointed cone (left) compared with the CFD Mach contour plot (right). Comparing the two images, the external flow field demonstrates strong resemblance. The wave angles were measured manually using AutoCAD Inventor Professional: schlieren $\beta = 26.4°$, CFD $\beta = 26.3°$, and theoretical (Hinman (2024)) $\beta = 26.3°$. This represents an uncertainty limit of 0.34% of the theoretical wave angle, demonstrating that the three angles show good agreement across all of the methods. This same agreement across the theoretical, numerical and experimental shock angles was present across all of the remaining solid shapes.

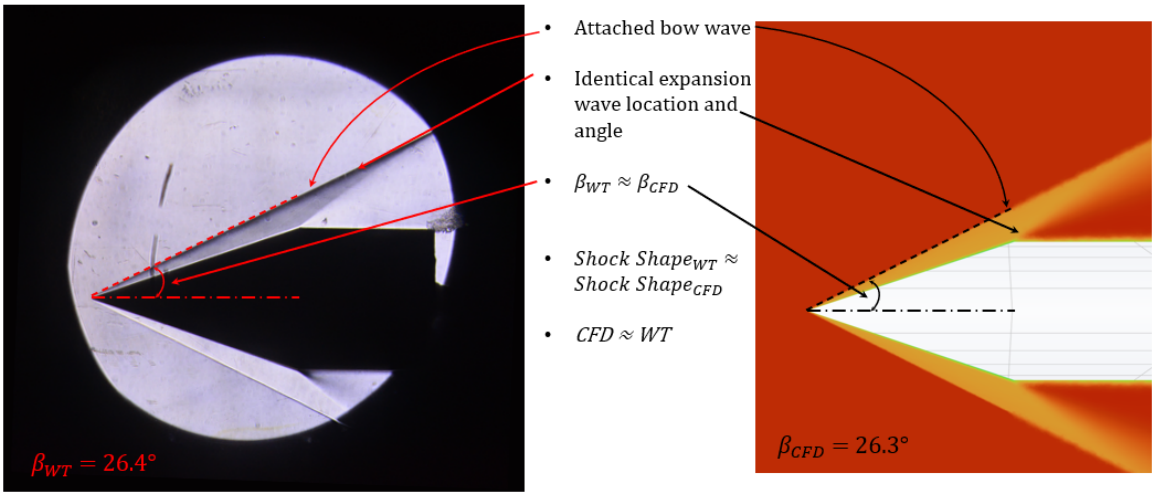

Figure 63: Annotated schlieren photograph (left), and CFD Mach contour plot (right) of solid pointed cone at Mach 3.5 (L/D = 1.5).

The straight shape of the wave and shock attachment location at the tip are also in good agreement between the two visuals, as well as the expansion fan location and angle. These key parameters (including bow shape, attachment type and shoulder expansion fan angle) are consistent among all of the other solid profiles, and as such are not mentioned again.

It can thus be said with confidence that the experimental and CFD results correspond. In this, the visual CFD and experimental results validate each other across the solid shape data set. Since the same experimental and numerical set-up and methodology were used across all of the conical models tested, strong agreement is present in all of the visual data.

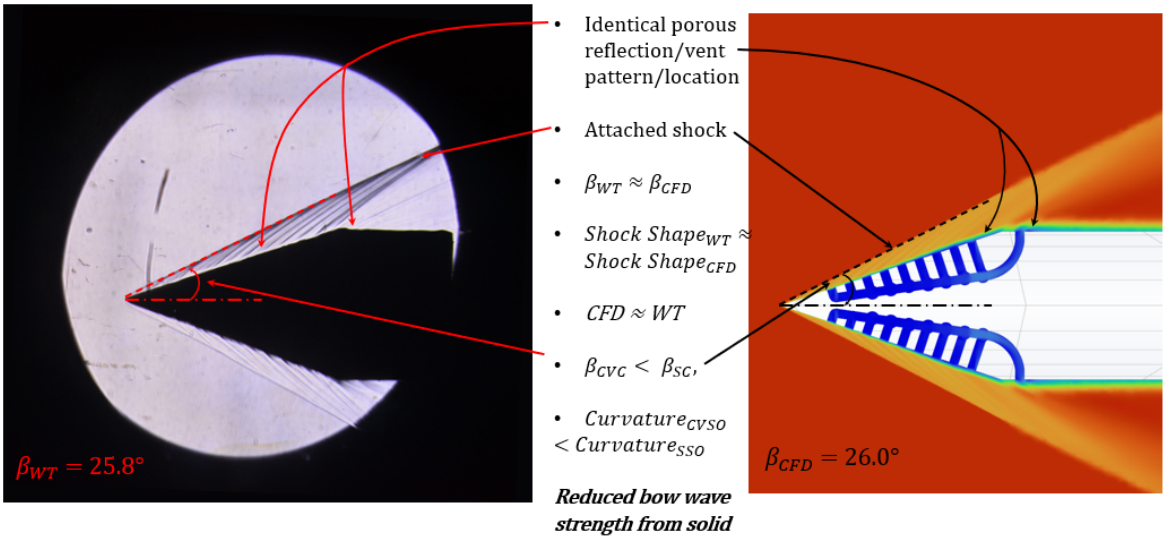

Figure 64: Annotated schlieren photograph (left), and CFD Mach contour plot (right) of BS0 pointed cone at Mach 3.5 (L/D = 1.5).

Figure 64 demonstrates the experimental and numerical BS0 porous cone images. The porous cones exhibit uniformity of the key parameters, with some meaningful additions. The BS0 cone has a reduced bow wave angle relative to the solid cone, and again the angle is essentially the same across the schlieren and CFD images ($\beta = 25.8°$ and $\beta = 26.0°$ respectively. The shape of the bow wave in both images is similarly changed, having higher curvature further downstream on account of the influence of the jet from the venting pore.

From Figure 64 and Figure 65, it is pertinent to note that the experimental images can be used with most confidence near the region around the centre of the image (near the origin of the plot), which is closest to the centre of the images. This is clear in the plot, where beyond 5 on the x-axis agreement gradually lessens. This is due to spherical aberration[iii]. A degree of spherical aberration is visible in all of the experimental images. This is on account of the parabolic mirrors and z-configuration of the schlieren system (Hosch and Walters (1977)). As the edge is approached, it also creates a slight warping around the edges of the schlieren images. Nevertheless, these differences are small, since the wave angles lie within the 95 % confidence interval error bounds and the visual similarity of the flow features is still maintained.

Both the experimental and numerical BS0 images in Figure 65 show an identical porous surface interaction pattern with regards to the number of shocks reflected off of the pores, the wave angle and general pattern. The same decrease in shock angle in bow wave angle is also visible in both images.

Correlation in the the external venting flow behavior is also present, as shown by both the location and shape of the weak flow features generated at the downstream edge of the 90° exit vent. The effect of the vertical exit vent jet is visible in both images as a bump in the bow wave. This bump increased the cross sectional area of the wave from this point, thereby increasing the wave drag over the cylinder portion of the body. These congruent venting characteristics and identical porous shock patterns were present in all of the 90° vented model shape images, and will not be mentioned again.

[iii] Spherical aberration is an optical phenomenon in which the outer region of a lens does not focus light rays to the same extent as the central region. Light rays passing through the lens nearer the centre are focused farther away than the rays passing through a circular zone near its edge (Britannica (2023)).

Comparison of the various bow wave shapes in isolation further validated the visual findings. Figure 65 shows the normalised shock angle plots for the solid cone (SC) and BS0 porous cone (BS0) for the numerical images (CFD) and experimental schlieren photographs (WT). The curve showing the calculated theoretical solid wave shape (Hinman (2024)) is also plotted. The graphical bow wave data was extracted from the each schlieren photograph and CFD image manually using ten points divided along the length of the cone in AutoCAD Inventor Professional software.

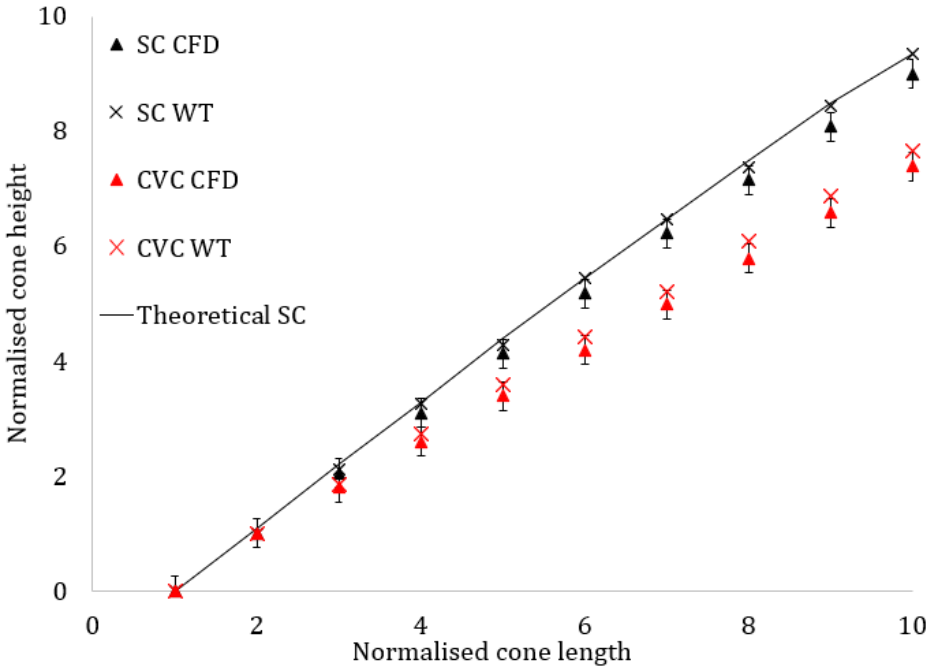

Figure 65: Plot of the shock angles for the WT, CFD and theoretical pointed cone at Mach 3.5 (L/D = 1.5).

There is very strong agreement between the experimental and numerical visual data for both the solid and porous cones with regards to the flow parameters which govern the flow field. The visible changes in the flow field, particularly the reduction in wave angle and change in shock shape pictorially confirm the reduction in bow wave strength. The reduction in wave angle for BS0 (as demonstrated by the change in the curve shape) in Figure 65 confirms that mass removal has occurred by addition of the pores to the solid cone. The correlation between the numerical and experimental plotted data shows that the numerical model correctly predicts the change in mass flow, asserting confidence in the numerical method and drag results.

The equivalent data for the ellipsoid, hemisphere and ogive corroborated this. The reduction in mass flow similarly occurred in the later numerical results, indicated again as a visible reduction in bow wave angle (notably the BS4 and BSOE cones). The reduction in wave angle and removal of mass signified a decrease in the bow wave energy and subsequently a reduction in wave drag by introduction of the pores. The bow wave strength directly correlates to the amount of wave drag acting on the body during flight. Thus, by proving through visual comparison that the addition of the pores has resulted in bow wave attenuation, it may be said that drag is also reduced in the same way.

It is relevant to mention the aspect ratio (AR) of both image sets. By comparing the AR of the images (in terms of pixel resolution) with the measured 'known' AR of the solid cones, an indication of the level of visual accuracy may be established. The actual cone AR (Length/Height) was 3. The AR of the solid cone schlieren image and CFD image (Number of length pixels/Number of height pixels) was 2.86 and 2.93, respectively. These values are acceptably close to the actual AR. The schlieren image difference is slightly greater due to the spherical aberration, where the image is distorted toward the outer edges. It may therefore be said that the geometry expressed in the experimental and numerical images is equivalent to the real-life geometry, and as such the results are comparable to each other and the theoretical calculations.

Figure 65 confirms the correlation between the experimental and numerical wave angle, as well as the reduction in angle due to the pores. The experimental shock angles could then be compared to the numerical angles with confidence for validation purposes.

The uncertainty analysis was performed on the raw shock angle β data for the solid validation case and BS0 pointed cones at Mach 3.5. In the images, the cone alone was considered, from tip to shoulder only. The cone length was then divided by ten, and the shock angle at each of the ten length increments was measured. The data in terms of cone geometry was normalised in order to allow only the change in shock angle to be observed. This measurement method allowed the shock angle to be comprehensively captured. A Gaussian distribution for small sample sizes was assumed (Morris (2011)), and the mean and standard deviation were calculated accordingly.

The uncertainty limits within the 95% confidence interval were determined for the angular measurements taken from each image. The theoretical shock angle was also determined (Hinman (2024)) and plotted on the same axes. The plot shows the strong agreement between all three data sets. The error is shown in Figure 65 as error bars, where the difference between the measured CFD and schlieren shock angles is minimal.

Figure 65 shows that the theoretical curve closely matches the shock angle obtained by the CFD. In this, the same result was obtained through the three separate methods (numerical, experimental and theoretical), and that these results are all comparable. This further validates the results of all three data sets, asserting that the visual data may be used with confidence to predict changes in the flow field and drag performance.

The analysis of Figures 63 and 64 show that visible changes to the flow field (by addition of the pores) can successfully indicate changes in wave drag by means of confirming bow wave attenuation (and to a lesser extent the effect of venting).

The method of analyses described above (including for β measurements, uncertainty, visual and AR comparison) were applied to the other shapes of interest, achieving equivalent, highly similar results across all of the cases as briefly mentioned below.

6.4.4.2 External flow - Secant Ogive

The secant ogive is referred to here broadly, as it is relatively similar to the pointed cone in terms of its flow behaviour. Figure 66 shows the agreement between the numerical and experimental solid images.

In Figure 67, the effect of the pores on the flow field is visible. There is a visible reduction in shock height and flattening of the bow wave due to the presence of the pores, and the bow shock remains attached. Both methods again show an identical shock interaction pattern at the porous surface, with the same weak compression wave generated at the vent exit edge. Additionally, similar downstream behaviour is visible in both, suggesting changes in boundary changes and turbulence. The visible reduction in bow wave size and angle indicates that the bow wave has been attenuated.

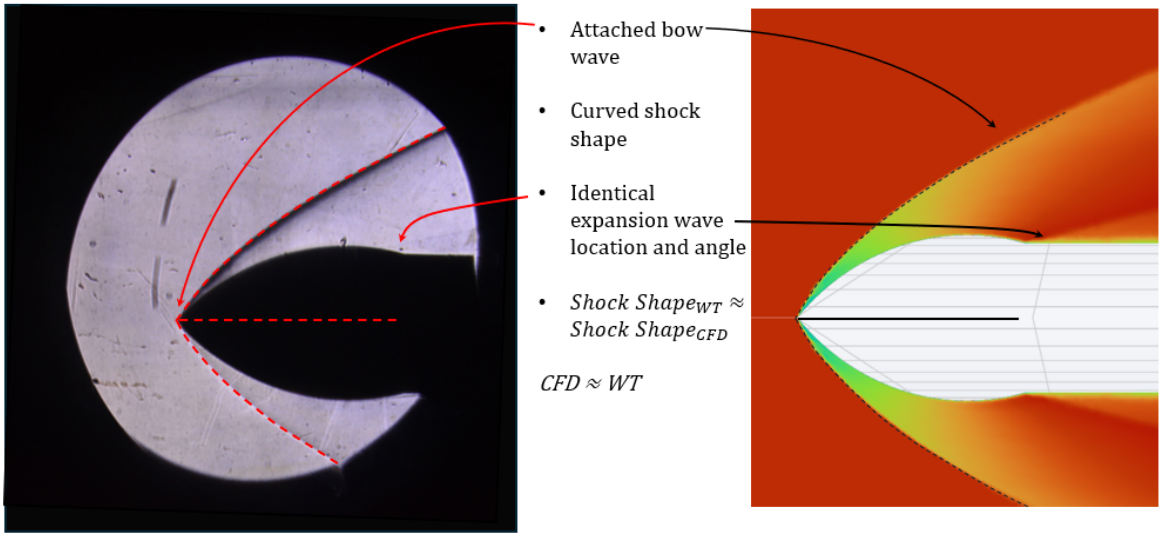

Figure 66: Annotated schlieren photograph (left), and CFD Mach contour plot (right) of solid SO at Mach 3.5.

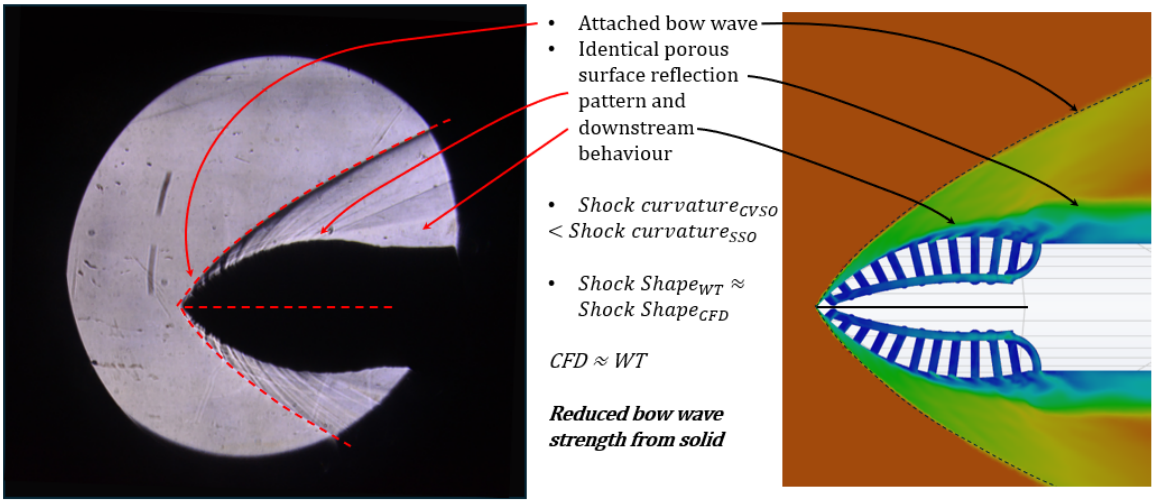

Figure 67: Annotated schlieren photograph (left), and CFD Mach contour plot (right) of BS0 SO at Mach 3.5.

As with the pointed cones, there is strong agreement between both sets of visual data. In this, conclusions may subsequently be drawn regarding the flow field. After comparing the solid and porous images, it may be said that the wave drag is reduced in the latter by means of bow wave attenuation, although only until the ogive shoulder. Beyond this point, the venting influence becomes significant, and this data is not available in the schlieren images.

Figure 68 shows the normalised shock angle plots for the solid secant ogive (SSO) and BS0 porous secant ogive (BS0 SO) for the numerical images (CFD) and experimental schlieren photographs (WT). The solid SO theoretical curve is also plotted.

As before, strong correlation is present between the numerical and experimental images when compared to the theoretical calculation. Here, both methods strongly validate one another. This is particularly useful for the secant ogive, as the experimental drag data for these models was unusable.

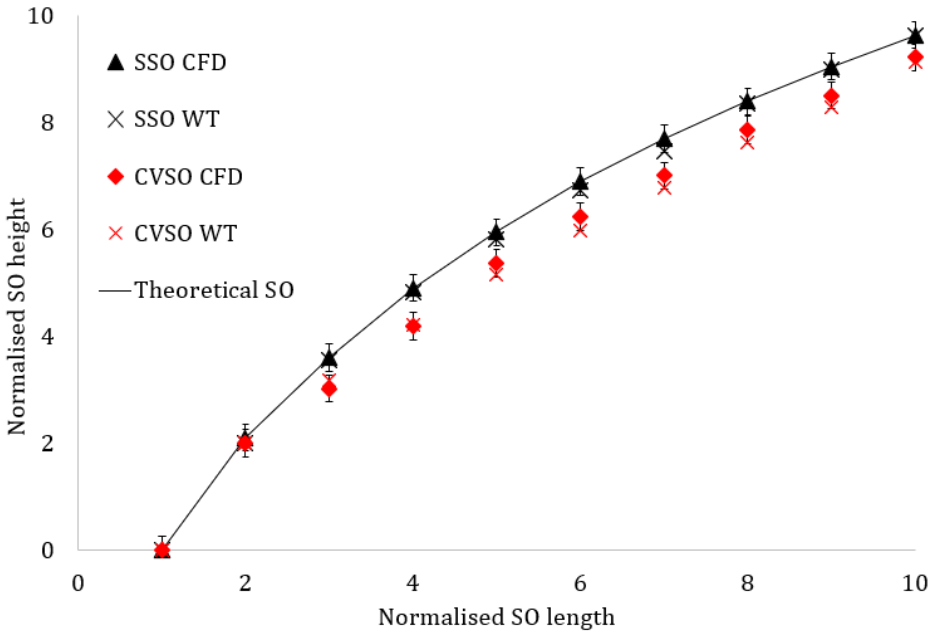

Figure 68: Plot of the shock angles for the WT, CFD and theoretical SO at Mach 3.5.

6.4.4.3 External flow - Ellipsoid

Figure 69 shows the CFD and schlieren comparisons for the solid ellipsoid, and Figure 70 the BS0 porous ellipsoid. Unlike the pointed cone and secant ogive, the ellipsoid generates a detached bow wave due to its blunt-nosed geometry. As before, there is strong agreement between the CFD and WT images regarding the governing flow parameters, including of bow wave shape and standoff distance $x_{standoff}$.

Figure 70 demonstrates the attenuating effect of the porosity on the detached bow wave, with strong visual coherence across the images. As before, the shape of the bow wave is altered by area reduction and by extension the weakening of the shock. Only the external flow field upstream of the vent is analysed due to the effects of venting not being adequately captured. The standoff distance in BS0 E was also increased, showing a reduction in wave drag by wave attenuation (Daso et al. (2009)). The WT and CFD porous standoff distances closely corresponded. This visual agreement again validates the use of both images for making

conclusions regarding the flow field, as well as validating both the numerical and experimental methods in conjunction with the theoretical curve.

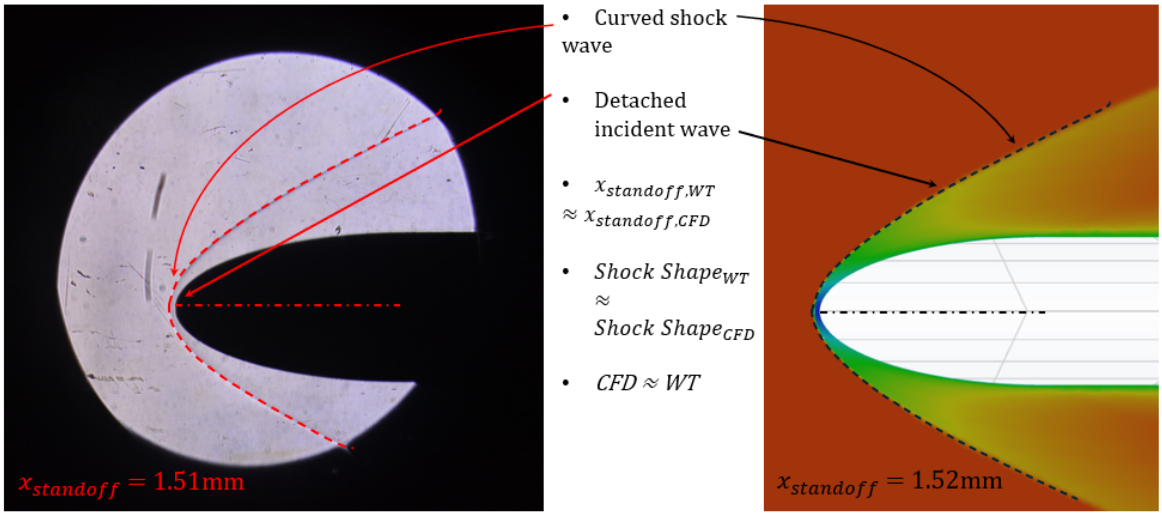

Figure 69: Annotated schlieren photograph (left), and CFD Mach contour plot (right) of solid ellipsoid at Mach 3.5.

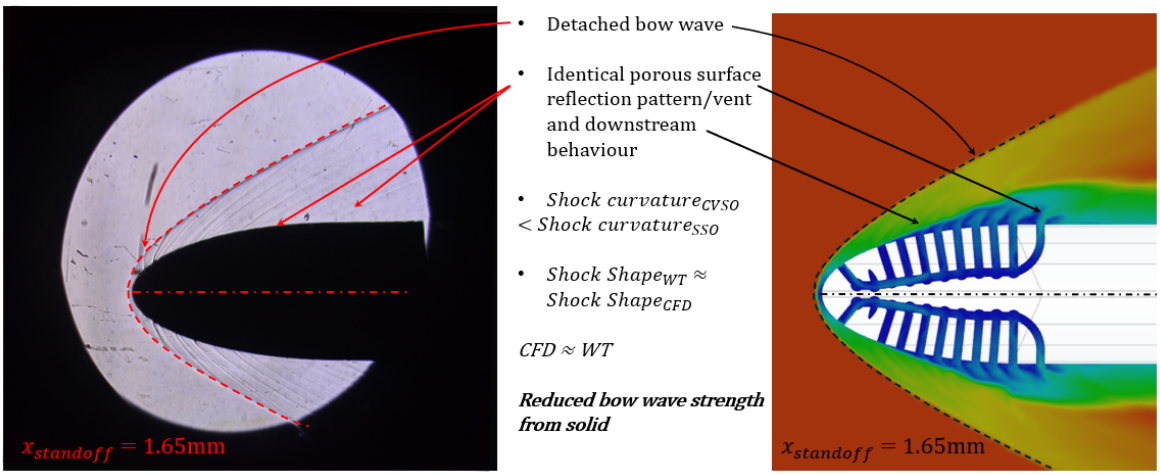

Figure 70: Annotated schlieren photograph (left), and CFD Mach contour plot (right) of BS0 ellipsoid at Mach 3.5.

Figure 71 shows the normalised shock angle plots for the solid ellipsoid (SE) and BS0 porous ellipsoid (BS0 E) for the numerical images and experimental photographs. There is good agreement with the graphical data and theoretical curves with regard to the previous shapes as well. This further demonstrates the congruence of all the experimental and numerical method, since similar results have been achieved across all of the shape and pore variations.

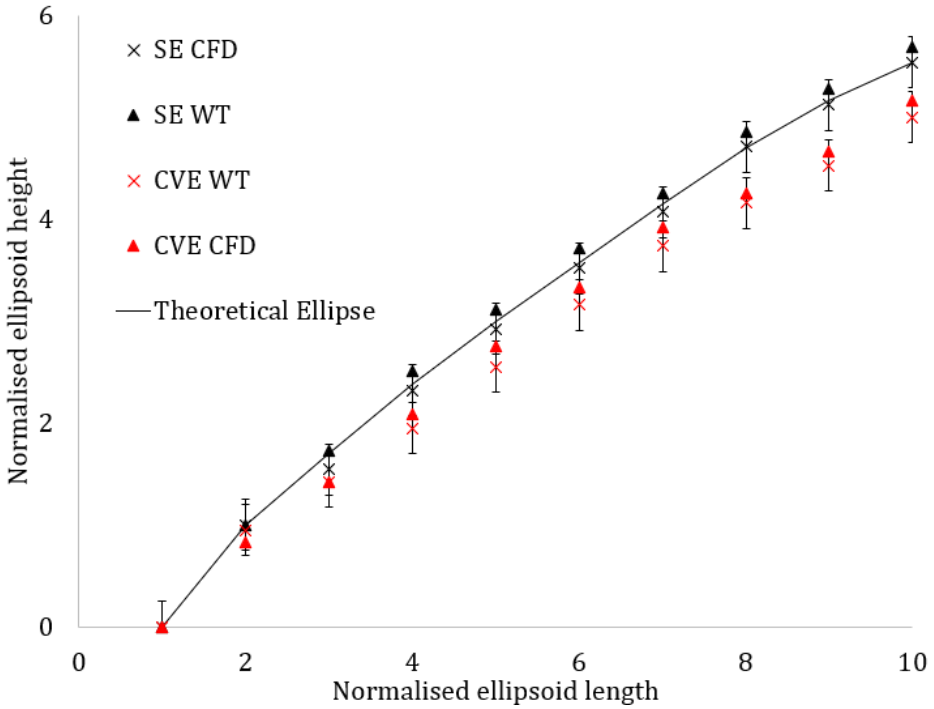

Figure 71: Plot of the shock angles for the WT, CFD and theoretical ellipsoid at Mach 3.5.

The ellipsoid experienced slightly less bow wave attention than the other shapes (shown in Figure 71 as a smaller difference between the solid and porous data) due to several factors. Of all of the porous models, the BS0 E featured the deepest radial pores, with very low outflow available for the amount of fluid inflow (discussed further in Section 7.8). This affected the mass flow rate through the porous structure, resulting in a smaller wave angle reduction. The geometry of the ellipsoid also meant that regions of both supersonic and subsonic flow were present behind the bow wave, meaning higher levels of turbulence. When this flow interacted with the high levels of spillage from the radial pores, affecting with the bow wave resulting in less attenuation.

6.4.4.4 External flow - Hemisphere

Figure 72 shows the annotated images for the solid hemisphere, and Figure 73 the BS0 porous hemisphere. As with the ellipsoid, the hemisphere generates a detached bow wave.

Figure 72 and Figure 73 demonstrate the same governing parameter correspondence as the other shapes, as well as the same bow wave attenuation by porosity introduction to the solid hemisphere. The BS0 H standoff distance was higher than the ellipsoid on account of the

higher curvature of the hemisphere, whereby the pores were able to have a stronger shock attenuating effect. The hemisphere also had a higher inflow-to-outflow ratio, meaning that even though both subsonic and supersonic flow were mixing behind the incident wave, the flow field experienced minimal leaking from the surface pores and turbulence behind the shock when compared to the other curved shapes. This emphasises the importance of profile shape when introducing porosity, in particular the post-shock flow condition.

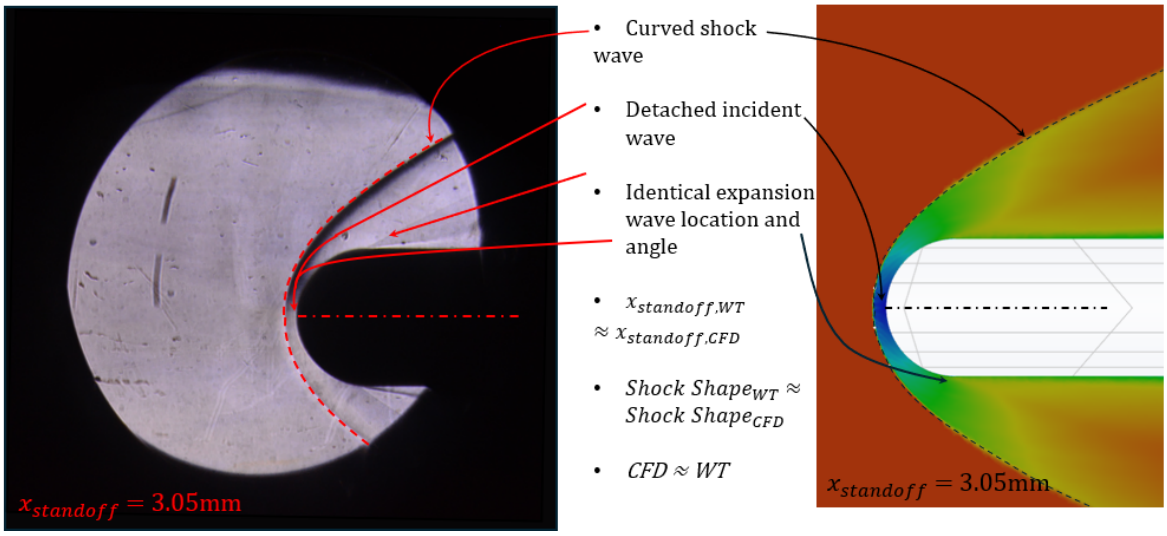

Figure 72: Annotated schlieren photograph (left), and CFD Mach contour plot (right) of solid hemisphere at Mach 3.5.

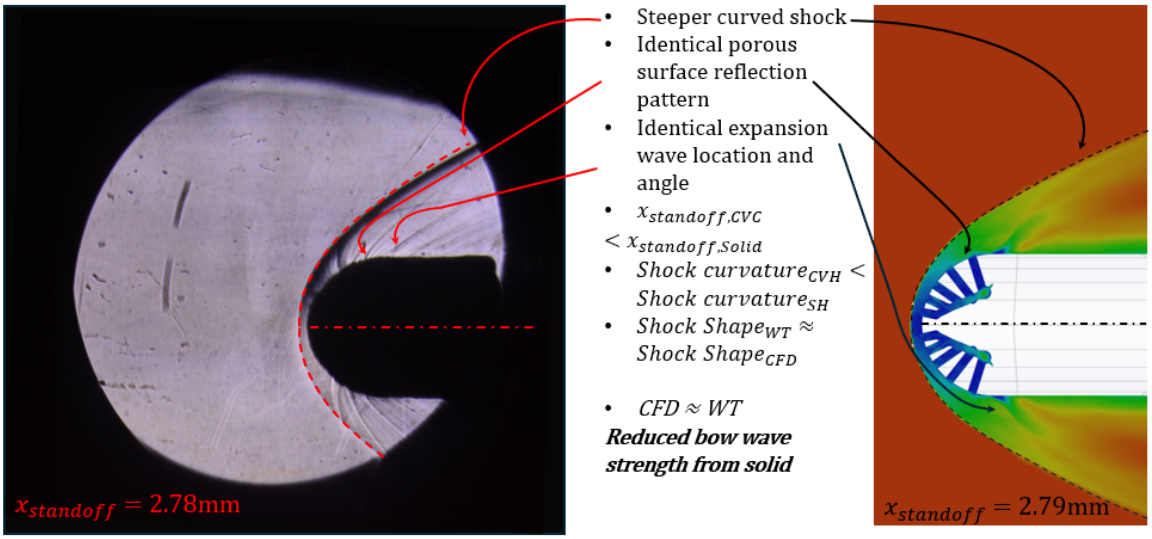

Figure 73: Annotated schlieren photograph (left), and CFD Mach contour plot (right) of the BS0 hemisphere at Mach 3.5.

The change in shock shape is confirmed by the normalised plot in Figure 74. The solid hemisphere (SH) and BS0 porous hemisphere (BS0 H) show good agreement across both the numerical and experimental data sets, as well as the theoretical calculation.

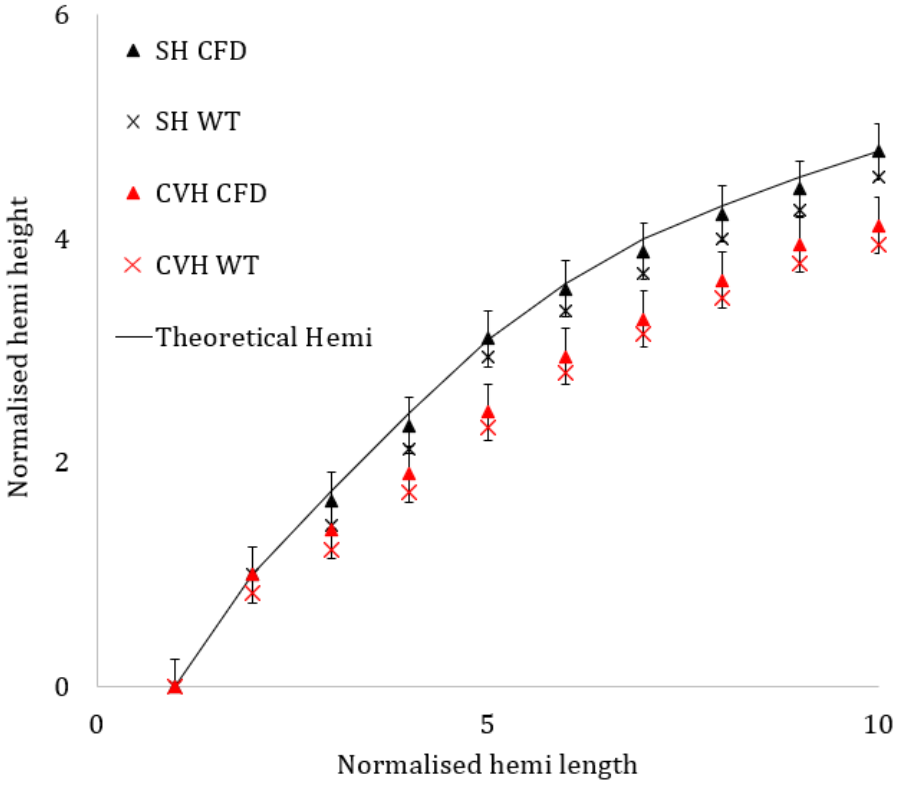

Figure 74: Plot of the shock angles for the solid and BS0 WT, CFD and theoretical hemispheres at Mach 3.5.

It is necessary to note that while the comparison of the above images has comprehensively demonstrated that the BS0 secant ogive, ellipsoid and hemispheres all show weakening bow wave attenuation on account of the porosity, the total drag of these models still increased overall when the venting structures and downstream effects were taken into account (as shown by CFD and WT drag results). This occurred for several reasons. The total aerodynamic drag of the porous models was affected by three main factors: the change in bow wave shape, the vent jet interaction and the momentum addition by the jet. In the schlieren images presented above, only the bow wave change may properly be accounted for, as the internal flow is hidden and the downstream jetting flow cannot be adequately captured. This means that the effect on drag on the flow field may only be assessed from visual analysis upstream of the vents.

As confirmed by Poplavskaya et al. (2017), the presence of the pores will definitely attenuate the bow wave to some degree (however minimal, regardless of venting structures), as inevitably some of the mass flow from the shock will be transferred into the porous network. The degree of this transfer (and thus the extent of the attenuation) depends on the arrangement of the surface holes, as well as their depth, density and the venting conditions.

From Section 7.5, it is known that the vertical 90° exit vent is an inefficient venting configuration, and indeed is unsuitable for the secant ogive, ellipsoid and hemisphere. This unsuitability is confirmed by the CFD images, which provide details of the internal, venting and downstream flow unavailable in the schlieren images. For example, the effect of the vertical jet on the bow wave is visible in the BS0 SO CFD image as the small impression in the bow wave above the vent. In this case the vent increased the size of the bow wave beyond this point, worsening the negative effects of the jetting. This explains why the bow wave attenuation occurs solely around the cone head, but may worsen or improve depending on the combination of jet behaviour, cone shape and internal geometry. This emphasises the importance of using the combined numerical and experimental results for understanding the flow physics acting on the models.

The preceding discussion ultimately confirms that the external flow field of the experimental schlieren are in full visual agreement with the numerical CFD images and the theoretically calculated data. The governing flow parameters of concern for comparison include bow wave shape, standoff distance, wave angle, expansion wave behaviour etc. These parameters are in agreement across the two methodologies within 95% confidence intervals of the theoretical data. The porous visual data (both numerical and experimental) shows the same level of agreement.

The governing parameters of the external flow field show close agreement across the numerical, experimental and theoretical results. The visible reduction of bow wave area indicates that attenuation of the bow wave has occurred, and that by extension the wave drag reduced in the BS0 validation case and others. As such, the visual data may be used with confidence and both the numerical and experimental methodologies are sufficiently validated by analysis of the flow field.

6.4.5 Internal flow - literature comparison

The visual comparisons were used in addition to the measured and calculated drag, visually confirming the physical flow phenomena present. It is implied across the literature that the images and force data are intrinsically linked and of equal importance. Significant drag reduction has a noticeable effect on the flow field. When particular flow features change, the performance is comparably affected. An example of this is the reduced shock angle, present in photographs, which naturally occurs with reduced drag.

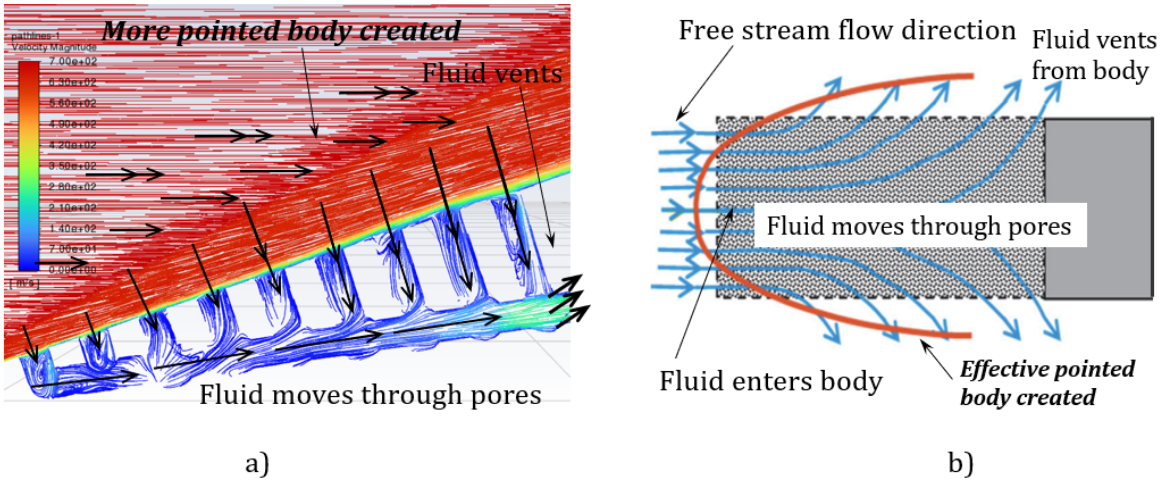

Figure 75: a) Velocity vectors coloured by static pressure for the BS0 cone, b) Drag reduction mechanism for the HPCM frontal-insert cylinder (Mironov, Maslov et al. (2015))

Fig. 75 assists in validating the overall drag reduction mechanism of the presented research. Fig. 75 demonstrates the fluid flow mechanism through which drag is reduced in a supersonic, porous body. a) shows the CFD velocity vectors of the BS0 (coloured by pressure), and b) depicts the flow movement for the same HPCM cylinder insert used as Poplavskaya et al. (2017), Maslov et al. (2019) and Mironov, Maslov et al. (2015). In a) the velocity vectors inside the BS0 porous structure show the flow direction into, through, and out of the structure via the venting pores. This matches the flow pattern in b) very closely, whereby the shock angle in (a is reduced in the same way that an equivalent pointed body is created in b). This pointed body is the drag reduction mechanism, reducing the strength of the shock wave to create an effectively slimmer, lower drag body.

The fluid motion through the pores (and altered shock wave) in Fig. 75 a) shows close visual similarity to b). This confirms that the manner in which drag is reduced in the BS0 models is the same as in the literature models in terms of governing flow physics. Therefore, a similar flow field (and drag result) can then be expected from the BS0 models when compared to the literature models. The similarities between the internal fluid motion of the two bodies of work aid in validating and verifying the physical drag reduction mechanism.

6.4.6 Venting flow - visual comparison

The final region of interest from the external flow was the post-shoulder flow field, in particular the venting pore. Fig. 76 shows the BS0 venting pore a) a greyscale density CFD plot and b) the schlieren photograph with geometry overlay. The BS0 90° vent provided very little additional momentum to the downstream flow field, and so limited jetting is visible in Fig. 76. A section of the porous geometry is overlaid in Fig. 76 (b) to show the location of the venting pore which is not visible in the schlieren image.

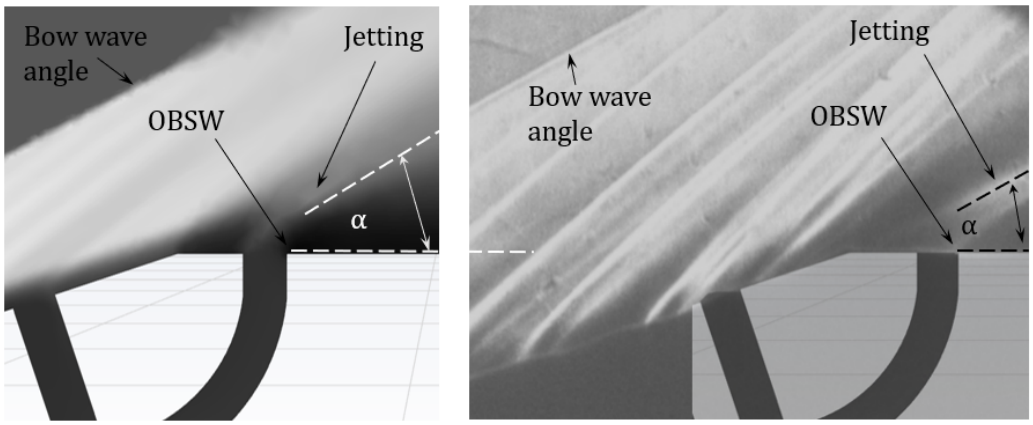

Figure 76: BS0 exit vent plots at Mach 3.5 a) Greyscale density plot b) Schlieren image with geometry overlay.

Due to the spherical aberration present in the schlieren image, a slight degree of warping is present around the edge of the image, however the effect is insignificant. Several other weak waves are visible in Fig. 76 upstream of the vent. This is a result of the three-dimensional effect of the porous cone and bow wave being picked up by the schlieren photography, resulting in waves all around the cone being visible. The identical bow wave angle β is noted between the images. As Fig. 76 indicates, some jetting occurs from the pores in both the numerical

a) and schlieren image b), leaking into the downstream flow. Both images show the weak shock wave present at the upstream exit corner of the vent, generated as the fluid exits the vent. The angle of both the oblique shock wave and jet ($\approx 27°$, annotated as α), as well as the position of the venting shock, is the same in a) and b). The angle of the expansion fan generated at the cone-cylinder shoulder also matches closely. Whilst the boundary layer and detailed jetting cannot be seen as the optical set-up was not sensitive enough, the visibility of the overall venting flow in both images is acceptable.

The similarity in venting flow structures between the computed and schlieren BS0 images indicates that there is good agreement between the numerical and experimental venting flows. By validating the venting flow using both methodologies, the venting performance obtained for analysis may be confirmed as true and reliable.

6.5 Conclusions

The validation study confirmed that there was good agreement between the flow visualisation, experimental drag measurements and literature for the cone case as presented. The similarity across the bodies of work in all shape cases provides strong evidence for the reliability of both the numerical and experimental results.

Even though some of the experimental drag data was unusable, the presented flow visualisation data was still valid, and compared favourably with what was expected from the literature. The presented schlieren photographs models strongly matched the numerical images in terms of the flow structures present. The porous network is also adequately represented by the single symmetry plane view. The experimental and numerical drag coefficients of the presented cone cases matched within an acceptably small error. The experimental drag data was also proven to be comparable with the drag coefficients communicated by the literature.

The overall research and experimental methodology were compared with the literature, and close similarity in both the methodologies and the results was observed across the board. The validity of the numerical method and its ability to produce reliable, repeatable data with a

high level of confidence was confirmed. The model may be applied to further porous cone designs in order to expand on the understanding of the physical flow phenomenon of interest.

Chapter 7

Results and Discussion

The results of the investigation of cunicular bodies (organised porosity in conic bodies of revolution) in steady supersonic Mach 3.5 flow are presented below. The results and discussion are focused on the overall effect of the porous structure on the flow field (including shock waves and interactions, separation and other phenomena of interest), as well as the effect of the porosity on aerodynamic drag reduction. The change in drag across the cunicular flow field originated from three sources: wave drag, jet interaction and the momentum addition to the flow field by the jet. The individual contribution of each of these sources was highly specific to the porous configuration investigated, whereby some changes in drag were always noticed (e.g. wave drag reduction at the porous conical forebody), whereas other changes were less predictable (e.g. the momentum addition by the jet).

Both the internal and venting networks were found to be connected, and simultaneously governed, by the internal network. The amount of inflow into the porous system was controlled by the pressure gradient within the internal network. If the internal pressure was too high, then bleeding (or outflow) from the surface would occur, which hindered the amount of wave drag reduction possible. Because the venting geometry and crossflow condition were both constant, the internal pressure was required to correct for the vent exit condition. In this way, sufficient outflow (fluid exiting the system through the pores) was required to sustain sufficient inflow (fluid entering the system via the inlet/internal network). If there was insufficient outflow (due to the vent geometry being incompatible with the crossflow), then 100%

inflow could not be sustained, and fluid would bleed out from the cone surface. The combined cunicular system was found to behave as a quasi-Converging-Diverging (CD) nozzle in this way, where subsonic fluid in the internal 'converging' section, was choked at the minimum area (the vent inlet or 'throat'), to be accelerated to supersonic speeds in the 'diverging' vent section.

The results of the non-porous baseline models are presented first (Section 7.1), so that they may be directly compared to the porous models in terms of drag coefficient, bow wave shape, wave angle and wave properties (e.g. velocity, Mach number and pressure). The porous flow topology and characteristics are then briefly referenced (Section 7.2).

The drag coefficient results of models of interest are then presented (Section 7.3), including the percentage reduction in drag from the relevant solid cones. The hypothesis of the drag attribution is summarised (Section 7.4), followed by the analysis of the inlet (Section 7.5), venting (Section 7.6) and internal (Section 7.8) flow fields.

The most successful venting configuration (BS4) applied to the other conic shapes is presented in Section 7.7. Finally, the limitations, conclusions and recommendations are presented in Section 7.9, Sections 8.1 - 8.8, and Section 8.9, respectively.

It is **highly** recommended that the flow visualisation results presented here be viewed in colour. While it is possible to distinguish the flow features in greyscale, the high degree of complexity in the flow flow field is better represented in colour.

Only a single Mach number (Mach 3.5) and specific porous configurations are discussed here, as being representative of most of the results contained in the entire data set. Select results by way of example from tests at Mach 3 are found in the Appendix G.

7.1 Non-porous baseline

The solid conic section results are presented to provide a baseline to compare the subsequent porous results to. Four solid conic profiles were examined: the pointed cone, secant ogive (SO), ellipsoid and hemisphere. The cunicular structures were applied to the four solid cones.

Each conic profile represented a particular bow wave shape and related drag response. The weakest bow wave and lowest drag coefficient (C_d) in the group occurred in the pointed cone (attached, strongly supersonic downstream). The hemisphere represents the strongest bow wave and highest drag coefficient (detached, low mixed subsonic/supersonic downstream). The secant ogive and ellipsoid represented medians between the two shape extremes. The solid bow wave shapes and characteristics may be summarised as follows (shape names are abbreviated):

- Curvature: $Cone < Ellips < SO < Hemi$.
- Shock type: $Cone_{Attached} < Ellips_{Detached} < SO_{Attached} < Hemi_{Detached}$.
- Shock angle (strength): β_{Cone} (32°) $< \beta_{SO} < \beta_{Ellips} < \beta_{Hemi}$ (90°).
- Drag coefficient: $C_{d,Cone} < C_{d,SO} < C_{d,Ellips} < C_{d,Hemi}$
- Downstream shock flow: $Cone_{M>>1} > SO_{M>1} > Ellips_{M>>1;M<1} > Hemi_{M>1;M<<1}$.

In Figure 77, the changes in 2D shock shape (specifically wave angle, curvature, detachment and overall wave strength) are visible.

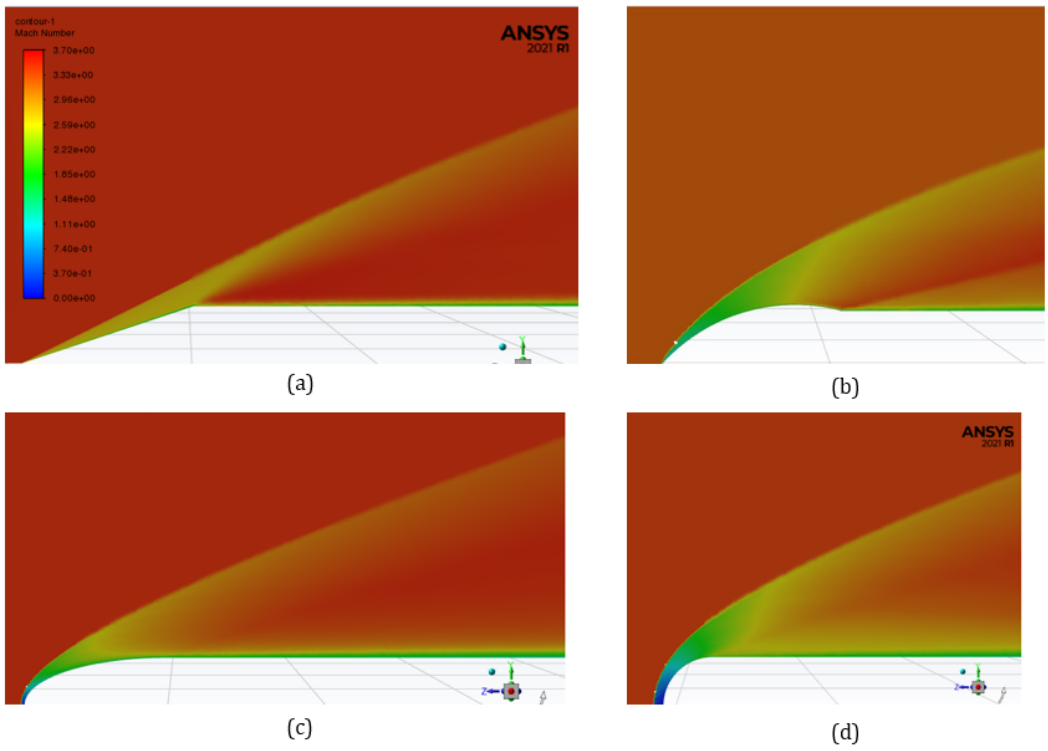

Figure 77: Mach number flood plots of solid models at freestream Mach 3.5 a) pointed cone b) secant ogive c) ellipsoid d) hemisphere.

Figure 78 demonstrates the 3D shape of the bow wave across the solid models. The boundary layer on the cylinder is greyed out for simplification. 3D flow visualisation is useful for identifying and examining the changes to the bow wave shape and formation, the effects of porosity and the jet behaviour for the vented models. Both 2D and 3D flow visualisation results are presented here to provide a more comprehensive overview of the flow field changes between the solid and porous models. Specifically, the to drag and shock behaviour are of interest, where the solid C_d and wave angles and wave shapes will be compared to those of the porous cases.

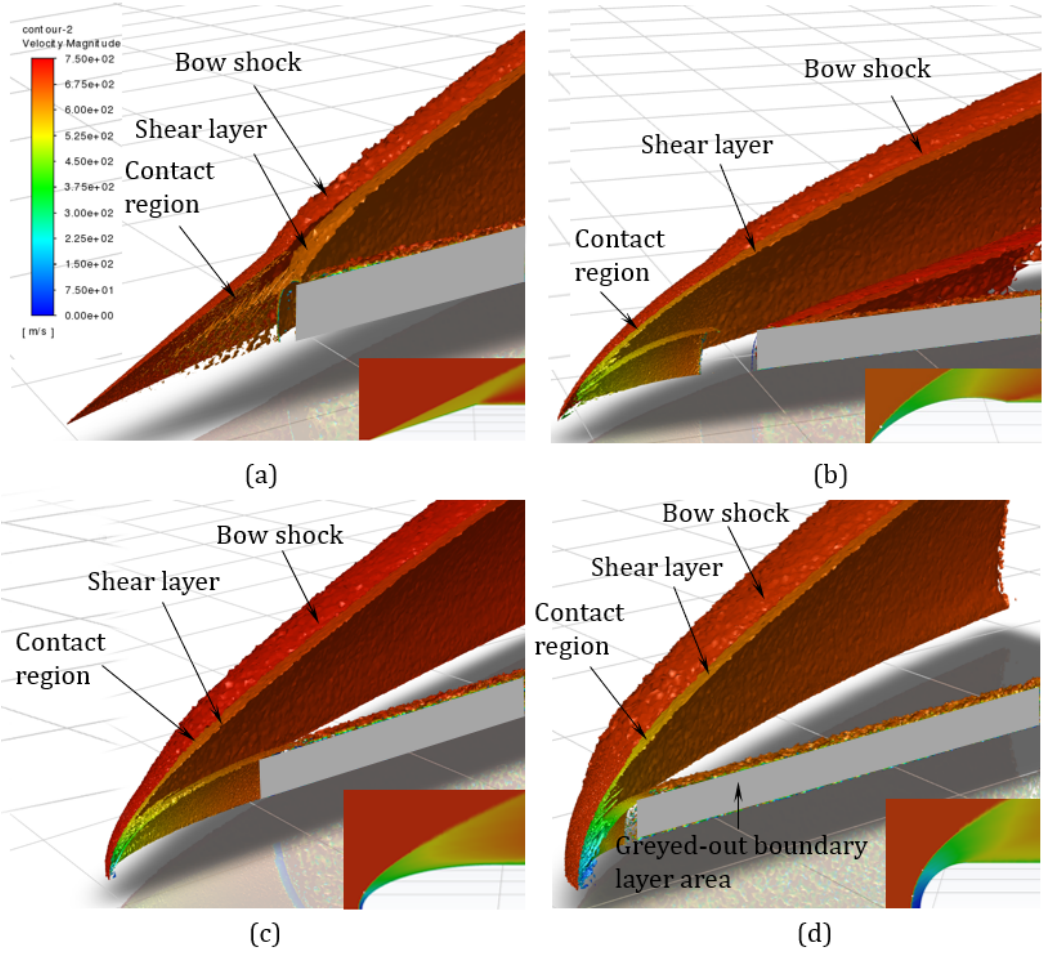

Figure 78: Velocity surface plots at freestream Mach 3.5 of the a) pointed cone b) secant ogive c) ellipsoid d) hemisphere, with side-view.

7.2 Flow field characteristics and porous flow topology

In order to investigate how the introduction of organised porosity affects aerodynamic drag performance, an overview of the porous flow field is described, prior to the characteristics of the porous flow field being analysed. This is necessary before comparing the flow fields, in order to establish an understanding of the physical mechanisms behind the phenomena of interest. The results of the porous flow field are separated into three sections, namely the inlet, internal and venting structures. The three separated sections are identified as follows:

- Inlet - the flow field between the freestream flow and the inlet pores on the cone surface (Section 7.5).
- Internal - the flow field inside porous conical forebody region (Section 7.8).
- Venting - the flow field from the vent inlet until downstream of the vent outlet (Section 7.6).

Each section provides a particular contribution to the drag reduction mechanism. The wave drag of the body is affected by the internal flow, while the downstream drag (including pressure and interference drag) is affected by the venting configuration. The internal network governs both the internal and venting systems, controlling the balance between them and determining the overall drag reduction. The venting configuration contributed to several sources of change in drag to the system.

Certain porous cone configurations are more heavily emphasised in the specific sections depending on their relevance to the particular phenomenon observed. The BS0 - BS4 pointed cones mainly describe the inlet and internal porous flow field. The venting structure is then described using the OE and UE pointed cone cases.

Important sources of drag in the baseline models included wave drag (bow wave), interference drag (from pore-affected flow and jetting), skin friction drag (from the surface holes and inner channels) and form drag (different cone shapes). These sources affected the drag performance of each model to a varying extent depending on the geometry. Considering this, the C_d

and wave angle of each porous model is compared with their solid counterpart, in order to determine the mechanisms behind the drag reduction/increase as a result of the porosity.

7.3 Conic cunicular drag results

The validated numerical drag coefficient (C_d) data is presented below. The drag results in Table 8 were obtained using the numerical method described in Chapter 5, at Mach 3.5. The cones shared the same common geometric characteristic: L/D ratio of 1.5 (except hemisphere; $L/D = 1$), base ⌀= 32 mm, # surface pores = 144, # vents = 14 (except BS0/BS1 Cone; = 22 vents), inlet pore ⌀= 2 mm. The porosity across all of the cunicular models (including vents) was ≈ 60%.

Table 8: C_d of the solid and porous cones (select venting configurations), and the percentage difference (%Δ) between them for the relevant shape family

		Drag Values	
Shape	Vent type	C_d	% Δ
Cone	Solid	0.29	
	BS0 (90° vent)	0.28	-3 %
	BS1	0.23	-22 %
	BS2	0.24	-19 %
	BS3	0.20	-31 %
	BS4	0.18	-39 %
	OE	0.38	35 %
	UE	0.20	-32 %
	LE	0.31	6 %
	HV	0.44	36 %
	72 Holes BS4	0.32	10%
Ellipsoid	Solid	0.39	
	BS4 E	0.24	-40 %
Hemisphere	Solid	0.90	
	BS4 H	0.91	16 %
Secant Ogive	Solid	0.49	
	BS4 SO	0.4	25 %

The Reynolds number of the external wedge was 3.9×10^5 and 4.38×10^3 for the internal porous flow, respectively. The parameters of the free stream were: characteristic length D = 0.0032 m (frontal cone diameter), free stream velocity V = 701 m/s. The parameters of the internal porous flow were: characteristic length (D = 0.0002 m (internal pore diameter),

velocity inside the pores $V = 125$ m/s). The local free stream and internal densities were used respectively. The reduction in Reynolds number was due to the small diameter of the internal channels. This conveyed that the internal flow had much greater friction-induced losses than the external flow and that the internal flow therefore had a major influence on the overall functioning of the system. The characteristics of the cones and naming convention described in Table 8 is as follows:

- BS - The porous conic forebody configuration applied to all presented models (includes toroids, longitudinal and radial pores).
- BS0 - BS4 - The baseline (zeroth-iteration) porous models.
  - BS0: 90° vent angle (minimum-momentum jetting). 90° inlet pores. $(A/A^*) = 1$ $\Rightarrow$ Least drag reduction.
  - BS1: 45° vent angle; 90° inlet pores. $(A/A^*) = 1$
  - BS2: 18° vent angle; 60° inlet pores. $(A/A^*) = 1$
  - BS3: 18° vent angle; 60° inlet pores. $(A/A^*) > 1$
  - BS4: 18° vent angle; 90° inlet pores. $(A/A^*) > 1 \Rightarrow$ Greatest drag reduction.
- OE, UE, LE - Overexpanded, Underexpanded, Linearly Expanded. Refers to the (A/A^*) and shape of the vent. Attached to BS cone.
- HV - Horizontal Vent. Horizontally-aligned vent configuration. No venting from the shoulder occurred. Attached to BS cone.
- 72 Hole model - 50% less inlet holes than regular BS4 Cone model. Investigates the effects of reduced inflow on the system.
- BS4 E (Ellipsoid)/ BS4 H (Hemisphere)/ BS4 SO (Secant ogive)- The BS4 Cone porous configuration (forebody and vent) applied to the other solid shapes.

The pointed cone family included the baseline (BS0 - BS4) and geometry-specific vent configurations (OE, UE, HV). The percentage difference between each cunicular model and the relevant solid model (as shown) is also presented. A negative difference represents a reduction in drag, and a positive difference an increased drag. The baseline pointed cones were

investigated first, and the venting configuration that produced the greatest drag reduction (BS4, 39%) was then inserted into the other shape families, resulting in BS4 E (Ellipsoid) and so on. The effect on C_d and bow wave shape was investigated in each case. Schematics of all of the conic models may be found in Appendix H.

Significantly, the BS4 porous configuration applied to the ellipsoid (BS4 E) resulted in the greatest overall drag reduction (40%), however worsened the drag in the BS4 H/SO cases. This confirmed that the BS4 porous structure was highly sensitive to the cone shape and incident bow wave condition, in particular the state of the downstream shock.

7.4 Hypothesis of drag attribution

In the cunicular model, three sources of change in drag were present across the system: wave drag, jet interaction and momentum addition by the jet. These sources affected the drag performance (increase/decrease), to varying degrees.

7.4.1 Wave drag

The reduction in wave drag was associated with the condition of the bow wave, specifically the decrease in wave angle and increase in post-shock Mach number. The bow wave covered two regions: the immediate cone region (conical forebody) and the downstream cylinder region. The change in shock angle β and M_2 is mainly affected by the presence of the surface holes in the cone region of the bow wave, and less so by the presence of jetting from the cylinder. A positive/negative change in wave drag depended on the combined effect of the inlet/internal and venting structures. It was found that the wave drag around the conical forebody was always reduced due to the porous surface, however, the overall drag could be further improved (or worsened) by the venting configuration. The wave drag reduction by venting was caused by the introduction of positive momentum to the post-shock flow field, which assisted in reducing the overall size of the bow wave further downstream. The change in wave drag was affected by several factors, including the amount of inflow able to enter the

porous structure, the mass flow rate within the internal network, and the exit angle of the vent.

7.4.2 Jet interaction

The second source of change in drag arose from the jet's interaction with the supersonic crossflow. The jet interaction had the greatest effect on the change in drag across the cunicular body. The extent of this drag change depended on the vent exit angle, expansion ratio (A/A^*), crossflow condition and P_e/P_b of the jet. The jet interaction drag was minimised by aligning the vent exit as closely to the horizontal crossflow direction as possible, to reduce energy losses and dissipation. The vent (A/A^*) should accelerate the flow such that the exit pressure P_e matches the back pressure P_b outside of the vent as closely as possible in order to achieve a critically expanded jet shape (or close to it). This ensured that minimum momentum losses were incurred as a result of the change in direction to the flow during impingement with the horizontal freestream. The interaction drag was also minimised by carefully considering the expansion ratio of the vent. The expansion ratio needed to be such that the flow condition at the jet exit matched the freestream as closely as possible in order to mitigate pressure losses due to the mixing of the streams. This meant that the vents which provided the greatest acceleration performance did not necessarily produce the greatest drag reduction.

7.4.3 Momentum addition by the jet

The final source of change in drag in the porous system was the momentum addition by the jet. This was closely linked to the jet interaction source and was dependent on both the crossflow regime at the vent exit and the vent P_e/P_b. Momentum recovery from the jet was maximised by ensuring that vent $P_e \sim P_b$, and that the vent P_b was similar to the crossflow pressure. The terms 'similar' or 'near' are used as it is impossible to achieve a perfect pressure match in a system of this complexity. The static pressure of the crossflow region surrounding the vent is critical as it influences the shape of the jet. If a critically expanded jet is injected into a crossflow of matching pressure, maximum momentum recovery and momentum addition into the crossflow will occur.

In this case, the drag reduction on account of the momentum addition would be significant. Conversely, if an over (or under) expanded jet is formed, the static pressure of the crossflow would not match the jet. This jet-crossflow interaction would cause considerable momentum loss, with little momentum recovery taking place in the flow. In such cases, very limited drag reduction (if any) would occur. The change in drag associated with the momentum addition by the jet could be positive or negative and was strongly dependent on both the inflow/internal conditions, the vent configuration and the crossflow.

7.4.4 Flow field aspects of interest

In order to asses the aerodynamic drag reduction mechanisms, several areas of the flow field require examination. The reduction in bow wave angle and changes to the bow wave shape enable the wave drag effect to be described. The behaviour of the inlet structures and their effect on the bow wave and internal flow is essential for understanding the inflow mechanism. The mass flow rate in the internal network and vent allows for the momentum recovery to be examined and its effect on drag determined. The flow inside and outside of the vent (specifically the jet shape, velocity and pressure ratios) allows for the jet interaction and effects on the crossflow to be examined, and for the associated effect on drag to be described. The vent pressure ratio P_e/P_b, as well as the jet designation (OE, UE etc.), is critical in this. The change in momentum between the domain inlet and outlet (correlated with area-weighted average dynamic pressure) also assists in explaining the momentum change across the system. The overall changes in velocity of the flow field, specifically the crossflow and post-shock velocity, influence the jet interaction condition downstream. The flow within the porous cone network is also of interest in order to determine the relationship between the inlet and venting systems.

7.5 Inlet Flow Field

The inlet network refers to the fluid inflow into the porous body, via many organised holes located on the cone surface. The inlet holes provide a path of least resistance, or transfer

route, for the supersonic air flowing over the body. This air is absorbed into the internal cunicular structure, where it is mixed and redistributed within the channels. From the internal network, it is directed towards the venting structures.

The inlet network was intended to reduce the bow wave angle and attenuate the strength of the shock wave, functioning as a wave drag reduction mechanism. This was achieved using surface pores connected to the internal cunicular structure. The pores allowed for fluid removal and mass transfer across the porous boundary. The mass flow downstream of the bow wave was absorbed into the porous network driven by a pressure gradient, whereby the bow wave incidence and thus pressure across the bow wave was reduced. Due to the weaker bow shock, there was reduced momentum/energy loss to the system.

With reference to the inlet network, drag reduction occurred by means of shock attenuation by reduced entropy loss across the shock. The following section examines the wave drag reduction mechanism induced by the inlet system of the cunicular body. BS4 represented the greatest drag reduction for each of the three major sources of change in drag. As such, it is consistently used as the reference case throughout the discussion.

7.5.1 BS0 - BS4 Overview

The pointed cone models BS0 - BS4 are presented:

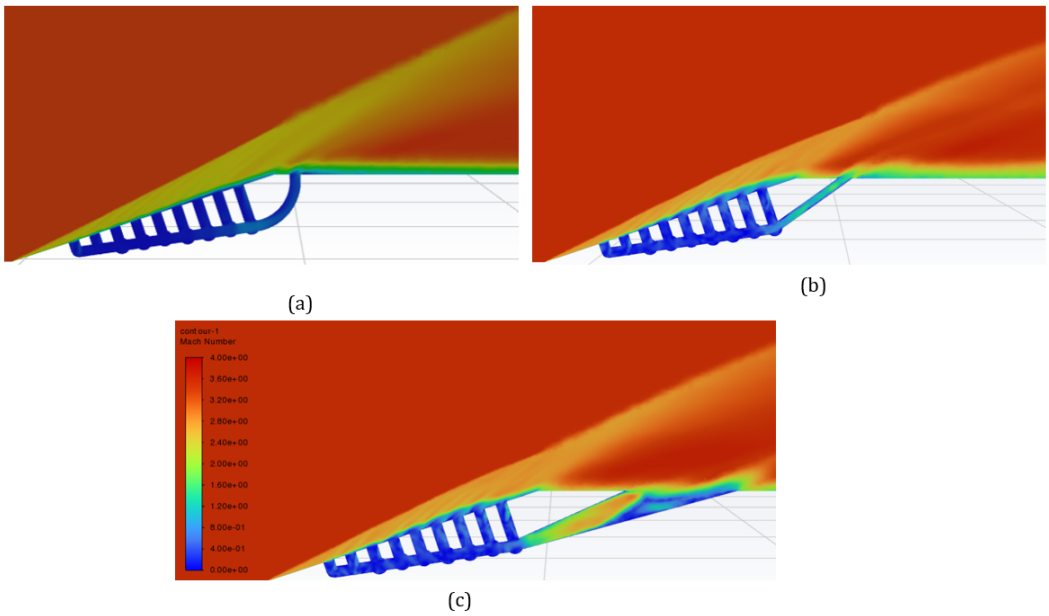

Figure 79: Mach contour flood plot of ZY-plane pointed cone a) BS0 b) BS1 c) BS4 at Mach 3.5.

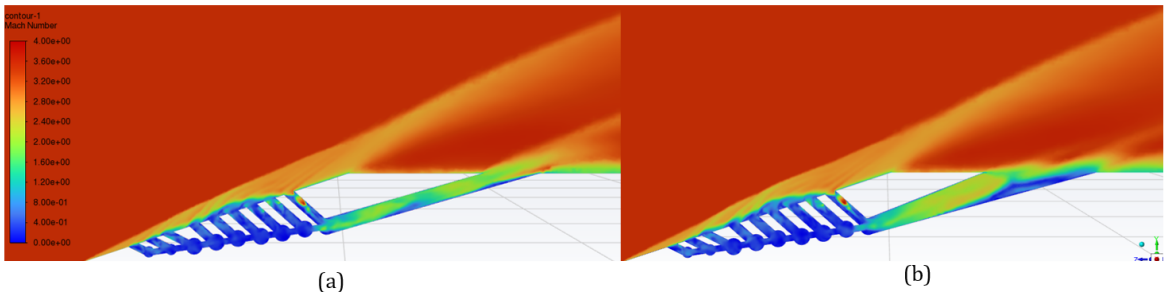

Figure 80: Mach contour flood plot of ZY-plane pointed cone a) BS2 b) BS3 at Mach 3.5.

Models BS0 - BS4 were the original models used to investigate the bow wave behaviour occurring as a result of the porous geometry. The design of all subsequent models was based on the results of BS0 - BS4 (specifically BS4). The velocity contour plots of BS0, BS1, BS4 and BS2, BS3 are shown in Figure 79 and Figure 80, respectively. Comparisons of parameters are constrained to the flow topology indicated in the ZY-symmetry plane images. Between BS0/BS1/BS4 and BS2/BS3, only three parameters were changed with respect to the inlet and internal network geometry: inlet pore angle, longitudinal pore diameter and toroid diameter. The effect of these geometry changes is described as follows:

- Longitudinal pore diameter - In BS2/BS3 a smaller longitudinal pore (1 mm ⌀) was used. The effect on the flow field was largely negligible, and the flow still choked at the vent inlet. A slight reduction in the internal mass flow rate was noted. Because of this, as well as increased manufacturing difficulty, the larger diameter in the BS4 configuration was retained.

- Inlet pore (inflow) angle - Two inflow angles were investigated: 90° to the cone surface in BS0/BS1/BS2 and 60° in BS2/BS3. As in the 90° case, 60° pores still reduced the equivalent body CSA, but to a slightly lesser extent. The key finding was that the inclined pores allowed for increased inflow if the correct pressures were present. Additionally, weaker shock waves were generated at the 60° inlet holes than in the 90° case. These factors caused the porous shock pattern within the oblique shock wave to change, where the inclined pores resulted in a greater Mach number downstream of each pore. Consequently, a higher overall post-shock Mach number was achieved, with a lower wave angle. Whilst this was advantageous, the forward-inclined pores were subject to heavy bleeding from the cone surface.

- Toroidal cross sectional area - In BS2/BS3 a larger toroidal pore diameter was used. This resulted in a higher toroid pressure, whereby the overall pressure of the internal network (and at the porous surface) was increased. The internal mass flow rate also increased on account of the area increase.

As the comparison of the straight and inclined pores highlighted, the effect of mass flow rate and fluid inflow on the bow wave attenuation was significant. It was thought that the flow in the inclined pores may have been contributing to the reduced mass flow rate, given the internal geometry of the flows identified in the shock mesh interactions studied by Law and Skews (2009). It is difficult to definitively identify the flow phenomena at play within the inclined pores, and as such further work is required (discussed in Section 8.9).

BS0 - BS4 had the same number of inlet pores at the surface, the same internal channel arrangement (longitudinal, toroidal and radial pores) and the cone half-angle was constant across all models at 18.43°. Comparing Figure 79 and Figure 80, the internal mass flow rate varies along the porous arrangement. In Figure 79 (BS0/BS1/BS4), the mass flow rate at

the aft-most toroid in these models is very similar due to the matching toroid area (2 mm ⌀). In Figure 80 (BS2/BS3), the same is noticed, although for a larger-area toroids (3 mm ⌀). The increased toroid area allowed for a greater mass flow rate within the internal porous structures of BS2/BS3.

Figure 81 demonstrates the outer conical shock surfaces for the solid, BS0, BS3, and BS4 cones at Mach 3.5. Here, the reduction in wave angle and shock attenuation is visible in the change in bow wave shape and formation. In Figure 81 a), the shock surface over the solid cone region was uniform in velocity, whereafter it was uniformly accelerated by the expansion wave at the cylinder shoulder to meet the free stream condition as its effects dissipated. Two distinct regions of the bow wave are visible and denoted: the cone and cylinder. The shape of the bow wave is uniform and linear. Note that the number of surface pores is the same across all models.

In Figure 81 d), the overall size of the bow wave and wave angle was visibly reduced, while the overall velocity (particularly after the final vent) was greatly increased. This indicated that the bow strength was attenuated, and that wave drag reduction had occurred as a result of the porous geometry. Over the porous conical forebody, some bleeding was visible on the cone surface. This was a result of the slight mismatch between the venting and inflow geometry, meaning that too little outflow from the vent was occurring to completely support the inflow. The inlet wave drag reduction mechanism was still highly effective, even though less-than-perfect inflow occurred.

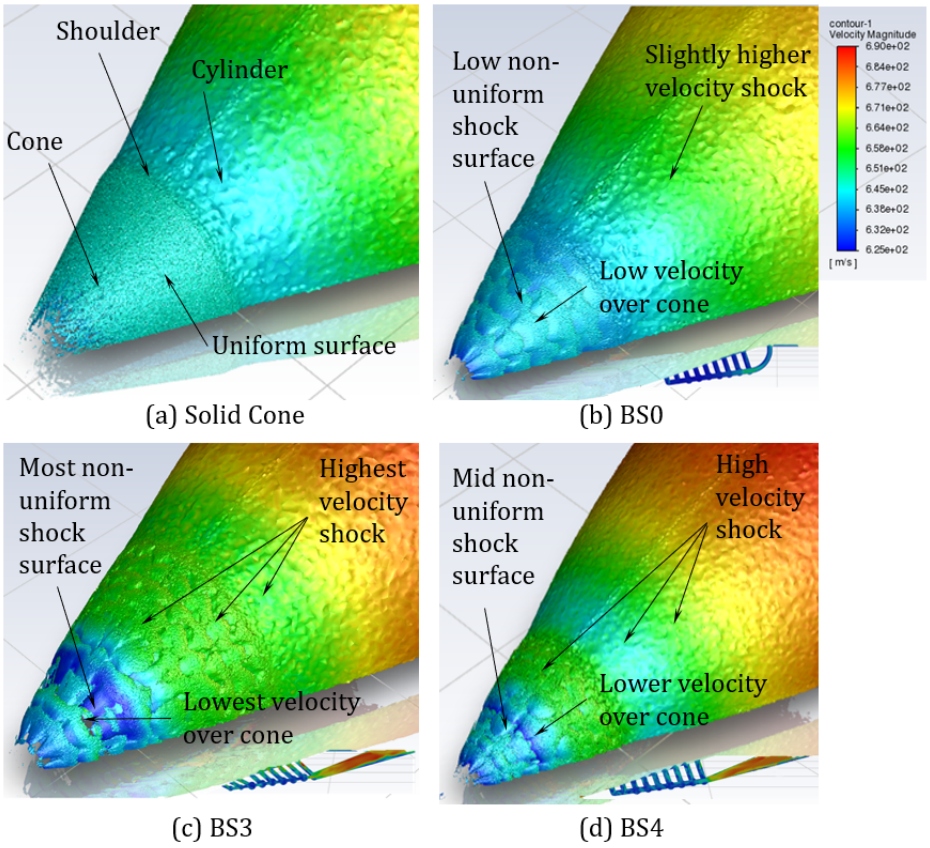

Figure 81: Mach 3.5 shock surface plot (a-solid cone, b-BS0, c-BS3, d-BS4)

When the BS4 shock surface is compared with Figure 81 (b, BS0), BS0 experiences far less shock wave attenuation, as indicated by the larger wave size and wave angle. Comparing the solid and BS0 wave surfaces in Figure 81 a) and b) downstream of the shoulder, very little velocity variation or change in wave shape was noticed. This indicated that the 90° vent had a very limited effect on the bow wave attenuation. This confirmed the BS0 (and 90° vent) to be the limiting venting case, whereby the minimum possible momentum was recovered during venting. In this, the inlet pores were confirmed to govern the incident bow wave attenuation mechanism.

Comparing Figure 81 (a, b and d), where b) and d) have the same porous forebody arrangement, the visual contributions to the bow wave from the inlet and venting systems are visible. The inlet system attenuates the bow shock over the cone region, creating a dimpled surface pattern in this region. Beyond the cone shoulder, the effect of the inlet and venting system is also visible. The BS4 case utilises a higher-performance vent design, whereby the downstream flow experiences greater acceleration than the other cases. This further narrows

the bow wave. The overall effect of the porous network in (b/d) is to reduce the CSA of the wave to varying degrees, thereby reducing the C_d.

In Figures b), c), and d), the dappled pattern is visible on the shock surface at the cone region. The very dark flow patches on the shock surface are from the surface bleeding affecting the shock. The greatest bleeding from the surface was seen in BS3, visible in a large amount of stagnation flow bleeding into the incident bow wave and altering its shape. When compared to the solid cone wave surface, significant losses in momentum, energy and velocity occur in BS3 due to the bleeding. This is detrimental to wave drag performance, as adequate inflow cannot be achieved.

7.5.2 The effect of mass flow rate on bow wave reduction

Between BS0 - BS4, the mass flow rate in the aft-most toroid was found to increase, as indicated by the increased velocity. Figure 82 a) depicts the plot of bow wave angle β versus mass flow rate (g/s) at the aft-most toroid location for BS0 - BS4. b) depicts the C_d versus mass flow rate (g/s) for the same conic model set. The plot demonstrates a linearly decreasing relationship between wave angle and mass flow rate, and a similarly decreasing drag reduction pattern across the models is also noticed. This suggests that the greater the mass flow rate within the internal network (specifically at the vent inlet), the greater the energy absorption across the bow shock wave through the pores, and into the internal network. In doing this, the incident shock angle β is reduced as the energy loss to the system is reduced.

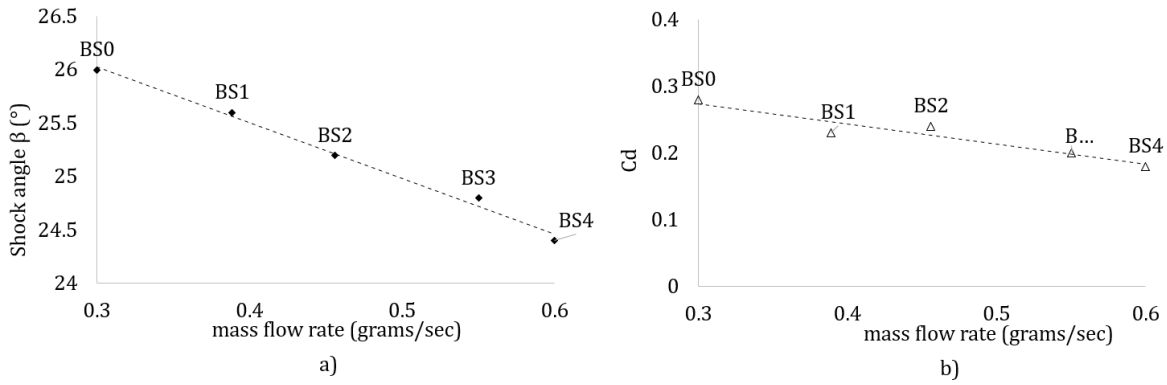

Figure 82: Mass flow rate (g/s) vs shock angle β (°) for internal porous structure of BS0 - BS1 pointed cones at Mach 3.5

The difference in rate of flow removal across BS0, BS1 and BS4 is visible in Figure 79. The pressure of fluid behind the porous boundary was indicative of the fluid removal rate. If the pressure was higher, then a less steep gradient was present, and by extension, less mass was removed. The pressure below the boundary is significantly lower in BS4 (Figure 79 c)) than in BS1 (Figure 79 b)), with hardly any occurring in BS0. This indicates that BS4 removed mass (and weakened the bow shock), far more effectively than BS0 and BS1. With regards to flow rate and mass removal, BS4 reduces the wave drag most efficiently around the conical forebody.

The results presented in Figure 79 - Figure 82 indicate that BS0 - BS4 all exhibited reduced aerodynamic drag when compared to the solid cone.

7.5.3 Effect of vent angle on bow wave attenuation - BS0, BS1, BS4

To investigate the effect of vent exit angle on the wave drag reduction, cones BS0, BS1 and BS4 are discussed. The cones all used the same 90° inlet pore conical forebody, with different vent exit angles as follows: 90° = BS0; 45° = BS1; 18° = BS4. BS0 and BS1 had an expansion ratio $(A/A^*) = 1$, whereas BS4 had an $(A/A^*) = 2.6$. Only the effect of vent angle is investigated here.

Solid cone wave angle

Figure 83 demonstrates the velocity isosurfaces of the solid and pointed cones BS0, BS1 and BS4 to identify the changes in three-dimensional (3D) flow structure across the models. The solid cone plot in Figure 83 a) shows the large bow wave angle and smooth, undisrupted shock surface over the cone-cylinder. An inner shear layer is present, and an expansion wave is generated by the shoulder, accelerating the flow downstream.

In Figure 83 b), c) and d) the same near-stagnant, highly viscous flow is visible in the porous conical forebody. The velocity varies within the internal network in c), demonstrating the fluid recirculation and inflow into the internal network. In b), c) and d), the strength of the incident shock wave is visibly reduced by the presence of the pores, indicated by the region

between the inlet pores and shock surface (contact surface) being higher velocity than the solid cone a).

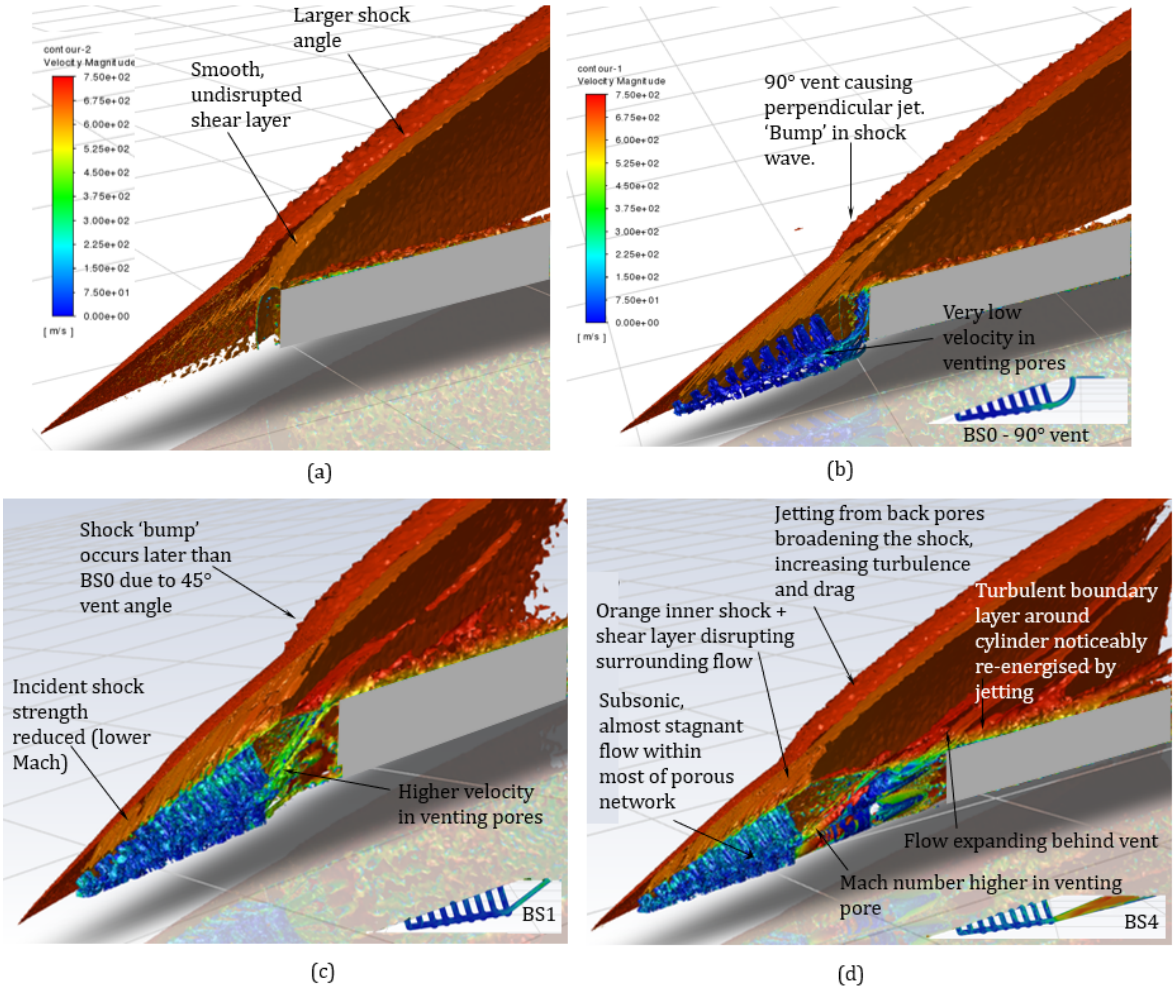

Figure 83: Mach 3.5 velocity shock surface plot of the pointed cone a) solid b) BS0 c) BS1 d) BS4

90° vent angle

In BS0 (Figure 83 b)), the effect of the 90° vent exit angle on the bow wave is visible as a 'bump' in the bow wave, visible above the vent exit position. The bump was caused by the fluid exiting the vent perpendicularly to the freestream, resulting in a sudden increase in shock cross-sectional area at this location. The 90° vent jet impinged upwards into the horizontal free stream. According to Newton's 2nd Law, momentum is conserved in the perpendicular (y) direction. As such, in the 90° case, only y-momentum (upwards direction) was added to the system, and none in the z-direction. BS0 therefore experienced no drag reduction as a result of momentum addition by the 90° vent, as aerodynamic drag is governed by momentum

changes in the streamwise (z) direction. This established that due to the vent direction, BS0 was the worst-case drag-reduction model. This also confirmed that the 3% drag reduction that BS0 experienced was due to the inlet/internal drag reduction mechanisms, discussed further below. Thus, the 90° exit angle had no meaningful effect on reducing the bow wave angle or recovering momentum from the vented internal flow.

45° vent angle

In Figure 83 c), BS1 and the 45° vent exit angle is demonstrated. The effect of the 45° angle was to accelerate the flow inside the vents more efficiently than BS0 (visible as increased vent velocity in Figure 83 c)), due to the straight vent better conserving the flow momentum. The 45° vent also energised the boundary layer significantly more than the BS0 model (comparing b) and c) at the cylinder surface), further accelerating the flow downstream of the vent and increasing momentum. As Figure 83 c) shows, the vent exhausts further downstream than BS0, slightly reducing the bow wave angle. By conservation of momentum, positive momentum addition in the z-direction occurs as a result of the 45° jet impingement, and as a result, a 22% overall drag reduction was achieved. The mass flow rate inside the vent was greatly affected by the shape of the vent, inducing bends, constrictions, expansions and the pressure and velocity conditions upstream and downstream. Examination of BS0 and BS1 confirmed that the shape of the vent definitively contributed to drag performance since the (A/A^*) and the inlet conditions were constant. The elbow-bend in BS0 caused a lower mass flow rate (shown by velocity in b)) within the vent and at the exit due to the significant direction change experienced by the flow inside the structure. The mass flow rate in the BS1 vent was higher on account of the limited direction change (visible in c)). The effect of the greater mass flow rate at the exit was to accelerate the crossflow, reducing the pressure and effectively pulling the bow wave inwards toward the jet. This changed the bow wave shape, reducing its size.

18° vent angle - BS4

In Figure 83 d), BS0 and the 18° vent exit angle is shown. After the inflow into the porous surface, considerable outflow occurred due to the expanded vent, creating a more expansive, faster flow field around the body. The BS4 vent jetting was mostly aligned in the z-direction,

resulting in a positive momentum addition to the flow and less flow disruption, turbulence and momentum dissipation. From the comparison of the shear layers in Figure 83 a) and c), the presence of the pores disrupted the incident shock wave, confirming the presence of shock waves at each pore.

BS4 represented the model with the greatest overall change in drag for each of the three major drag sources and consequently was used as the reference case for this discussion. The wave drag was reduced by the inlet pores, while the 18°-inclined expanding vent introduced positive momentum to the system with a minimised jet interaction.

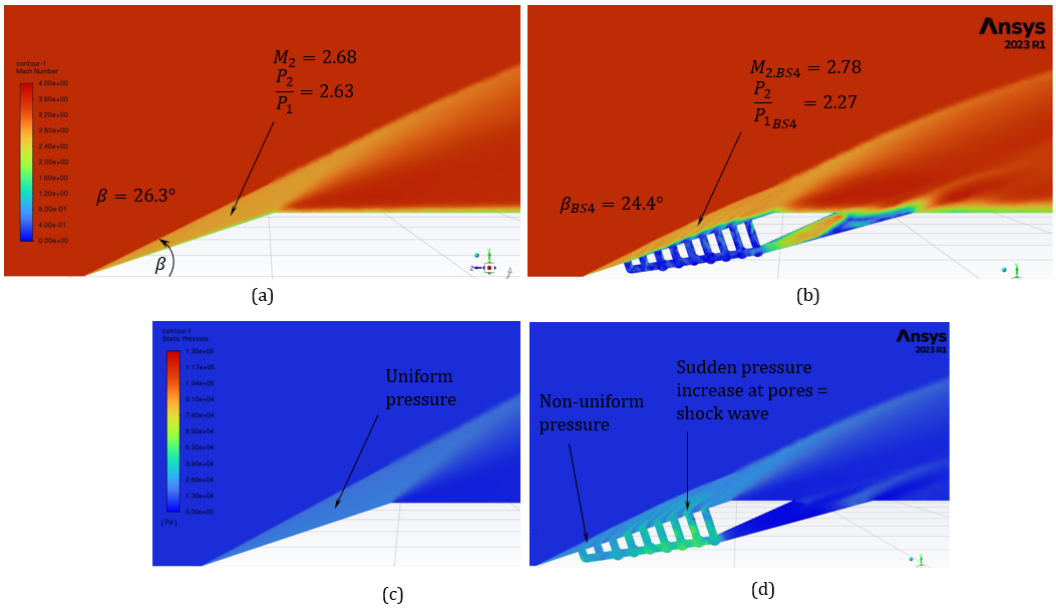

Figure 84: Mach 3.5 ZY-plane Mach contour flood plot of the a) solid pointed cone, b) BS4 cone.

Figure 84 compares the solid cone a) and BS4 b) Mach contour flood plots at the ZY-symmetry plane. The reduction in wave angle and overall change in shock properties on account of the porous inlet condition is simply illustrated in Figure 84.

In Figure 84, the BS4 shock angle (β_{BS4}) is noticeably reduced when compared to the solid, approximately 2° less. This reduction in wave angle corresponded to an increased post-shock Mach number and reduced pressure ratio across the shock wave, indicating reduced momentum loss across the shock. The porous surface shock behaviour was confirmed in Figure 84 (c, d), which demonstrated the static pressure flood plot of the solid and BS4 cones at Mach 3.5. In Figure 84 b), the static pressure over each pore site increased rapidly,

creating a patterned effect within the oblique shock. This sudden increase in pressure as a result of a reduction in area (at the pore) confirmed that a shock wave was generated at each pore.

The presence of the surface holes created an effectively smaller, more pointed body as a result of the wave angle being decreased (as in Poplavskaya et al. (2017))). Bow shock attenuation occurred as a result of the decrease in post-shock Mach number and reduction in wave angle. Within the bow wave, at each surface-pore location, a weak oblique shock wave (β_p) was generated due to the sudden change in area. The weak pore shock interacted with the bow shock, weakening it by introducing regions of higher pressure inside the wave, thereby increasing the overall pressure within the wave. This reduced the intensity of the pressure change across the bow shock, increasing the post-shock Mach number to attenuate the wave and lowering the wave angle. This phenomenon is only possible if the bow wake is weaker.

By examining the vent shapes, drag was worsened when the flow was required to change direction. Sharp corners, inclination and curvatures in the structure all worsened drag by causing the flow to change direction, significantly impacting the fluid momentum. In this, the force acting on the fluid also changed. As such, by changing the vent shape from rounded (BS0) to straight (BS4), a significant drag improvement was observed.

The effect of the solid profile shape also when combined with the porous structure also greatly affected the bow wave shape and attenuation. An example of this was when comparing the BS4 Hemisphere and BS4 Ellipsoid, where an identical porous structure (including venting) was used in the different shapes. In the BS4 hemisphere, the crossflow Mach number was too low for the vent expansion ratio, causing an overexpanded jet to form and significant momentum loss to occur on account of the jet interaction. In this case, any drag reduction was more due to the effects of wave drag reduction near the conical forebody and less so the momentum (interaction or recovery). The pressure ratio between the vent and cross-flow also caused the bow shape to increase over the vent, worsening the wave drag downstream.

Conversely, in BS4 E the crossflow Mach number matched that of the jet, enabling a near-critically-expanded jet to form, reducing the size of the bow wave and causing all three sources to contribute to reduced drag.

7.5.4 Effect of inclined pores on bow wave attenuation - BS2, BS3

In order the investigate the effect of mass flow rate into the wedge, the inlet pores in models BS2 and BS3 were inclined 60° towards the flow, also creating reduced pore separation at the cone surface in these models. Additionally, the internal structure was altered to encourage greater inflow by increasing the toroid diameter. This increased the vent inlet area, which allowed for a higher internal mass flow rate. BS2 and BS3 had identical conical forebody structures, where only the venting configuration was different.

Figures 85 and Figure 86 show the velocity isosurface plots at Mach 3.5 for the a) BS2 and b) BS3 cones, and the 2D Mach plots of the solid cone versus BS3, respectively.

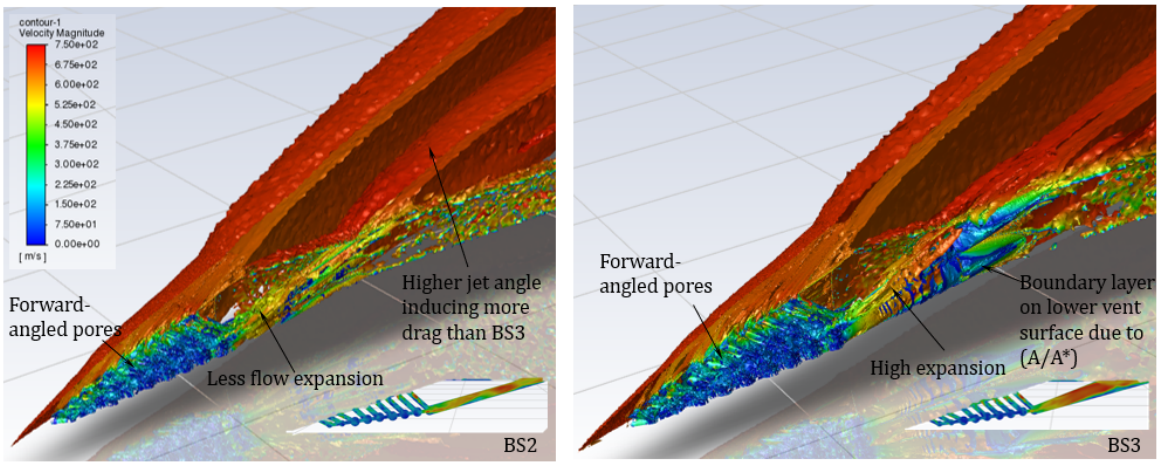

Figure 85: Mach 3.5 velocity shock surface plot a) BS2 b) BS3

BS3 experienced a greater drag reduction than BS2 on account of the vent geometry. BS2 had a vent $(A/A^*) = 1$, and 18°. BS3 had an $(A/A^*) = 2.76$ for the same 18° exit angle. With respect to the effect on the inlet, the vent exit angle affects the mass flow rate of the system, and this in turn causes changes to the bow wave shape and amount of momentum recovered from the jet.

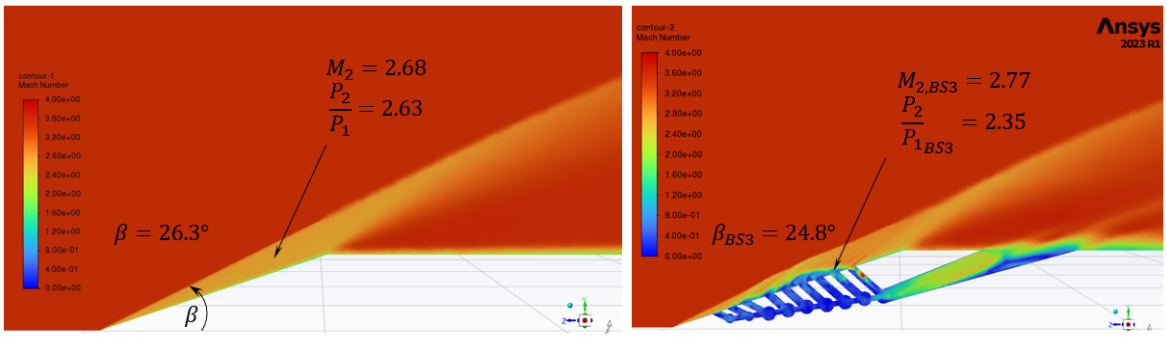

(a) (b)

Figure 86: Mach 3.5 contour flood plot of ZY-symmetry plane a) solid cone, b) BS3 cone.

The BS2/BS3 vent angles were largely aligned with the z-axis, indicating that minimal energy was lost during venting on account of excessive direction changes. Referring to Figure 86, this also meant that minimal negative changes to the bow shock were caused by venting, as the physical jet stream avoided the bow wave entirely. However, in the other cases (e.g. BS4 E), the jet angle did affect the bow wave shape, particularly in the cases where curved bow waves were generated. If the condition of the crossflow was similar enough to the vent exit condition in terms of pressure and Mach number, the pressure behind the bow wave is able to regulate and reduce. This caused the size of the wave to decrease, where the bow wave is 'pulled' inwards towards the vent exit and the curvature of the bow wave is increased, as in Figure 88.

The 90° pore entry angle was driven by local static pressure only. The effect of the pores inclined 60° to the freestream flow was that a dynamic pressure component was added, whereby the total pressure around the porous inlet is increased. Comparing Figure 79 a) (BS0) and Figure 80 (BS2/BS3), more bleeding from the surface is observed (mostly from the middle pores) in the cones with inclined inlet pores. The addition of the dynamic pressure component increased the pressure in the pores, particularly around the pore surface. As mentioned, the overall effect of the surface pores was to reduce the post-shock pressure. The difference in pressure caused the high-pressure fluid from within the pores to move into the lower-pressure shock region, resulting in bleeding from the surface. This effect was worse at the centre of the cone, as the first three pores had a lower inclination angle (40°) and thus a far lower dynamic pressure component.

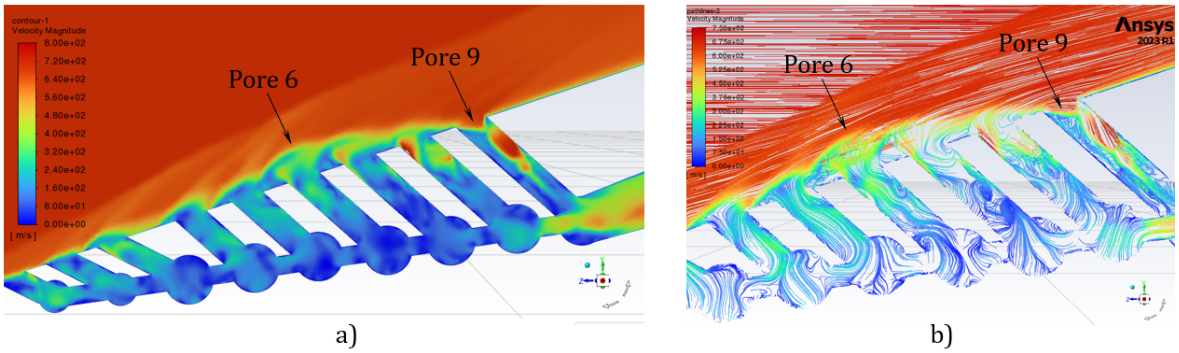

Figure 87: Enlarged view of the Mach number contours a) and velocity streamlines b) of the BS3 inlet structures.

Figure 87 shows an enlarged view of the Mach number contours a) and velocity streamlines b) of the BS3 inlet and internal structures. Two pores are examined, pores 9 and 6 (as indicated). In pore 9 (P9), significant inflow into the pore surface is visible, indicated by the lack of bleed and 'sucked in' fluid at this location. This pore (and the aft-most toroid it is attached to) has the highest velocity and lowest pressure of the internal network. This occurs because at 60° inflow, maximum fluid inflow from the shock wave happens. At P9, there is sufficient outflow to support fluid inflow at the surface. This is made possible by the high velocity in the aft toroid, as the high mass flow rate in the aft-toroid adjusts the velocity condition in the pores.

Because there is sufficient outflow, the forward-incline of the pore allows for more efficient inflow into the surface. The inclination also allows for less fluid momentum loss as it enters the pore (on account of a less abrupt direction change) while achieving a higher mass inflow rate on account of the highly favourable pressure gradient. The inclined pores increased the amount of area available to the incoming flow, thereby increasing the velocity and reducing the pressure at the inlet boundary more than the perpendicular-entry pores. This is confirmed by the patches of high-velocity flow (in green) in Figure 81 c), just before the separation region occurs.

Whilst the forward-inclined pore had a positive effect in the case of pore 9, when there is insufficient outflow available from the toroids (as in pore 6 and surrounding pores), then significant leaking from the porous surface occurs. Consider pore 6 in the BS3 configuration displayed in Figure 87. The inclined pores allow for more inflow into the porous body, as the flow is met with less resistance (in the form of a smaller entry angle) as it enters the pores.

Figure 88 demonstrates the Mach 3.5 Mach flood plot for BS3 a) and BS4 b) to assist with comparing the changes in the inlet/internal structure to bow wave behaviour.

As Figure 88 shows, in BS3 the internal network pressure is higher (and velocity lower) than in the BS4 case due to the increased toroid diameter in BS3. This is problematic in the middle pores (where pore 6 is located) because the more-stagnant toroid condition means that an adverse pressure gradient is established in this region. Because of this, the fluid flows from the high-pressure porous region towards the low-pressure shock region, resulting in bleeding. This does not happen in pore 9 because it is connected to the vent-toroid, where the pressure is lower than at the pore surface, establishing a favourable, inflow-supporting pressure gradient. Because of this, the fluid enters the body at a higher mass flow rate, however, the flow is also more restricted as the holes are closer together on account of the inclination.

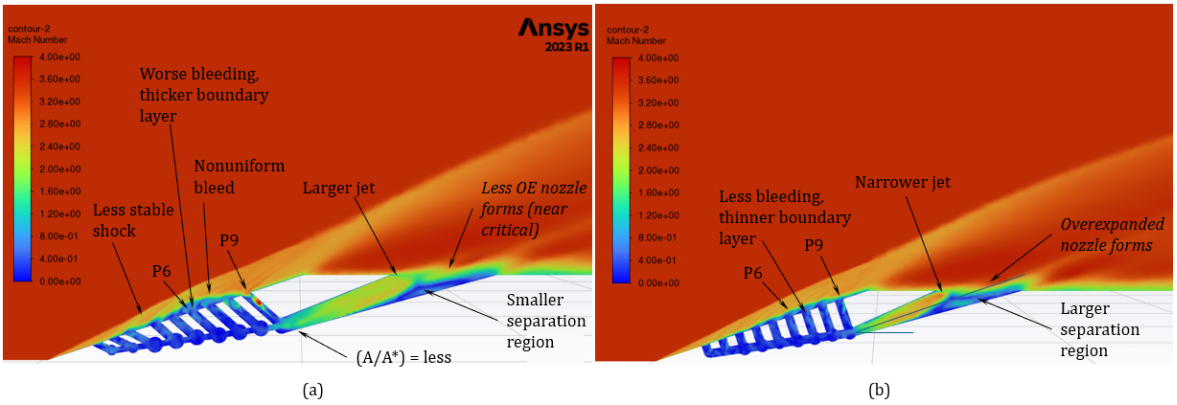

Figure 88: Mach 3.5 freestream Mach flood plots of the a) BS3 cone b) BS4 cone, at the ZY symmetry plane.

The same bleeding effect is noticed in BS1 and BS4 (90° pores), however, the smaller toroid diameter reduces the intensity of the adverse pressure gradient, meaning that less severe bleeding occurs even though the inflow angle is less advantageous by allowing less inflow. The 60° forward-inclined pores do in fact, allow for better fluid inflow and a higher mass flow rate, however, the toroid diameter is of critical importance in determining whether proper inflow without bleeding can occur.

The other issue with the inclined pores was the distribution of the surface holes was less even and less separated when compared to the 90° pores. This meant that at the tip and central region of the BS3 cone (where the pores were more densely located), the flow was constricted

more suddenly at the surface than in the 90° case where more spread was exhibited. The increased flow constriction was problematic as it represented a more sudden decrease in area, negatively affecting the mass flow rate into the structure by increasing the energy loss to the system as the fluid crossed the porous boundary.

The effect of the inclined pores in the case of BS3 also created a very uneven, unstable oblique shock wave. The instability in the BS3 bow wave surface due to the inclined pores is visible in Figure 81 c), indicated by significant pools of dark blue boundary layer bleed from the inlet pores, resulting in pockets of low-velocity flow in the incident wave. This is visible when comparing Figure 87 a) and Figure 84 b). For clarity, BS3 and BS4 have a similar venting configuration and hence are compared here. While there is surface bleeding in both cases, the porous bow wave in BS4 has a uniform internal shock wave pattern, uniform wave surface and a fairly even, connected bleed layer. In BS3, the outer bow wave shape and internal shock pattern are highly irregular, wherein the bleed layer is unstable and disjointed.

BS4 experienced the overall greatest drag reduction (39%) from the solid cone, slightly more than BS3 (31%). The inflow into BS4 was not optimal, due to the presence of the surface bleeding as demonstrated in Figure 84 b). However, BS4 experienced greater overall inflow and a higher mass flow rate into the internal structure than BS3. This is confirmed when comparing the internal flow fields between BS3 and BS4 in Figure 84. In BS3, there is only inflow into pores 1, 2 and 9 (33% inflow). In BS4, there is inflow into pores 1-4, and 9 (55% inflow). Thus, BS4 experiences 20% more inflow than BS3. This allowed for more flow into the surface of BS4, even though the flow rate was slightly lower due to the 90° pore angle. The increase in flow into the system meant that more of the wave energy was absorbed into the porous structure, while the loss of energy to the system was effectively reduced. This was shown by the reduced pressure ratio across the shock wave and higher post-shock Mach number, which indicated that the bow wave angle had been reduced and the wave attenuated.

As such, the BS4 conical forebody arrangement was more efficient at reducing wave drag than BS3, even though certain individual components of the BS3 structure had greater merit. Even though less inflow was present in the BS3 model on account of the toroid geometry, the forward-inclined pores increased the mass flow rate into the system very effectively, and as

such a strong wave drag reduction was achieved in the same way as BS4. The result proves that even with a highly unstable wave and bleeding, the inclined pores still absorbed enough energy and mass flow from the bow wave to greatly reduce the wave angle and attenuate the shock wave. Given the correct internal toroid geometry, 60° pores would provide stronger mass inflow and wave drag reduction.

The 90° inlet pores were used exclusively for the later models, as the uniform pore distribution and bow shock behaviour allowed for better, more consistent comparison to the other configurations. The comparison of BS3 and BS4 confirmed that the structure and positioning of the inlet pores greatly impacted the aerodynamic behaviour by controlling the amount of inflow into the system.

Because BS4 had the greatest overall wave drag reduction performance (in terms of inlet/internal structure), it was decided to maintain the BS4 inlet/internal structure in the subsequent models and focus on investigating alterations to the venting structure. Further investigation into the internal porous structure is required to fully grasp the effects of geometric changes on the flow field (see Section 8.9).

7.5.5 Effect of mass flow on wave angle

In the solid cone, the bow wave is generated at the cone tip when the supersonic freestream is deflected by the sudden reduction in area, forcing the flow to turn onto itself. The wave angle β is dependent on the turn angle θ, and the freestream Mach number M_1. Smaller turn angles result in smaller wave angles. According to the standard drag force equation (5), the drag force F_d generated on the cone body is dependent on the cross-sectional area of the body. Thus, a decrease in shock wave area (due to a decrease in wave angle), will by extension reduce aerodynamic drag.

$$F_d = 0.5 \times \rho \times V^2 \times C_d \times A \tag{5}$$

The conic surface holes created an effectively smaller, more pointed body, as previously mentioned. These holes allow for some of the energy from the flow to be absorbed into the internal porous structure. In doing this, energy/momentum was removed from the wave (thereby weakening it) and transferred inside the pores. In this, the mass flow rate ($\rho \times V \times A$) within the porous system was significant. The momentum is defined as mass times velocity, and as such by relating momentum and mass flow, the aerodynamic forces depend on the mass flow rate over the body. The amount of mass absorption through the porous surface was found to significantly influence the drag coefficient of the body.

Increased inflow (and mass absorption) through the inlet pores increased the mass flow rate in the system. The amount of inflow was dictated by the internal porous geometry, where favourable pressure gradients between the porous surface and internal network allowed the shock fluid to be effectively pulled into the pores. The success of this fluid drawing was mostly dependent on the toroid geometry, specifically the condition of the aft-most toroid which connected to the vent. For optimal wave angle reduction, the mass flow rate in the final toroid was required to be as high as possible. This was achieved by geometric changes, or by altering the vent (A/A^*).

The bow wave induced an intense and rapid change in pressure. The interconnected pores within the cone provided an alternative pathway for the fluid to interact with the material. The porous structure had the ability to redistribute and spread the pressure increase over a larger area, attenuating the shock waves more efficiently. There is a loss of total pressure associated with a shock wave due to entropy increase. By attenuating the shock wave using the pressure redistribution properties of the porous structure, the bow wave angle β was decreased, the tangential velocity component V_t was increased and V_n decreased. The weaker shock wave resulted in a lower ΔP and $\Delta \rho$ across the shock wave. This in turn reduced the wave drag (the component of pressure drag) acting on the body.

7.5.6 Conclusions

From the discussion above, it was determined that the inlet drag reduction mechanism was dependent on the bow wave angle reduction and attenuation. These phenomena were controlled by the inlet and internal conical forebody structures. The inlet arrangement (including the inflow angle and pore separation), defined the maximum amount of mass inflow able to enter the porous structure. However, the degree to which inflow was realised was governed by the condition of the internal network.

The pressure and mass flow rate within the toroids were required to be such that a favourable pressure gradient was established between the porous surface and internal network, in order to establish sufficient inflow. The condition of the toroids was dependent on the vent inlet geometry and back pressure condition.

The C_d and wave angle of the body were both found to decrease with increasing internal mass flow rate. By extension, wave drag reduction was directly dependent on the amount of inflow into the porous system. However, considering the sensitivity of the inlet system to the internal network, the internal network required closer scrutiny and investigation. The internal network was found to govern the effectiveness of both the internal and venting systems. Further investigation is required to understand the dual-interaction, and how it can be balanced for improved drag reduction.

7.6 Venting Flow Field

In the following section, the venting contribution is discussed. The Outlet (Venting) Network refers to the series of patterned ducts arranged around the cylindrical part of the body, exiting behind the cone shoulder. The vents connected to the internal network and expanded the flow, expelling it from the body with the aim of further reducing drag. The venting network geometry was found to have the greatest impact on drag performance. Several nozzle (vent) geometries were explored, including different shapes and expansion ratios (A/A^*).

The following sections will discuss the results of several venting configurations which provide the most comprehensive description of the three sources of change in drag associated with venting. The three sources of change in drag are as follows: wave drag, jet interaction, and momentum addition by the jet. In order to investigate the effect of the vent shape on the resulting jet, two standard nozzle configurations were analysed, resulting in the following jet formations: the over expanded (OE) and under expanded (UE) nozzles.

These venting configurations were attached to the BS4 conical forebody, resulting in the BSOE (Overexpanded) and BSUE (Underexpanded). These models represented opposite extremes of jet behaviour, where BSOE represented the largest possible vent expansion, and BSUE represented the largest possible vent contraction. The geometries demonstrated a wide range of flow phenomena to aid in the vent geometry examination. The results of the OE and UE venting geometries were applicable to most of the other configurations tested. Figure 89 shows schematics of the a) overexpanded, b) linearly expanded and c) underexpanded vents.

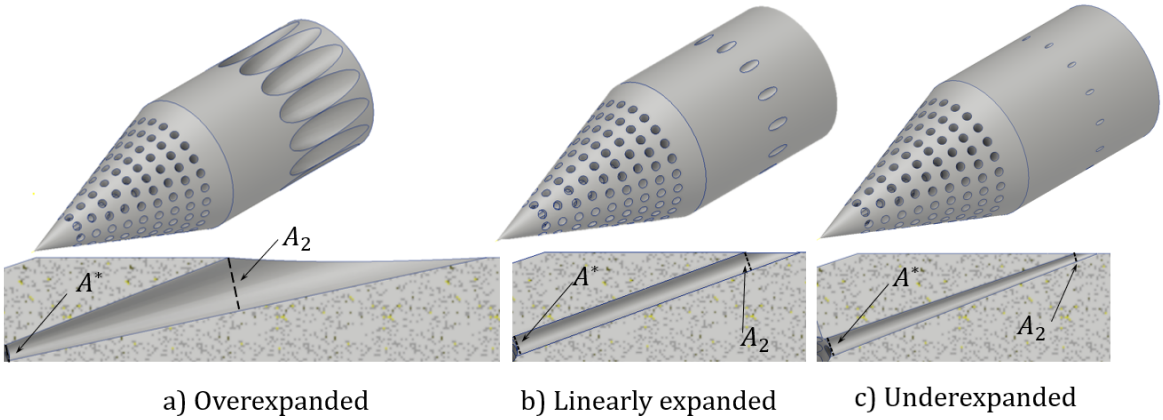

Figure 89: Schematic of the vented BS4 configurations (above-isometric cone view, below symmetry slice exposing internal structure) a) overexpanded (UE) b) linearly expanded (LE) c) underexpanded (UE).

Figure 89 b) shows the linearly expanded (LE) vent configuration, where the vent expands uniformly, $(A/A^*) = 1$, at vent angle = 18°. BSLE behaved akin to a less efficient version of BS2, with a drag increase of 2.3%. Similarly, 72 Hole BS4 increased the drag by 10% while behaving much like the HV case. These cases added little insight, whereby the other venting geometries describe the phenomena much more comprehensively. As such BSLE and 72 Hole BS4 are not mentioned here, however select BSLE results are shown in Appendix G.

Critically expanded nozzle

To be precise, the best venting performance would occur for a critically expanded (CE) vent geometry, the nozzle geometry which achieves perfect expansion and pressure matching across the vent exit. The critically expanded (CE) vent geometry represents the transition between over-and-under expanded states. However, such jetting behaviour is difficult to achieve and sustain on account of the complex upstream flow conditions and geometry. Additionally, it was impossible to accurately define the expansion ratio for this case, since it was unknown how the porosity would affect the bow wave and subsequent back pressure conditions. Thus, no venting configuration here was designed specifically to achieve a critically-expanded jet. Interestingly, particular vented cunicular models did exhibit some (or near) critically expanded jet behaviours, such as the BS4 E case discussed below. Hereafter, any jetting behaviour that results in a matched exit vent and crossflow pressure behaviour, irrespective of whether it it generated by an 'overexpanded' vent, is referred to as critically expanded, or 'CE'.

Therefore, only the OE, UE and HV cases are considered here. The change in drag associated with the aforementioned three sources (wave drag, jet interaction and momentum addition by the jet), will be examined primarily using BSOE and BSUE, whereafter the other configurations will be referenced and considered.

Venting behaviour - overview

The expansion ratio of the vent was highly sensitive, and a small percentage of area changes caused significant changes to the flow field. For example, by increasing the vent exit area by 10% ($<$ 1 mm $\Delta\varnothing$), the pressure ratio across the vent increased by 15%. Depending on the intensity of the vent expansion, this change in pressure could greatly alter the physics in the flow field, potentially transforming the vent from an overexpanded to an underexpanded configuration. Due to its sensitivity to geometry changes, the vent is the most constrained element of the porous structure.

The behaviour of the nozzle expansion process was governed by pressure ratios between the nozzle exit, the external environment into which the nozzle exhausts and the stagnation pressure of the inlet. The shape and design of the nozzle are such that it converts as much thermal and pressure energy into thrust as possible. In an ideal nozzle designed for optimal

performance, the exit pressure (P_{exit}) is equal to the ambient pressure of the external atmosphere (P_b). In this case, the flow inside the nozzle expands perfectly to fit the nozzle, maximising thrust and minimising pressure losses to the crossflow. The cylindrical body was of fixed length, so the vents could not be overly long or large otherwise they would interfere with the other parts of the vehicle functioning.

The vent design was critical to the aerodynamic performance of the body. Whilst the internal and inlet networks both provided a small drag reduction in isolation, the optimal drag reduction was not possible without these other systems. If the vent geometry was incorrect, the overall drag was significantly worsened. Whilst a great deal of drag reduction was possible, it required a delicate balance, with feasible expectations.

7.6.1 Overexpanded configuration

When discussing the overexpanded venting configurations, it must be noted that BS4 (like BSOE) also utilises an overexpanded nozzle configuration. However, the overexpanded vent in BS4 is less-expanded (exit Mach = 3.6) than BSOE (exit Mach = 4.33), and this greatly affects the performance of the cunicular bodies.

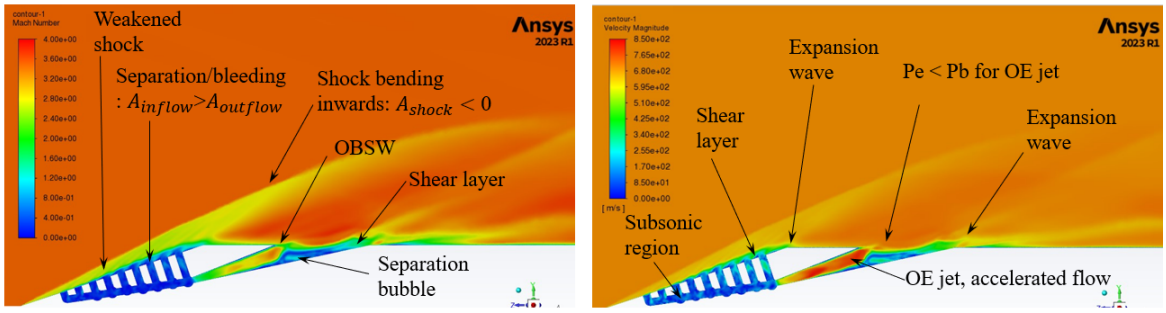

Figure 90: Contour flood plots of a) Mach number and b) velocity for the cylinder nozzle at Mach 3.5, nozzle expansion ration (A/A^*)= 14.31

Figure 90 demonstrates the flow field in the ZY-plane for the over BSOE nozzle configuration at Mach 3.5. Figure 90 a) shows the Mach number flood plot which identifies flow features that are associated with density changes, and b) is the velocity flood plot which identifies changes in velocity gradients across the flow field. As Figure 90 shows, downstream of the bow wave, a turbulent, non-uniform supersonic cross flow is generated due to the presence of

the pores. This induces a crossflow velocity greater than that of the freestream Mach number at the nozzle exit.

The expansion ratio of the overexpanded nozzle was $(A/A^*) = 14.31$, corresponding to a nozzle exit flow of Mach 4.33 (very high supersonic). The freestream Mach number was 3.5, and the drag increase across the system was 35%. The OE vent configuration provided a mixed result, where certain elements reduced the drag, while others worsened it. BSOE also proved that the overexpanded vent could produce considerable drag reductions (as in BS4) or greatly worsen the drag (as in BSOE), depending on the extent of the expansion and the crossflow conditions.

From the velocity plot, the flow choked inside the nozzle at the throat, as indicated by the uniform Mach wave present at the smallest area inside the vent. The nozzle configuration caused an overexpanded supersonic jet to form within the nozzle, which impinged on the turbulent supersonic cross-flow. At the nozzle exit plane, the static pressure inside the jet was far less than that of the free stream outside. The mismatch in pressures caused part of the flow from the interaction zone to be drawn back into the nozzle. This further narrowed the overexpanded jet and induced separation of the boundary layer from the lower nozzle wall. A large separation region formed on the lower nozzle wall near the exit, reducing the amount of nozzle area available to the flow. The separation bubble caused the jet to change direction, turning upwards instead of following the nozzle. This change in flow direction dissipated a greater amount of energy by reducing the jet size and free stream momentum, worsening the drag.

Flow field within isolated OE vent

Figure 91 and Figure 92 represent the modified BSOE geometry, where the conical forebody is removed in order to isolate and focus on the jet behaviour by removing all other parameters and interferences.

Figure 91 b) depicts the velocity streamlines of the separation bubble at the lower nozzle wall near the exit. The streamlines are more highly concentrated near the top-right corner of the nozzle, where a shear layer is likely to occur. The streamlines show a discontinuous change

in flow direction at the wall, suggesting the presence of a shock in advance of the separation bubble. As the streamlines in Figure 91 show, the bubble acts as a physical boundary to the flow, further narrowing the shape and deflecting the jet. The type of jet created at the vent exit is governed by the shape of the vent (or nozzle). The geometric nozzle parameters of interest include the inlet and exit areas, and the design of the upper and lower nozzle walls. The geometry of the nozzle greatly affects the performance of the jet.

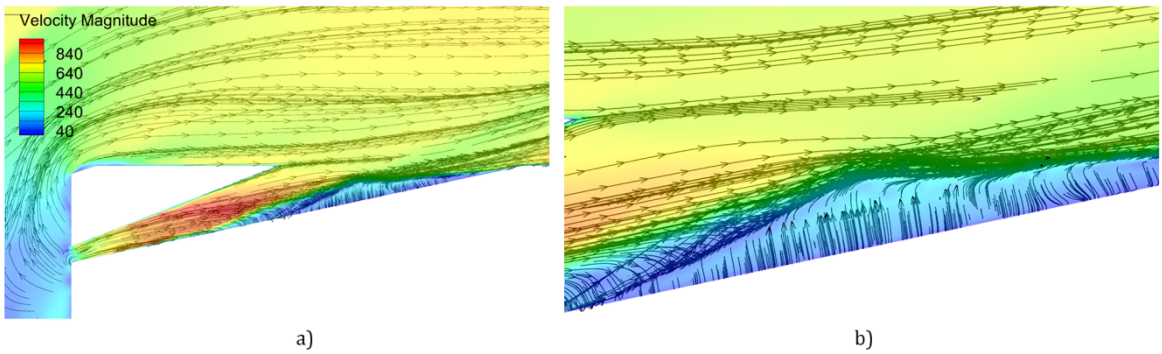

Figure 91: Velocity streamlines of the overexpanded jet a) global view b) near-wall view.

For optimal jet performance, the shape of the nozzle is designed for critical expansion of the flow, where the flow exit pressure matches the back pressure into which the fluid is expanding. Traditionally, these nozzle walls are curved, creating curved shock waves. The cunicular models deviate from this in that the walls of the vent are straight, generating straight shock waves. Generally, straight shocks are weaker than curved shocks, indicating that less pressure loss will occur at the vent exit, thereby reducing the momentum loss to the system. By weakening the shock wave at the vent exit, the momentum addition to the freestream by the jet will be greater, thereby reducing C_d. Additionally, straight nozzle walls reduce manufacturing complexity. The advantages to the straight-walled nozzle are counteracted in BSOE due to the vent geometry being incompatible with crossflow conditions, thus creating a very inefficient nozzle and jet.

When an overexpanded flow passes through a nozzle, the higher atmospheric pressure causes the flow to be squeezed back and inward, separating from the walls of the nozzle. In symmetric nozzles, this "pinching" of the fluid reduces the ability of the nozzle to achieve critically expanded flow (thereby decreasing the nozzle efficiency) since the extra nozzle wall area is essentially wasted, doing nothing to generate any additional jetting or flow expansion. This

is confirmed in Figure 91, where the separation bubble covers all of the 'wasted' lower nozzle wall. As such, the shape of the nozzle is critical to achieving the most efficient jetting flow possible, i.e. flow which fills the entire vent with no wall separation and a matched back and exit pressure.

Flow field within isolated OE vent - jet formation and expansion

The formation of the separation bubble was affected by numerous factors. When the high-speed jet encountered the upstream corner of the nozzle, the flow turned on itself to adjust to the flow, compressing it as it did so. This formed an oblique bow shock wave at the corner, as shown in Figure 90. Figure 92 demonstrates the static pressure Mach 3.5 flood plot of the jet impingement region.

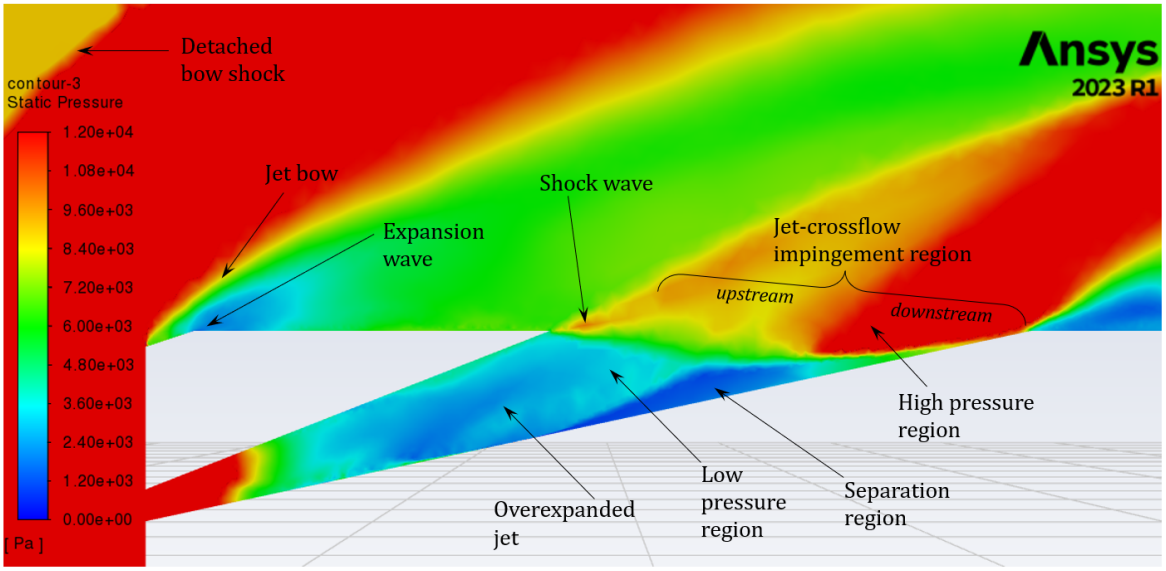

Figure 92: Static pressure contour flood plot of the overexpanded nozzle jet impingement region for the cylinder nozzle at Mach 3.5, nozzle expansion ration $(A/A^*) = 14.31$.

The shock wave (identified in Figure 92) increases the pressure and decelerates the flow in the downstream interaction region (identified by bracketed region 'jet-crossflow impingement' in Figure 92). Three distinct pressure regions were created on generating the shock (low in the nozzle, medium in the free stream, and high downstream). From the corner, the shock wave cut across the nozzle and hit the lower wall, causing an adverse pressure gradient to be induced by the pressure difference. Shock-induced separation occurred at the wall-shock interaction point, due to the sudden pressure increase at the wall. The separation was worsened by the overexpanded nozzle behaviour mentioned above.

It is important to note that the upstream-corner shock wave is 3D, wrapping around the jet. The CFD plots represent only a 2D slice. The 3D effect of the flow field is mainly relevant to the jet interaction, as the nature of supersonic flow combined with the axisymmetric cone design meant that most of the local supersonic flow phenomenon could adequately be captured in 2D image slices. The jet and jet interaction behaviour deviates from what is expected for axisymmetric supersonic flow, and thus further investigation using 3D flow visualisation is required (not examined at here, however holds relevance for future work).

Additionally, in BSOE the nozzle was inclined 18° to the horizontal, expanding asymmetrically. Due to the inclination angle, the expansion of the upper and lower nozzle surface was uniform until approximately 70% down the duct, after which the lower nozzle expanded (much more so than the upper nozzle). Due to the non-uniform increase in nozzle area (whereby the lower surface experiences a more rapid area increase than the upper surface), the pressure at these two surfaces also decreases non-uniformly. This non-uniform pressure decrease added to the existing adverse pressure gradient in the nozzle (present due to the pressure decreasing in the direction of the flow), worsening the flow separation. It is also noted that the separation bubble increased dramatically at the exact cross-sectional perpendicular to the midpoint flow. i.e., the separation bubble only worsened when the duct became asymmetric. This suggests asymmetric vent design is unfavourable.

Flow field within isolated OE vent - momentum

The overall flow field was highly complex and turbulent. A weak expansion wave was generated at the cone-cylinder shoulder, which accelerated the freestream near the wedge surface. Figure 92 shows that three velocity streams were generated in the flow field, which all intersect in the region just after the upstream nozzle corner: the crossflow, jet and boundary layer (separation bubble). As indicated by Figure 92, each stream had a different velocity. A shear layer was formed when each stream separated from the wall to which it was attached (i.e. the cylinder, upper vent and lower vent wall), merging later downstream. The pressures matched across the shear layer, however the velocity, temperature and energy of the streams typically did not.

A change in momentum was observed across the system on account of the dissipation in momentum by the jet impinging on the crossflow. The flow inside the nozzle underwent momentum changes caused by geometric changes and flow direction deviations, as well as supersonic flow phenomena such as shock waves and expansions caused by changes in pressure. The oblique shock at the nozzle exit plane indicated an entropy increase within the fluid and an inherent loss of momentum.

In BSOE, the jet impinged on the crossflow at 18°, forcing the flow to change direction relative to the principal streamwise direction. In changing the direction and mixing the two streams, momentum was lost. Inside the jet, the flow was rapidly accelerated to high Mach numbers due to the high expansion ratio while the mass flow rate remained constant. In this, the momentum of the fluid inside the nozzle was very high. The momentum of the crossflow was notably lower than the jet, but still supersonic since the stream underwent very little obstruction or area change after the incident wave. The OE jet was mostly (81%) aligned with the freestream (100%) along the z-axis. Momentum is an additive property, meaning that the jet impingement contributed to an overall increase in the system momentum by means of the accelerated flow and similar flow directions.

The higher static pressure of the crossflow caused the disintegration and diffusion of the jet, eventually mixing into the freestream. A high vorticity shear layer region existed at the interface between the jet and flow, as visible in Figure 92, where the large eddies decayed into turbulence downstream, further adding to the kinetic energy of the flow field. It was noticed that the flow fully equilibrated only much later downstream, however examination of this was beyond the scope of this work. At the nozzle exit corner, an expansion wave was generated which further accelerated the downstream flow.

The change in momentum across the system was also determined by calculating the percentage difference between the area-weighted average of the dynamic pressure ($\rho U_\infty{}^2/2$) at the inlet and exit planes. The momentum increase across the system was found to be 64% in the OE case. Dynamic pressure may be used as an indicator of momentum change since it represents a measure of the average linear momentum of fluid molecules in a constant-mass flow rate in the system. The overall increase in momentum (and thus efficiency of the system)

was attributed to both the jet contributing additional momentum to the system (allowed by the porous system), as well as incident shock velocity being increased to accelerate the cross-flow. The flow properties of the jet were a result of the inclination and expansion ratio of the overexpanded nozzle.

The position of the vent exit and vent shape were also significant. To conserve as much momentum in the vents as possible, as little direction change and obstruction to the flow was required. Straight vents exiting further downstream enabled a more gradual direction change to better-conserved momentum while the pressure ratio was favourable, resulting in improved drag. The vent exit area was critical. Since the internal structure could not easily be altered, the exit area was the only way to match the pressure ratio.

With regards to the three sources of change in drag, the OE presented a highly mixed result. The wave drag was slightly reduced by the presence of the pores, however, due to the surface bleeding this effect was limited. From the jet interaction, a significant increase in drag was noted, since the interaction between the crossflow and the overexpanded jet resulted in significant momentum loss and energy dissipation to the environment. However due to the highly accelerated jetting and vent angle, positive momentum addition to the freestream occurred. Thus in terms of momentum recovery, it is difficult to precisely define the effect. Whilst there are factors which improved recovery, allowing for a momentum increase to be established (such as the inclined nozzle), the overall effect is destabilising on the flow, with significant pressure losses. As such, whilst the overall drag increases by 35%, the exact drag contribution of each component in the OE case requires further analysis.

Venting comparison - BS3 vs BS4 vs OE

The positive effect of less-overexpanded jets is noted when comparing BS3 to BS4. While both vents produced overexpanded jets, BS3 was less overexpanded than BS4.

In BS3, the lesser-expanded vent resulted in a higher exit pressure than in BS4. Less suction of the crossflow into the vent was induced as a result, reducing the separation bubble at the lower nozzle wall. The smaller separation bubble reduced the intensity of the interaction between the nozzle-corner shock wave and the bubble, meaning that the jet was less narrow,

and a result far closer to the pressure-matched ideal state was achieved. The larger jet meant that greater momentum addition to the flow field occurred, resulting in strong drag reduction from the BS3 vent configuration. For the porous pointed cone crossflow generated, the venting drag reduction experienced with the BS3 was greater than the BS4 vent. If the wave drag reduction in BS3 was improved (by reducing the surface bleeding), the overall drag reduction from all three components (wave, jet, and momentum) would be greater than BS4.

It should be noted that the analysis of BS3/BS4 confirms that the overexpanded nozzle configuration represents a highly sensitive spectrum for nozzle performance. BS3 and BS4 produce strong drag reduction capabilities, however, BSOE provides a mixed result, with some aspects improving and others worsening the performance. As such, OE venting geometries can be used successfully, however careful balance is required to ensure the negative aspects are mitigated as far as possible.

Applicability of OE vs CE venting configurations

An additional observation was that an OE flow field would be less sensitive to real-life conditions than the critically expanded configuration. In a real-life system where $P_e = P_b$, any change in direction (especially pitch) would cause the critically expanded (CE) pressure to no longer hold as P_b was changed. This is unrealistic for any projectile. In an OE configuration, $P_e < P_b$ already, meaning direction changes have a less dramatic effect on the venting performance. In conclusion, while BSCE might have an ideal drag reduction at a single angle of incidence, BSOE may have an adequate drag reduction at many performance conditions. This is a design trade-off which requires further investigation.

Applicability of OE vs CE venting configurations

The OE performance was also decreased as the OE vents experienced slight interference with the neighbouring vents. 3D flow effects were noticed in the region around the vent exit and the jet. The vent exits were very large, with little area existing between the neighbouring holes. This caused the flow exiting the vent to merge and interact with the flow in the neighbouring hole. In the OE case, this was problematic as the flow inside the nozzle (and the flow outside) was already being sucked back inside. The merging of the excess fluid

outside of the vents worsened the suction by increasing the pressure difference and reducing the nozzle efficiency. It was suspected that this neighbouring bleed also contributed to the worsened drag performance in BSOE.

To fully describe this region of the flow field, the 3D interaction of the bow shocks with the jets, as well as the cross-flow between the jets, required investigation. Due to the complexity of these interactions, and the limited scope of this work, the jet interactions have been left for future work.

7.6.2 Underexpanded configuration

The opposite extreme to the overexpanded nozzle was the underexpanded venting configuration, known as the BSUE cone. The expansion ratio of the UE nozzle was $(A/A^*) = 4.86$, corresponding to a nozzle exit flow of Mach 3.15 (mid-supersonic, closer to freestream condition M = 3.5). The vent inlet area was the same as all of the other vent configurations, however the exit area was made very small in order to investigate the effect of contracting the flow. As before, the three sources of change in drag (wave drag, jet interaction and momentum addition by the jet) were examined in order to determine the overall effect of the combined cunicular porous cone and underexpanded vent on drag reduction.

In the underexpanded flow, the crossflow pressure (back pressure) is lower than the jet exit pressure. Because of the mismatch in pressure, the flow continues to expand outside of, and beyond, the nozzle exit. The presence of external expansion means that proper momentum recovery is impossible, thereby reducing the performance efficiency of the nozzle (and thus limiting the amount of drag reduction possible by momentum recovery). This momentum cannot be converted into thrust and is dissipated to the surrounding flow, where the thrust effect of the jet is greatly reduced.

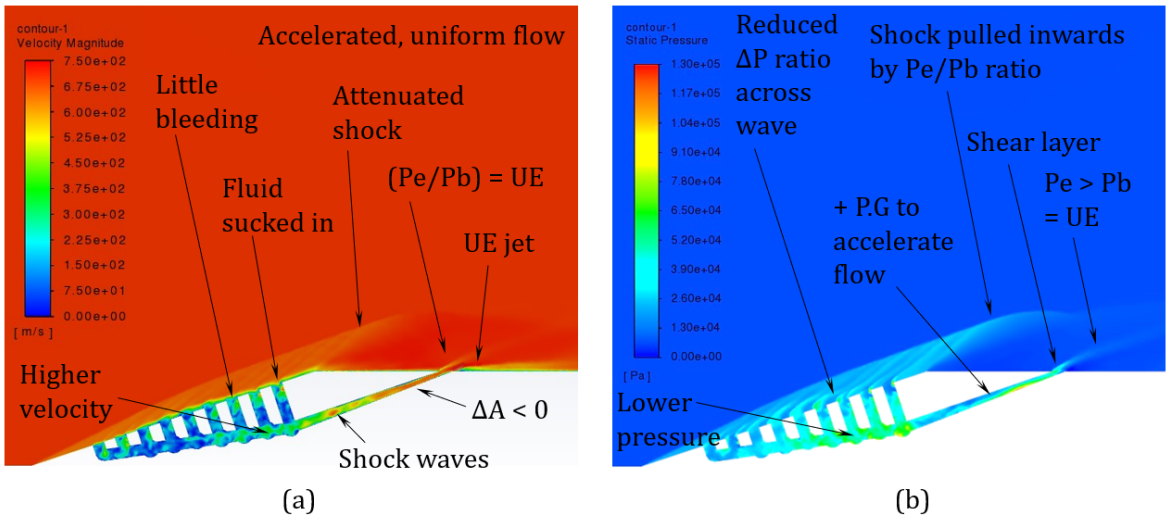

Figure 93: Mach flood plot of the BSUE model a) velocity b) static pressure in the ZY symmetry plane at Mach 3.5.

From the velocity plot in Figure 93 a), the flow choked inside the nozzle at the vent inlet, as before. Unlike the OE case, the flow inside the UE nozzle was uniform and smooth, with a very small separation bubble at the nozzle exit. The nozzle geometry caused an underexpanded supersonic jet to form outside of the nozzle, which impinged on the turbulent supersonic cross-flow. At the nozzle exit plane, the static pressure inside the jet was far greater friction-induced loss than that of the external free stream. As with the other venting cases, the drag reduction and porous flow field were still characterised by the bow wave angle (and size), and the size of the jet.

From the maximum area at the vent inlet (at Mach 1), the cross-sectional area of the duct decreases. To maintain continuity, the reduction in cross-sectional area necessitates an increase in flow velocity. The acceleration of the flow is linked to a decrease in pressure according to Bernoulli's principle. The flow reaches its maximum velocity at the nozzle exit. As the supersonic jet exits the nozzle, it expands continually in an attempt to match its pressure with that of the surrounding crossflow, however, this is impossible. The mismatch between the exit pressure and ambient pressure can lead to the formation of shock waves in the jet. As in the OE case, the internal flow field of the jet is highly complex and detailed, requiring further investigation in order to further improve drag performance and reduce overall losses.

As the accelerating supersonic flow travels through the duct, a small deflection of the flow occurs due to the direction associated with the inclined nozzle, generating weak shock and

expansion waves inside the duct. This is visible as the pockets of high-velocity wave interactions and reflections on the nozzle walls in Figure 93 a). These compression waves result from the abrupt changes in pressure, density, and temperature as the high-speed jet encounters slower-moving ambient air. The presence of these shocks represents an increase in entropy within the duct and an associated loss of momentum/energy. This means that fluid exiting the vent has less energy, and as such contributes less momentum addition to the free stream. The jet is therefore weaker overall.

From Figure 93, the UE case experiences significantly less bleeding (almost none) when compared to the OE case. It was noticed that in some of the cones, bleeding was excessively high (e.g. BSOE, HV, and BS4), however in the other models there was hardly any bleeding (the BSUE, BS0). Because the conic forebody of these models was identical, it was identified that the design of the vent design was the primary cause of the bleeding (or lack thereof).

As with the other BS models (with the combined cunicular conical forebody and venting system), BSUE also behaved as a quasi-CD nozzle. The converging (inlet/internal) section at the cone was constant, drawing flow in and choking it within the porous structure of the cone. The diverging part of the nozzle (the UE vent) was dependent on the pressure ratio between the nozzle exit and the atmosphere. If $P_e > P_{back}$, then an underexpanded jet formed, as in BSUE. Because of the pressure difference established, and there being equivalently too much pressure within the nozzle at the exit, the flow was drawn out of the nozzle further, into the crossflow. The flow being sucked out of the nozzle affected the upstream porous condition.

The flow at the BSUE inlet behaved similarly to the BS0 case, where only slight uniform bleeding from the surface was experienced, as demonstrated in Figure 93 a). The contracting vent geometry and underexpanded pressure ratio across the vent exit caused the pressure in the internal network to reduce in order to match the freestream. This resulted in lower pressure just under the porous surface (and in the toroids, visible in the last four pores), encouraging high levels of inflow from the BSUE inlet surface. The increased inflow caused a higher mass flow rate in the aft-most toroid, which allowed the flow in the vent to be accelerated very efficiently in the contracting vent.

The wave angle was reduced as the energy from the shock wave was absorbed into the shock and the pressure ratio across the wave was reduced, reducing the strength of the bow wave. The size of the wave is visibly reduced in Figure 93 a). The BSUE cone reduced the drag by 32%, and the BS0 by 3%. Both utilised underexpanded nozzle configurations. The efficiency of the inflow into the inlet/internal system was significantly improved when utilising the underexpanded vent configuration, as the UE expansion ratio allowed for sufficient outflow and jetting to support high inflow. Additionally, very good wave drag reduction was achieved in the underexpanded configuration when suitable venting was applied.

This explains the poorer drag behaviour of the BSOE configuration. The OE jet pressure ratio was too high, causing the flow inside the nozzle to be pushed further inside. In order to compensate, the pressure in the converging system was increased, as indicated by Figure 92. The pressure was the highest at the final toroid and reduced towards the cone tip. The pressure in the pores was increased, however the porous incident shock pressure remained the same (lower). This caused the pressure-affected flow to be pushed out of the pores and into the shock region. This was possible because the fluid in the pores was very slow, meaning that the dynamic pressure effect was limited and the static pressure dominated.

A shear layer region existed between the porous inflow and oblique shock wave in Figure 93. This surface formed as a result of the different velocities between the adjacent layers of fluid between the shock and porous regions. The shear layer is inherently associated with the boundary layer visible at the porous-wall boundary, where significant changes in velocity and pressure were observed. The boundary layer on the solid cone surface was originally laminar and smooth, with a uniform fluid motion. Upon interacting with the addition of the surface pores, the boundary layer underwent the transition to turbulent flow. This is evident in the latter pores of the OE case, where the boundary layer increases in size periodically with the fluid. The boundary layer flow at the porous boundary is non-uniform, where the turbulence in the boundary layer contributed to the formation of the shear layer.

The reasons discussed describe why shear/boundary layer formation was worse in the models with high bleeding (where the bleeding and thickened boundary layer and shear layer occurred). Additionally, no bleed was present in the UE model as the configuration acted as

a boundary layer control mechanism where suction reduced the momentum thickness of the boundary layer. The shear layer contributed to the incident shock wave behaviour.

The change in drag associated with the cunicular bodies was due to the incident shock wave attenuation and the effect of the jet. In the cases with no bleed (BSUE cone), a much smaller, weaker incident shock wave was noticed on account of there being less obstruction to the inflow through the surface pores. This resulted in increased energy absorption from the shock wave into the porous system, reducing the momentum loss across the shock wave and reducing the wave angle. Simultaneously the normal component of the shock wave was reduced, resulting in a weaker bow wave. This is the same wave drag reduction mechanism utilised in all of the BS models, however BSUE is particularly efficient due to the venting configuration. Because the pressure downstream of the shock was lower due to the UE nozzle configuration, the incident shock wave is 'pulled' down by the pressure difference, reducing and weakening the size of the wave and wake.

Conversely, in the OE case, the pressure downstream of the shock was higher than that of the shock. In order to equilibrate and match continuity, the shock wave was pushed outwards and extended to increase the shock area so as to lower the high pressure under the shock. This increased the cross-sectional area of the shock wave, increasing the drag. The incident shock wave was better controlled in the UE case. The inlet flow was designed to manage the incoming flow so that sudden pressure changes were avoided.

The momentum increase calculated across the UE system was 15%, less than the OE case. This was expected for several reasons. Because of the UE vent geometry, P_e/P_b was closer to 1 (the ideal case), when compared to the OE case, even though it was still underexpanded. The Mach numbers of the crossflow and jet were very similar, and so were the pressures. The jet area was also far smaller, thus less turbulence and acceleration were introduced to the crossflow and consequently less momentum loss occurred. However, The UE nozzle behaved the most like the ideal $P_e = P_b$ case, resulting in minimal pressure losses and strong drag performance. For application purposes, BSUE presents a strong case (along with the lesser-expanded BS4 vents) as it experienced very little bleeding and separation at the conic front, indicating good incident shock performance, as well as minimum pressure losses from the

vent. Both overexpanded (BS4, or less-overexpanded) and underexpanded vent configurations have performance advantages and disadvantages, where the disadvantages in each case must be carefully considered in order to determine the configuration with the greatest real-life applicability.

7.6.3 Horizontal Vent

The HV utilised the same BS0 conical porous forebody design, however applied a slightly-expanded, horizontally-positioned venting configuration which exhausted from the cylindrical base. This investigated the effects of base-venting, as opposed to the shoulder-venting present in all the other BS models. As such, the effect of zero freestream-jet impingement on the drag performance was of interest. The HV underexpanded vent geometry was: $(A/A^*) = 2.72$, corresponding to an exit flow of Mach 2.53.

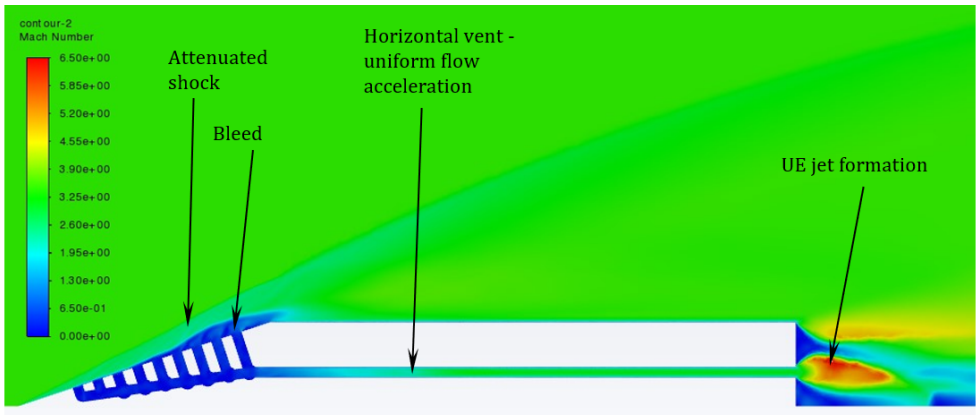

Figure 94: Mach flood plot of the a) HV model in the ZY symmetry plane at Mach 3.5 (Mach 6 shown to include base jetting).

Figure 94 demonstrates the Mach contour flood plot for the BSHV nozzle configuration in the ZY-plane at Mach 3.5. A higher Mach number is plotted to visualise the base-venting. Figure 94 depicts the base of the cone to show the underexpanded jet formation at the exit.

Two calculations were performed for the HV: including the base drag (as depicted in Figure 94), $C_d = 0.79$ (65% drag increase from the solid cone); excluding the base drag (the HV cone attached to an infinite-cylinder, as with the other conic models), $C_d = 0.44$ (36% drag increase). As expected, the base drag greatly increases the overall drag of the body, however

even with the infinite-cylinder model the drag was still worsened using the horizontal venting configuration.

As Figure 94 indicated, the conic front of the HV behaved similarly to the previous cases, where not enough outflow was available to support the inflow and separation occurred at the porous boundary.

The HV further confirmed the effects of the venting angle. The horizontal vent does not allow for the freestream momentum to be increased in the same way as the shoulder-vented models, however, this is potentially advantageous. The HV allows for direct, undisrupted mass transfer through the cylindrical base. Very little momentum is lost in this venting configuration as very limited direction change is observed.

An underexpanded jet is formed at the base, however, the effect is not strong enough (and is too far downstream) to reduce the size of the bow wave around the body, as in Figure 94. This suggests that the expansion ratio of the H-vent must be increased such that the exit pressure may be lowered. P_{exit} (the base pressure), is associated with wave drag. In this case, the cylindrical base behaves most similarly to the underexpanded nozzle geometry described earlier, where an underexpanded jet is exhausted from a symmetrical nozzle. The difference in pressure between the higher-pressure vented fluid and the lower-pressure ambient region contributes to increasing the overall drag experienced by the body.

The horizontal effect has a profound impact on the aerodynamic performance and understanding of the effect of the vent. All of the other vents exhaust behind the cone-cylinder shoulder, resulting in a jet which impinges on the crossflow. This impingement was either constructive or destructive depending on the pressure condition the jet induced in the post-shock freestream. The HV vented from the cylinder base, meaning that it had no direct influence on the downstream flow after the shock. This confirmed several points. Firstly, the conic forebody was directly influenced by the vent geometry. Extremes in the vent geometry caused bleeding from the pores which reduced performance by interfering with the bow shock wave. Additionally, it confirmed that the relationship between the system back pressure (at the vent exit) directly affected the ability of the porous network to retain or extract the fluid. It also showed that having the vent exit at the shoulder can be a very useful tool for

increasing flow momentum and reducing drag, as in the UE and OE vents. The system is very sensitive to vent geometry and orientation.

The HV configuration performance could be improved by increasing the expansion ratio of the vent or by modifying the vent exit to a bell nozzle geometry to improve the pressure differential.

7.7 BS4 in Ellipsoid, Hemisphere and Secant Ogive

The porous configuration with the greatest drag reduction (BS4) was introduced into the other solid shapes (hemisphere, ellipsoid and secant ogive) to investigate its effect on bodies of varying curvature and radius.

7.7.1 BS4 Ellipsoid

Figure 95 demonstrates the Mach number flood plot of BS4 ellipsoid and cone a), c) next to the solid ellipsoid b), d) for a freestream Mach number of 3.5. The BS4 Ellipsoid had a drag reduction of 40% compared to the solid ellipsoid, the greatest drag reduction of the study. The ellipsoid has varying curvature and a detached bow shock wave. Despite its venting configuration being classified as 'BS4/less-overexpanded', the BS4 Ellipsoid exhibited critically expanded jet behaviour from the vents.

As Figure 95 a) shows, the elliptical shock wave strength is attenuated by the presence of the pores, as indicated by the higher average Mach number of the wave, as well as the reduced overall size of the wave when compared to the solid. The sonic line separating the subsonic and supersonic regions of the flow behind the bow shock occurs just before the first pore, as indicated. This confirms that the flow around the pore boundary is supersonic, as in the previously discussed pointed cone cases, whereby the same discussion applies. For future studies, the position of the first pore is significant depending on where the sonic line is generated. The strength of the bow wave is greatly reduced, particularly around the vent exit region, proving that the wave drag attenuation is influenced by the jetting.

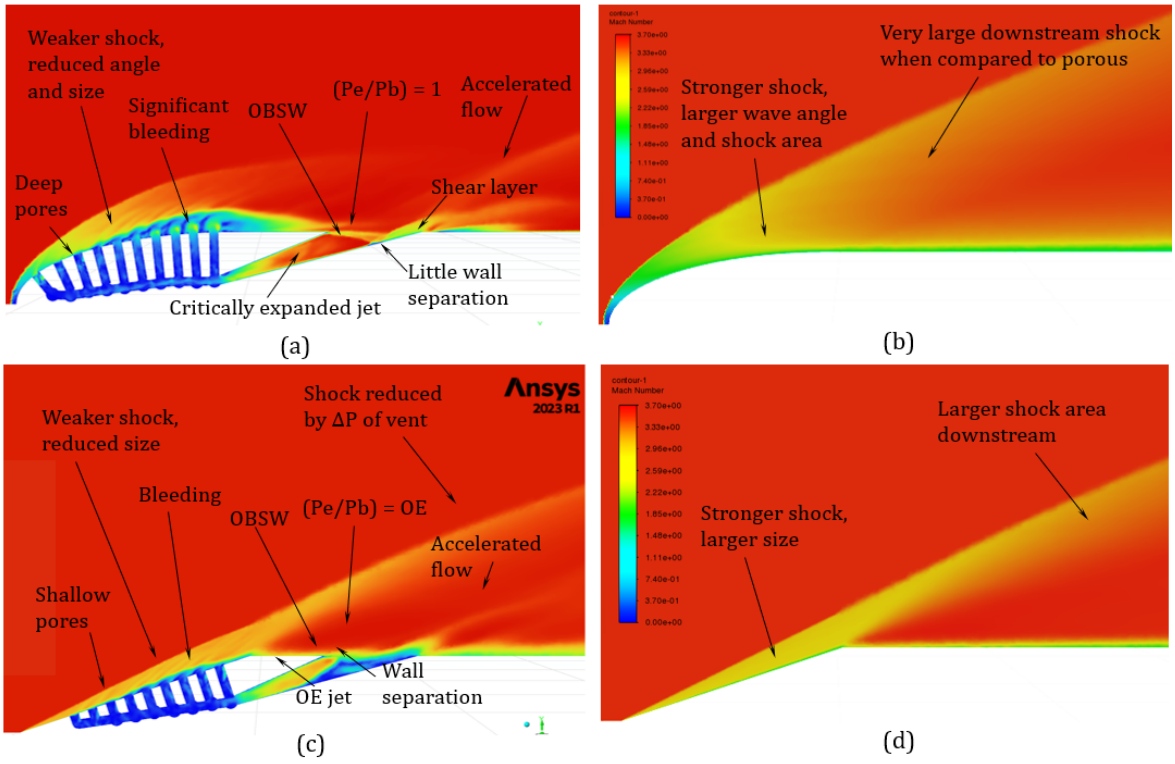

Figure 95: Mach flood plot of the a) BS4 Ellipsoid b) BS4 Cone models in the ZY symmetry plane.

The internal porous flow field was largely the same as the pointed cases, however, more bleeding from the conic front was noticed on account of the toroidal pores in the ellipsoid being much deeper than in the conic cases. The internal area of the internal porous ellipsoid structure was greater than that of the cones, thereby increasing the internal pressure more and establishing an adverse pressure gradient across the porous boundary. As in the OE cases, this resulted in the fluid being pushed out of the ellipsoid. This effect was slightly worsened by the increasing curvature of the body.

Critically-expanded nozzle - BS4 Ellipsoid

The venting configuration of the BS4 Ellipsoid exhibited the greatest nozzle performance. For the BS4 vent in this shape, $P_e/P_b \sim 1$ (very close), where in effect the vent behaved as a critically-expanded nozzle. This is demonstrated in Figure 96, where the velocity and pressure matching of the jet and crossflow are visible in a) and b), respectively.

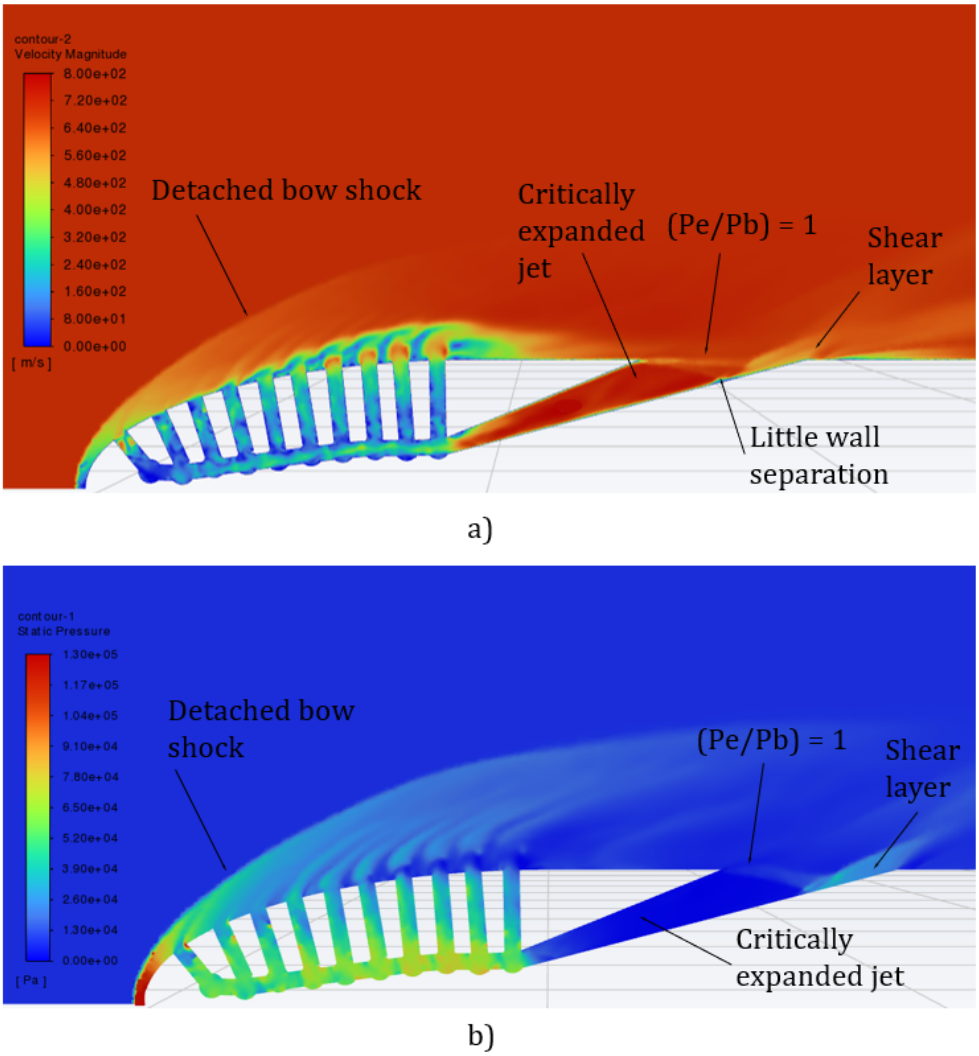

Figure 96: Mach 3.5 BS4 Ellipsoid critically expanded a) Mach contour flood plot b) static pressure contour flood plot in the ZY-symmetry plane.

By matching the exit and ambient pressure conditions at the nozzle, no separation was induced on the lower nozzle wall, as indicated in Figure 95 b). At the upstream nozzle exit corner, the oblique shock wave was generated, cutting across the nozzle (as indicated by the lower-velocity wave region), and hitting the lower nozzle wall. This shock-wall interaction did induce slight separation, as shown by the small blue region, on account of the adverse pressure gradient interaction with the nozzle wall boundary layer. Comparison with the BS4 cone confirmed that the OE nozzle P_e/P_b was the cause of the separation bubble which affected the flow field so dramatically. The interaction region between the cross-flow and jet was cumulative and positive, whereby the similar Mach numbers and pressures of the streams resulted in very low momentum loss and energy dissipation across the impingement.

As the shock wave generated at the upstream nozzle corner cut across the vent (known as a jet bow shock) hit the separation region, a strong velocity gradient was induced at the boundary of the shock front, forming the shear layer. The shear layer was encouraged to move upwards by both the accelerated flow leaving the vent and by the increased fluid momentum influencing the flow direction. The shear layer size was increased by the separation region at the wall and the adjustment of the fluid to the surrounding flow. The shear layer encountered the expansion wave generated at the cone-cylinder shoulder, which rapidly accelerated the flow velocity and redirected the flow to the freestream direction.

The BS4 Ellipsoid vent closely resembled a critically expanded nozzle. The vent configuration maximised thrust efficiency (force acting normal to the surface, horizontal here) by matching the exit condition to the ambient pressure, where no under or overexpansion was present. As discussed, overexpansion caused excess pressure within the nozzle, while underexpansion resulted in wasted energy resources. The CE configuration minimised the formation of the shock waves within the nozzle and at the exit by maintaining the optimal exit pressure. By reducing the shock wave contribution, aerodynamic drag was reduced. Most importantly, by design the critically expanded nozzle minimised flow separation, whereby little exhaust flow detached from the nozzle surface. Flow separation created additional drag while reducing the propulsive efficiency. The resultant nozzle flow was more streamlined and efficient, with less turbulence and aerodynamic losses. The above factors caused the drag coefficient of the conic body to reduce, allowing for higher velocities and increased efficiency in supersonic flight.

By utilising angled venting, momentum is being recovered that would otherwise be lost (normal vent). This recovered momentum produces a propulsive thrust component which augments drag reduction.

7.7.2 BS4 Hemisphere and BS4 Secant Ogive

Figure 97 demonstrates the Mach contour flood plot for the BS4 hemisphere and secant ogive a), c) next to the solid hemisphere and secant ogive b), d) at freestream Mach number 3.5. The BS4 Hemisphere and BS4 Secant Ogive models were both found to increase the

aerodynamic drag, by 16% and 25%, respectively. The hemisphere has constant curvature and a detached shock wave, while the SO has an attached bow wave and varying curvature.

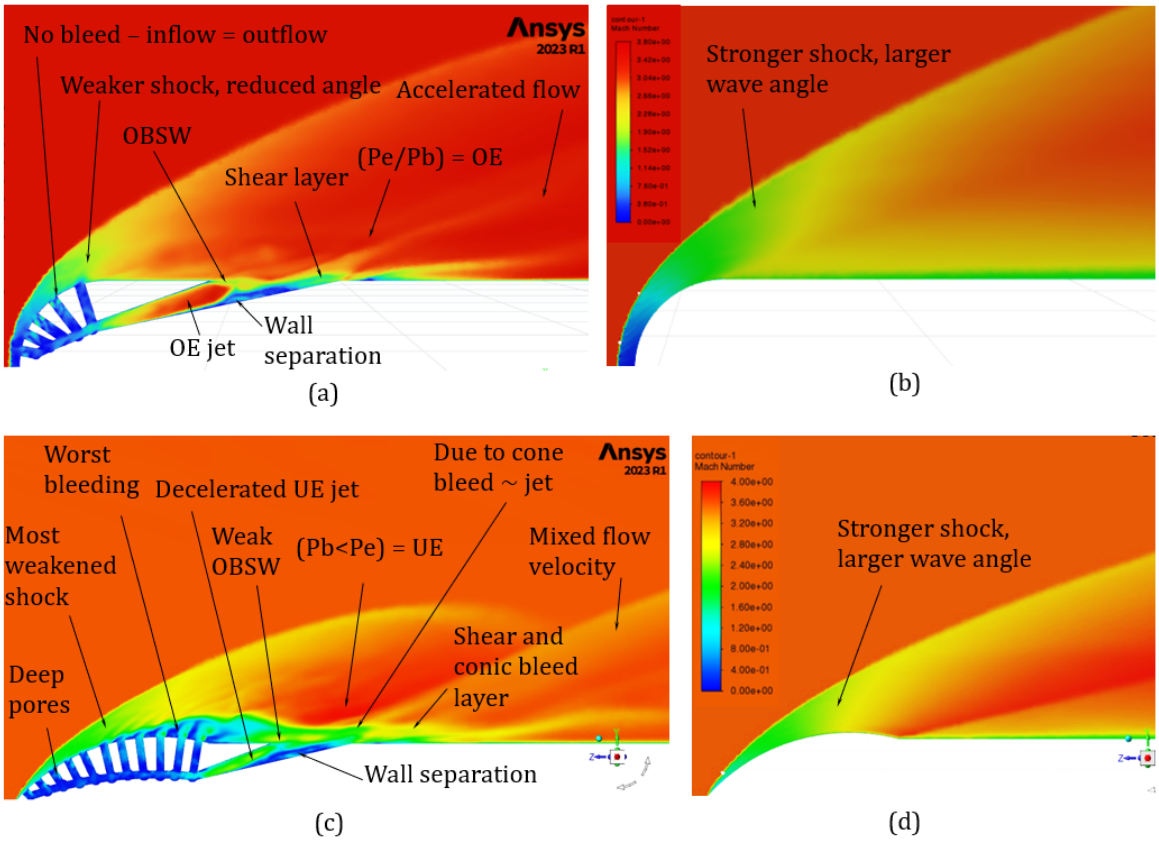

Figure 97: Mach flood plot of the a) BS4 Hemi b) BS4 Secant Ogive models in the ZY symmetry plane.

The secant ogive represented a body with the combined geometric properties of the pointed cone and ellipsoid. The internal section of the SO behaved similarly to the BS4 Ellipsoid, with the same upper cone front bleeding. The porous SO greatly affected the bow shock wave in the same way already described, where the reduction in overall wave size and angle is visible in Figure 97 c) when compared to the solid d). However, the drag was worsened by several contributing factors. A significant underexpanded jet formed in the venting structure. The pressure change that this induced inside the porous structure caused significant jetting from the later pores at the cone surface, which bled into the freestream towards the vent. A large pool of low-supersonic flow covered the cone shoulder, vent, and downstream, rapidly increasing the ambient pressure. This altered the P_e/P_b, forming a large underexpanded jet and separation bubble at the lower wall. This case presented very good shock attenuation, however poor vent performance. The region between the latter half of the cone and the vent

greatly disrupted the flow field, introducing highly unstable flows with mismatched freestream and cone-affected regions. In particular, there was no drag reduction caused by either the jet interaction or momentum addition. This result suggested that the total aerodynamic wave drag was heavily governed by the vent interaction and the momentum addition of the vent, as an overall negative drag result was achieved because of these mechanisms, even though the shock angle and wave drag were reduced. The aerodynamic effects cannot be conclusively defined on the secant ogive without further investigation and modelling.

The porous hemisphere represented a model where fewer inlet holes were possible due to the shape. The BS4 hemisphere behaved similarly to the BS4 cone with an overexpaned jet, however, the crossflow condition of the hemisphere resulted in a worsened drag result. The hemisphere generated a bow shock, resulting in a slower supersonic post-shock flow at the vent exit. The post-shock flow experienced more turbulence and instability on account of the bow shock, however, the P_e/P_b ratio still applies. The deep, perpendicular entry pores do not exhibit bleeding because the hemispherical frontal surface experiences far less inflow than the other shapes, and thus the outflow supplied by the fourteen vents (as in the other cases), is this time enough to sustain the inflow at the correct balance, resulting in complete inflow with no bleed. As shown in Figure 97 a), significant bow wave shock attenuation was achieved due to the high levels of inflow, where a higher post-shock Mach number and reduced wave angle are observed when compared to the solid wave.

This successful inflow-to-outflow ratio allowed for strong bow wave attenuation and outflow through the vents. However, the overexpanded jet present in the BS4 hemisphere was greatly hindered by the hemisphere crossflow, more so than in the BS4 cone overexpanded jet. The reason for the drag increase was due to the vent interaction and momentum increase caused by the vent. The vent expansion ratio required a very high crossflow Mach number and low back pressure in order to match the exit condition. Because the crossflow was generated from a blunt hemisphere, the flow Mach number interacting with the vent was lower-supersonic (around Mach 2.8). This mismatch in pressure caused a significant overexpanded jet to form in the vent, introducing considerable momentum losses to the flow field.

The BS4 SO and BS4 Hemi wave drag reduction were comparable, and the jet interaction in BS4 SO was far more disjointed than in BS4 H (due to the pool of low-subsonic flow blocking the vent), indicating that the drag was worsened more in the SO due to the loss of momentum from the system over the large bleed region. The results of BS4 SO, BS4 H, BS4 Cone and BSOE demonstrate that the venting geometry is highly complex and that over-or-under expanded jetting may occur in any shape, depending on the incident Mach number and geometry of the solid cone. As such, careful design consideration is required when designing these systems, as the results indicate that many factors are at play.

7.8 Internal Flow Field

The internal flow field was found to control the behaviour of both the inlet and venting structure simultaneously and largely decided whether a positive or negative effect on performance occurred. The internal flow field is centred around the pressure and velocity gradients within the internal porous network, specifically those around the aft-most toroid/vent inlet. The internal flow facilitated communication between the inlet and venting structures. The internal flow field was responsible for the amount of bow shock attenuation possible, and directly affected the vent performance by dictating the choking location in the venting pore.

7.8.1 Internal network fluid behaviour

The internal network refers to the porous structure held within the conical forebody and comprises the combined longitudinal, toroidal and radial pores. The movement of fluid into and around the structure, as well as key points of interest, are shown in the greyscale Mach streamline plot of the BS4 internal structure in Figure 98. The internal network behaves as a mass and momentum transfer route for the fluid flow in order to effect a set of mechanisms for drag reduction.

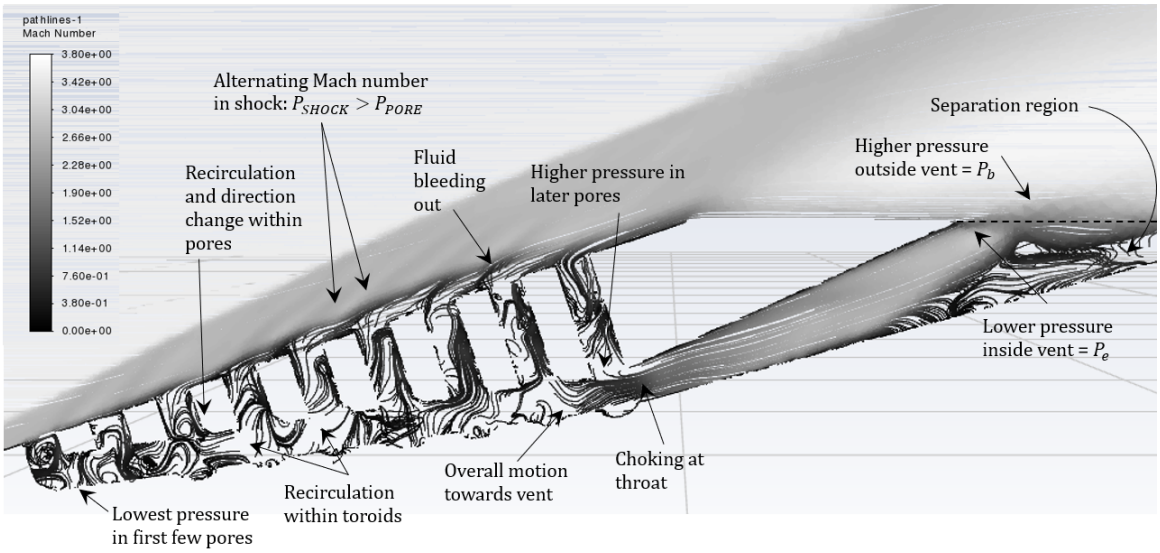

Figure 98: Velocity streamlines the BS4 cone coloured by greyscale Mach number, key internal flow features labelled.

Due to the flow entering the internal network through the surface pores as mass inflow, an equivalent 'inlet area (A_1)', was defined, as equal to the sum of all the surface hole areas around the cone. The flow then travelled to the vent inlets, where the choking area ($A*$) was defined as the sum of all of the vent inlet areas. The surface pores and channel diameter were kept constant at 2 mm, however, the toroid diameter was 3 mm. The vent geometry was patterned around the z-axis, meaning that the vent inlet area was the same at each vent location.

Once the flow was inside the channels, the highly viscous, subsonic flow moved downstream by conservation of fluid momentum and the internal pressure and velocity gradient. Inside the internal network, very little area contraction, and by extension flow acceleration, occurred. The pressure across the internal system also changed only slightly for the same reason. Even so, a favourable pressure gradient was achieved which encouraged flow motion towards the vents. As the vent was approached and the flow area compressed, the sound speed decreased as the flow was compressed as the Mach number increased. During this time, the main purpose of this region was to allow for pressure redistribution and regulation between the inlet and venting systems.

For the 'converging' section of the porous system, the equivalent cross-sectional area decreased from the inlet pores to the (far smaller) vent inlet. This increased the fluid velocity in the

converging section in order to maintain continuity. Due to the Venturi effect, the pressure in this section decreased in the direction of the airflow, establishing a favourable pressure gradient which created a driving force to accelerate the fluid to its maximum velocity at the throat (vent inlet). At the throat, the sonic condition was reached, and a vanishing strength shock formed as in Fig 88 b).

When the flow reached the vent inlet, the flow area was rapidly constricted to the narrowest point in the system, causing the flow to be accelerated to the sonic condition. It was at this point that the porous forebody was said to behave as a 'converging nozzle', since the flow area was decreased from the inlet (A_1) to the vent inlet area ($A*$), causing the velocity of the flow to increase by conservation of mass (where the mass flow rate is constant). As the flow velocity was increased, it eventually choked and reached the sonic condition at the throat. At this point, further reduction in the nozzle area would not increase the flow rate but rather cause maximum flow velocity to be achieved in the converging nozzle, dictated by the speed of sound. After the vent inlet, the vent geometry expanded to accelerate the flow to supersonic speeds, exhausting at the vent exit outside of the cylinder.

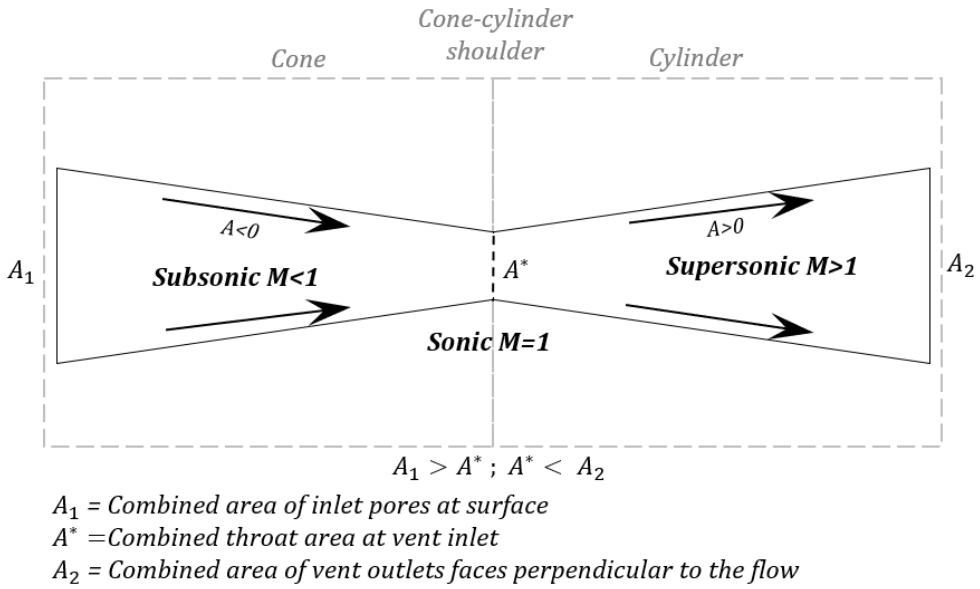

Figure 99: Schematic of the equivalent converging-diverging nozzle created by the porous cone.

From the analysis of the BS0 - BS4 cone, it was confirmed that the porous system (inlet, internal and venting) behaved similarly to a quasi-CD nozzle. The traditional geometry of a CD nozzle is demonstrated in Figure 99, with the inlet area A_1, choking area $A*$ and outlet

area A_2 illustrated. From Figure 99, the subsonic flow in the converging section is accelerated to the sonic condition (M = 1) at the minimum area (the throat). Thereafter, the flow is further accelerated to supersonic speeds at the exit by area expansion of the diverging section.

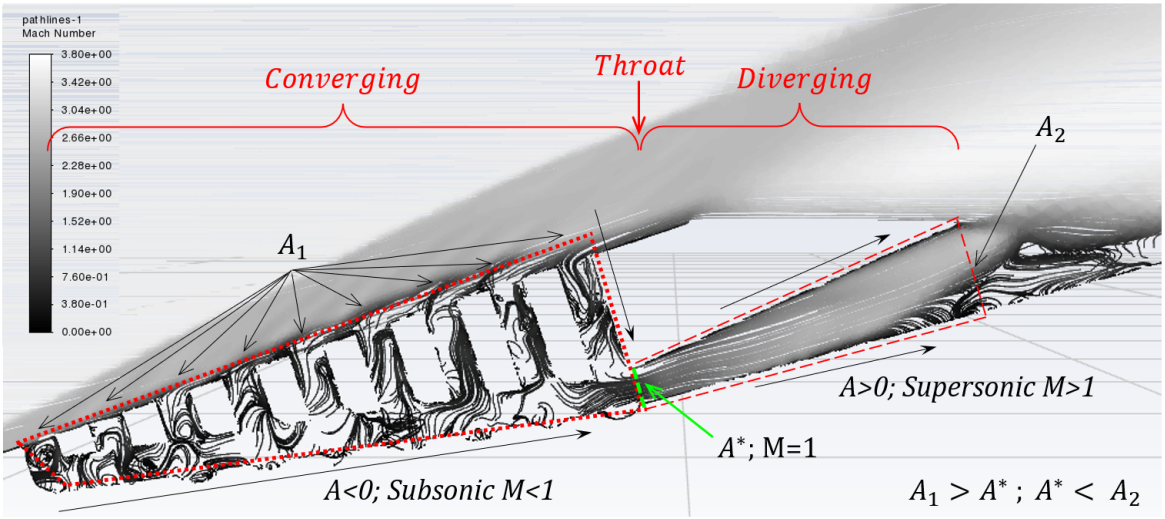

Figure 100: Velocity streamlines the BS4 cone coloured by greyscale Mach number. The inlet 'converging', outlet 'diverging', and choking sections are illustrated.

In the porous system, the same behaviour is observed, however, A_1 is equivalent to the combined surface pore inlet area, $A*$ is the combined vent inlet area, and A_2 is the combined vent outlet area. Figure 100 shows the CD-nozzle application to the cunicular system in detail. In this, the porous cone forebody is the diverging system (As $A_1 > A*$), and the venting structures are the diverging section ($A* < A_2$). Supersonic flow from the atmosphere entered the system at A_1, where it was immediately decelerated to the low subsonic regime across the surface pore boundary. The flow then moved through the internal network to reach the vent inlet $A*$ (sum of the face areas of the vent inlet), where it choked before being accelerated supersonically through the diverging vent to reach the exit area A_2 (sum of the venting pore exit faces perpendicular to the free stream). Figure 99 depicts the equivalent systems.

Depending on the combined arrangement of the internal, inlet and venting structure, a particular mass flow rate is achieved at the vent inlet, which remains constant through the diverging section. An increased vent mass flow rate leads to greater momentum at the vent exit (further improved by lower vent exit angles), which increases momentum transfer to the freestream from the jet. This in turn reduces the effect of drag on the body. Additionally,

the higher mass flow rate of the fluid exhausting from the vent may provide an additional thrust effect, which can offset the drag force acting on the body.

The balancing of the expansion ratios between the converging and diverging sections of the porous structure was found to be critical to the successful drag reduction of the system. The expansion ratio of the converging section was defined as $(A/A^*)_{inlet} = A_1/A*$. Similarly, the expansion ratio of the diverging section was defined as $(A/A^*)_{outlet} = A_2/A*$. $(A/A^*)_{inlet}$ was fixed for this research, as per the BS0 internal network, and only the diverging section ratio was explored through different venting geometries. If the converging and diverging (inflow and outflow) systems were unbalanced, several issues could occur. These included:

- Excessive bleeding from the cone surface - due to not enough inflow to balance the outflow between the two systems, i.e. the flow cannot be retained in the structure.
- Over/under expanded jets due to vent geometry - resulting in increased drag, and choking at the incorrect location (i.e., too far down the vent).

In particular, if $(A/A^*)_{inlet}$ was too large, the vent would choke too far downstream and optimal diverging nozzle performance could not be achieved. This was expanded upon in Section 7.6.

The system was dependent on the pressure ratio between the ambient pressure outside of the vent and the vent exit. If the pressure ratios are not balanced such that the correct gradients occur, then the diverging system could support the converging system, and the flow within the pores would be pushed back into the atmosphere through the inlet pores. The pressure gradient also induces the suction by which flow enters the system and greatly contributes to the working of the flow system. Therefore controlling the balance was critical. Since the inlet geometry was fixed, this was controlled by the vent geometry.

7.8.2 Pressure gradient in the internal structure

Inside the cone, the three-dimensional porous structure was found to have a significant effect on the behaviour of the fluid. The circular shape of the toroid encouraged the flow to

circulate continually within each ring. At the location where the staggered toroids merged with the longitudinal channels, a space was created where the two flows could mix together and recirculate within these cavities before moving to other structures. The toroids behaved as pressure-redistributing structures. Inside the cone, the flow was subsonic, mixing and recirculating within the pores. Figure 100 shows the motion of the fluid downstream, as well as the circular arrow path depicting the recirculation. The radial behaviour of the toroids is critical to the recirculation. The doughnut-like shape of the toroid means that fluid flows mainly along the radii of rotation, within the larger toroid structure itself. It is important to make the distinction that while there is local recirculation in the toroid sections in Figure 98, the most significant effect of the toroids occurs in the full, 3D shape.

The motion of the flow through the pores and towards the cone base was due to several factors. The pressure inside the pores was higher than the pressure at the vent inlet, establishing a pressure gradient. In the porous system (behaving as a quasi converging-nozzle), the pressure gradient was critical to the performance of the system, and influenced by the velocity and pressure of the flow within the pores. The gradient was high, enough to overcome the resistance presented by the porous geometry to flow, assisting in accelerating the flow to the sonic condition.

The strength of the pressure gradient affected where the normal shock wave would be located in the vent. The shape of the wave was also affected by its position. Depending on the conditions at the vent exit, the shock wave could occur as inclined or curved.

The pressure gradient also influenced the development of flow separation on the lower wall of the venting structure, particularly in the cases where the jet was overexpanded. This would in turn affect the shape and direction of the venting jet.

7.8.3 Jet Momentum

Internally, changes in velocity and direction redistributed momentum along the fluid elements. Inside the cone, a significant change in momentum transfer was observed. The level of momentum transfer was dependent on the fluid properties (such as velocity, density, and

viscosity), as well as the porous geometry. The system behaved in a somewhat contradictory manner, with some factors greatly increasing momentum whilst others decreased it.

Momentum recovery is critical for drag reduction as it assists in minimising the adverse effects of momentum loss in the flow field (in) and around the body. As the body travels through the fluid, it imparts momentum to the fluid which causes the flow to decelerate or change direction. This transfer of momentum results in a pressure gradient which generates aerodynamic drag on the body.

Several factors affected the momentum recovery of the system:

- Streamlined internal geometry - The internal channels were designed with streamlined shapes (smooth circular channels and toroids) in order to reduce momentum loss as the fluid moved through the structure. Smooth transitions between geometries and gradual bends helped to minimise turbulence and pressure losses, reducing momentum loss along the length of the porous system.
- Channel cross-sectional shape - The cross-sectional shape of the internal channels significantly affected momentum loss. Channel shapes which promoted uniform flow distribution, such as circular profiles used here, reduced momentum loss when compared to other irregular or non-uniform shapes.
- Channel length - Shorter pores with straighter paths were used to assist in minimising the severity of pressure changes and momentum losses when compared to longer, more convoluted pores.

Several factors increased momentum dissipation in the system:

- Porous-shock boundary deceleration - across the boundary, momentum decreased as the fluid transitioned from the supersonic to the subsonic regime, since velocity is directly proportional to momentum.
- Swirling/recirculation - recirculation zones (as in Figure 100 toroids) frequently experience increased turbulence and viscous dissipation. Turbulence in these regions dissipates momentum by internal friction, converting kinetic energy into thermal energy.

This dissipation decreases the momentum of the recirculating fluid, contributing to an overall loss in fluid momentum. Additionally, the recirculating fluid has the potential to block the channel by forming flow separation regions, creating areas of stagnant, low-pressure flow. The recirculating fluid may form eddies or vortices which effectively obstruct the channel by reducing the cross-sectional area available to the fluid. This blockage increases the resistance to the fluid, reducing the mass flow rate in the channel and impairing performance.

- Turbulence - the flow within the pores was highly turbulent, with a mixture of low and higher subsonic flow speeds, demonstrated in Figure 87. The average Reynolds number within the internal pores was 4380, in the turbulent flow regime where inertial forces governed the flow and momentum transfer was high. Several eddies and vortices were present, and increased mixing, particularly near the last toroid (as this pore experienced the greatest inflow) and at some corners. The complex geometry of the internal network increased the turbulence by introducing many sudden geometry changes. In channels, turbulence tends to increase momentum loss due to increased internal friction and energy dissipation.

From the factors listed above, the overall effect of the internal porous structure on momentum transfer and recovery is unclear, and thus further investigation is required. However, the flow choking at the vent area confirms that some momentum transfer successfully occurs within the internal network, indicating that while the system has factors which both contribute to and negate momentum recovery, the system is successful overall. The momentum transfer through the internal network ensures that a sufficiently large mass flow rate is achieved at the vent inlet, such that the flow in the vent may be successfully jetted into the downstream flow so that momentum addition may occur in order to reduce the incident wave strength and decrease drag.

7.9 Limitations

Several limitations were applied to the current work in order to simplify the extraction and understanding of the results. The limitations of this study are listed as follows:

- Only flow aligned with the axis was considered, i.e. viewing the flow field from other directions (e.g. from the front, from above), was not considered.
- The vent interactions were ignored due to complexity (2D or 3D from other directions).
- Only the flow field from the cone vertex to just after the vent was considered. Downstream flow interactions were ignored.
- Only cones with an infinite-length cylindrical base were investigated. As such the base interactions are unknown.
- Only a single angle of incidence was considered here.
- A single supersonic Mach number and cone half-angle were investigated here.
- Only axisymmetric bodies of revolution were considered here.

The limitations ensured that the scope of the project was manageable, however, there is significant room for further work in this field, as discussed in the recommendations section (Section 8.9).

Chapter 8

Conclusions

In order to determine the effect of organised porosity on aerodynamic drag reduction, an organised porous structure was inserted into different solid bodies of revolution. Four solid cone shapes were chosen to universally describe the geometric characteristics of conic bodies of revolution. Several types of organised porous channel arrangements were designed and applied to the solid conic bodies. The porous network included inlet, internal and venting channels for fluid momentum transfer. The conic models had a common $\Delta L/D = 1.5$, and an average porosity of $\approx 60\%$. Mach 3.5 ($\mathrm{Re} = 3.9 \times 10^5$) was chosen for the investigation. A numerical and experimental investigation was carried out in steady, supersonic flow, however the solution exhibited pseudo-transient behaviour due to the presence of unsteady elements in the flow field.

The supersonic wind tunnel facility at the University of the Witwatersrand was used for the experimentation, where schlieren photographic results were captured along with experimental drag force measured for the solid and baseline porous cones. Numerical pseudo-steady CFD simulations were carried out for a wider range of porous configurations using ANSYS Fluent R22.2. The experimental and numerical drag and flow visualisation results, in combination with the literature, were used for validation of the research methods. The shock wave reflections and interactions, expansion waves, momentum change and flow structures (steady and unsteady) in and around the porous body (inlet, internal and venting structures) are of

interest. The effect of these structures on the flow field, and the flow physics causing and affecting the behaviour is also relevant.

8.1 Validity and confidence

An extensive validation study was carried out in order to establish confidence in both the numerical method, as well as the experimental results. This was achieved by using well-established experimental and numerical methodologies presented. In conjunction with this, the presented results were extensively compared to the results of relevant, comparable literature. Both quantitative (C_d) and qualitative (flow visualisation images) numerical and experimental data were used for validation.

The experimental schlieren images closely mirrored the numerical images in terms of the key flow features, including bow wave angle, wave and feature shape, expansion fans and shock interactions. The presented flow visualisation compared favourably with regards to bow wave angle reduction and drag reduction through porous inflow (Poplavskaya et al. (2017), Mironov, Maslov et al. (2015), Maslov et al. (2019)). The presented experimental and numerical drag C_d values agreed within an acceptably small margin (less than 1% error) after statistical error analysis was applied. The presented drag values were also found to be comparable to the drag coefficient values published in the literature (Poplavskaya et al. (2017), Mironov, Maslov et al. (2015), Maslov et al. (2019)).

The validation study confirmed that there was good agreement between the flow visualisation, experimental drag measurements and the literature for the presented cone cases. The similarity of the results across the different bodies of work provides strong evidence that the numerical and experimental results and the method that produced them are reliable, repeatable and may be used with a high level of confidence.

8.2 Conic model drag reduction

Application of certain cunicular arrangements effectively reduced the drag in some shapes, while other configurations worsened the drag. In order to quantify the change in drag as a result of the porosity within the different shapes, three sources of change in drag were identified - wave drag, jet interaction, and momentum addition by the jet. These sources resulted from the flow interactions occurring within the inlet, internal and venting structures.

The intensity of the change in drag varied depending on many factors, including vent geometry, expansion ratio, exit angle, inlet geometry and crossflow condition, to name a few. Depending on the porous design and crossflow combination, the intensity of the reduction (or increase) in drag across the system varied. Wave drag reduction was dependent on the reduction in bow wave angle and shock attenuation (and by extension the cone shape), while the jet interaction and momentum recovery were dependent on vent expansion ratio and exit angle. The effect on drag reduction was cumulative and was highly dependent on the individual case.

8.3 Bow wave attenuation

The wave drag of the cunicular cones affected two regions: the conical forebody, and the downstream cylinder (where the vent was located). The conical forebody drag was reduced by the presence of the pores on the cone surface. The inlet pore represented an alternative path for the fluid within the bow wave to follow, whereby fluid from the bow was removed and transferred into the internal network. The bow wave interaction with pores resulted in the normal velocity component behind the shock wave increasing, thereby reducing the pressure ratio across the shock wave and decreasing the bow wave angle. The overall energy loss to the system was reduced across the porous shock wave, where the combined result was an attenuated bow wave. The wave drag was consistently reduced over the porous conical forebody region, as some amount of inflow into the system always occurred, irrespective of shape or vent geometry.

The wave drag over the downstream bow wave shape and strength was affected by the jetting condition at the vent exit, which depended on the expansion ratio and vent angle. If the pressure ratio across the vent exit was close to 1, the flow behind the shock was pulled inwards, reducing the strength of the shock and wave drag by reducing the shock area and mitigating the pressure losses to the system. This is visible in BS4 Ellipsoid, where a critically-expanded jet occurred. Conversely, improper jetting (either from an excessively high jet angle or over-expanded vent geometry) increased the strength of the shock wave and increased its area, increasing the drag significantly. This is visible in the BS4 Hemisphere, where a severely overexpanded jet formed.

8.4 Jet interaction

The jet interaction (controlled by the vent geometry, expansion ratio and pore-affected crossflow) had a significant effect on the overall drag reduction of the system. Due to the supersonic nature of the jet stream and crossflow, it was unlikely that any meaningful drag reduction occurred from the jet impingement. However, the factors affecting the jet stream could be controlled to mitigate the losses in momentum, energy and pressure caused by the jet interaction.

The jet interaction drag was minimised by aligning the vent with the z-axis as much as possible in order to improve momentum recovery both within the vent and during the jet impingement. In addition to this, the vent expansion ratio was critical as it defined the vent exit conditions for the constant inlet area. The minimum drag from the jetting occurred when the vent exit condition matched the crossflow condition, as when the pressures matched a critically-expanded jet formed, with minimal losses to the system as the streams interacted. The vent exit angle was particularly important for this, any fluid contribution in the y-direction significantly reduced momentum and dissipated energy. This was observed in BS0, where the perpendicular jet direction severely increased the jet drag, causing an overall lower drag reduction with the positive wave drag reduction from the inlet. BS0 also increased the

size of the downstream wave size by increasing the pressure behind the wave. A critically-expanded vent was observed in the BS4 Ellipsoid case, where the greatest drag reduction also occurred.

8.5 Inflow - Outflow

The bow wave angle β was found to decrease with increasing flow rate. In particular, the greatest drag reductions were observed when the mass flow rate within the internal network was high. Increased mass flow rate was mostly affected by the amount of inflow into the system, and was observed when the internal network pressure was high and no surface bleeding occurred. The internal pressure could be increased by increasing the toroid area, since the internal flow was subsonic and highly viscous. The internal pressure was also affected by the vent expansion ratio. In the OE vent, if the vent back pressure and exit pressure did not match, the internal network pressure would drop. This induced bleeding from the surface pores due to the adverse pressure gradient established across the porous surface boundary. The bleeding directly affected the wave drag reduction around the conical forebody, as this large separation region surrounding the pores obstructed inflow.

Forward-inclined inlet pores were found to increase the amount of inflow into the pores, since the flatter angle provided a path of lesser resistance than the perpendicular pores, thereby reducing fluid momentum losses upon entering the structure. However, careful balancing of the outlet conditions was required for this case, as insufficient outflow resulted in significantly worsened bleeding from the cone surface.

The nature of the porous arrangement was that it behaved as an interconnected system, where both the inlet and venting flows were governed by the internal flows. Changes in venting directly affected the inlet, and vice versa.

8.6 Momentum addition by jet

The drag over the porous cone was reduced by the momentum addition by the jet. This intensity of the reduction depended on several factors, including the crossflow condition, the vent exit angle and the vent expansion ratio. The momentum addition was closely linked to the jet interaction. In this, the direction of the vent exit was significant. By conservation of momentum, momentum recovery from the jet was maximised by the vent angle being as closely aligned with the crossflow, since little deviation from the major flow path (the horizontal crossflow) occurred.

As with the jet interaction, the expansion ratio of the vent was critical. By designing the vent for a matched pressure and exit vent condition, momentum recovery was maximised as minimal pressure losses were experienced. Depending on these factors, the increase in linear momentum across the system could be significant. An increase in momentum signified an increase in dynamic pressure, the dominant flow parameter in the drag equation. The drag across the system was reduced by the positive momentum addition from the jet, as best observed in the critically expanded BS4 Ellipsoid case.

8.7 BS4 in Cone, Ellipsoid, Hemisphere and Secant Ogive

The BS4 model produced the greatest drag reduction for the pointed cones (39%), and as such was introduced into the other shapes to create BS4 H, BS4 E and BS4 SO. The greatest drag reduction occurred in BS4 Ellipsoid (40%), where a critically-expanded jet formed.

BS4 Cone

The BS4 (39% drag reduction) cone had acceptable results from all three drag reduction mechanisms. The bow wave angle and size were reduced by adequate inflow into the inlet pores, however, some surface bleeding occurred from the slightly OE venting configuration. A very high mass flow rate occurred within the internal network, indicative of a greatly attenuated shock wave. As such, the effect of the wave drag reduction was considerable.

The vent geometry was overexpanded and mostly aligned with the z-axis, resulting in high acceleration at the exit and strong momentum addition from the jet. Thus, the drag reduction component from momentum addition was strong. However, the mismatch in pressure due to the jet expansion meant that the jet impingement with the crossflow caused momentum, pressure and energy losses to the system.

BS4 Ellipsoid

BS4 Ellipsoid (40% drag reduction) experienced the greatest drag reduction overall, where all three of the drag mechanisms worked effectively together to create a more aerodynamically efficient body. Strong results were achieved in both the drag reduction by jet interaction and momentum recovery by the jet, with modest wave drag reduction overall. While bleeding occurred at the most concave part of the elliptic surface due to the pores, strong bow wave attenuation was achieved due to the reasons already described. Additionally, the vent configuration of BS4 E generated a critically expanded jet (where the jet exit pressure matched the crossflow back pressure) which further reduced the wave drag and increased the momentum addition to the system efficiently.

BS4 Secant Ogive/ BS4 Hemisphere

BS4 SO/H both experienced increased drag when utilising the same porous structure as BS4 E/C. This proved the importance of the crossflow and bow wave (cone shape) condition for drag reduction.

BS4 Hemi behaved very similarly to BS4 Cone, where an overexpanded jet formed. The porous surface increased the post-shock Mach number, reducing the wave angle maximally as complete inflow with no bleed occurred. However, the Mach number of the pore-affected crossflow was far lower than the Mach number at the vent exit (due to the high vent expansion ratio). This caused an overexpanded jet to form on account of the back pressure being greater than the exit pressure. Due to the velocity of the crossflow over the vent, a large walled-off separation region was created, blocking the majority of the outflow from the vent. This meant that while the flow in the vent was highly accelerated, very little jet was actually impinging on the freestream. The interaction was essentially null, and as such no momentum addition

from the flow was experienced. The flow field momentum was worsened by the lower-nozzle wall system of separation regions, shock waves and shear layer creating irregularities in the flow field.

The BS4 SO venting configuration caused an underexpanded jet to form, where the crossflow was affected by a significant bleed region at the base of the ogive. This lower supersonic flow covered the entire venting region, and the same obstructed vent effect as in BS4 H was observed, although far worse. The implementation of porosity into these shapes requires careful design consideration, and the combination of the inlet, internal, venting and crossflow systems results in a highly sensitive and complex flow field.

8.8 Drag reduction mechanisms - summary

The drag across the porous system was reduced by a combination of three sources of change in drag: wave drag, jet interaction, and momentum addition by jet expansion. The presence of the conic surface pores allowed for the shock wave to be attenuated and the wave angle reduced. The jet interaction generally increased the drag of the system, however, the effects of this were mitigated by using low vent angles with correct expansion ratios. The vent angle and expansion ratios were also used to maximise the momentum recovery introduced by the jet. The effect of the combined system was specific to the particular case, as the crossflow had a significant effect on the overall functioning of the system.

8.9 Recommendations

Given that the current field of supersonic drag reduction in porosity is relatively novel, opportunities exist for further research. Areas of future work may be identified from the completed work, in conjunction with the recommendations, listed below:

- A single, high supersonic Mach number (3.5) and cone half-angle (18.43°) was investigated here. Given that conical shock wave behaviour is directly affected by cone angle

and Mach number (according to the θ-β-M relationship), the effect of organised porous structure for a wider range of Mach numbers and cone angles is warranted. In doing this, the full extent of the organised porosity on the supersonic flow regime may be understood. In particular, θ and M_1 approaching the shock detachment condition would be useful to understand the transition from bow shock to attached shock across an organised porous structure.

- The experimental testing should be repeated using a more robust three-component internal force balance, specifically designed for the SSWT facility. The improved force balance should measure two forces (lift, drag) and one moment (pitch), to completely describe the aerodynamics of the model. This would advance the scope of possible measurements taken during the testing, thereby improving the accuracy and relevance of the study. In order to protect the internal balance (strain gauges, DAQ wires, soldering), a hollow sting mount covering is recommended, to be used in conjunction with the model mounting apparatus. The covering has no effect on the force measurements, however, allows for the force balance to be reused continually and reliably without damage.

- Only the effects of a few geometric changes were investigated here. Further geometry changes to the internal porous structure should be implemented to investigate the effects on the flow field, including increasing the toroidal area in successive rows of pores, shortening the radial pores in the blunt-body cases, and changing the surface hole distribution for maximum inflow.

- The inclined inlet pores require further investigation to determine the mechanisms behind the flow behaviour. In particular, it was suspected that the flow was choking in the pores, however this was difficult to identify. It is recommended that the shock mesh grid work of Law and Skews (2009) be repeated for inclined plates to gain insight into what into the flow phenomena at play.

- The experimentation should be repeated using more sophisticated optical flow visualisation techniques. Specifically, 3D colour schlieren images were taken at various angles around the cone, to visualise the full three-dimensional effect of the porous flow field (which is invisible using the current set-up). Colour schlieren allows for additional, more detailed information than greyscale schlieren. This will also allow for the vent

jetting to be investigated further. Photographs focused on the venting flow interactions (with improved direction sensitivity) should also be obtained to better understand the shock and flow interactions in this region.

- As presented, the models were attached to infinite-cylinder structures in order to simplify the analysis. The upstream flow field was mostly focused on, however the downstream flow regime is highly complex and turbulent. The downstream effect remains largely unknown. Modelling the porous cones attached to finite-length cylinders enables a more accurate representation of the downstream (and overall) flow field. The effect of the porous cones on real-life projectiles may then be commented on, and design recommendations made. If time dependent flow is to be modelled, the base separation should be modelled.

- The 3D element of the flow field, specifically the 3D bow wave interactions with the jets, as well as the cross-flow interaction between jets, requires exploration. These interactions are highly complex and require further localised modelling in order to interpret the effect on the flow field.

- At increased angles of attack, the shock wave and drag performance changes dramatically. The drag on the body is increased at increasing angles of attack, and the effect of the organised porosity on this drag is of interest. Angles near the stall limit are particularly important, as the presence of the pores could potentially alter this limit due to the effects observed on the zero-incidence model. This would broaden the understanding of the current model while focusing on applicability.

- Application of the organised porosity to bodies of different shapes (e.g frustums, airfoils) is recommended. This includes asymmetric bodies, as many real-life aerodynamic structures are asymmetric. Only simple, two-plane symmetric conic shapes were investigated here. Application of the organised porosity to more complex shapes expands the scope of the research and begins to focus the research in a more applications-focused direction.

- The effect of accelerations on the internal and external flow fields should be explored to gain insight into how this system would behave during launches, landings acceleration periods.

- The experimental models were successfully manufactured using the 3D printing half-model method, however, some asymmetry existed in the test pieces after joining. Symmetric, whole-printed conic models are thus preferred. This could be achieved by outsourcing to a professional 3D printing manufacturer. Alternatively, the conic forebody and base could be separated and printed separately. While the two parts would still need to be joined, a symmetric whole-cone would be achieved, which was paramount. Test models of higher quality improve the experimental results, particularly the flow visualisation. Alternatively, metal 3D printing could be utilised to reduce shrinkage, however this process is very costly.

- The investigation into other flow regimes, such as transonic and hypersonic, is pertinent given the significant drag reduction observed in the supersonic regime. In particular, the effect of the pores to hold higher temperatures than the surrounding flow field is relevant to the hypersonic regime, where considerable changes in heat and kinetic energy are observed.

- The drag reduction in the presented work was positive, however to achieve this same percentage reduction in other shapes requires significant work to tune the pressure and expansion ratios for optimal performance. In terms of optimisation, the presented porous design has high levels of complexity and an excessively large parameter set. An optimisation exercise of this kind would be extremely time-consuming and computationally expensive. It is thus recommended to rather expand on the successful geometry and further understand the flow physics in more meaningful ways, such as changing the body angle of incidence, input shape and speed regime.

References

Ahmed, M. and N. Qin (2011). 'Recent advances in the aerothermodynamics of spiked hypersonic vehicles'. In: *Progress in Aerospace Sciences* 47.6, pp. 425–449. ISSN: 0376-0421. DOI: https://doi.org/10.1016/j.paerosci.2011.06.001.

Ali, S. et al. (2018). 'Boundary layer flow interaction with a permeable wall'. In: *Physics of Fluids* 30 (8). DOI: https://doi.org/10.1063/1.5043276.

Anderson, J. (1990). *Modern Compressible Flow: With Historical Perspective, 4th Edition*. New York: McGraw Hill. Chap. 4, pp. 128–188. ISBN: 1260471446.

Anderson, J. (2001). *Fundamentals of Aerodynamics, 3rd Edition*. McGraw-Hill. ISBN: 978-0-07-237335-6.

ANSYS Inc. (2023a). *6.1.3 Choosing the Appropriate Mesh Type*. URL: https://www.afs.enea.it/project/neptunius/docs/fluent/html/ug/node164.htm (visited on 2023).

ANSYS Inc. (2023b). *7.3.14 Wall Boundary Conditions*. URL: https://www.afs.enea.it/project/neptunius/docs/fluent/html/ug/node250.htm (visited on 2023).

ANSYS Inc. (2023c). *7.3.15 Symmetry Boundary Conditions*. URL: https://www.afs.enea.it/project/neptunius/docs/fluent/html/ug/node251.htm (visited on 2023).

ANSYS Inc. (2023d). *7.3.9 Pressure Far-Field Boundary Conditions*. URL: https://www.afs.enea.it/project/neptunius/docs/fluent/html/ug/node245.htm (visited on 2023).

ANSYS Inc. (2023e). *ANSYS CFX Solver Theory Guide*. URL: https://dl.cfdexperts.net/cfd_resources/Ansys_Documentation/CFX/Ansys_CFX-Solver_Theory_Guide.pdf.

ANSYS Inc. (2023f). *Step 11: Adapting the Mesh*. URL: https://www.afs.enea.it/project/neptunius/docs/fluent/html/tg/node24.htm (visited on 2023).

ASM (1990). *Metals Handbook: Properties and Selection. Irons, Steels and High-Performance Alloys*. ASM International. ISBN: 978-0-87170-654-6.

Badcock, K. et al. (2000). 'Simulation of unsteady turbulent flows around moving airfoils using the pseudo-time method'. In: *International Journal for Numerical Methods in Fluids* 32, pp. 585–604. DOI: 10.1002/(SICI)1097-0363(20000315)32:5<585::AID-FLD976>3.0.CO;2-1.

Ben-Dor, G. (2001). *Oblique Shock Wave Reflections*. Elsevier. Chap. 8.1, pp. 67–179. ISBN: 978-0-12-086430-0. DOI: 10.1016/b978-012086430-0/50022-1.

Berger, M. and P. Colella (1989). 'Local adaptive mesh refinement for shock hydrodynamics'. In: *Journal of Computational Physics* 82.1, pp. 64–84. ISSN: 0021-9991. DOI: 10.1016/0021-9991(89)90035-1.

Bernstein, L. and R. Pankhurt (1975). *Force Measurements in Short-Duration Hypersonic Facilities*. report AD-AO18 842. Neuilly Sur-Seine, France: ADVISORY GROUP FOR AEROSPACE RESEARCH and DEVELOPMENT. Chap. 4, pp. 104–136.

Borg, A., B. Paulsen and O. Nja (2014). 'The concept of validation of numerical models for consequence analysis'. In: *Reliability Engineering and System Safety* 125, pp. 36–45. ISSN: 0951-8320. DOI: 10.1016/j.ress.2013.09.009.

Britannica (2023). *spherical aberration*. URL: https://www.britannica.com/technology/spherical-aberration (visited on 2024).

BSI British Standards (2011). *Metallic materials — Calibration of force-proving instruments used for the verification of uniaxial testing machines*. report ISO 376:2011(en).

Busemann, A. (1929). 'Verdichtungsstosse in ebenen Gasstromungen'. In: *Vortraye aus dem Gebiet der Aerodynamik*, p. 162.

Celik, I. (2008). 'Procedure for Estimation and Reporting of Uncertainty Due to Discretization in CFD Applications'. In: *Journal of Fluids Engineering* 130.7, pp. 0780011–0780014. ISSN: 0098-2202. DOI: 10.1115/1.2960953.

Chen, Y. et al. (2021). 'Porous ceramics: Light in weight but heavy in energy and environment technologies'. In: *Materials Science and Engineering: R: Reports* 143, p. 100589. ISSN: 0927-796X. DOI: 10.1016/j.mser.2020.100589.

Creality (2024). *CREALITY LD-002R 3D PRINTER*. URL: https://dc3dprinters.co.za/product/creality-ld-002r-lcd-resin-3d-printer/ (visited on 2024).

Crowell, G. (1996). *Descriptive Geometry of Nose Cones*. report. Archived from the original (PDF) on 11 April 2011. VCP Program, pp. 1–6.

Cummings, R., H. Yang and Y. Oh (1995). 'Supersonic, turbulent flow computation and drag optimization for axisymmetric afterbodies'. In: *Computers and Fluids* 24.4, pp. 487–507. ISSN: 0045-7930. DOI: 10.1016/0045-7930(94)00040-6.

Daso, E. et al. (2009). 'The Dynamics of Shock Dispersion and Interactions in Supersonic Freestreams with Counterflowing Jets'. In: *Aiaa Journal - AIAA J* 47, pp. 1313–1326. DOI: 10.2514/1.30084.

Davoudinejad, A. et al. (2018). 'Geometrical and feature of size design effect on direct stereolithography micro additively manufactured components'. In: *Procedia Structural Integrity* 13, pp. 1250–1255. ISSN: 2452-3216. DOI: 10.1016/j.prostr.2018.12.256.

Doyle, G. and B. Skews (1999). 'actions With Porous Beds'. University of the Witwatersrand.

Ferziger, J. and M. Peric (2002). *Computarional Methods for Fluid Dynamics*. 3rd. New York, Springer-Verlag, pp. 118, 149. ISBN: ISBN 3-540-42074-6.

Filippi, A. (2017). 'Effect of internal surface curvature on steady axisymmetric shock waves'. University of the Witwatersrand.

Fomin, V. M., S. G. Mironov and K. M. Serdyuk (2009). 'Reducing the wave drag of bodies in supersonic flows using porous materials'. In: *Technical Physics Letters* 35.2, pp. 117–119. ISSN: 1090-6533. DOI: 10.1134/s1063785009020060.

Fomin, V. et al. (2001). 'Flow regimes formed by a counterflow jet in a supersonic flow'. In: *Journal of Applied Mechanics and Technical Physics* 42, pp. 757–764. DOI: 10.1023/A:1017984124396.

Friend, W. (1958). *The interaction of a plane shock wave with an inclined perforated plate*. UTIA Tech Note 25. University of Toronto.

Fu, J., H. Thomas and C. Li (2021). 'Tortuosity of porous media: Image analysis and physical simulation'. In: *Earth-Science Reviews* 212, p. 103439. ISSN: 0012-8252. DOI: 10.1016/j.earscirev.2020.103439.

Georgiadi-Stefanidi, K. et al. (2011). 'Numerical simulation of the nonlinear bending response of fibre-reinforced cementitious matrix beams and comparison with experimental

results'. In: *Engineering Structures* 33.12, pp. 3579–3589. ISSN: 0141-0296. DOI: 10.1016/j.engstruct.2011.07.022.

Haack, W. (1941). *Geschoßformen kleinsten Wellenwiderstandes. Bericht 139 der Lilienthal-Gesellschaft.*

Hinman, S. (2024). *CompressibleCalccF*. MATLAB Central File Exchange.

Hosch, J. W. and J. P. Walters (1977). 'High spatial resolution schlieren photography'. In: *Appl. Opt.* 16.2, pp. 473–482. DOI: 10.1364/AO.16.000473.

Kafle, A. et al. (2021). '3D/4D Printing of Polymers: Fused Deposition Modelling (FDM), Selective Laser Sintering (SLS), and Stereolithography (SLA)'. In: *Polymers* 13.18, p. 3101. ISSN: 2073-4360. DOI: 10.3390/polym13183101.

Kleine, H. (2001). 'Measurement Techniques and Diagnostics'. In: pp. 683–IV. ISBN: 9780120864300. DOI: 10.1016/B978-012086430-0/50017-8.

Kobayashi, S., T. Adachi and T. Suzuki (1995). 'Regular Reflection of a Shock Wave Over a Porous Layer: Theory and Experiment'. In: pp. 175–180. ISBN: 978-3-642-79534-3. DOI: 10.1007/978-3-642-79532-9_28.

Lal, H., A. Uthaman and S. Thomas (2022). 'Fundamentals of Porous Materials'. In: pp. 1–15. ISBN: 978-3-030-85396-9. DOI: 10.1007/978-3-030-85397-6_1.

Law, C. and B. Skews (2009). 'Perturbed wave patterns in the flow behind a shock reflecting off a porous wall'. In: pp. 2–7.

Li, H. and G. Ben-Dor (1997). 'A parametric study of Mach reflection in steady flows'. In: *Journal of Fluid Mechanics* 341, pp. 101–125. ISSN: 1469-7645. DOI: 10.1017/s0022112097005375.

Liepmann, H. and A. Roshko (2001). *Elements of Gasdynamics*. Dover Publications. ISBN: 978-0-486-41963-3.

Liu, X. et al. (2024). 'Investigation on the effectiveness of transpiration cooling under the influence of shock wave'. In: *Applied Thermal Engineering* 236, p. 121831. ISSN: 1359-4311. DOI: 10.1016/j.applthermaleng.2023.121831.

Maslov, A. A. et al. (2019). 'Effect of porous inserts on aerodynamics of flying vehicles'. In: *Journal of Physics: Conference Series* 1382.1, pp. 12–23. ISSN: 1742-6596. DOI: 10.1088/1742-6596/1382/1/012023.

Mathelin, L. and M. Hussaini (2003). 'Uncertainty Quantification in CFD Simulations: A Stochastic Spectral Approach'. In: *Computational Fluid Dynamics 2002*. Springer Berlin Heidelberg, pp. 65–70. ISBN: 9783642593345. DOI: 10.1007/978-3-642-59334-5_5.

Mehta, U. B. (1991). 'Some Aspects of Uncertainty in Computational Fluid Dynamics Results'. In: *Journal of Fluids Engineering* 113.4, pp. 538–543. ISSN: 1528-901X. DOI: 10.1115/1.2926512.

Meng, Y.-S. et al. (2020). 'Numerical exploration on drag and heat reduction mechanism of a spike-tipped supersonic blunt nose'. In: *Modern Physics Letters B* 34.32, p. 2050370. ISSN: 1793-6640. DOI: 10.1142/s0217984920503704.

Menter, F. R. (1993). 'Zonal Two Equation k-w Turbulence Models For Aerodynamic Flows'. In: *23rd Fluid Dynamics, Plasmadynamics, and Lasers Conference*. American Institute of Aeronautics and Astronautics. DOI: 10.2514/6.1993-2906.

Menter, F. R. (1994). 'Two-equation eddy-viscosity turbulence models for engineering applications'. In: *AIAA Journal* 32.8, pp. 1598–1605. ISSN: 1533-385X. DOI: 10.2514/3.12149.

Menter, F. R. et al. (2004). 'A Correlation-Based Transition Model Using Local Variables: Part I — Model Formulation'. In: *Volume 4: Turbo Expo 2004*. GT2004. ASMEDC. DOI: 10.1115/gt2004-53452.

Merriam-Webster (2021). *"Porosity"*. URL: https://www.merriam-webster.com/dictionary/porosity.

Merzkich, W. (1987). 'Optical Flow Visualization'. In: *Flow Visualization*. Elsevier, pp. 115–231. ISBN: 9780124913516. DOI: 10.1016/b978-0-08-050658-6.50007-2.

Mironov, S. G., S. V. Kirilovskiy et al. (2019). 'Effect of the structure of skeleton models of cellular materials on the drag of a cylinder with a frontal gas-permeable insert in a supersonic flow'. In: *Journal of Physics: Conference Series* 1404.1, p. 012032. ISSN: 1742-6596. DOI: 10.1088/1742-6596/1404/1/012032.

Mironov, S. G., A. A. Maslov et al. (2015). 'Modeling of a supersonic flow around a cylinder with a gas-permeable porous insert'. In: *Journal of Applied Mechanics and Technical Physics* 56.4, pp. 549–557. ISSN: 1573-8620. DOI: 10.1134/s0021894415040021.

Morris, M. (2011). *Design of Experiments*. Chapman and Hall/CRC. Chap. Regression experiments: second-order polynomial models, pp. 299–316. ISBN: 9780429108983.

Morse, J. M. et al. (2002). 'Verification Strategies for Establishing Reliability and Validity in Qualitative Research'. In: *International Journal of Qualitative Methods* 1.2, pp. 13–22. ISSN: 1609-4069. DOI: 10.1177/160940690200100202.

Nemec, M., M. Aftosmis and M. Wintzer (2008). 'Adjoint-Based Adaptive Mesh Refinement for Complex Geometries'. In: *46th AIAA Aerospace Sciences Meeting and Exhibit*. American Institute of Aeronautics and Astronautics. DOI: 10.2514/6.2008-725.

Ntantis, E. et al. (2023). 'Numerical Study on a Supersonic Flow around a Bullet'. In: *WSEAS TRANSACTIONS ON FLUID MECHANICS* 18, pp. 1–9. ISSN: 1790-5087. DOI: 10.37394/232013.2023.18.1.

Oezcan, M. (2020). *How to Predict Darcy and Forchheimer Coefficients for Perforated Plates Using Analytical Approach?* URL: https://shorturl.at/kQDPG (visited on 2020).

Onodera, H. and K. Takayama (1990). 'Interaction of a plane shock wave with slitted wedges'. In: *Experiments in Fluids* 10–10.2–3, pp. 109–115. ISSN: 1432-1114. DOI: 10.1007/bf00215018.

Pang, C. et al. (2021). 'Enhanced adaptive mesh refinement method using advanced vortex identification sensors in wake flow'. In: *Aerospace Science and Technology* 115, p. 106796. ISSN: 1270-9638. DOI: 10.1016/j.ast.2021.106796.

Papamoschou, D. and D. G. Hubbard (1993). 'Visual observations of supersonic transverse jets'. In: *Experiments in Fluids* 14.6, pp. 468–476. ISSN: 1432-1114. DOI: 10.1007/bf00190201.

Pieterse, F. (2002). 'Design and development of a three component strain gauge wind tunnel balance'. Thesis. University of Johannesburg. DOI: https://hdl.handle.net/10210/7055.

Pish, F. et al. (2020). 'Computational study of the cavity flow over sharp nose cone in supersonic flow'. In: *International Journal of Modern Physics C* 31.06, p. 2050079. ISSN: 1793-6586. DOI: 10.1142/s0129183120500795.

Poplavskaya, T. V. et al. (2017). 'Numerical simulation of highly porous materials in application to supersonic aerodynamics'. In: *AIP Conference Proceedings*. Author(s). DOI: 10.1063/1.5007613.

Reshetova, A. I. et al. (2018). 'Influence of the sound-absorbing coating structure on the disturbance evolution in the hypersonic flow of vibrationally excited gases'. In: *AIP Conference Proceedings*. Author(s). DOI: 10.1063/1.5065281.

Salim, S. M. and S. Cheah (2009). 'Wall y+ strategy for dealing with wall-bounded turbulent flows'. In: *Int. MultiConf. Eng. Comput. Sci. (IMECS)* 2, pp. 1–6.

Samuels, R. (2005). 'Intercontinental Ballistic Missiles (ICBMS)'. In: *Encyclopedia of United States National Security*. DOI: https://doi.org/10.4135/9781412952446.

Schmidt, B. (2015). *Schlieren Visualization, Laboratory report*. California: California Institute of Technology.

Sebastian, R., T. Lurkens and A.-M. Schreyer (2020). 'Flow field around a spanwise-inclined jet in supersonic crossflow'. In: *Aerospace Science and Technology* 106, p. 106209. ISSN: 1270-9638. DOI: 10.1016/j.ast.2020.106209.

Skews, B. (1994). 'Oblique reflection of shock waves from rigid porous materials'. In: *Shock Waves* 4.3, pp. 145–154. ISSN: 1432-2153. DOI: 10.1007/bf01417430.

Skews, B. (2005). 'Shock wave interaction with porous plates'. In: *Experiments in Fluids* 39.5, pp. 875–884. ISSN: 1432-1114. DOI: 10.1007/s00348-005-0023-7.

Skews, B. et al. (1997). 'Use of high-speed visualization for the study of shock-wave interactions with deformable porous materials'. In: *22nd International Congress on High-Speed Photography and Photonics*. Ed. by D. L. Paisley and A. M. Frank. SPIE. DOI: 10.1117/12.273457.

Smith, S. W. (2003). 'Digital Signal Processors'. In: *Digital Signal Processing*. Elsevier, pp. 503–534. ISBN: 9780750674447. DOI: 10.1016/b978-0-7506-7444-7/50065-0.

Struchkov, A. et al. (2020). 'Numerical simulation of aerodynamic problems based on adaptive mesh refinement method'. In: *Acta Astronautica* 172, pp. 7–15. ISSN: 0094-5765. DOI: 10.1016/j.actaastro.2020.03.019.

Surujhlal, D. (2018). 'Three-dimensional shock wave reflection transition in steady flow'. PhD Thesis. University of the Witwatersrand.

Taylor, G. I. and J. W. Maccoll (1933). 'The air pressure on a cone moving at high speeds.—I'. In: *Proceedings of the Royal Society of London. Series A, Containing Papers of a Mathematical and Physical Character* 139.838, pp. 278–297. DOI: 10.1098/rspa.

1933.0017. eprint: https://royalsocietypublishing.org/doi/pdf/10.1098/rspa.1933.0017.

Thurmond, V. (2001). 'The Point of Triangulation'. In: *Journal of Nursing Scholarship* 33.3, pp. 253–258. DOI: https://doi.org/10.1111/j.1547-5069.2001.00253.x. eprint: https://sigmapubs.onlinelibrary.wiley.com/doi/pdf/10.1111/j.1547-5069.2001.00253.x.

Tucker, J. (2000). *Evaluating Data Acquisition Specifications*. URL: https://www.electronicdesign.com/home/article/21200478/evaluating-data-acquisition-specifications (visited on 2024).

Valiullin, I. R. et al. (2023). 'Similarity parameter for a supersonic flow around a cylinder with a frontal high-porosity insert'. In: *AIP Conference Proceedings*. AIP Publishing. DOI: 10.1063/5.0133386.

Van Dyke, M. and S. Widnall (1983). 'An Album of Fluid Motion'. In: *Journal of Applied Mechanics* 50.2, pp. 475–475. ISSN: 1528-9036. DOI: 10.1115/1.3167071.

Wackers, J. et al. (2022). 'Adaptive grid refinement for ship resistance computations'. In: *Ocean Engineering* 250, p. 110969. ISSN: 0029-8018. DOI: 10.1016/j.oceaneng.2022.110969.

Wendt, J. (1972). *Drag Coefficient of Cones*. Final Scientific Report AD0750042. von Karman Institute for Fluid Dynamics Rhode Saint Genese Belgium: Air Force Flight Dynamics Laboratory et al., pp. 5–54. ISRN: AFFDIYTM 72-23 FXG.

Wessam, M. E. and Z. H. Chen (2015). 'Flow Field Investigations and Aerodynamic Characteristics of Artillery Projectile'. In: *Advances in Engineering Research*. eame-15. Atlantis Press. DOI: 10.2991/eame-15.2015.73.

Whitaker, S. (1986). 'Flow in porous media I: A theoretical derivation of Darcy's law'. In: *Transport in Porous Media* 1.1, pp. 3–25. ISSN: 1573-1634. DOI: 10.1007/bf01036523.

Wilcox, D. C. (1993). *Turbulence and Transition Modeling for High-Speed Flows*. DOI: 10.21236/ada266748.

Wilcox, D. C. (2006). *Turbulence Modeling for CFD*. Turbulence Modeling for CFD. DCW Industries. ISBN: 9781928729082.

Wisconsin Geological and Natural History Survey (2023). *Understanding Porosity and Density*. URL: https://shorturl.at/KPaDj (visited on 2024).

Yanbo, H. and L. Tong (2019). 'Sonic-supersonic solutions for the two-dimensional pseudo-steady full Euler equations'. In: *Kinetic and Related Models* 12.6, pp. 1197–1228. ISSN: 1937-5093. DOI: 10.3934/krm.2019046.

Yen, D. and F. Brauchle (2000). *Calibration and Uncertainty Analysis for the UC Davis Wind Tunnel Facility*. UCD Wind Tunnel Calibration Document. University of California, Davis.

Zmijanovic, V. et al. (2013). 'Thrust vectoring effects of a transverse gas injection into a supersonic cross flow of an axisymmetric convergent-divergent nozzle'. In: *Progress in Propulsion Physics*. EUCASS. EDP Sciences. DOI: 10.1051/eucass/201304227.

Appendix A

Apparatus/Equipment Specifications

The following details the specifications of the apparatus and equipment used during the research process.

Table 9: Air drier specifications

Company	Arlec Engineering Works CC.
Makers no.	J38996
Working pressure	2136kPa
Test Pressure	2777kPa
Working temperature	100^oC
Design temperature	100^oC
Cubic capacity	0.036
Code	ACIF8101A02

Table 10: Supply pressure vessel specifications]

Year of manufacture	1968
Code	BS 1515, 1965
Design temperature	122^oF
Capacity	319cuft
Radiography	Spot
Test pressure	146psi
Vessel no.	5:01
Company	Kies & Travers Ltd

Table 11: Test section pressure transducer specifications

Company	Kyowa Electronic Instruments Co. Ltd
Type	PG - 2KU
Capacity	2kg.f/cm$\hat{2}$
Serial no.	YP9468

Table 12: Settling chamber pressure transducer specifications

Company	Kyowa Electronic Instruments Co. Ltd
Type	PG - 10KU
Capacity	10kg.f/cm$\hat{2}$
Serial no.	YB9330137

Table 13: Programmable time delay unit specifications

Company	ElectroDi
Trigger	3.0V
Exposure Time	3300u

Table 14: Induction motor specifications

Company	English Electric Benoni Works
Serial no.	PC5927/18
Size	C286
Power	25hp
Speed	1455rpm
Voltage	380V
Connection	3-phase delta
Current	36.3A, 50Hz
Standard	2613
Bearings	DE: SKF 6310 [t] NDE: SKF 6308 [b]
Insulation class	E
Lubricant	Shell Alvania no.2 (Li-base grease)
Overhaul co.	L.H Mathinusen (ref: 92.6680)

Table 15: Compressor specifications

Company	Reavell
Model	CompAir
Type	CSA GE
Machine no.	226092
Speed	1000rpm
Pressure	450psi
Oil	Shell Turbo Oil T 78

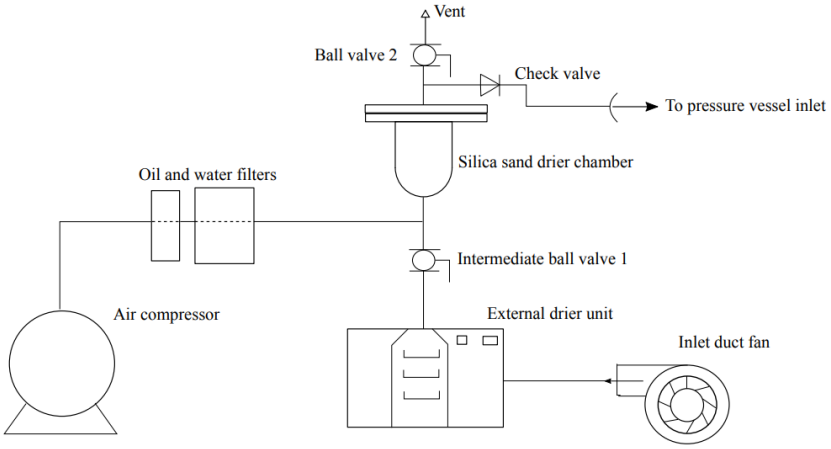

Figure 101: The network diagram of the equipment controlling the air compression and direction into the tunnel (Surujhlal (2018))

Appendix B

Safety during experimentation

During experimentation, several standard procedures and protocols were followed to ensure a safe operating environment, experimental apparatus and models. Failure mode analysis (FMA), is concerned with how and why particular failures occur in a given environment. This includes the identification of the failure modes, analysis of these modes in terms of severity and likelihood, consequences and finally mitigation procedures. The implementation of mitigation measures minimises the risks associated with potential failure modes in the SSWT testing environment, thereby ensuring the safety of the users and equipment while simultaneously retaining the quality of the experimental results. The FMA of the SSWT experimentation is presented below:

Instrument failure:

- Failure: Malfunction or failure of pressure/temperature sensors, flow meters, data acquisition systems or other measurement apparatus.
- Analysis:
  - Severity: High, as incorrect or incomplete data may cause incorrect conclusions to be drawn or hazardous operating conditions.
  - Likelihood: Low - moderate, depending on the quality and maintenance level of the instrumentation.

- Consequences: Experimental data may be compromised (time and resources wastage) and potentially hazardous testing environment.
- Mitigation:
  - Regular maintenance and calibration of the instrumentation and apparatus.
  - Continual monitoring of sensor and DAQ performance during experiments (e.g. plotting a pressure trace during each test to monitor pressure supply through the system).

Structural failure:

- Failure: Structural failure or damage of the experimental components, including the test section/windows, sting apparatus or test pieces, and external components (e.g. compressor or drier).
- Analysis:
  - Consequences: Experimental results may be compromised (time and resource wastage), and potentially harmful operating environment.
  - Analysis:

    Severity: High, as structural failure may cause equipment damage, potentially injure users, and disrupt experimentation.

    Likelihood: Low to moderate, depending on the condition (age), quality of design and manufacturing (for sting and test pieces), and maintenance schedule of the wind tunnel components.
- Consequences: Experiment interruption, potential injury to personnel, costly repairs, and downtime for the facility.
- Mitigation:
  - Regular inspections and maintenance of the SSWT and associated systems.
  - Installation of structural health monitoring systems to the tunnel and associated systems.

  - Use of robust materials and strict adherence to design standards for construction. For example:
    * Design model/sting using a safety factor of at least 7, as used in ISO/BS and SABS standards on pressure vessel design, and using FEA on the models to confirm this.)
    * Before using unfamiliar materials (resin polymer for conic models), FEA was applied to the models using identical SSWT conditions to test the part strength.

Flow control system failure:

- Failure: Loss of control over flow parameters, including Mach number, pressure and temperature.
- Analysis:
  - Severity: High, as incorrect flow conditions may be present in the test section, causing experimental data to be compromised or incorrect, or potentially damaging the test model (e.g. from too much moisture on account of incorrect temperatures).
  - Likelihood: Low, depending on the quality and reliability of the flow control systems.
- Consequences: Incorrect data, possible damage to the test model, and unsafe testing environment on account of the uncontrolled flow conditions.
- Mitigation:
  - Implement redundant flow control systems with automatic failure shut-down mechanisms.
  - Routine testing, calibration and inspection of the flow control apparatus.
  - Adherence to emergency shutdown procedures in case of system breakdown.

Test model mounting failure:

- Failure: Failure or detachment of the model mounting apparatus in the tunnel test section.
- Analysis:
  - Severity: High, potential safety hazard safety hazard. Can lead to loss/damage of the sting apparatus, test piece, potential damage to the SSWT, and potential injury of the operator if failure causes the test section doors to shatter.
  - Likelihood: Low to moderate, depending on the reliability and robustness of the sting apparatus.
- Consequences: Equipment damage, loss of data, interruption/delay of experiments and potential injury to personnel.
- Mitigation:
  - Design sturdy and reliable mounting/sting apparatus to secure the model.
  - Inspection of sting apparatus and joints/fasteners before each experiment.
  - Installation of safety clamps and belts on SSWT doors to prevent opening during testing if sting integrity is compromised. Implement plexiglass test section windows to prevent shattering if sting or model breakage occurs.

During experimental testing, the described mitigations of the failure modes were all strictly adhered to by reproducing the SSWT Standard Operating Procedure (including Precautions). These procedures ensured that testing was safe, such that the equipment and personnel were protected while quality results were gathered.

Appendix C

Manufacturing apparatus

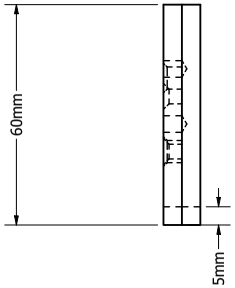

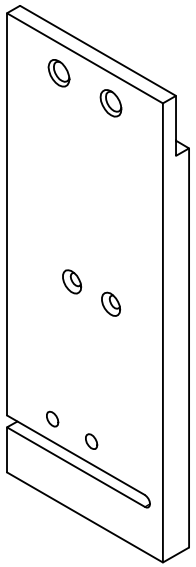

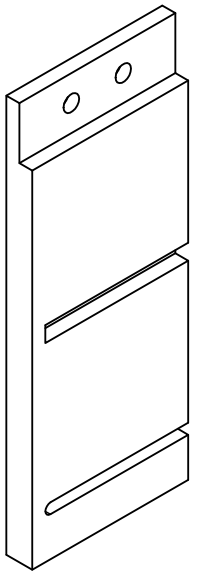

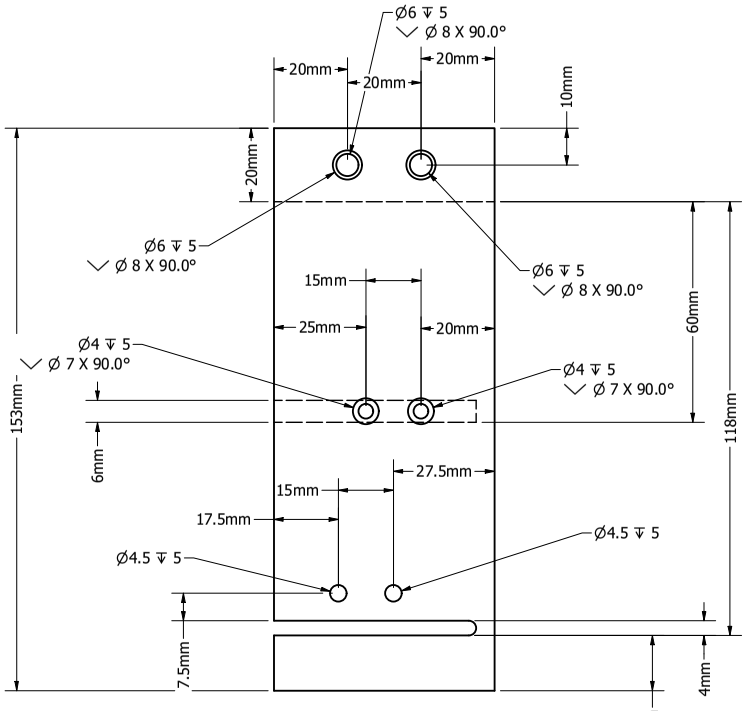

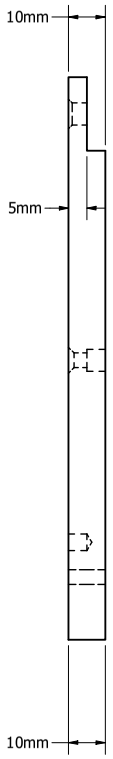

Material: bright steel

DRAWN Sabrina	2021/04/07	UNIVERSITY OF THE WITWATERSRAND	
CHECKED			
QA		TITLE SIDE PLATE MIRROR LEFT	
MFG			
APPROVED	P6		
		SIZE C	DWG NO Side Plate 3_MIR1 REV
		SCALE 1 : 1	SHEET 1 OF 1

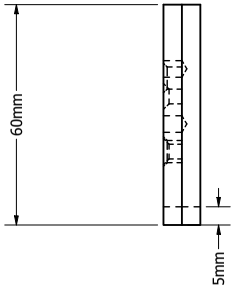

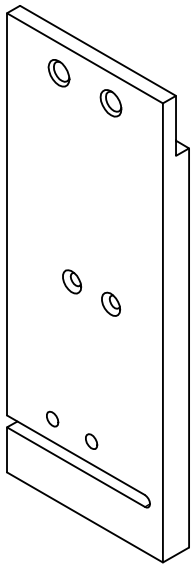

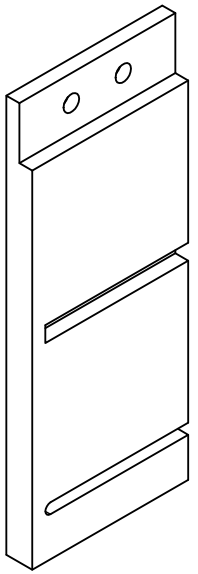

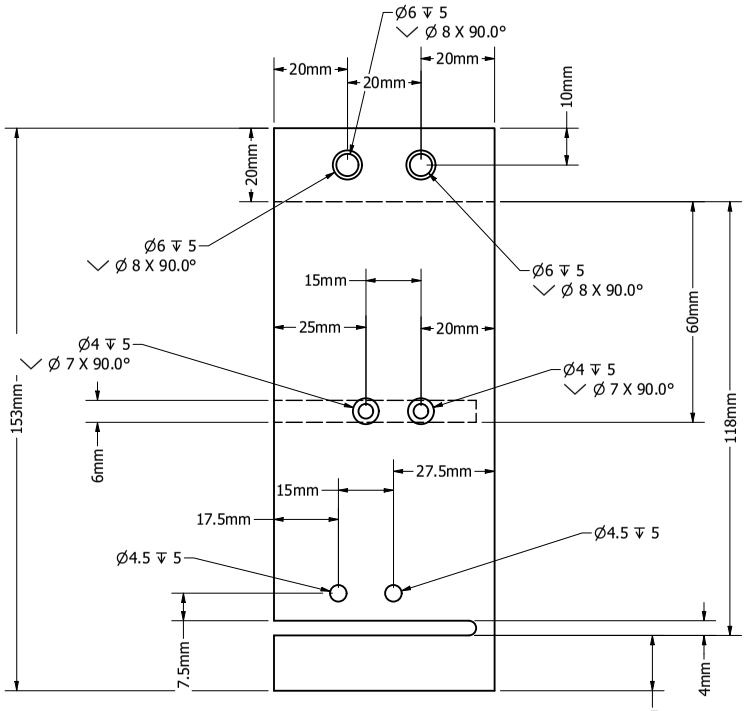

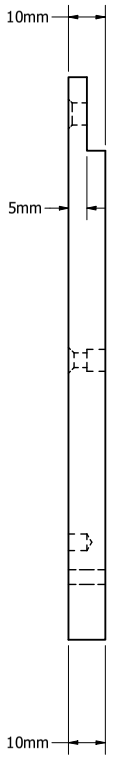

Material: bright steel

DRAWN Sabrina	2021/04/07	UNIVERSITY OF THE WITWATERSRAND	
CHECKED			
QA		TITLE SIDE PLATE MIRROR LEFT	
MFG			
APPROVED	P6		
		SIZE C	DWG NO Side Plate 3_MIR1 REV
		SCALE 1 : 1	SHEET 1 OF 1

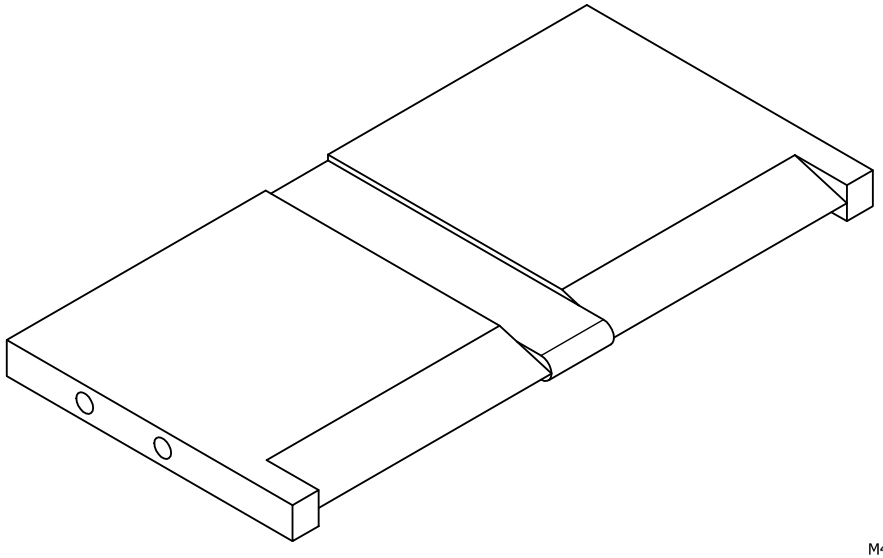

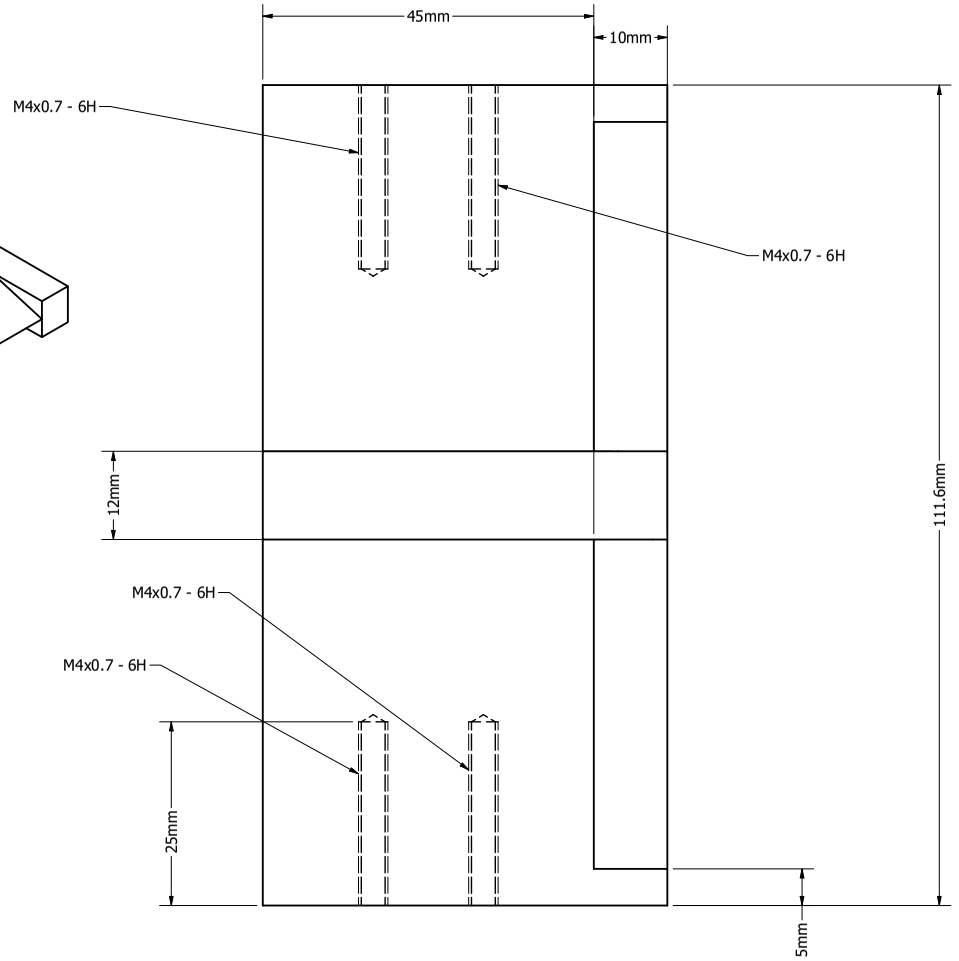

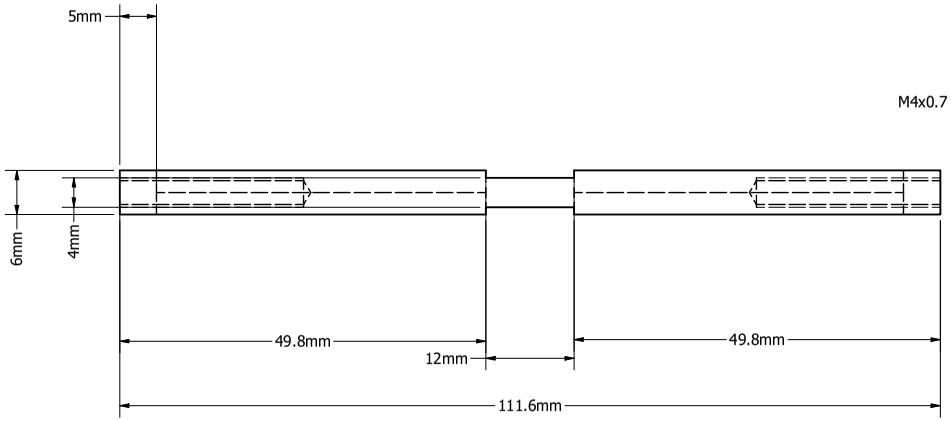

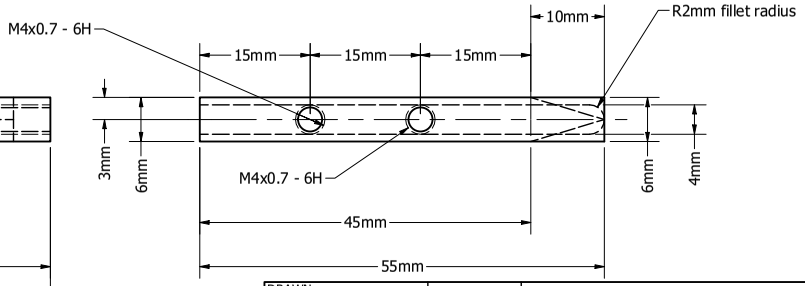

Material: bright steel

DRAWN Sabrina	2021/04/05	UNIVERSITY OF THE WITWATERSRAND	
CHECKED		TITLE FLYER PLATE	
QA			
MFG			
APPROVED	P10		
		SIZE C	DWG NO FlyerPlate3 / REV
		SCALE 2: 1	SHEET 1 OF 1

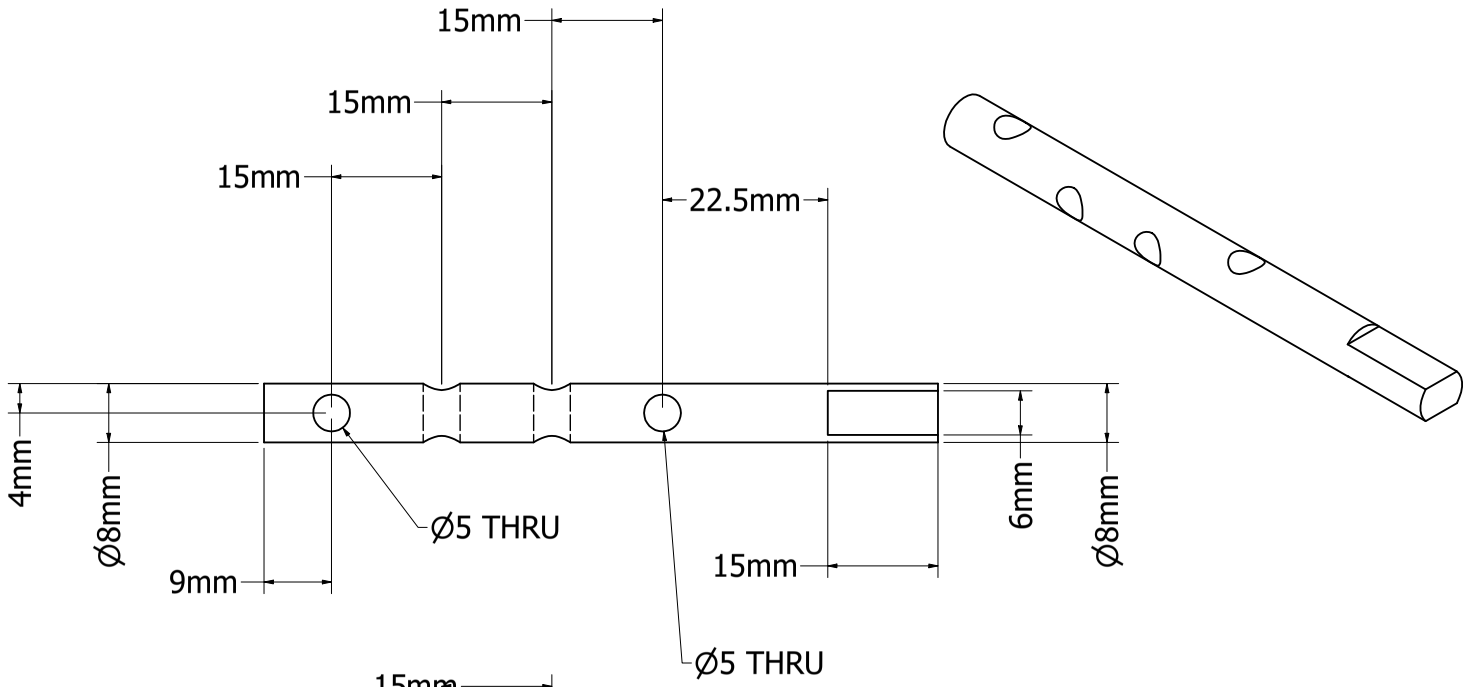

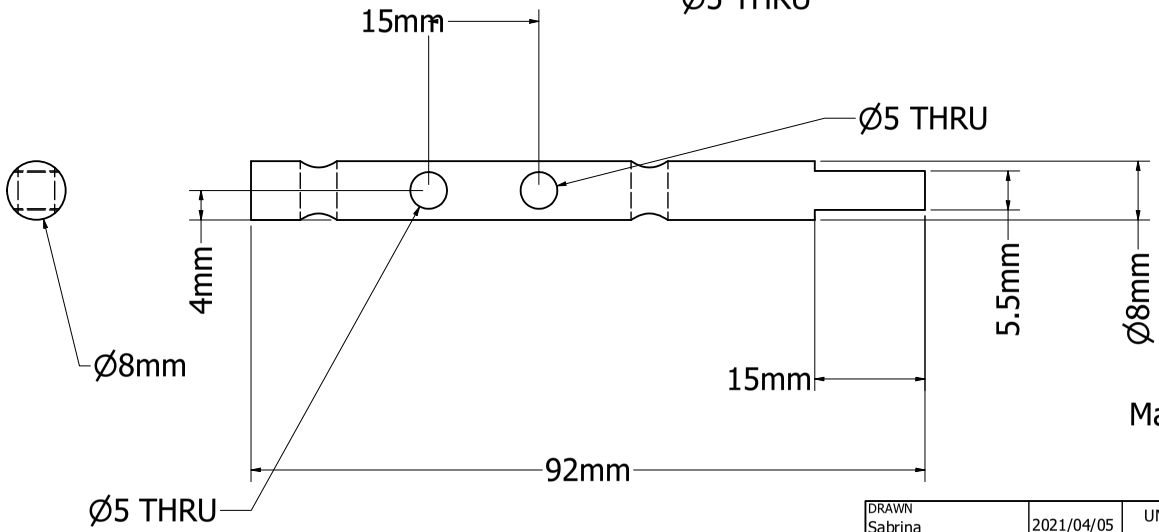

Material: bright steel

DRAWN Sabrina	2021/04/05	UNIVERSITY OF THE WITWATERSRAND
CHECKED		TITLE: INNER STING
QA		
MFG		
APPROVED	P9	
SIZE C	DWG NO Inner Sting 3 1	REV
SCALE 2: 1	SHEET 1 OF 1	

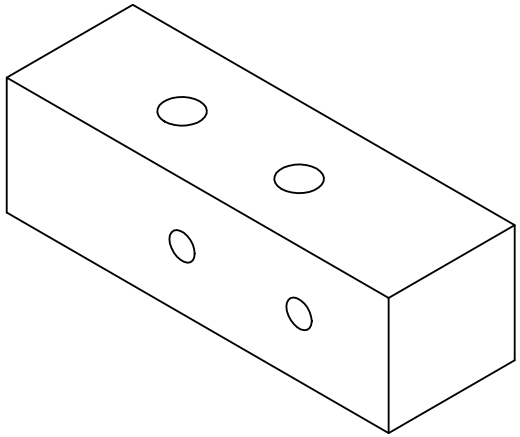

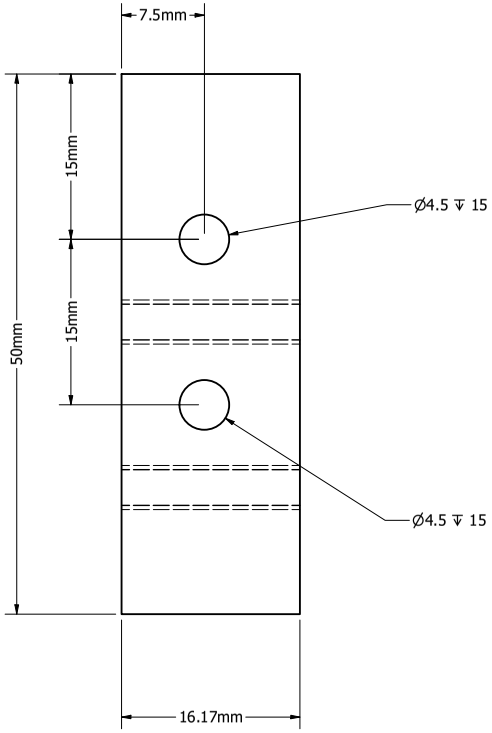

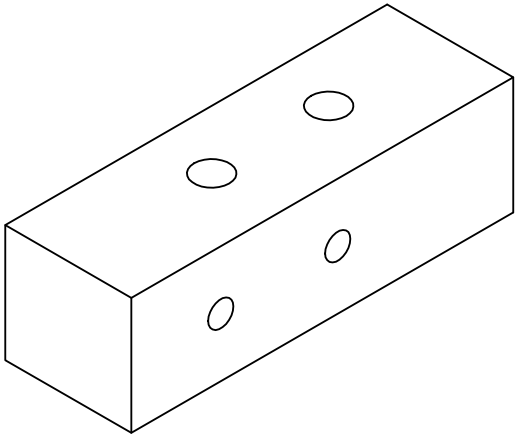

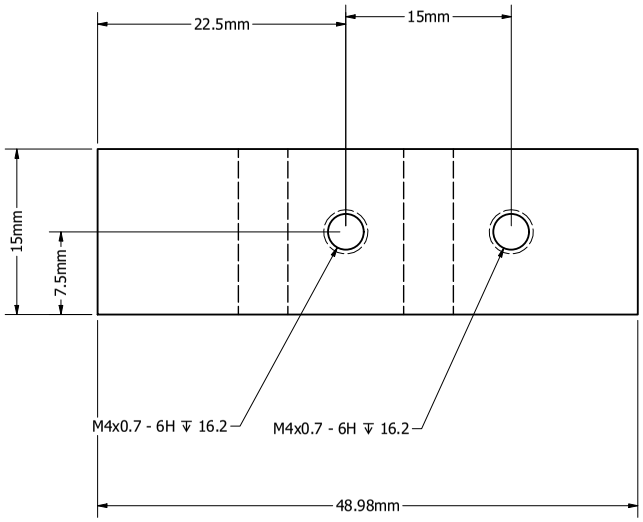

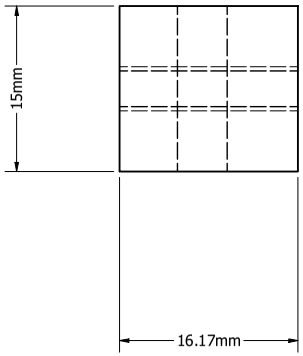

Material: bright steel

DRAWN Sabrina	2021/04/06	UNIVERSITY OF THE WITWATERSRAND	
CHECKED		TITLE SIDE BLOCK MIRROR	
QA			
MFG			
APPROVED	P7		
		SIZE C	DWG NO Side Block_MIR2 REV
		SCALE 3: 1	SHEET 1 OF 1

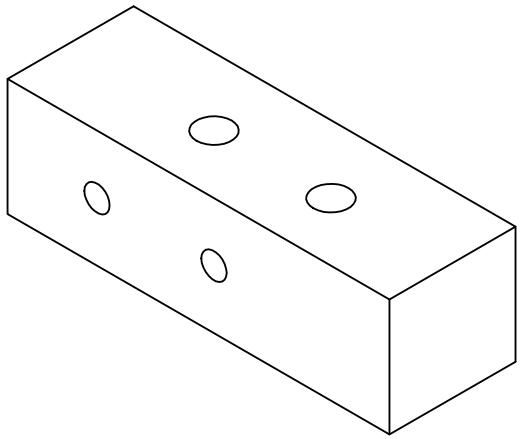

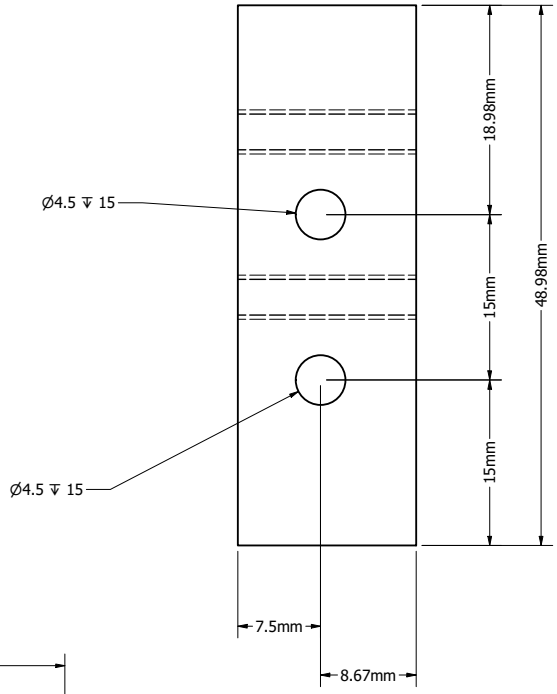

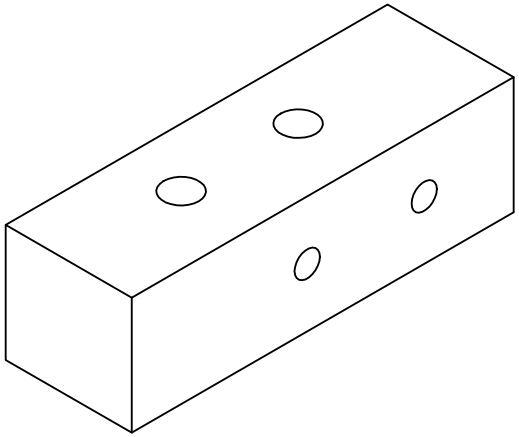

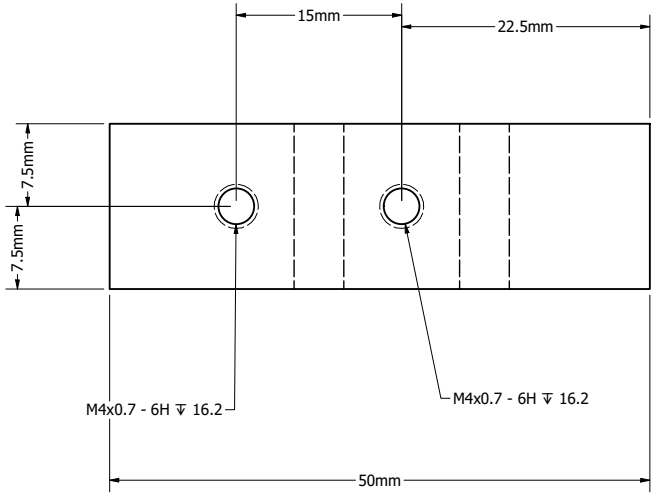

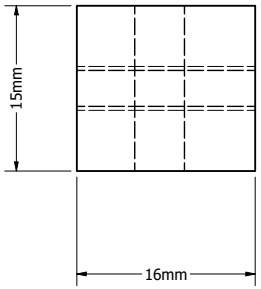

Material: bright steel

DRAWN Sabrina	2021/04/05	UNIVERSITY OF THE WITWATERSRAND
CHECKED		TITLE: SIDE BLOCK
QA		
MFG	P8	
APPROVED		
		SIZE C / DWG NO Side Block / REV
		SCALE 3: 1 / SHEET 1 OF 1

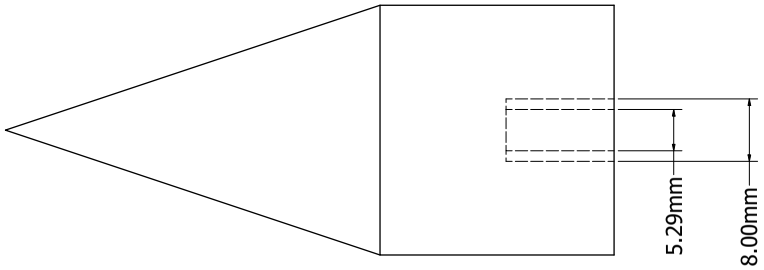

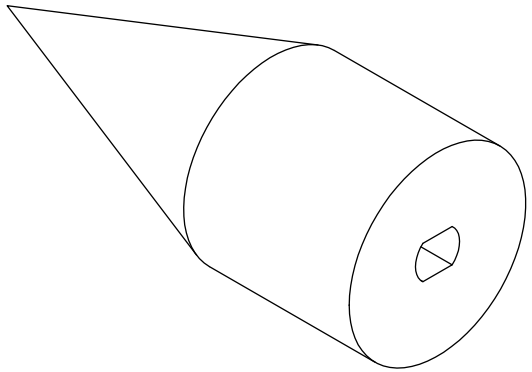

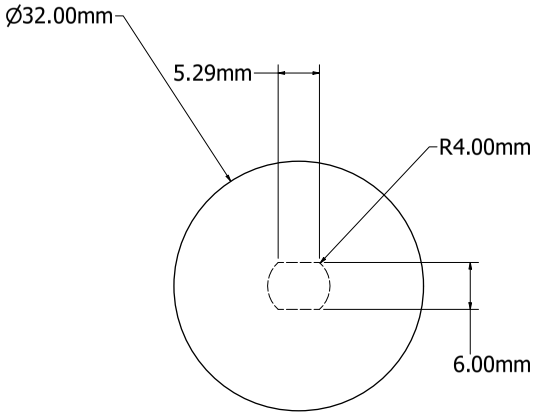

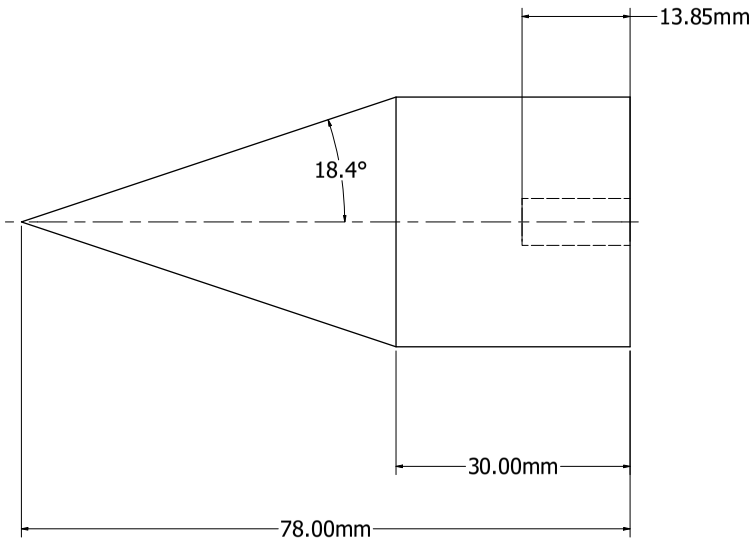

DRAWN Sabrina	2021/03/23	UNIVERSITY OF THE WITWATERSRAND
CHECKED		TITLE: SOLID CONE
QA		
MFG		
APPROVED		
		SIZE D · DWG NO SolidCone3 · REV
		SCALE 3 : 1 · SHEET 1 OF 1

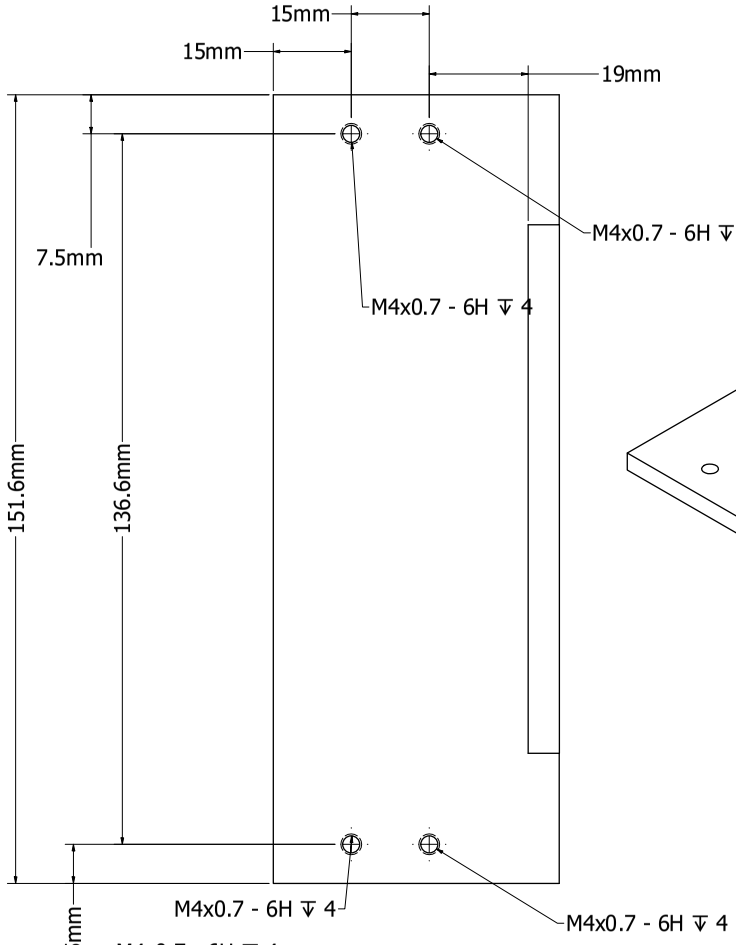

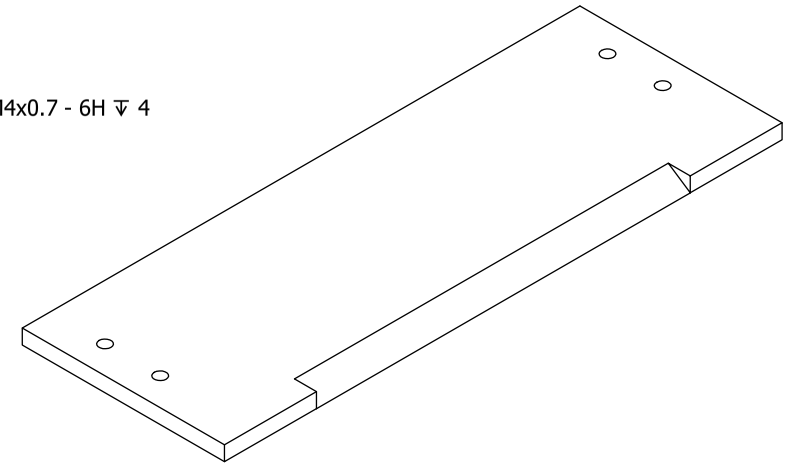

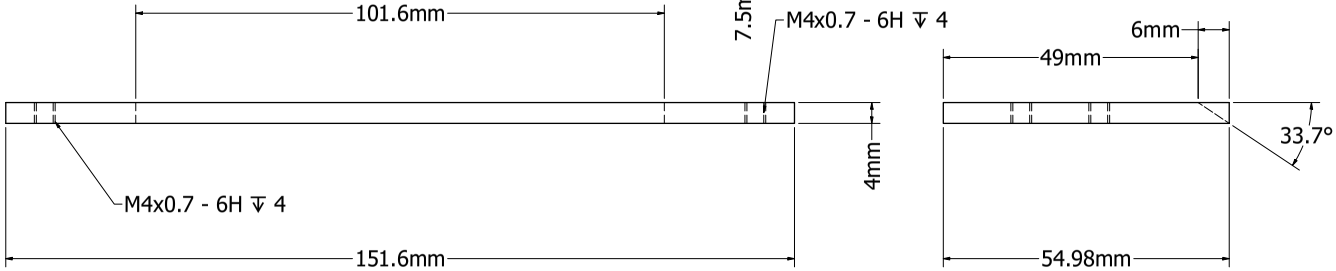

Material: bright steel

DRAWN Sabrina	2021/04/05	UNIVERSITY OF THE WITWATERSRAND
CHECKED		TITLE: SPLITTER PLATE
QA		
MFG		
APPROVED		
	P4	SIZE D · DWG NO Splitter plate · REV
		SCALE 2 : 1 · SHEET 1 OF 1

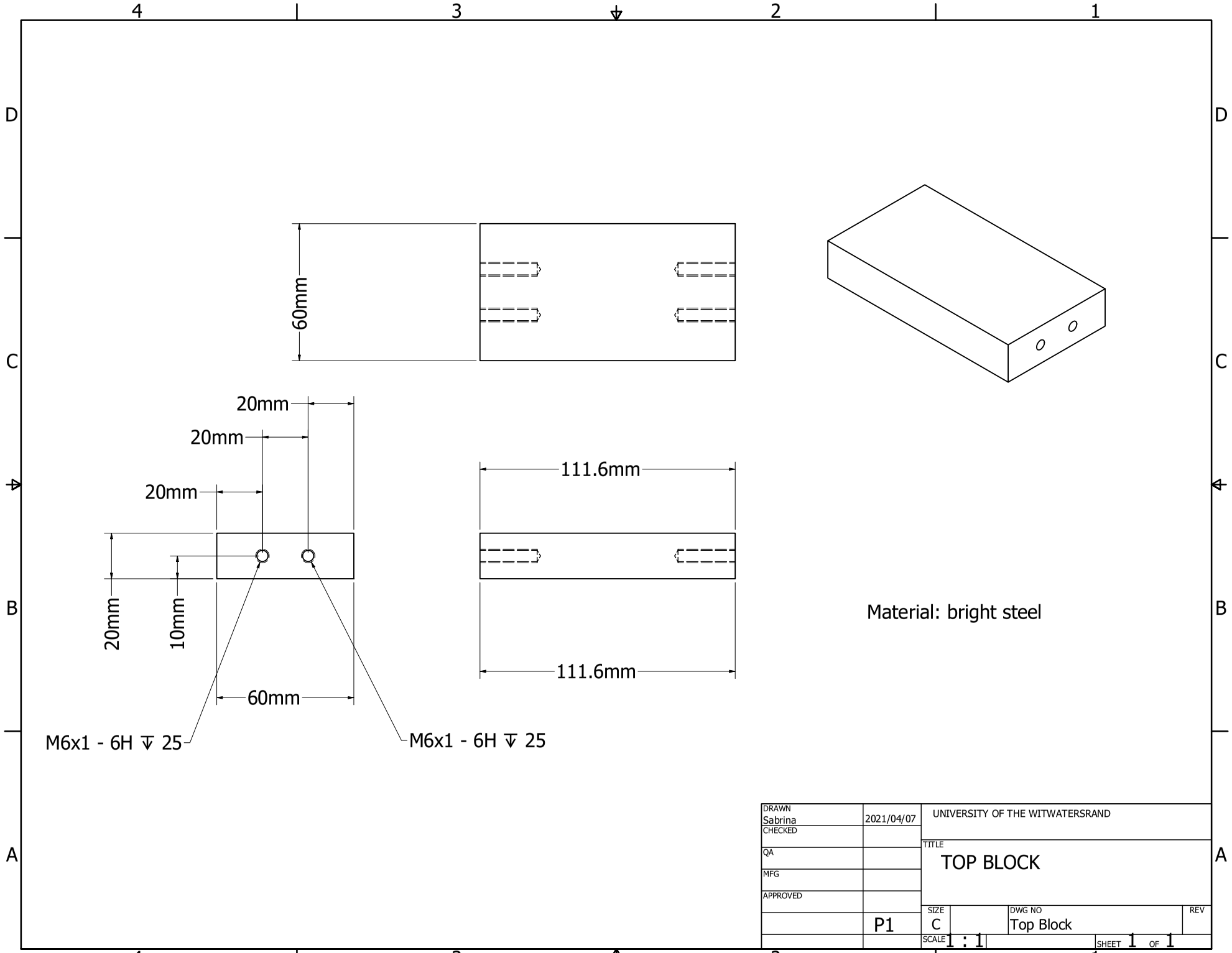
4
3
2
1
D
C
B
A
60mm
20mm
20mm
20mm
20mm
10mm
60mm
111.6mm
111.6mm
M6x1 - 6H ↧ 25
M6x1 - 6H ↧ 25
Material: bright steel
DRAWN
Sabrina
2021/04/07
CHECKED
QA
MFG
APPROVED
P1
UNIVERSITY OF THE WITWATERSRAND
TITLE
TOP BLOCK
SIZE
C
DWG NO
Top Block
REV
SCALE
1 : 1
SHEET 1 OF 1

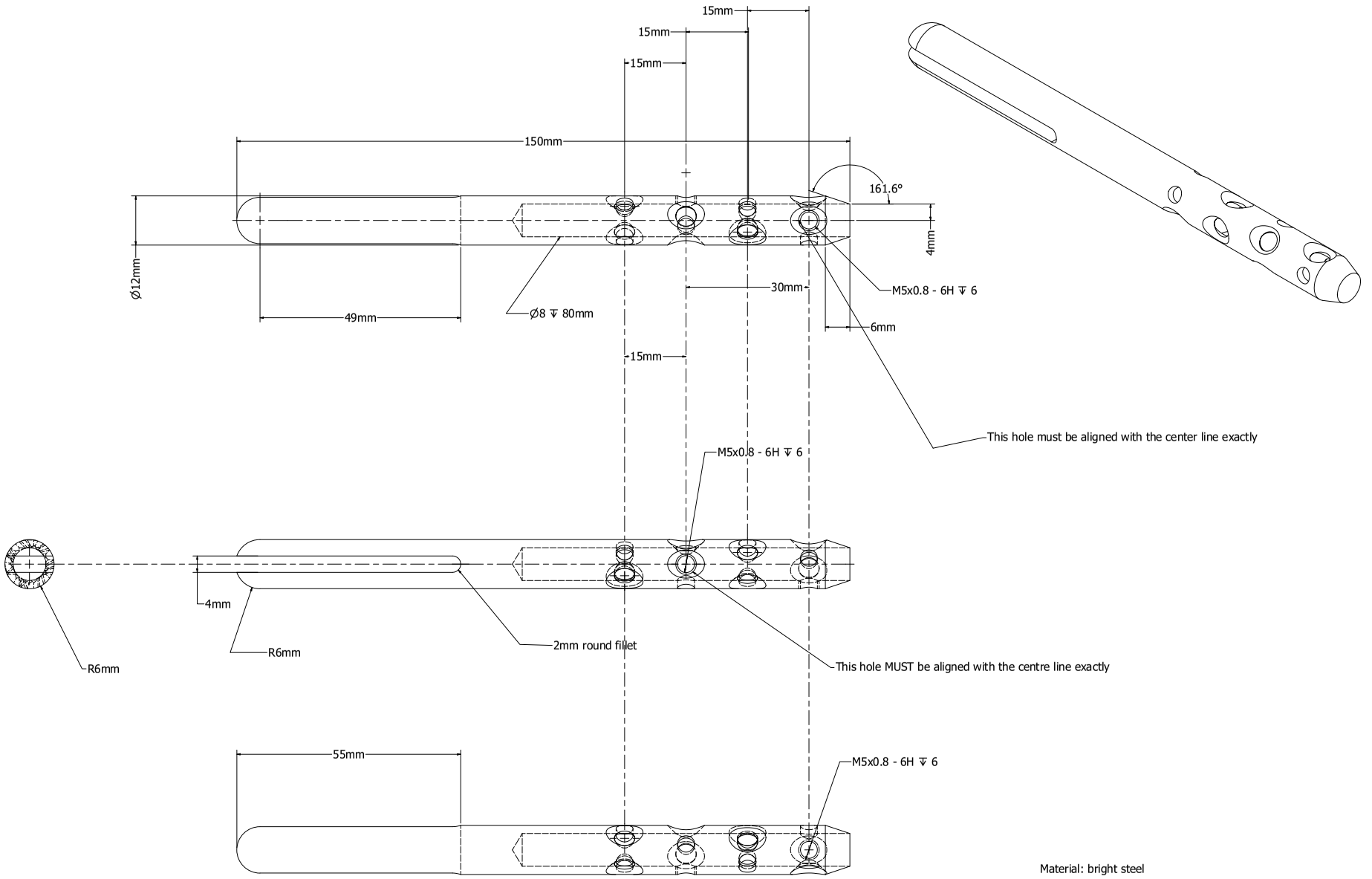

DRAWN Sabrina	2021/04/06	UNIVERSITY OF THE WITWATERSRAND
CHECKED		TITLE STING PERMANENT
QA		
MFG		
APPROVED		
	P2	SIZE E · DWG NO Sting unaltered 3 · REV
		SCALE 3: 1 · SHEET 1 OF 1

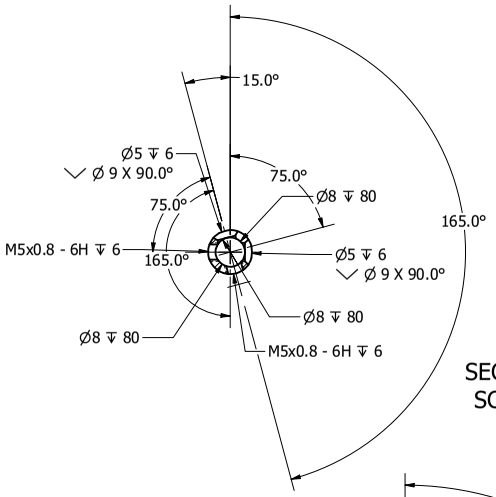

SECTION A-A
SCALE 1 : 1

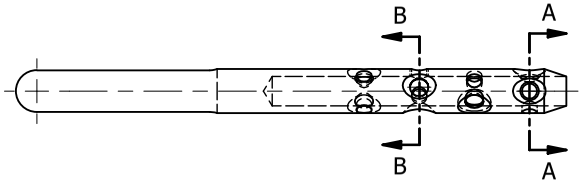

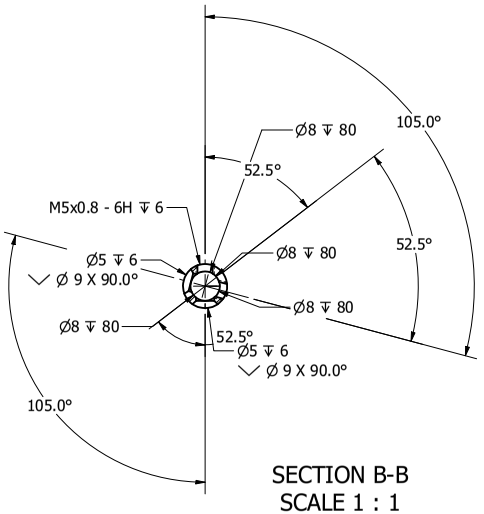

SECTION B-B
SCALE 1 : 1

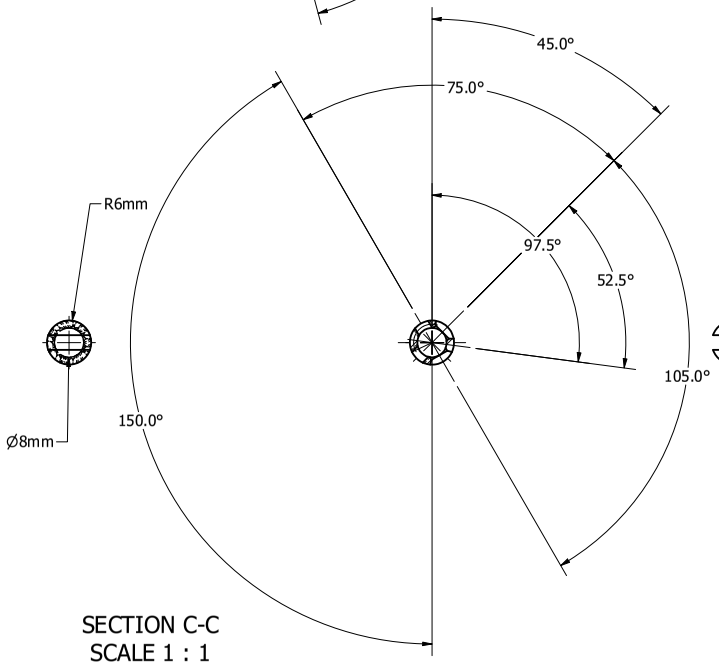

SECTION C-C
SCALE 1 : 1

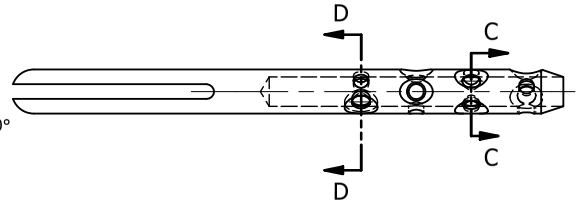

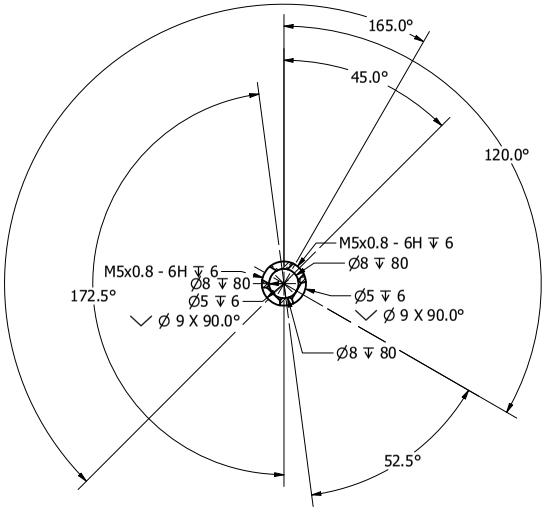

SECTION D-D
SCALE 1 : 1

Material: bright steel

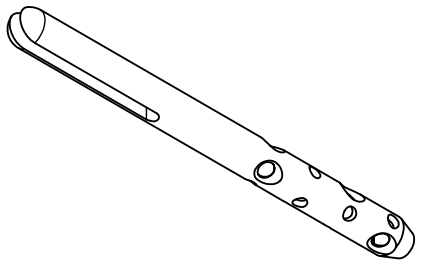

Angles must be accurate to
+/- 0.2°

DRAWN Sabrina	2021/04/06	UNIVERSITY OF THE WITWATERSRAND	
CHECKED		TITLE PERMANENT STING SECTION VIEW	
QA			
MFG			
APPROVED	P3		
		SIZE C	DWG NO Sting unaltered 3 VIEWS REV
		SCALE 1 : 1	SHEET 1 OF 1

Appendix D

Nose Cone Profile

To define the nose cones, Pish et al. (2020), Samuels (2005), Haack (1941) is referenced. In all nose cone geometries, L is the overall length of the nose cone, R is the radius of the base of the nose cone. Each profile is described by a unique r(x) equation, with the generated profile depending on the chosen input R and L. Fig. 102 shows the ellipsoid nose cone diagram in (a) and the formulation of the tangent ogive in (b).

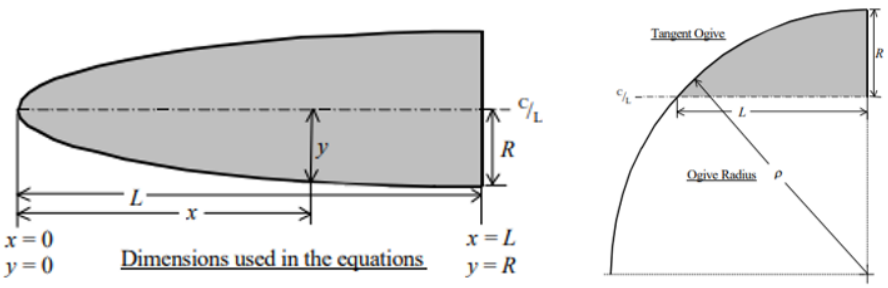

Figure 102: Diagram showing the general nose cone dimensions (Pish et al. (2020))

The chosen profile shape of a projectile dictates the performance, and every profile shape has its own advantages and disadvantages. The blunted nose of some projectiles, for example causes a bow shock. For other, pointed profiles, boundary layer separation may occur sooner than for other shapes. These factors, as well as the associated wave drag, negatively affect performance. As such, a means of reducing shock strength, boundary layer separation and wave drag must be explored. The profiles are explored are demonstrated in Fig. 103.

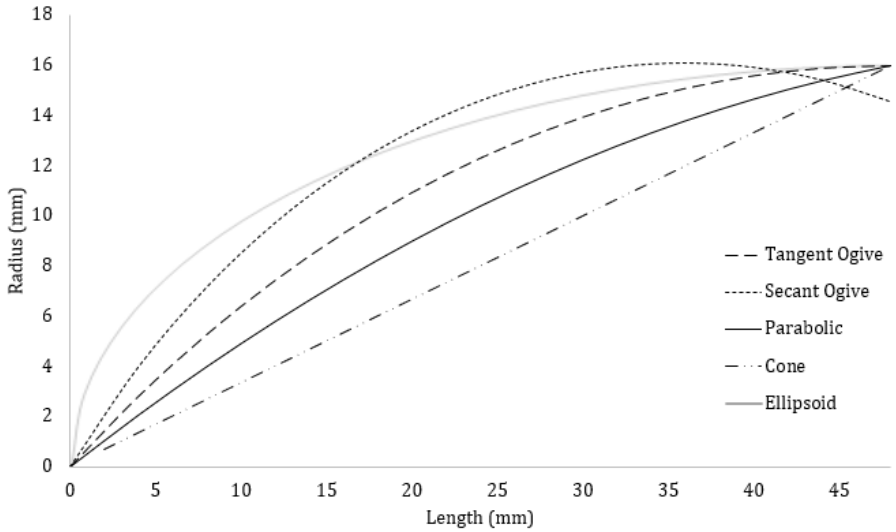

Figure 103: Curves of the different types of nose cone profiles

D.1 Conical Profile

The most common nose cone and projectile shape is the regular cone. The sides are straight lines and the diameter equation is as follows.Cones are defined by their half angle ϕ:

$$y = \frac{xR}{L} \tag{6}$$

Cones are defined by their half angle ϕ:

$$\phi = \arctan \frac{R}{L} \tag{7}$$

$$y = x \tan \phi \tag{8}$$

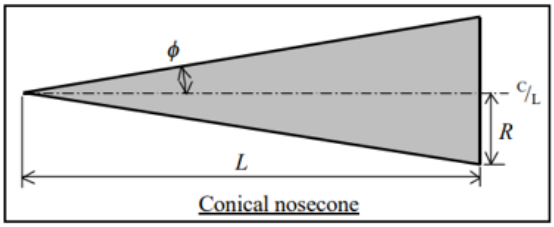

Figure 104: Schematic of the pointed nose cone profile Pish et al. (2020)

D.2 Secant ogive

The secant ogive is also formed from the segment of a circle, but the base of the shape is not on the radius of the circle defined by the ogive radius (Crowell (1996)). The body is not tangent to the curve of the nose at its base. The ogive radius ρ is not determined by R and L, but is instead a factor which is chosen to define the nose shape.

$$\phi > \frac{R^2 + L^2}{2R} \tag{9}$$

$$\alpha = arctan(\frac{R}{L}) - arccos(\frac{\sqrt{L^2 + R^2}}{2\phi}) \tag{10}$$

The radius y at any point x, as x varies from 0 to L is:

$$y = \sqrt{\rho^2 - (x - (\rho)cos\alpha)^2} + \rho(sin\alpha) \tag{11}$$

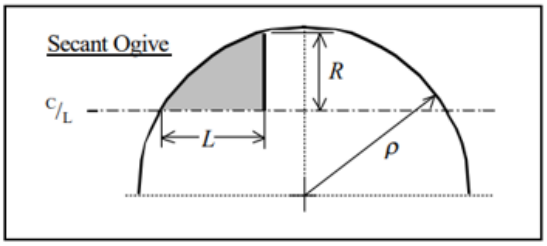

Figure 105: Schematic of the secant ogive profile Pish et al. (2020)

D.3 Ellipsoid profile

This profile is half on an ellipse, with the major axis being along the horizontal centreline and the minor axis being along the vertical centreline. This shape has a blunt nose and tangent base, which is advantageous for subsonic flight.

$$y = R\sqrt{1 - \frac{x^2}{L^2}} \tag{12}$$

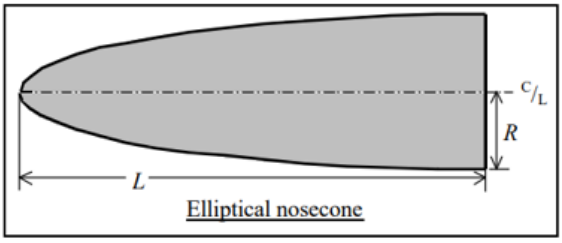

Figure 106: Schematic of the ellipsoid profile Pish et al. (2020)

Appendix E

Creality LD-002R 3D Printer - Technical Specifications

E.1 Printer function

This technology used a conventional light source, such as an arc lamp, with a crystal liquid display panel (Davoudinejad et al. (2018)). A vat of liquid polymer was exposed to UV light behind a clear tinted housing. The sliced 3D image was then imported to the printer where a in-built projector rested underneath the resin bath, projecting slices of the 3D image onto the build platform as a thin layer of resin. This first layer of photopolymer, or resin, was exposed to the UV light and hardened, or cured. This process continued until all the layers of the 3D part had been printed and a full part was created. The part was suspended from the build platform by numerous supports, also created in layers during printing.

Table 16: Creality LD-002R 3D Printer Specifications

Printing Technology	DLP (LCD Shadow Masking Technique)
Build Volume	119 x 65 x 160mm
	Actual Bed Size = 138 x 78mm
Chassis Size (Desk Space Required)	221 x 221 x 403mm
3D Resin Compatibility	405nm Photosensitive Resin
Extrusion/Curing Style	Digital Light Processing: LCD Masking Technique
Extruder/Curing Assembly	40W Parallel Matrixed UV Array
Print Platform Style	Aluminium Plate
Print Platform Levelling System	Single Nut Locking System
Printing Speed (Stable)	20mm / hour
Printing Speed (Max)	30mm / hour
XY Resolution	47 microns (with 4X/8X Anti-Aliasing)
Z Resolution (Layer Height)	26 to 50 microns
LCD Projection Size	119 x 65mm (2560 x 1600 Resolution)
Motherboard / Primary Controller	Creality DLP Motherboard V3
User Interface	3.5” Full Colour Touchscreen
File Transfer Method	USB Drive
Included Slicing Software	CHITUBOX / ChiTuBox Slicer <- Latest Version
Light Insulation Cover	Orange UV Resistant Moulded Cover
Chassis Materials	Anodised Aluminium / Injection Moulded ABS
Distinct Features	Intelligent Anti-Aliasing Function
	Volume-Marked Resin Vat
	Simplified Semi-Automatic Levelling
Weight (Printer)	7kg
Weight (Package)	9kg
Operating Voltage	12V DC
Power Supply Input	110 to 240V Auto-Switching - 50/60Hz
Power Supply Output	12V, 72W, 6A

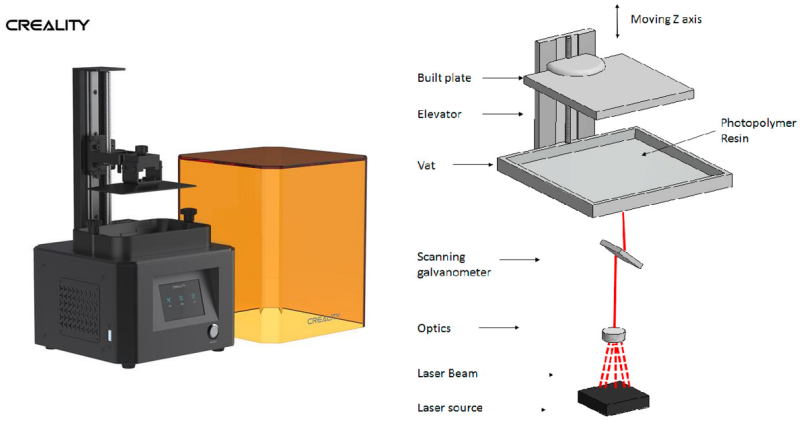

Figure 107: Image showing (a) the Creality 3D resin printer (Creality (2024)) (b) a diagram showing the different parts of the printer (Davoudinejad et al. (2018))

Fig. 108 (a) and (b) show the sliced half-model using the DLP Chitubox software. Whilst external supports were present, no internal supports were required, leaving all the holes and channels open. DLP resin is more costly than FDM filament. However, around twelve prints could be achieved with 500 ml of resin, which was acceptable.

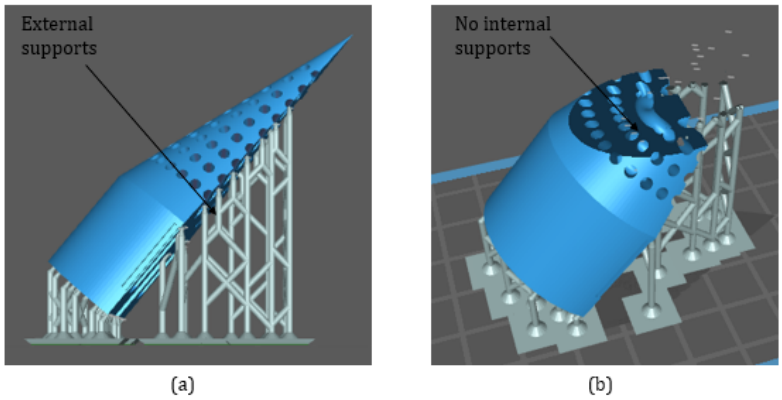

Figure 108: Image showing the sliced DLP 3D printer image (a) full view (b) section view showing no internal supports

E.2 3D printing safety precautions

During printing with resin, several safety precautions were adhered to. The resin used was toxic to both the environment and user. The resin was a mixture of photosensitive monomers and oligomers, which releases natural fumes that can irritate the respiratory system and skin if contact is made. Exposure to the working environment, such as contact surfaces, can also be

dangerous as the substance is carcinogenic. These risks were mitigated by wearing Personal protective equipment (PPE) at all times when handling the resin, including nitrile gloves and a mask at all times. Working in a well-ventilated room was ensured. Work surfaces were cleaned thoroughly with isopropyl alcohol 99% regularly to remove any traces of resin, and aluminium foil and plastic coverings were used to additionally cover all surfaces. The printer also held in a foil tray to catch any resin run-off for easier, safer clean-up.

Several measures were taken to ensure that the conic model print quality and symmetry were sufficient, thus ensuring the success of the validation process. The acceptability of the print was decided based on the symmetry factors outlined:

E.3 3D Conic model manufacturing

The printed experimental models required a very high degree of symmetry and precision in order to be comparable with the CFD models. The final conic models used in the experimentation were manufactured by printing each half of the model as a separate part. The criteria for symmetry and print quality are listed as follows:

1. Overall model circularity and trueness to shape and design
2. Cone-cylinder shoulder evenness (i.e. shoulder height above the central axis constant around the entire body)
3. Sting-hole straightness and shape (i.e. hole malformation)
4. Pores shape and clarity (i.e. holes/channels malformed or rough)
5. Cone versus cylinder shape (i.e. symmetry, trueness to shape)

The final conic models used in the experimentation were manufactured by 3D printing each half of the model as a separate part. Printing whole models resulted in extreme asymmetry and unusable prints. The whole models were too heavy for each successive build layer to cure in time, resulting in the model sagging increasingly as it was printed on account of excessive

Poissons stress in the part. Ample supports were required to prevent part deformation, in particular around the centre, as shown in Fig. 111. The points below outline the measures taken to eliminate the weight problem.

1. All Autodesk Inventor conic models were sliced in half - reducing overall part weight.
2. A hole (a hollow ring inside the cylinder which reduced the weight by 50% whilst having no effect on the functionality or strength of the base) was added - reducing overall part weight.
3. Half-cone build angle of 40° to the horizontal - allowed greater area for increased build supports.

These measures resulted in two near-perfect half-cone prints, as in Fig. 109 c). Note that Fig. 109 does not represent the true degree of symmetry since the photographs were taken at a slight angle. The print's outer surface was smooth, as most of the supports existed on the flat-cut side of the cone-cylinder. After support removal, the rough cut surface was lightly sanded and smoothed a). The two halves were then hand-joined using both Pratley Epoxy Resin and superglue, as in c). The edge where the half-models were joined was known as the 'seam'. Any gaps were carefully filled with epoxy resin, as in d). The sting hole was acceptably symmetric and straight to allow for correct mounting.

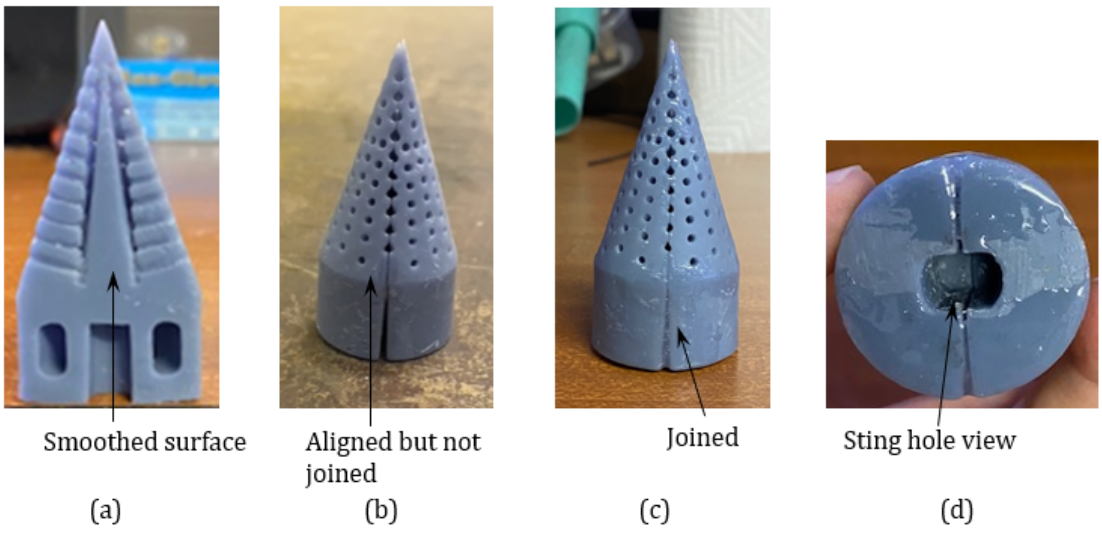

Figure 109: Combined unvented cone a) half model after sanding c) aligned but not joined c) bonded/joined halves d) base view of the joined model

Fig. 110 shows two views of the baseline, jointed 3D printed BS0 cone mounted on an inner sting. The models were mounted to the sting using Pratley Epoxy Resin, and a lathe was used to ensure that the inner sting, cone and global horizontal wind tunnel axis were coaxial to eliminate pitching. Any pitching visible in the schlieren images was due to slight manufacturing asymmetry. 20 wind tunnel models were made.

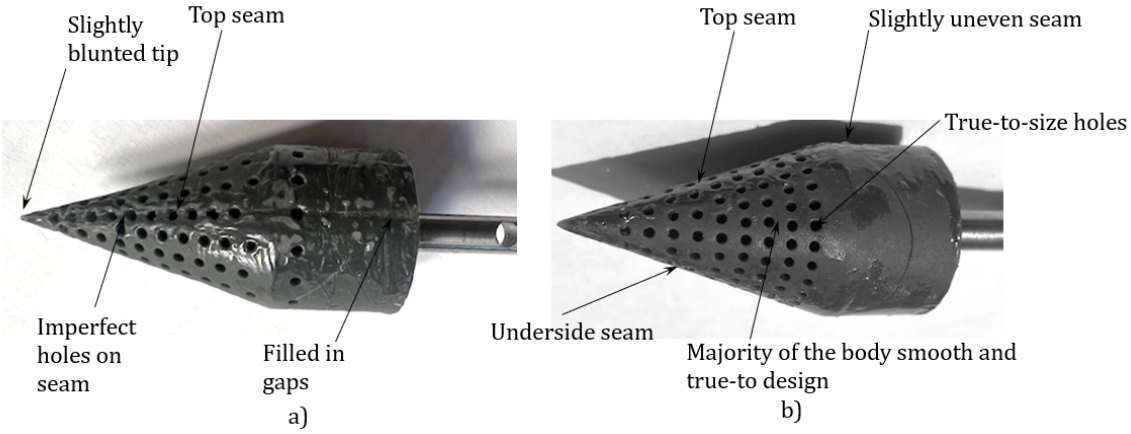

Figure 110: Annotated 3D printed BS0 cone a) seam-view c) view of smooth side

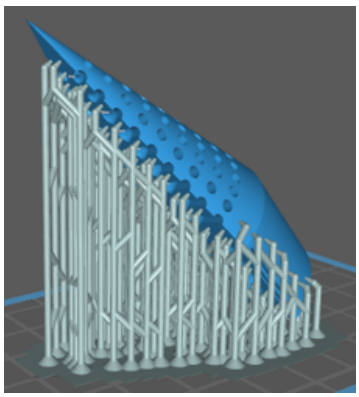

Figure 111: Unvented combined half-cone on the Chitubox build plate, with supports.

Appendix F

3D Printed Cone Iterations

Table 17: Table showing the 3D printed model iterations and the key factors affecting outcome

Iteration	Model printed	Process	Light-ening hole	Print angle	Cone	Sting	Outcome
1st	Full	Print with default supports	No	45°	Significant asymmetry	Significant asymmetry	Failiure
2nd	Full	Print with more supports	No	40°	Significant asymmetry	Significant asymmetry	Failiure
3rd	Full	Print with more supports and machine on lathe	No	40°	Significant asymmetry and irreparable damage to the cone	Significant asymmetry	Failiure
4th	Half	Print halves then join	Yes	40°	Symmetric	Symmetric	Success

The following images depict the various print iterations.

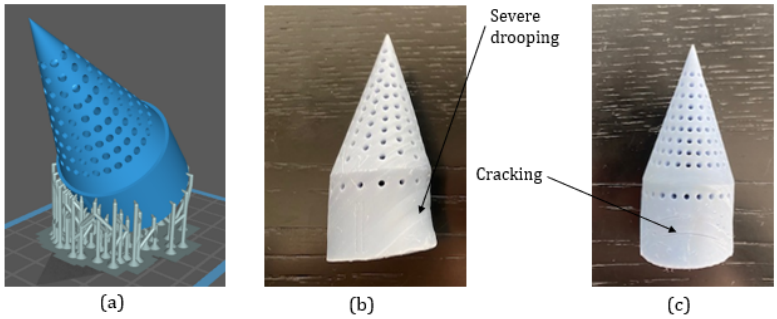

Figure 112: Image showing the first print iteration (a) supports used (b) side view (c) front view

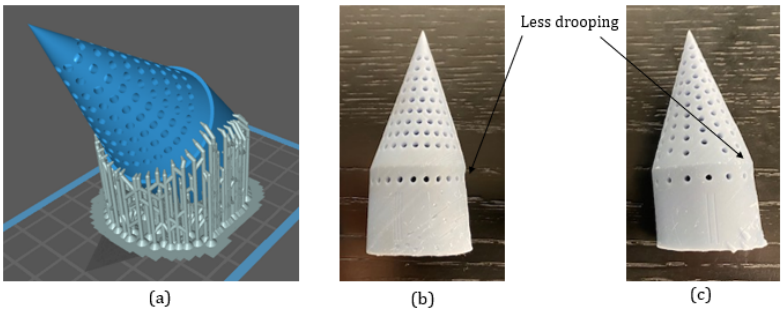

Figure 113: Image showing the second print iteration (a) supports (b) first derivative (c) second derivative

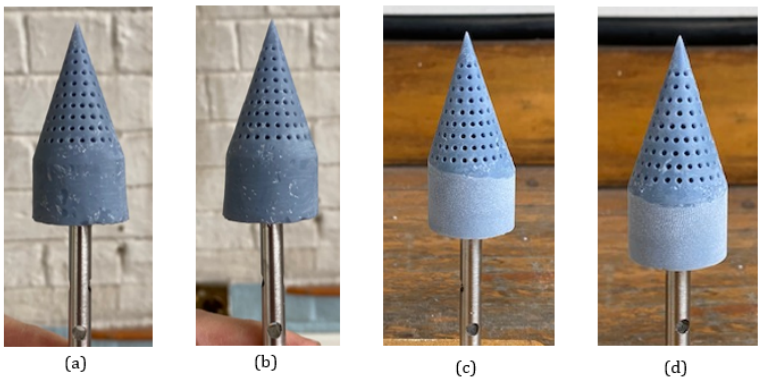

Figure 114: Image showing the comparison between the solid printed cone (a) front view before machining (b) side view before machining (c) front view after machining (d) side view after machining

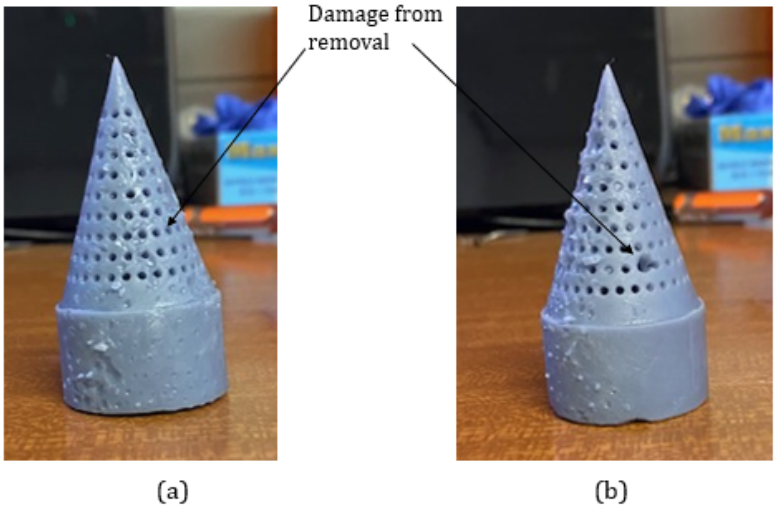

Figure 115: Image showing the solid printed cone before machining

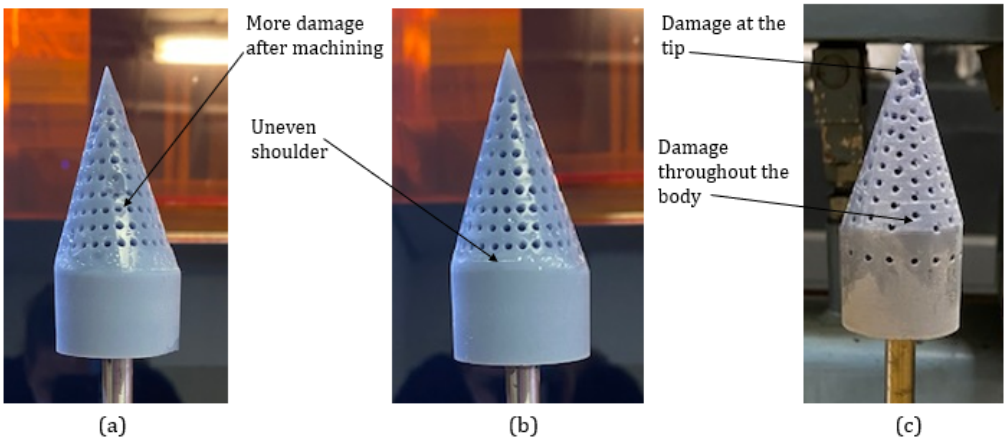

Figure 116: Image showing (a) and (b) the solid cone after machining (c) the damage caused by machining

Appendix G

Experimental schlieren Mach 3.5; Mach 3 results

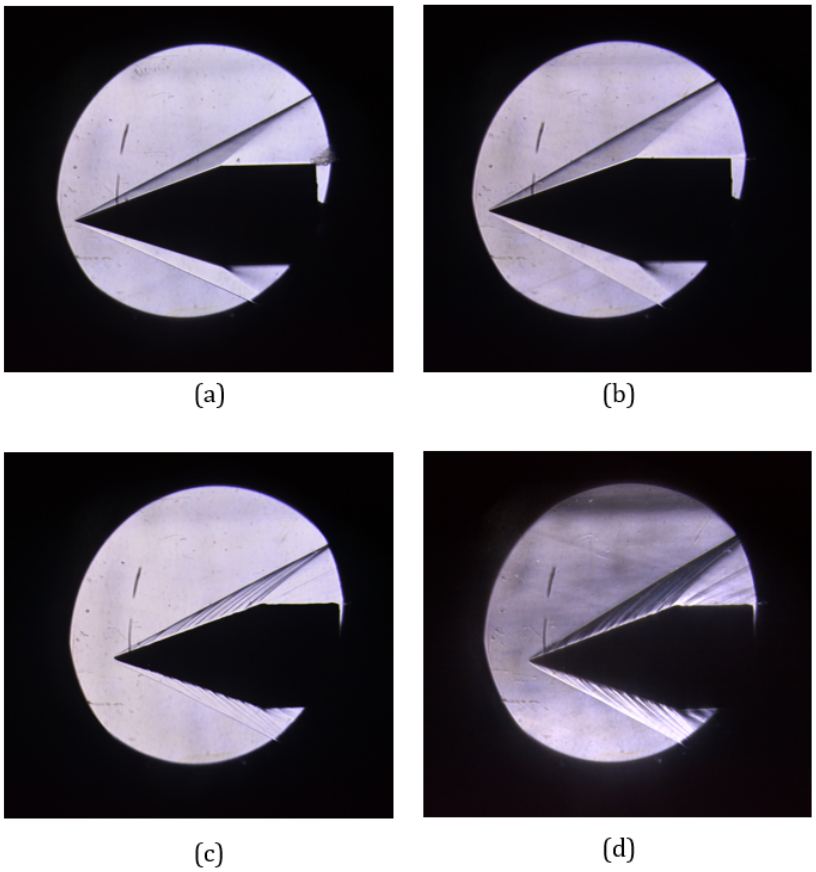

Figure 117: Schlieren images of pointed cones (a) solid M3.5 (b) solid M3 (c) BS0 cone M3.5 (d) BS0 cone M3.

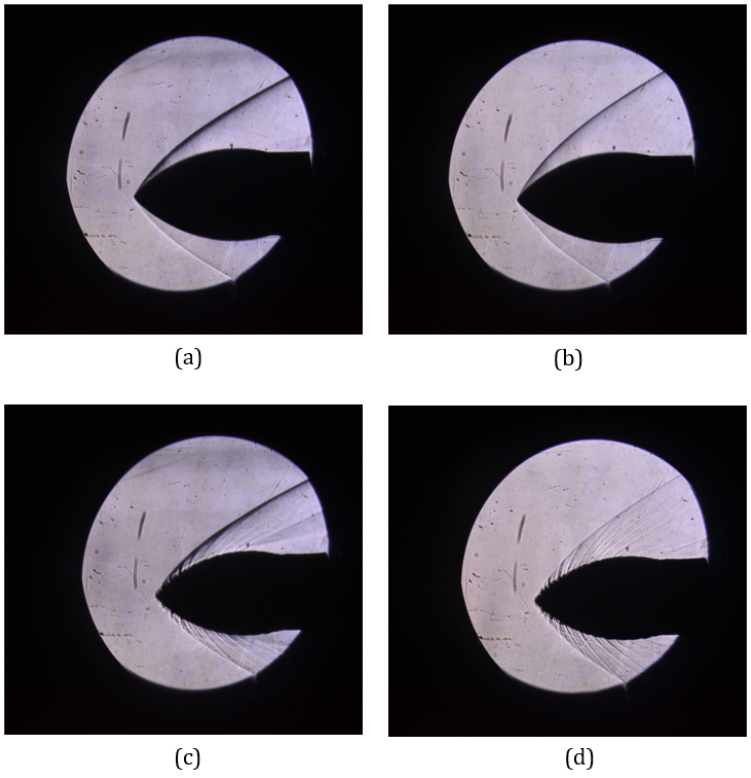

Figure 118: Schlieren images of secant ogive (a) solid M3.5 (b) solid M3 (c) BS0 M3.5 (d) BS0 M3.

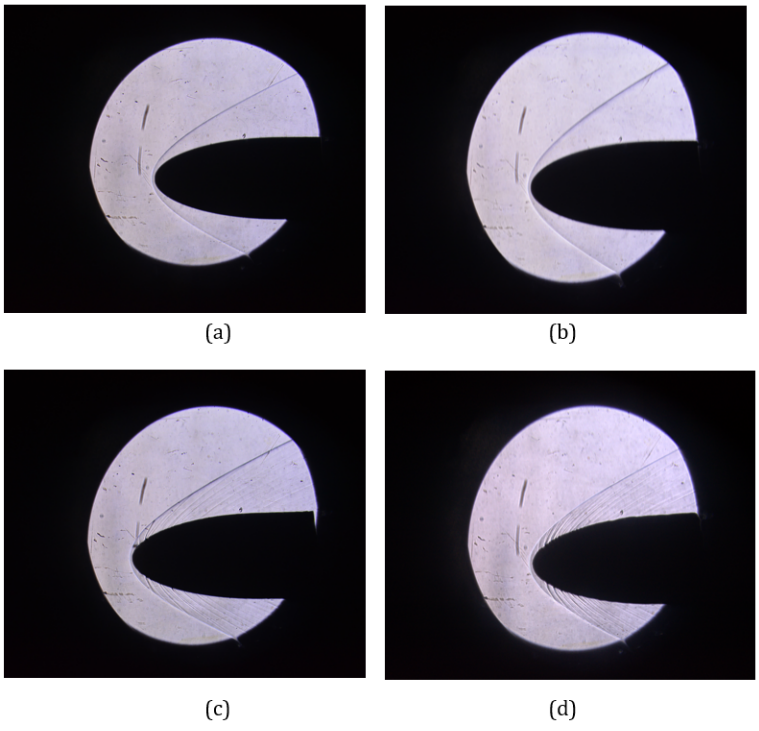

Figure 119: Schlieren images of ellipsoid (a) solid M3.5 (b) solid M3 (c) BS0 M3.5 (d) BS0 M3.

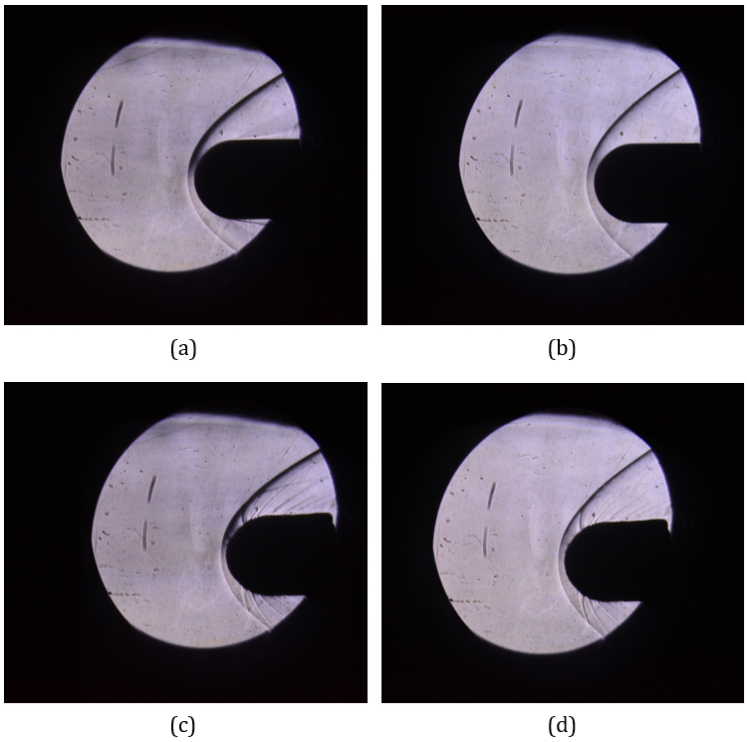

Figure 120: Schlieren images of hemispheres (a) solid M3.5 (b) solid M3 (c) BS0 M3.5 (d) BS0 M3.

G.1 CFD Pointed Cone Mach 3 - BS0/Solid

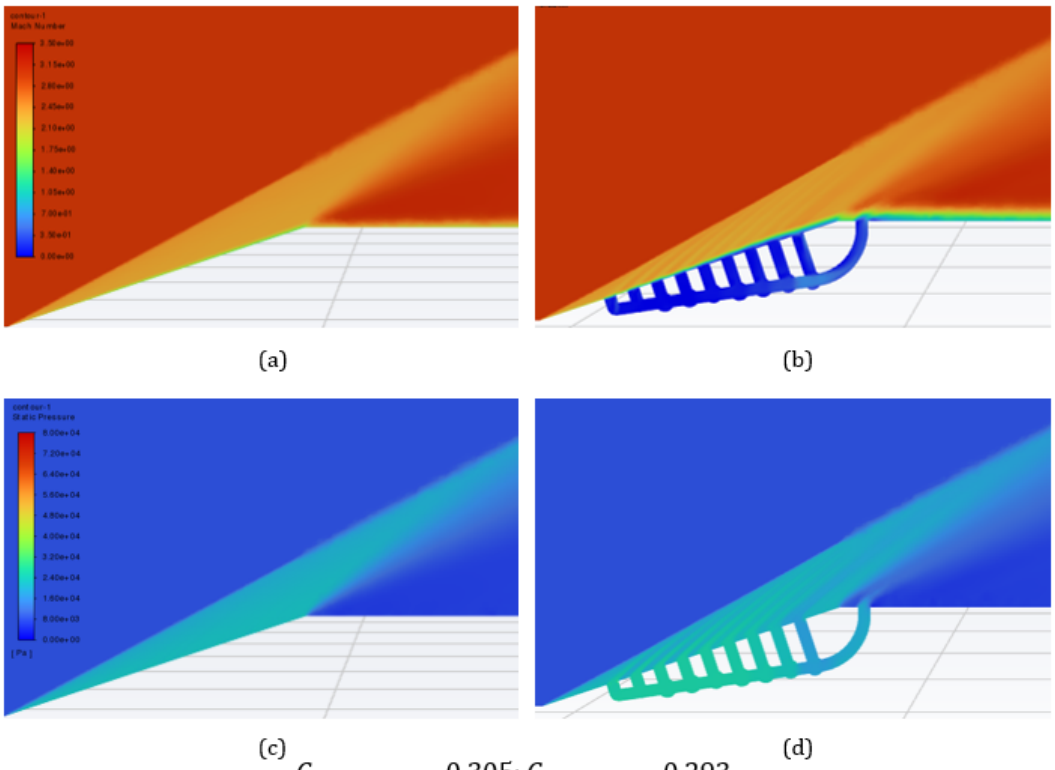

Figure 121: Flooded contour plots of pointed cones at Mach 3 (a) solid Mach plot (b) BS0 Mach plot (c) solid static pressure (d) BS0 static pressure.

G.2 Results of Unvented Combined Pointed Cone Mach 3.5

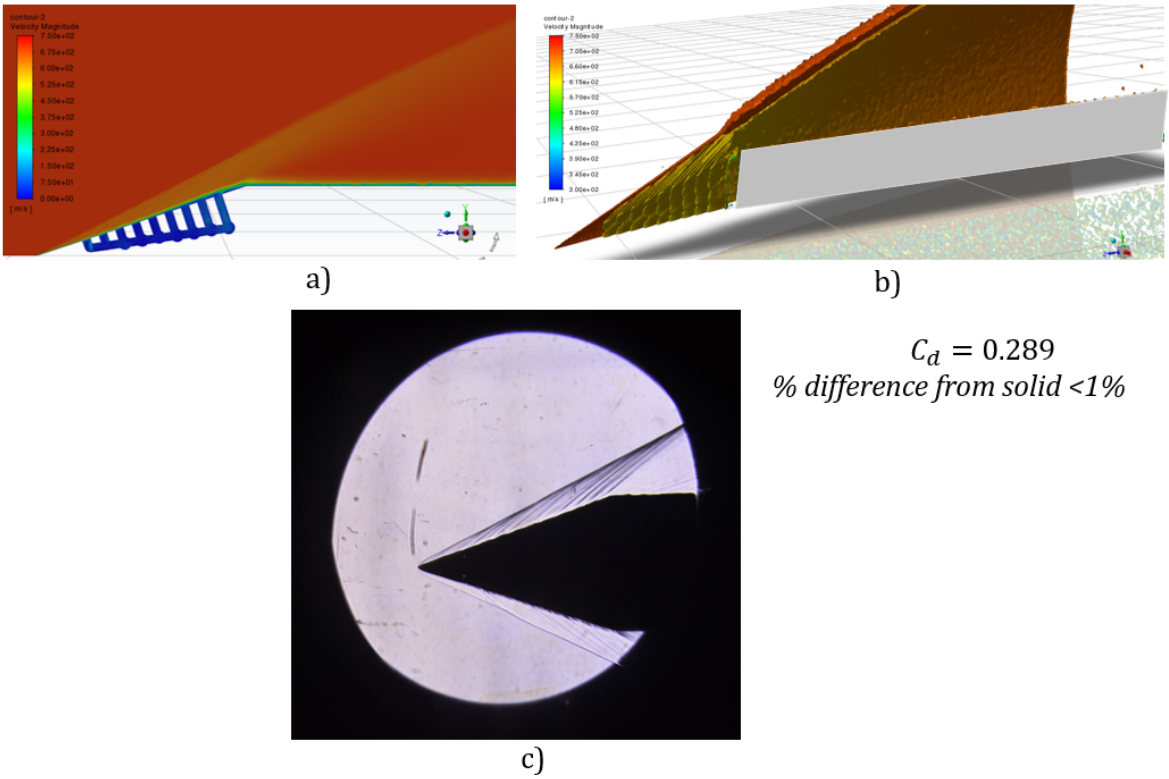

Figure 122: Images of the unvented combined cone at Mach 3.5 a) flooded CFD contour plots b) CFD velocity isosurface of the bow wave c) schlieren photograph.

Appendix H

Conic model schematics

H.1 Pointed cones - Combined/Radial/Longitudinal models

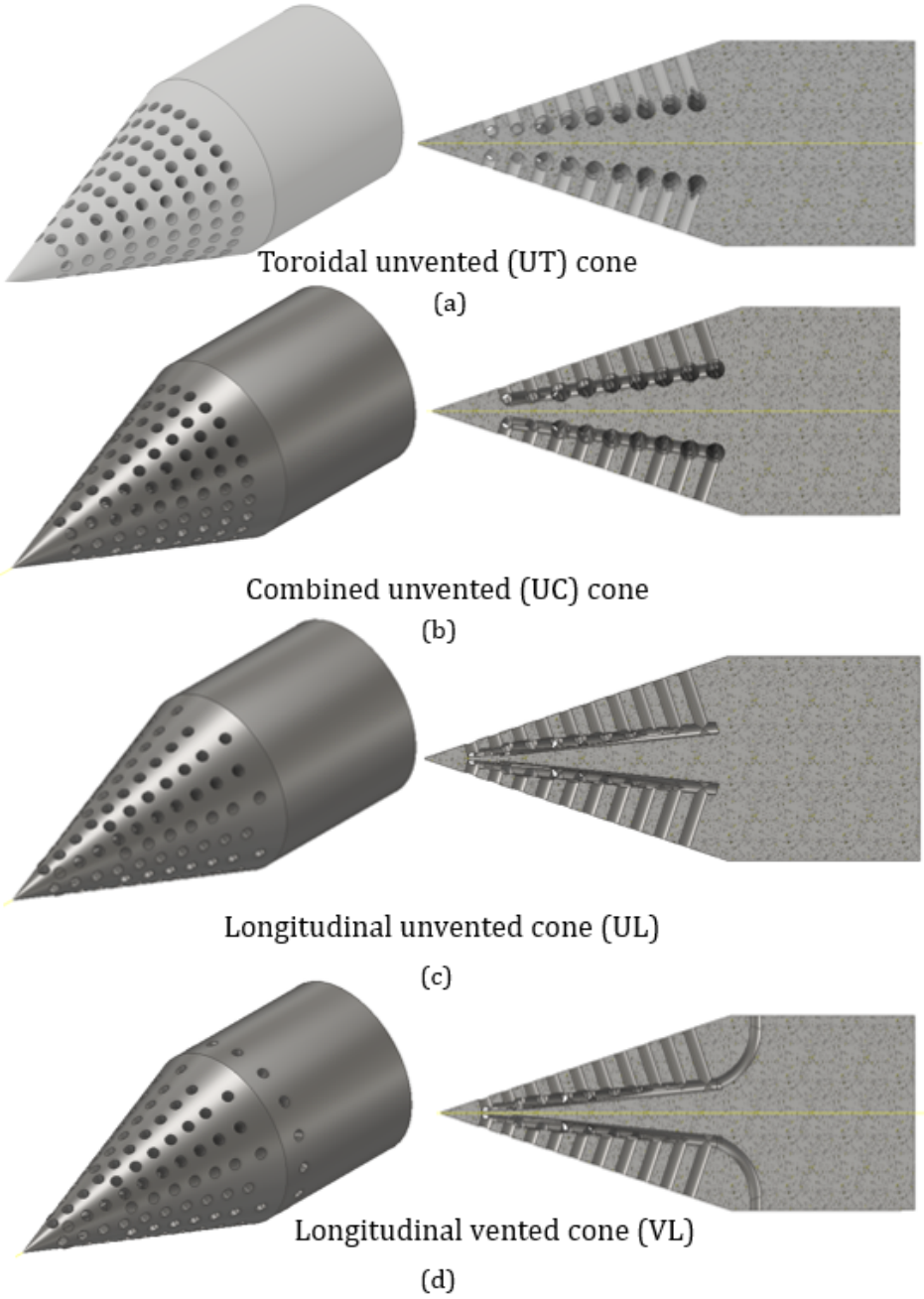

Figure 123: Schematics of pointed cones BS (a) Toroidal UV (b) Combined UV (c) Longitudinal UV (d) Longitudinal Vented.

H.2 Pointed cones - BS0 - BS4

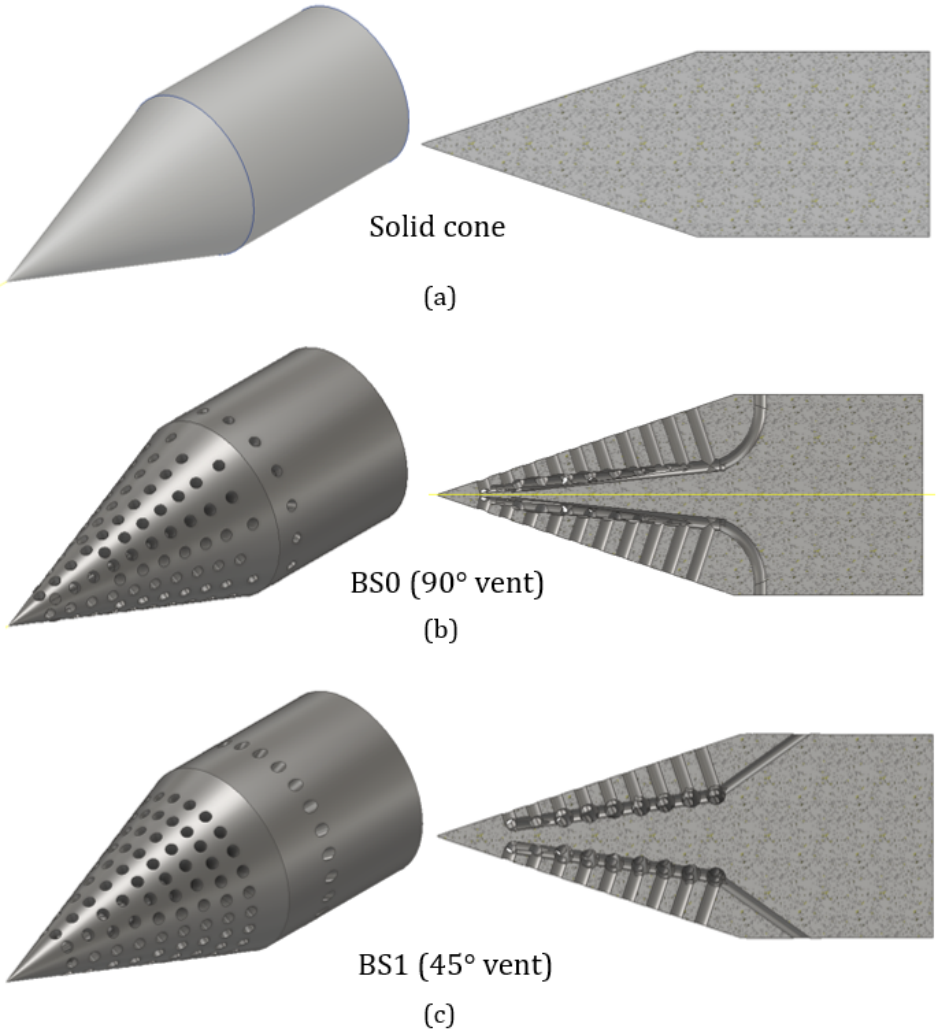

Figure 124: Schematics of pointed cones (a) solid (b) BS0 (c) BS1 (outside and internal view).

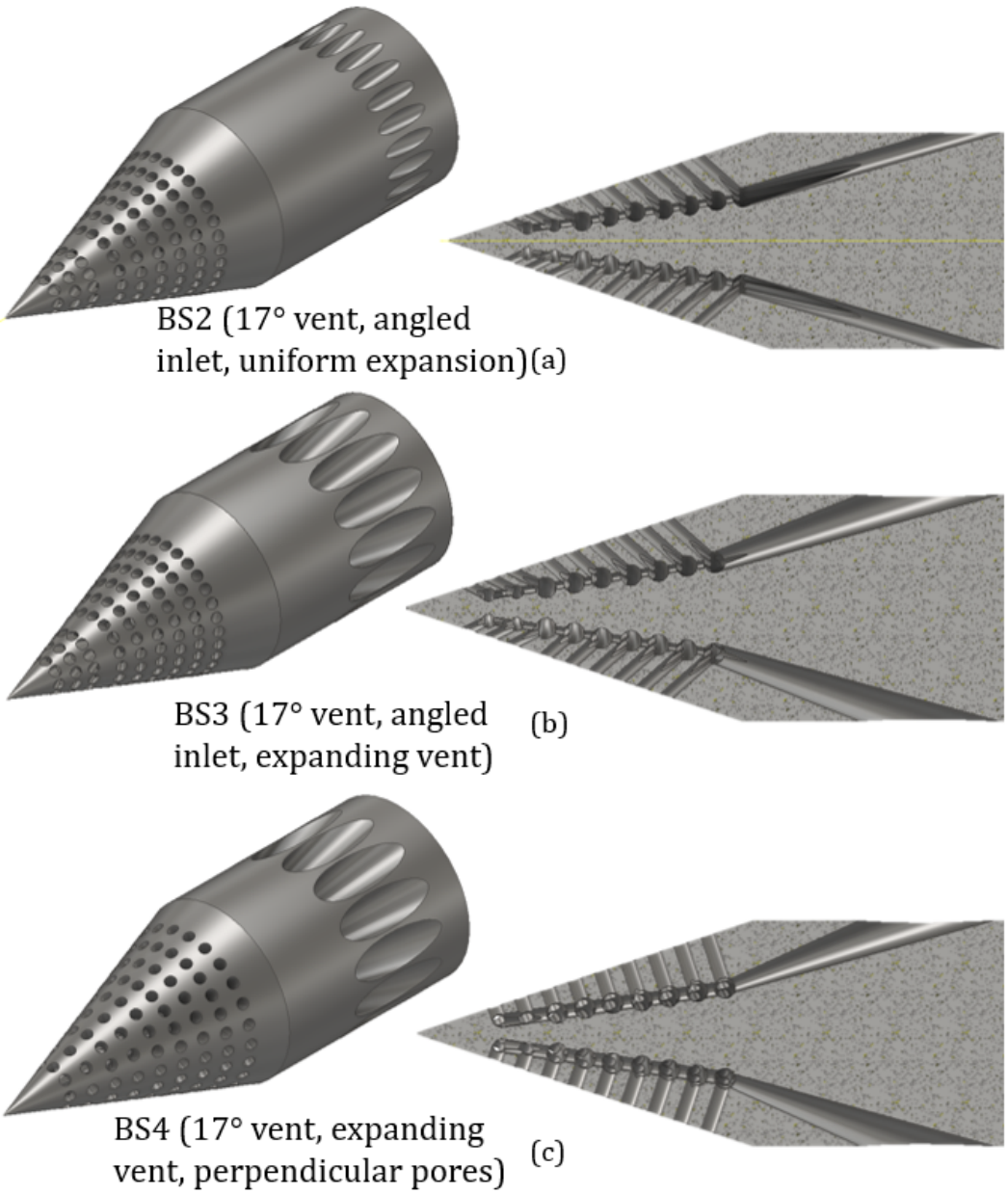

Figure 125: Schematics of pointed cones (a) BS2 (b) BS3 (c) BS4 (outside and internal view).

H.3 Pointed cones vent-specific - OE, UE and CE

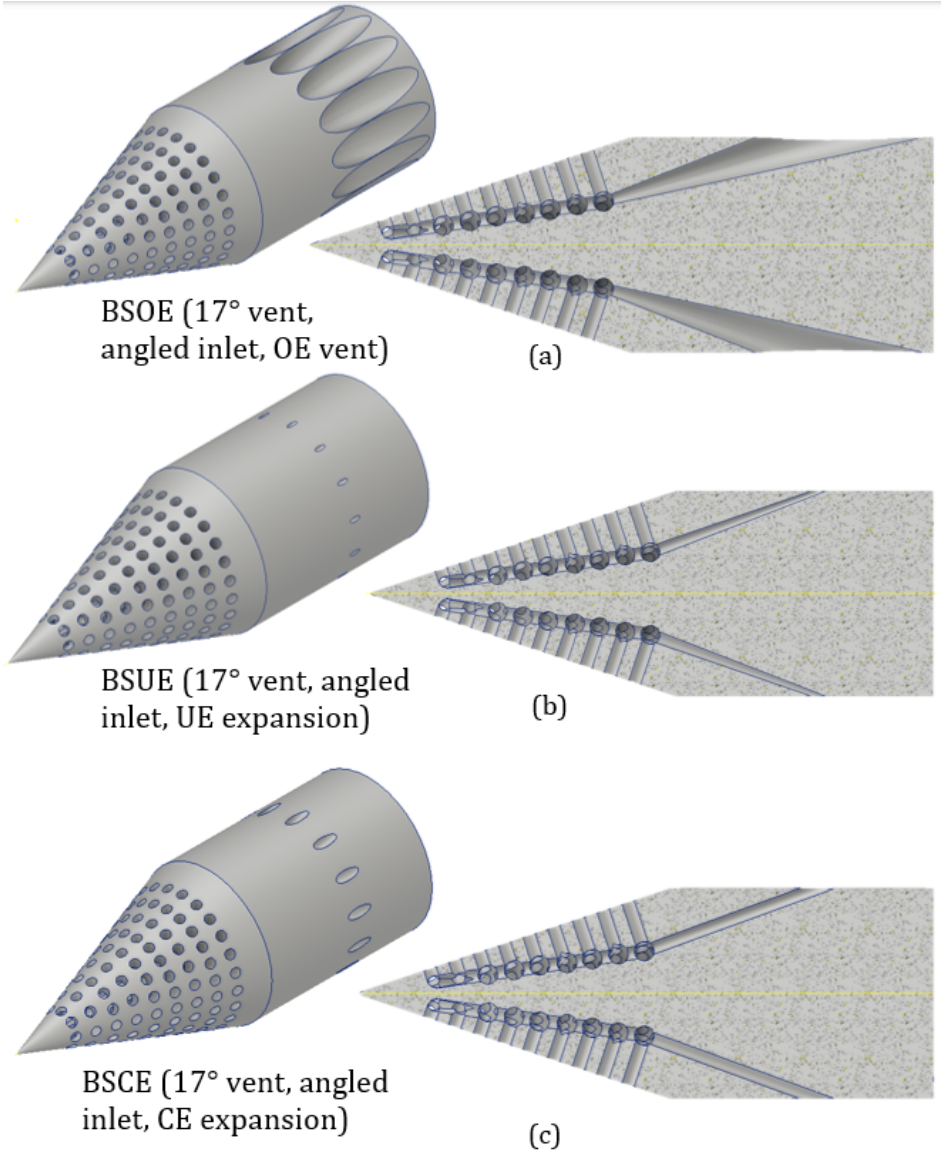

Figure 126: Schematics of pointed cones BS (a) OE (overexpanded) (b) UE (underexpanded) (c) CE (critically expanded) (outside and internal view).

H.4 Pointed cones miscellaneous- HV and 72 Holes

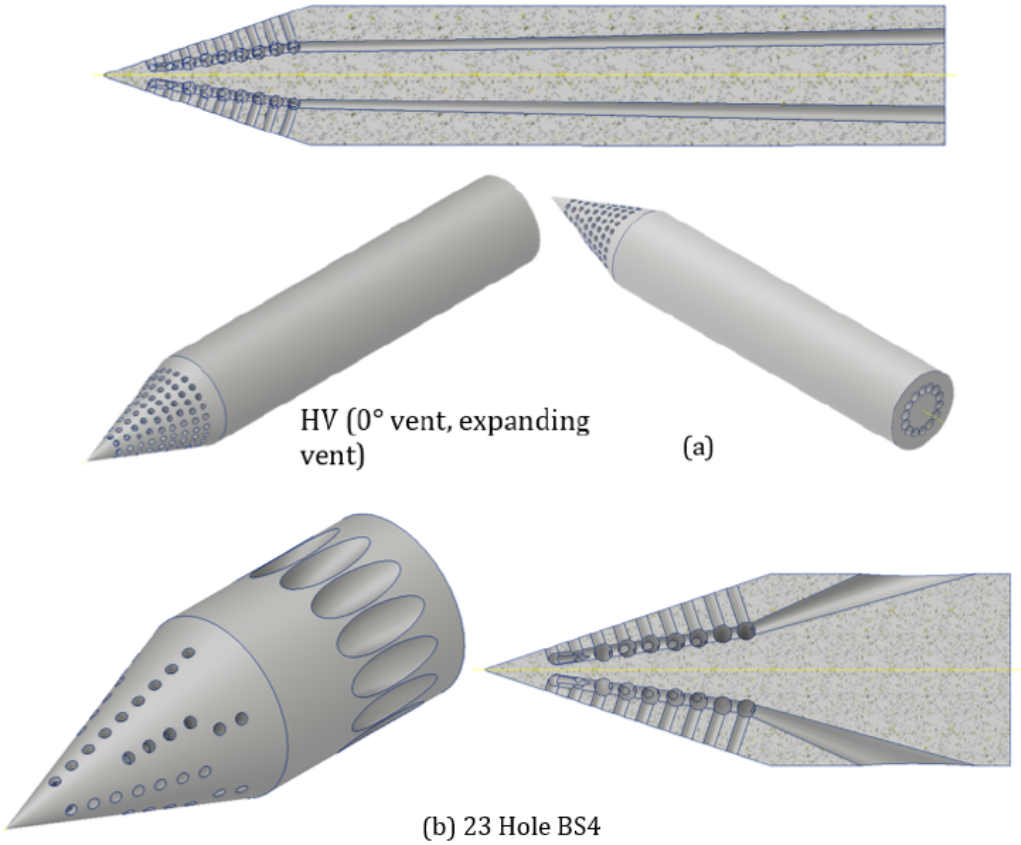

Figure 127: Schematics of cone (a) HV (b) 72 Holes (outside and internal view).

H.5 Hemisphere and secant ogives - Solid and BS4H/S

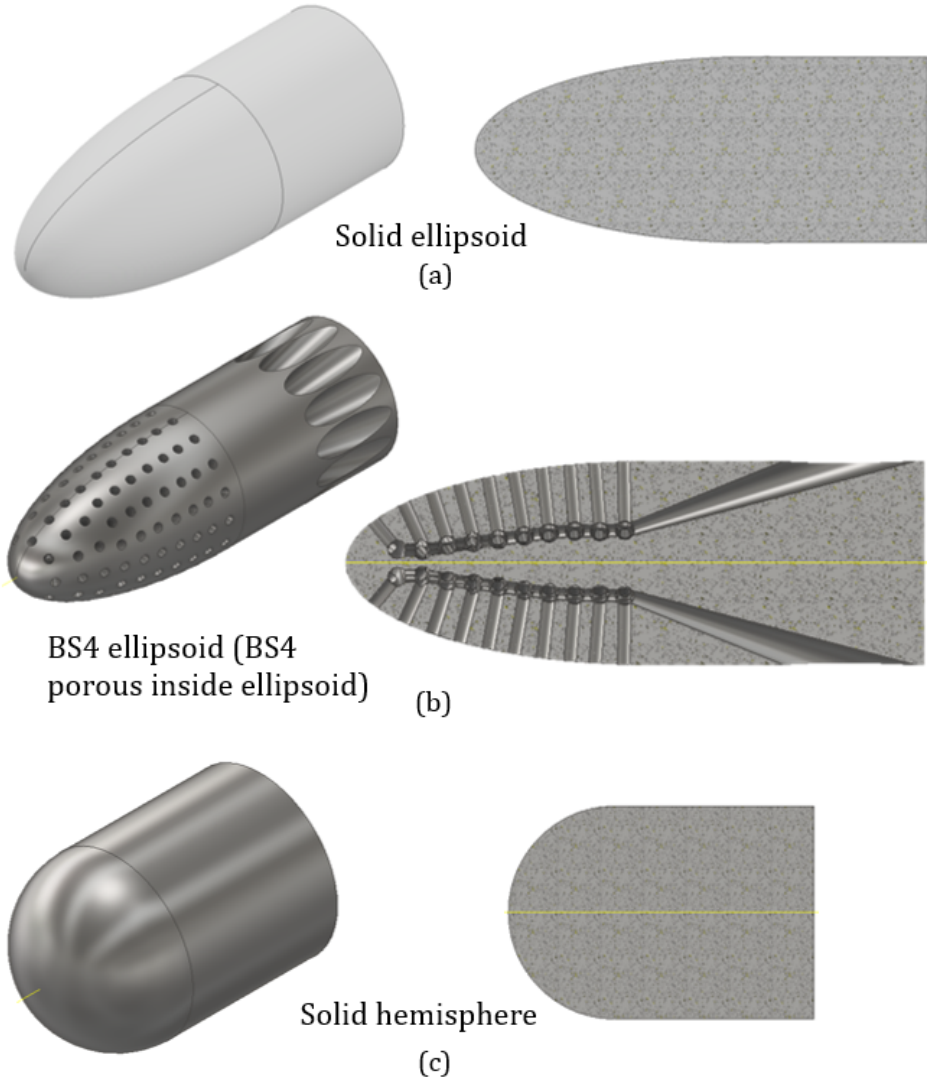

Figure 128: Schematics of cones (a) solid ellipsoid (b) BS4 ellipsoid (c) solid hemisphere.

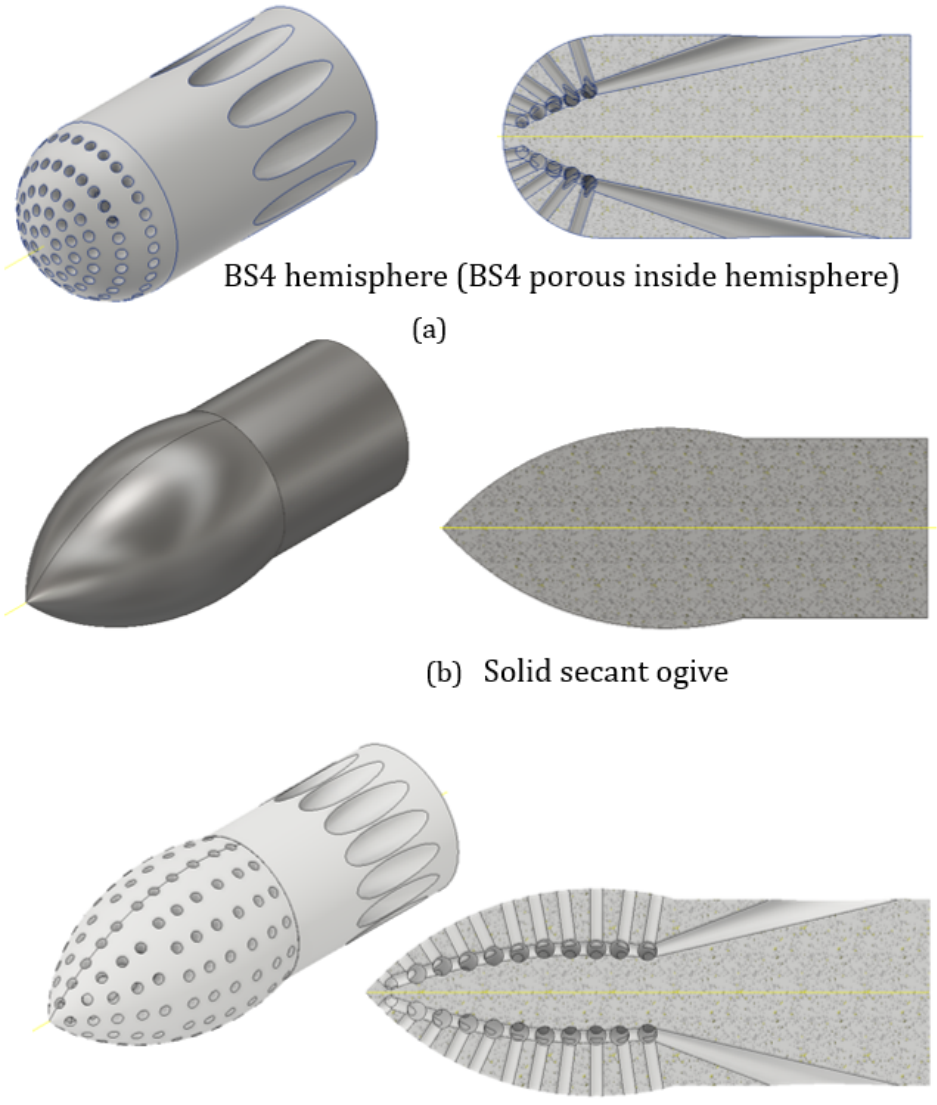

Figure 129: Schematics of cones BS (a) BS4 hemisphere (b) solid secant ogive (c) BS4 secant ogive.